

Markus Ganser

**ON THE ELECTRO-CHEMO-MECHANICAL
COUPLING IN SOLID STATE BATTERIES
AND ITS IMPACT ON MORPHOLOGICAL
INTERFACE STABILITY**

SCHRIFTENREIHE DES INSTITUTS
FÜR ANGEWANDTE MATERIALIEN

BAND 90



**Scientific
Publishing**

Markus Ganser

**On the Electro-Chemo-Mechanical
Coupling in Solid State Batteries
and its Impact on Morphological
Interface Stability**

**Schriftenreihe
des Instituts für Angewandte Materialien
*Band 90***

Karlsruher Institut für Technologie (KIT)
Institut für Angewandte Materialien (IAM)

Eine Übersicht aller bisher in dieser Schriftenreihe erschienenen Bände
finden Sie am Ende des Buches.

On the Electro-Chemo-Mechanical Coupling in Solid State Batteries and its Impact on Morphological Interface Stability

by
Markus Ganser



Karlsruher Institut für Technologie
Institut für Angewandte Materialien

On the Electro-Chemo-Mechanical Coupling in Solid State Batteries
and its Impact on Morphological Interface Stability

Zur Erlangung des akademischen Grades eines Doktor-Ingenieurs
von der KIT-Fakultät für Maschinenbau des Karlsruher Instituts für
Technologie (KIT) genehmigte Dissertation

von Markus Ganser, M. Sc.

Tag der mündlichen Prüfung: 30. April 2020

Referent: Prof. Dr.-Ing. Marc Kamlah

Korreferent: Prof. Dr.-Ing. Thomas Böhlke

Impressum



Karlsruher Institut für Technologie (KIT)

KIT Scientific Publishing

Straße am Forum 2

D-76131 Karlsruhe

KIT Scientific Publishing is a registered trademark
of Karlsruhe Institute of Technology.

Reprint using the book cover is not allowed.

www.ksp.kit.edu



*This document – excluding the cover, pictures and graphs – is licensed
under a Creative Commons Attribution-Share Alike 4.0 International License
(CC BY-SA 4.0): <https://creativecommons.org/licenses/by-sa/4.0/deed.en>*



*The cover page is licensed under a Creative Commons
Attribution-No Derivatives 4.0 International License (CC BY-ND 4.0):
<https://creativecommons.org/licenses/by-nd/4.0/deed.en>*

Print on Demand 2021 – Gedruckt auf FSC-zertifiziertem Papier

ISSN 2192-9963

ISBN 978-3-7315-1047-5

DOI 10.5445/KSP/1000123310

On the Electro-Chemo-Mechanical Coupling in Solid State Batteries and its Impact on Morphological Interface Stability

Zur Erlangung des akademischen Grades
Doktor der Ingenieurwissenschaften
der KIT-Fakultät für Maschinenbau
Karlsruher Institut für Technologie (KIT)

genehmigte
Dissertation
von

Markus Ganser, M. Sc.

Tag der mündlichen Prüfung: 30. April 2020
Referent: Prof. Dr.-Ing. Marc Kamlah
Korreferent: Prof. Dr.-Ing. Thomas Böhlke

Zusammenfassung

Festkörperbatterien mit einer Lithium Metall Elektrode gelten in Bezug auf die erreichbaren Energiedichten als die nächste Generation in der Hochenergie-Batterietechnologie. Lithium Metall tendiert jedoch zu Dendritenwachstum, das ein Zellversagen zur Folge haben kann. Der Einsatz von Festelektrolyten ist ein vielversprechender Ansatz um die Lithium Metall Grenzfläche zu stabilisieren, die Mechanismen und die diesbezüglichen Materialanforderungen sind jedoch bisher weitgehend unbekannt. Im Rahmen dieser Arbeit wird ein elektro-chemo-mechanisches Modell einer binären Festkörperbatterie hergeleitet, um die morphologische Grenzflächenstabilität von Lithium Metall zu analysieren.

Das Modell beinhaltet eine Transporttheorie, welche die Elektrostatik, den Massentransport und die geometrisch nichtlineare Mechanik, darunter das Anschwellen des Elektrolyten beschreibt. Die Butler-Volmer Reaktionskinetik wird derart verallgemeinert, sodass sie mechanische Spannungen an der Grenzfläche berücksichtigt. Zudem wird eine Kinematik vorgestellt, die die Anlagerungs- und Ablöseprozesse als auch mechanische Deformationen während des Ladens und Entladens konsistent beschreibt.

Basierend auf der vorgestellten Theorie werden Einflussgrößen auf die morphologische Stabilität von Polymerelektrolyten untersucht. Die Ergebnisse dieser Analyse zeigen sowohl einen positiven Zusammenhang zwischen den mechanischen Eigenschaften und der Stabilität, als auch, dass bessere Transporteigenschaften die Anforderungen an die Mechanik reduzieren. Die Resultate numerischer Studien sowie analytischen Betrachtungen lassen zudem den Schluss zu, dass Dendritenwachstum insbesondere durch inhomogene Grenzflächenwiderstände entsteht.

Abstract

Solid state batteries with a lithium metal electrode are considered the next generation of high energy battery technology. Unfortunately, lithium metal is prone to harmful protrusion or dendrite growth which causes dangerous cell failure. Although solid state electrolytes have shown a promising potential to stabilize the interface morphology, a clear understanding of the related mechanisms and material requirements is still missing. Within this work the problem of protrusion growth is tackled by deriving a novel electro-chemo-mechanical theory tailored for binary solid state batteries which is then used to discuss the impact of mechanics on interface stability by extensive numerical studies.

An ion transport theory in finite strain continuum mechanics is developed that captures electrostatics, component transport and nonlinear mechanical interaction such as swelling, stress driven diffusion and deformation. An enhanced version of Butler-Volmer reaction kinetics enriched by the influence of mechanics is carefully derive. Furthermore, a model is proposed that consistently describes material deposition during charging and coupled deformation of metal electrode and solid electrolyte.

The comprehensive theory then is used to analyze morphological stability for polymer electrolytes. Quasi static simulations reveal not only that increasing the mechanical stiffness favors interface stability but also that the stiffness required for stability decreases with increasing transport properties. The result of a transient numerical study and an analytical network model show that inhomogeneous interface conductivities are a likely reason for harmful protrusion growth.

Acknowledgements

This doctoral thesis is the result of three challenging and exciting years at the Institute for Applied Materials (IAM-WBM) of the Karlsruhe Institute of Technology (KIT) in a close collaboration with the Cooperate Research department of the Robert Bosch GmbH. Numerous people supported me during this formative time and I would like to sincerely thank all of them.

First and foremost, a special thanks to my supervisor Prof. Dr.-Ing. Marc Kamlah for giving me the opportunity to write this thesis. Every discussion with him was inspiring and encouraging and his thoughtful guidance enabled me to successfully complete this work. I am also deeply grateful to collaborate with Prof. Robert McMeeking. He not only invited me to a three month mindblowing stay at the University of California Santa Barbara (UCSB), a research visit financially supported by a scholarship of the Karlsruhe House of Young Scientists (KHYS), he also impressed me many times in his attitude to tackle complex mechanism in "simple" analytical expressions. In addition, I would like to thank Prof. Dr.-Ing. Böhlke for agreeing to be the second referee of my thesis committee.

I would like to express my deepest gratitude to Felix Hildebrand for continuously supporting, pushing and inspiring me during my PhD time. We already met during my first year at the University of Stuttgart and I am since then impressed by his spirit and deep knowledge. It was also due to his positive influence that I followed up with an academic carrier and by fortunate coincidence, I was then lucky to have him as advisor, colleague and friend.

I would also like to thank my colleagues of the battery project where I had the opportunity to work with an extraordinary interdisciplinary team with many fruitful interactions that went beyond my theoretical focus. I want to address special thanks to Matthias Hanauer and Markus Klinsmann for all the intense discussions and contribution to this work, it was a great pleasure working with you. Furthermore, I thank my colleagues at CR/ARM for the great atmosphere during the PhD time.

I am very grateful to have gone through this challenging time with many awesome fellow doctoral candidates. I especially thank Leonard Blume, who shared live saving snacks with me, and Fabian Simon for all the wonderful discussions - be it technical ones or sometimes necessary distraction. I would further deeply thank Nadine Dannehl and Verena Wurster. I will never forget how we started the challenge of the PhD almost at the same day and, in particular, how we went through the hard times of writing together. It was great having you there. It was also great joy to spend this time with Larissa Kutscha, Felix Ischinger and Samuel Wagner, be it the organization of awesome events within the Bosch PhD program or inspiring discussions after work. Many thanks that you and many more have accompanied me in this demanding time.

Above all, I deeply thank my family for their everlasting support. This work could not have been achieved without having you at my side.

Stuttgart, June 2020

Markus Ganser

Contents

Zusammenfassung	i
Abstract	iii
Acknowledgements	v
1 Introduction	1
1.1 Basics of Lithium Batteries	1
1.1.1 Fields of Application	2
1.1.2 Design and Working Principle	4
1.1.3 Dendrites and Solid State Electrolytes	7
1.2 State of the Art of Battery Modeling	10
1.3 Objectives and Overview	13
2 Mathematical Preliminaries	17
2.1 Kinematics of a Solid Material	17
2.1.1 Deformation Gradient	17
2.1.2 Volume and Surface Transformations	19
2.2 Kinematics of Mobile Components	21
2.2.1 Spatial Description	21
2.2.2 Material Description	23
2.2.3 Reynolds Theorem in Finite Deformations	24

3 Theory of Ion Transport in a Binary Solid Electrolyte	25
3.1 Field Variables	26
3.2 Balance Principles	29
3.2.1 Balance of Mass	29
3.2.2 Balance of Charge and Gauss' law	30
3.2.3 Balance of Linear Momentum	32
3.2.4 Balance of Angular Momentum	33
3.2.5 Balance of Energy	35
3.2.6 Balance of Entropy	39
3.3 2nd Law of Thermodynamics	39
3.4 Material Description	42
3.4.1 Swelling of the Host Material	43
3.4.2 Constitutive Helmholtz Energy	48
3.4.3 Constitutive Equations	50
3.4.4 Multicomponent Mass Flux in Finite Strain	53
3.4.5 Modeling Anisotropy in Solid Electrolytes	55
3.4.6 Relation to Maxwell-Stefan Theory	56
3.4.7 Ionic Current and Mass Fluxes	58
3.5 Binary Electrolyte	61
3.5.1 Full Formulation	63
3.5.2 Towards Balance of Charge	64
3.5.3 Electroneutral Description	65
3.5.4 Steady State Current in a Binary Electrolyte	68
3.5.5 Conversion of Transport Parameters	70
3.5.6 Thermodynamically Consistent Parameters	73
3.6 Summary	74

4 Understanding Ion Transport in a Binary Solid Electrolyte	77
4.1 Simulation Environment	77
4.2 Material Data	78
4.2.1 Electrochemical Transport Parameters	78
4.2.2 Mechanical Properties	81
4.3 Double Layer in a Solid Electrolyte	82
4.3.1 Material	83
4.3.2 Boundary Value Problem	84
4.3.3 Results	84
4.3.4 Discussion	85
4.4 Galvanostatic Charging	86
4.4.1 Boundary Value Problem	87
4.4.2 Results - General Remarks	88
4.4.3 Results from the Full Model	88
4.4.4 Results from the Extended Newman Formalism	91
4.4.5 Discussion	91
4.5 Mechanically Deformed Electrolyte	92
4.5.1 Setup	93
4.5.2 Boundary Value Problem	94
4.5.3 Results	97
4.5.4 Discussion	99
4.6 Summary	99
5 Extended Butler-Volmer Interface Kinetics	101
5.1 State of the Art	102
5.2 General Framework	105
5.2.1 Gibbs Energies of Electrode and Electrolyte	106
5.2.2 Reaction Kinetics	109

5.3	Mechanical Energy of Deposition	119
5.3.1	Macroscopic Motivation	120
5.3.2	Deposition on Ion Scale	122
5.4	Examples	123
5.4.1	Dilute Electrolyte Storage Particle (ideal)	124
5.4.2	Dilute Electrolyte Metal Electrode (w/o mechanics) .	126
5.4.3	Concentrated Electrolyte Storage Particle	126
5.4.4	Concentrated Electrolyte Metal Electrode	128
5.5	Application within Concentrated Solution Theory	130
5.6	Influence of Mechanics	132
5.7	Interface Properties	135
5.8	Summary	137
6	Morphological Stability: A Quasi Static Analysis	139
6.1	The Boundary Value Problem	140
6.2	Effect of Deformation on Interface Current Density	142
6.3	Morphological Stability Map	148
6.3.1	Definition of Morphological Stability	148
6.3.2	Influence of the Protrusion Height	150
6.3.3	Variation between PEO and PS-PEO	151
6.3.4	Variation of Selected Parameter for PS-PEO	152
6.3.5	Heterogeneous Interface Conductivity	155
6.3.6	Discussion	156
6.4	Summary	158
7	The Metal Electrode	161
7.1	Kinematics of Material Deposition	161
7.1.1	Volume Description	162
7.1.2	Interface Compatibility	164

7.1.3 Growth Rate	166
7.2 Material Properties of Lithium Metal	168
7.2.1 Material Model	169
7.2.2 Ohm's law	170
7.3 Summary	171
8 Morphological Stability: A Transient Analysis	173
8.1 The Boundary Value Problem	174
8.2 Analysis of Instability Triggers	177
8.2.1 Four Hypothesis on Trigger Mechanisms	177
8.2.2 Results and Discussion	179
8.3 Stability Analysis	181
8.3.1 Lithium Metal and PEO Electrolyte	182
8.3.2 Lithium Metal and PS-PEO Electrolyte	186
8.3.3 Discussion	189
8.4 An Analytical Assessment of Morphological Stability	191
8.4.1 Network Model of Ion Transport	192
8.4.2 Discussion	195
8.5 Recap of the Coupling Mechanisms	196
8.6 Summary	201
9 Conclusion and Outlook	203
A Nomenclature	207

1 Introduction

1.1 Basics of Lithium Batteries

Batteries are electrochemical storage devices that convert chemical energy into electric energy. Depending on the type of the electrochemical process and the materials used, a number of classes of battery storage devices are distinguished. Usually, one differentiates between primary batteries in which discharge is possible only once due to irreversible processes, and secondary batteries which can be operated reversibly in charge and discharge direction. The state of the art technology in today's secondary batteries is the lithium ion (Li-ion) technology, which dates back to 1970 by Whittingham at Exxon [1]. The first reversible lithium battery was commercialized in the late 1980s by Moli Energy with a lithium metal anode, a MoS₂ cathode material and a liquid electrolyte [2]. Although produced in millions, this early attempt of using a lithium metal anode caused tremendous safety problems, e.g. fire accidents caused by dendrite formation, and had to be recalled. In 1991, Sony was finally able to build a reliable Li-ion secondary battery cell by using ionic lithium with graphite as intercalation material and a liquid electrolyte. The basic concept of this electrochemical storage device has not been changed since then. The graphite material has become the quasi standard and the research focus was shifted to the counter-electrode cathode material.

Recently, batteries with lithium metal anode in combination with solid state electrolytes obtained much attention and might be the successor of Li-ion batteries. These solid state batteries (SSB) feature metallic lithium and solely solid components within the electrochemical cell to increase

energy density and safety beyond the classical Li-ion technology with liquid electrolyte. Furthermore, SSB might pave the way to far-future technologies such as lithium-sulfur and lithium-air where also elemental lithium is utilized.

Although this work is mainly motivated by the challenges of the lithium technology, we emphasize that many ideas can be transferred to alternative materials such as sodium based batteries.

1.1.1 Fields of Application

The availability of high energy secondary battery systems enables connectivity and electrification in daily life. Over the last decades, consumer electronics tremendously changed the way we communicate and work. Forecasts predict that the number of mobile phone users will rise to 4.8 billion people worldwide by 2020 [3]. Thereof, the more sophisticated smartphones have a share of 60%. This success is closely related to durable and affordable batteries with high energy densities. Despite the large amount of devices, the capacity of a standard smartphone in 2018 is quite small with roughly 10 W h, which explains the low fraction in the extrapolated market share, see Fig. 1.1. The rising market of the Internet of Things [4] with several billions of small, connected and battery driven devices will further boost the need for high energy batteries.

As can be seen in Fig. 1.1, most of the predicted battery demand will arise from the mobility sector and especially the automobile market with a single vehicle requiring 5 to 15 kWh [5]. Traditional gasoline and diesel combustion engines exhaust greenhouse gases such as carbonate dioxide and nitrogen oxides that are known to accelerate climate change and harm the individual human health. Several countries therefore enforce the reduction of exhaust emission by subsidizing new environmental friendly technologies or even by banning cars with high exhaust output from the streets [6]. A transportation system with an electrified powertrain

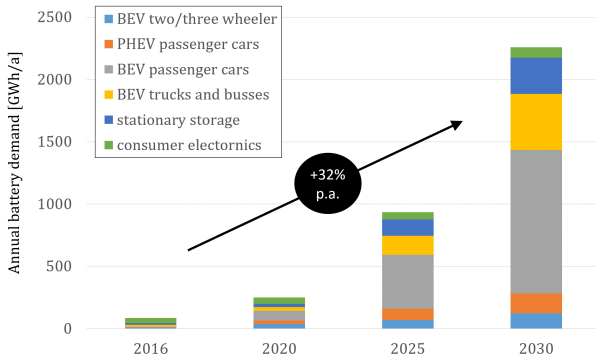


Figure 1.1: The annual battery demand is predicted to increase by 32% per year from 2016 to 2030 according to a recent study by McKinsey [7]. This is strongly driven by the mobility sector such as battery electric vehicles (BEV).

for motorcycles, cars, buses, trucks and even flying vehicles is therefore a logical and necessary step into the future of mobility. Political and economic factors such as oil price development and infrastructure investments further influence the future of mobility concepts. The requirements for electrochemical energy storage in transportation systems are high. The energy density, which is directly related to the driving range, has to reach critical values, especially because the users are accustomed to the high driving ranges of fossil fuels with their excellent energy densities, e.g. gasoline with $1700 \frac{\text{Wh}}{\text{kg}}$ [2]. For comparison, current Li-ion cells exhibit an energy density of up to $250 \frac{\text{Wh}}{\text{kg}}$ and lithium metal batteries have the potential of the double density with up to $440 \frac{\text{Wh}}{\text{kg}}$ [2]. Beyond that, it is mandatory that electrochemical storage devices provide a high level of safety. Hazards due to uncontrolled chemical reaction within the battery e.g. due to production faults [8] or accidents [9] have to be ruled out as far as possible. Other than mobile devices with a life span of approximately two years, batteries in cars also have to last at least one

decade before their capacity decreases below 80% [5]. Another important aspect for the acceptance of batteries in transportation devices is fast charging to enable reasonable waiting times for intermediate recharging stops. All of that has to be achieved for an affordable price, the major factor for the attractiveness of an electrified vehicle. Almost all major automotive manufactures provide or have announced fully or partially electrified vehicles, which can be distinguished in hybrid (HEV), plug-in hybrid (PHEV) and battery electric vehicles (BEV). The ultimate goal in the development of a BEV is to provide the same comfort and similar ranges compared to combustion driven vehicles to gain high customer acceptance.

Other applications for battery systems are stationary energy storages in combination with a smart grid infrastructure. Together with local energy generation such as photovoltaic or wind plants, they can potentially enable self-sustaining energy concepts for both single houses and communities and eliminate dependence on fossil fuels. As can be seen, secondary batteries play an increasingly important role in today's innovation, which explain the intense research activities.

1.1.2 Design and Working Principle

The working principle is very similar for a conventional battery with a liquid electrolyte and a solid state battery with a solid electrolyte and a lithium metal electrode. Fig. 1.2 shows the concept of both types including a description of the electrochemical and mechanical processes. We briefly describe the idea of a conventional battery before introducing the concept and advantages of a solid state battery with a lithium metal electrode.

An ordinary battery has three functional layers, two porous electrodes and an electrically isolating porous separator in between. The three layers are infiltrated by a liquid electrolyte to enable an ion conducting

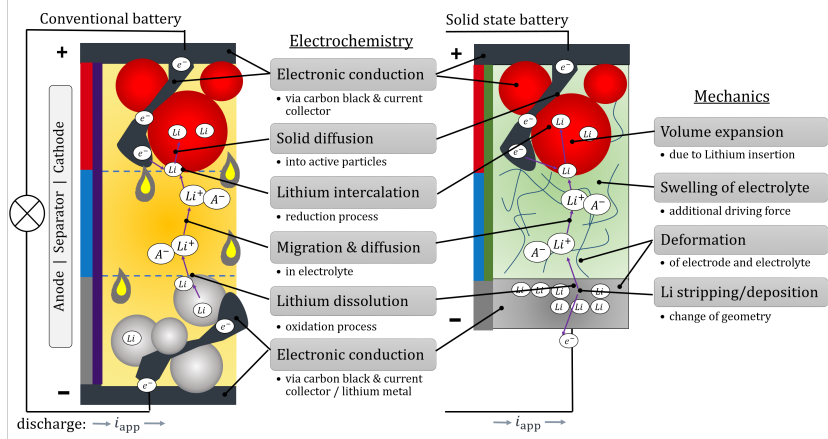


Figure 1.2: Conventional battery with a liquid electrolyte and graphite particles (grey) on the left and a solid state battery with a solid electrolyte and a lithium metal anode on the right. The dominant effects in a conventional battery are purely electrochemical whereas solid state batteries require the additional description of mechanics.

pathway between the two electrodes. A standard liquid electrolyte in Li-ion batteries is based on hexafluorophosphate ($LiPF_6$) as conducting salt and organic compounds, which are stable against the highly reactive ionic lithium. The porous electrodes are a composition of storage particles, binder and conductive carbon. The storage particles have both access to an electric pathway (with the conductive carbon) and to an ionic pathway (via the electrolyte). The storage particles determine the majority of the electrochemical response of the electrode and therefore, when speaking of electrode materials, one usually refers to the storage particles. The binder is necessary to obtain the mechanical integrity of the porous electrode. A commonly used combination of electrode materials is, for example, lithium graphite Li_xC_6 in the anode and lithium iron phosphate $Li_{1-x}FePO_4$ in the cathode where x ranges between 0 and 1. The battery

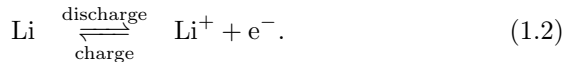
is completely charged for $x = 1$ meaning that the majority of lithium is intercalated in the graphite.

It can be seen that each Li-ion in a porous electrode is accompanied by several other compounds, be it the active storage material or the components to maintain electronic and ionic conductivity such that only a fraction of the electrodes contributes to energy storage. As we will see, one possibility to increase energy density is by substituting the porous anode with metallic lithium.

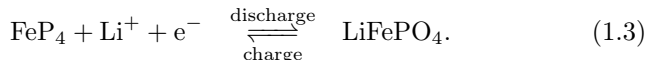
The fundamental principle of energy storage of a secondary battery is hidden in the electrode materials. The electrodes serve as the storage of lithium. Depending on the chemical composition of the electrode material, the electrochemical energy of the ions varies heavily. For example, a lithium metal electrode has a higher energetic level compared to the $\text{Li}_{1-x}\text{FePO}_4$ electrode. This means that Li-ions prefer to form a compound with $\text{Li}_{1-x}\text{FePO}_4$ to being in the metal phase. If the two electrodes are connected by an electronic and ionic pathway and no external voltage is applied, the ions perform a spontaneous reaction from the higher energetic level to the lower one. This is a consequence of the second law of thermodynamics stating that reaction follows the direction which minimizes the total energy. The process can be reversed by applying an external voltage and thus charging the battery. The corresponding reaction equation reads



which is a reduction-oxidation process and can be split into two steps. During discharge (charge) lithium is oxidized (reduced) at the metal electrode,



On the macroscopic level, this means that the amount of metal decreases (increases) layer by layer or, in other words, lithium is stripped from (deposited on) the metal electrode. In the second reaction, the Li-ion is reduced (oxidized) to form lithium iron phosphate



The involved ions and electrons are transferred between the electrodes through the electrolyte and the external circuit, respectively. The process of oxidation is also known as anodic reaction and reduction is known as cathodic reaction. By definition, the electrodes are named during discharge and therefore the lithium metal is denoted as anode and the iron phosphate as cathode. Alternatively, one can utilize the reduction potential (defined against a hydrogen electrode) and refer to the lithium metal with its relatively small reduction potential as negative electrode and the iron phosphate as positive electrode.

1.1.3 Dendrites and Solid State Electrolytes

Enabling batteries with metal electrodes instead of an intercalation material might be one of the next milestones in increasing the energy density in electrochemical energy storage. These systems do not require a storage material at the negative electrode (e.g. graphite, see Fig. 1.2) and therefore offer best in class energy density due to the lowest possible anode potential in combination with the best theoretical gravimetric ($3860 \frac{\text{Ah}}{\text{kg}}$) and volumetric capacity ($2 \frac{\text{Ah}}{\text{cm}^3}$) [2, 10]. However, pure lithium metal is highly reactive and has a low melting temperature of 180.6°C [11]. It is therefore rarely applied and only few characterizations have been executed to describe the complex mechanical response. The Young's modulus of lithium is reported to be $E = 1.9 - 8 \text{ GPa}$ [11–13]. It has a low mechanical strength (the reported strengths ranges from 1 MPa [12]

to 105 MPa [14]), shows visco-plastic behavior [15], is likely to creep and has an anisotropic micro-structure [14].

Unfortunately, a lithium metal electrode is highly unstable against traditional liquid-based electrolytes such as LiPF₆. Heterogeneous nucleation, most likely due to a heterogeneous solid electrolyte interface (SEI), causes an uncontrolled dendrite growth in form of mossy and needle-like structures [16–18] that might cause the battery to fail by short-circuits. For example, Steiger et al. [19] reports filaments of a diameter of approximately 500 nm and complex growing patterns. Several approaches have been presented to prevent dendrite growth in liquid electrolytes [10], e.g. using micro/nanostructures [20], concentrated liquid electrolytes [21] as well as coatings and additives [22] to modify the SEI.

An alternative approach is to substitute the liquid electrolyte and the porous separator with a solid electrolyte to enable metal anodes. The requirements on solid electrolyte materials in this context are a sufficient ionic conductivity of Li-ions, negligible electronic conductivity, a wide electrochemical stability window and mechanical stiffness which is said to suppress harmful dendrites growth. Besides addressing the issues of dendrites, solid electrolytes also have the potential to increase safety, specifically by decreasing flammability compared to liquid based systems [23]. A broad class of solid electrolytes, ranging from inorganic ceramics to polymers, are currently under investigation [24, 25]. Inorganic electrolytes, such as oxidic or sulfidic ceramics, belong to the class of single ion conductors. Usually, they offer a very high ionic conductivity with up to 1 $\frac{\text{S}}{\text{m}}$ at a wide temperature range [25] and mechanical stiffnesses of up to 20 GPa [26]. However, depending on the composition, they have issues with stability against moisture, processing and cost [27]. Furthermore, in combination with lithium metal, they are prone to dendrite growth in the grain boundaries [28], suffer from adhesive problems [29] and are therefore not yet ready for the mass market.



Figure 1.3: Protrusion growth in polymer electrolytes: (a) Photograph of a protrusion growth in a PEO polymer at high current density (taken from Brissot et al. [30]). (b) Three 3D renderings from a X-ray microtomography of a PS-PEO polymer (taken from Harry et al. [31]).

This work focuses on the class of polymer electrolytes that act as a solid solvent for a salt such as LiTFSi. In these electrolytes, both anions and cations are mobile leading to the classification as a binary conducting electrolyte. The most prominent polymer electrolyte is poly(ethylene oxide) (PEO). It is thermodynamically stable against lithium (up to 100 °C [32]), less flammable than liquid electrolytes and is usually operated at elevated temperatures in order to exceed the glass transition temperature (\sim 60 °C) to obtain sufficient ionic conductivity ($0.1 \frac{S}{m}$ [33]). The ion transport is in that case supported by segmentation motion of the PEO chains. However, at temperatures of e.g. 80 °C, PEO is viscous and, hence, tends to lose its mechanical integrity. Nevertheless, it is partially able to suppress classical mosslike dendrites but suffers from lithium intrusion on the length scale of micrometers [30, 34, 35] as shown in Fig. 1.3a.

Several polymer modifications have been suggested in order to increase electrochemical properties as well as mechanical strength [32, 36, 37], e.g. via adding ceramic nanoparticles [38], cross linking [39–41] or using gel electrolytes such as double polymer networks [42], zwitterionic copolymers [43] or ionic liquid-immobilized polymers [44]. Another approach are block/triblock copolymers [45–48] such as PS-PEO which follow the idea that a soft block (PEO) forms lithium conducting channels and a hard

block of polystyrene (PS) provides the mechanical strength. Nanochannels of ~ 10 nm [45] are able to conduct ions but block the growth of the beforementioned mosslike dendrites. Unfortunately, the microscopic structure of block copolymers reduces the transport properties since non-conducting material (PS) is added and also the segmentational motion of PEO is hindered [32, 49].

Although block copolymers decrease the likelihood and speed of harmful protrusion growth [31], the so-called globule and multi-globular structures [50] remain a challenge (see Fig. 1.3b). Recent experimental studies correlate their appearance with sub surface structures [51] and impurities [50] in the lithium metal anode. However, the exact mechanisms causing the undesired protrusion growth and the measures necessary to suppress them are questions of ongoing research.

Exploring undesired dendrite growth in experiments as well as synthesizing, processing and testing new kinds of solid electrolytes is complex, time-consuming and costly. Therefore, it is beneficial to derive mathematical models that accurately describe relevant effects of electrochemistry, mechanics and their coupling in order to increase the understanding of the different phenomena in solid state batteries.

1.2 State of the Art of Battery Modeling

Different theoretical model description have been proposed to assess the complex response in battery systems. One can distinguish models for single ion conductors (e.g. [52]) and more sophisticated models for binary electrolytes. Binary electrolytes are usually described by the well-established concentrated solution theory [53], initially derived for liquid electrolytes and later applied to binary solid state electrolytes [54]. The ion transport of non-ideal electrolytes is parametrized by four measurable transport parameters, namely conductivity, transference number,

diffusivity and thermodynamic factor [55–57]. Ferrese et al. [58] and subsequent works [59, 60] combine the conventional concentrated solution theory with a mechanical model to describe the in-plane redistribution of lithium metal during cycling. However, effects of stress driven diffusion, as e.g. known in active storage particles [61–67], are not taken into account even though quite stiff materials are assumed. Bucci et al. [68] propose a multi-component transport model of charged species in a deformable host. Similar ideas are found e.g. in hydrogels, where small molecules diffuse in a network of long fibers and where a change of local component concentration leads to heterogeneous swelling or shrinkage of the host material and consequently to mechanical stresses, which can in turn provide an additional driving force for diffusion [69].

Another ingredient for the description of an electrochemical system is the rate in which ions are deposited on and stripped from an interface. The Butler-Volmer equation is a well established form of reaction kinetics and relates the current density, to a jump of the electric potential along an interface [70]. The most prominent extension of the Butler-Volmer equation with respect to mechanics was proposed by Monroe and Newman [71], describing a dependence of the exchange current density on the mechanical stress of electrode and electrolyte. This serves as a starting point for several numerical studies, e.g. [58, 72–74] on morphological stability. Only some experimental evidence is available that indicates a correlation of interface kinetics and mechanics [75, 76].

Various studies have been presented to gain better understanding of dendrite growth in battery systems. Chazalviel [77] relates morphological stability of lithium with liquid electrolyte with the electrochemical transport properties of a binary electrolyte arguing that an anion depletion and therefore large electric fields are the cause of dendrite growth. His model predicts a correlation of dendrite growth time and the time until an anion depletion occurs, the so called Sand's time [29, 78]. Although

this behavior is linked to high current densities, similar findings have been observed for low current densities [78].

Other studies relate reaction kinetics at an SEI with the morphological stability of a lithium metal electrode. Barton and Bockris [79] discuss the impact of surface energies, which turns out to be of high relevance for dendrite radii in the range of 5 nm [80], but not for classical dendrites [81]. The model was extended by non-linear reaction kinetics [82], reevaluated with respect to thermodynamic reference points of PEO [83] and extended with mechanics [72]. The work of Monroe and Newman [72] is frequently cited and states that stable deposition can be achieved if the shear modulus of the separator is twice as high compared to a lithium metal electrode, and serves as starting point for more recently published studies [73, 84, 85]. However, Barai et al. [86] recognized an unphysical mechanical stress state in the analysis of Monroe and Newman [72] and conclude that, according to this type of analysis, no stable deposition is possible, only the growth speed can be slowed down. A follow up work discusses the impact of the non-elastic material properties of lithium for deposition [74]. Raj and Wolfenstine [87] describe the nucleation of dendrites within a ceramic electrolyte as a function of fracture strength.¹ Tikekar et al. [88] apply a perturbation analysis to study structured electrolytes neglecting elastic stiffness. This work was extended in a subsequent works Tikekar et al. [89, 90] by mechanics stating that modest Young's moduli are sufficient for morphological stability. Their result, however, was questioned by McMeeking et al. [91] who determine an analytic expression for the maximal wavelength of an heterogeneous metal electrode in contact with a single ion conductor as a function of elasticity and charging rate. Natsiavas et al. [92] deduce with an asymptotic analysis a positive effect of prestress onto surface roughening during cycling.

¹ Nucleation of Li-ions to lithium metal requires an supply of electrons which is not considered by Raj and Wolfenstine [87].

Klinsmann et al. [93] predict the requirements of ceramic electrolytes to resist cracking due to lithium growth.

Transient models of deposition and stripping during charge and discharge provide insights into the growing patterns of heterogeneous lithium growth. Ferrese et al. [58] combined in the first step the concentrated solution theory with an explicit model of boundary velocity and extended the model in a second step with the mechanical response of a stiff separator [59, 60]. Further approaches to understand dendrite growth on different length scales are phase field [94, 95], stochastic [96] and atomistic models [97].

1.3 Objectives and Overview

In this work, we seek a deeper understanding of the morphological interface stability of a solid state battery with a lithium metal electrode. To do so, we have to understand the multi-physics of the interface between lithium metal and solid electrolyte as well as the response of the adjacent materials, the solid electrolyte and the metal electrode.

We aim for a sound description for a binary solid electrolyte. Three properties of ions within the electrolyte have to be considered. First, the ions carry electric charge and thus are affected by an electric field. Second, diffusion of the different species has to be described and third, the size of the ions has to be accounted for. The former two involve non-idealities due to complex multi-component transport and require a concentration-dependent parametrization as known from the concentration solution theory [53]. Redistribution of ions of certain volume within a host material yields to swelling that has to be accounted for. Furthermore, the formulation has to capture the effect of deformation caused by e.g., an intrusion.

Another key aspect to understand protrusion growth is the determination of the deposition and stripping rate at the metal electrode. From an electrochemical point of view, this is usually done via the Butler-Volmer reaction kinetics describing the interface current density. However, it is not trivial to answer the questions of whether and how mechanics influence the reaction at an interface. We aim for a well defined formulation of the Butler-Volmer equation considering both electrochemistry and mechanics.

Furthermore, we want to describe the deposition and stripping process at the metal electrode involving geometrical changes. Together with an adjacent solid electrolyte, we expect a deformation of both electrolyte and the electrode if deposition occurs inhomogeneously. The complex interplay of deformation and electrochemistry shall be described in the course of this work.

Eventually, we want to deduce requirements for the electro-chemo-mechanical properties of the solid electrolyte such that morphological interface stability is achieved. Two comprehensive studies shall give insights into the correlation of mechanics and transport. The findings shall help to design robust solid electrolytes which are able to prevent harmful protrusion growth and pave the way for the next generation of energy storage.

This work is structured as follows: We briefly introduce some mathematical preliminaries in the context of finite strain continuum mechanics in **Chapter 2**. We then gradually increase the complexity of the battery modeling.

Chapter 3 presents the derivation of an electro-chemo-mechanical transport model of a binary solid electrolyte. Using conservation of mass, momentum, energy and entropy in combination with the second law of thermodynamics and Gauss' law, we derive a generic framework for multi-component transport in solid electrolytes. We then introduce constitutive models for the solid electrolyte and derive a simplified model based on the assumption of local electroneutrality in the spirit of concentrated

solution theory but extended by mechanical driving forces induced e.g. by swelling processes.

Thereafter, in **Chapter 4**, we introduce the electrochemical transport properties that are used throughout this work and analyze the ion transport in a solid electrolyte and its electro-chemo-mechanical coupling mechanisms with three examples. A blocking electrode setup shows the need of a model that solves the Poisson equation. The second example deals with galvanostatic charging and determines the influence of elasticity on the transport performance. The third example describes an externally deformed solid electrolyte and highlights the need of the comprehensive electro-chemo-mechanical model.

In **Chapter 5**, we present a rigorous derivation of an extended form of the Butler-Volmer equation based on the transition state theory. We put special emphasis on the mechanics of deposition and stripping. Furthermore, we present a novel concept which generalizes the Butler-Volmer reaction kinetics by means of electrode, electrolyte and barrier energies. This allows us to deduce standard formulations for reaction kinetics in liquid and solid battery systems found in literature as well as a consistent description of how mechanics influence the reaction kinetics.

Using the electro-chemo-mechanical transport model and the novel interface description, we carry out a first interface stability analysis in **Chapter 6**. We analyze the impact of the elastic stiffness at a perturbed interface and study the correlation of the required mechanical stiffness for stability and transport parameter using the parametrization of the two polymer electrolytes PEO and PS-PEO. Moreover, we vary selected transport and geometric parameters to determine their influence on the morphological interface stability.

Chapter 7 deals with the description of the metal electrode. The deposition and stripping of material is determined by the interface current. Besides the formulation of finite strains within the metal electrode, we discuss a second mapping to describe the growth of material. Two possible

compatibility conditions between electrode and electrolyte are presented. Furthermore, we describe Ohm's law in finite strain.

In **Chapter 8**, we carry out a second stability analysis by which the growth of lithium adjacent to a solid electrolyte is simulated. We discuss several hypotheses for the trigger mechanism of protrusion growth. Furthermore, we investigate the influence of the elastic stiffnesses on the growth velocity for both polymer electrolytes PEO and PS-PEO. To rationalize the findings, we present a analytical network model for an in-plane current that causes protrusion growth.

We conclude this work and give a brief outlook in **Chapter 9**.

2 Mathematical Preliminaries

In this chapter, we present mathematical preliminaries to lay the foundation for the description of solid electrolytes (Chapter 3) and metal electrodes (Chapter 7). Since solid electrolytes consist of a mechanically stiff host with mobile components, we utilize concepts of solid mechanics and mixture theory. We employ the concept of finite strain continuum mechanics [98, 99] to describe the kinematics of the host material of the solid electrolyte and the metal electrode. Hereby, the mathematical equations are written in a reference configuration associated to a undeformed material state, which is also known as the Lagrangian point of view. The motion of mobile components is commonly modeled within a mixture theory [100] in the Eulerian point of view where a fixed control volume acts as observer. We are going to combine both ideas by associating the fixed control volume of the Eulerian representation with the deformable host material. Furthermore, we link the motion of mobile components with the Lagrangian description. We note that this chapter is partially based on the work of Ganser et al. [101].

2.1 Kinematics of a Solid Material

2.1.1 Deformation Gradient

Following Holzapfel [98] and Truesdell and Noll [99], we employ the framework of finite strain continuum mechanics, and describe the deformation of a solid material at time $t \in T$ by the mapping φ_t between a reference

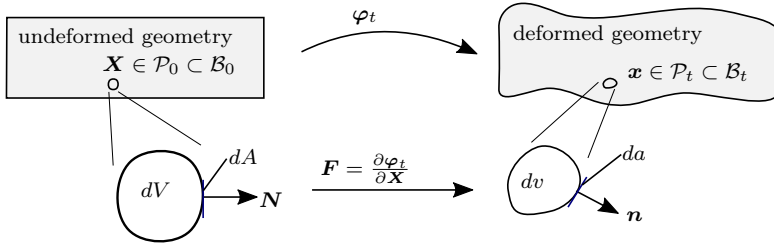


Figure 2.1: The mapping φ_t correlates undeformed (material) and deformed (spatial) geometry \mathcal{B}_0 and \mathcal{B}_t , respectively. Each property in the spatial description such as the volume element dv , area element da or normal vector \mathbf{n} is related via the deformation gradient \mathbf{F} to the material description of the corresponding properties dV , dA and \mathbf{N} .

configuration $\mathcal{B}_0 \subset \mathbb{R}^3$ with material coordinates $\mathbf{X} \in \mathcal{B}_0$ and deformed configuration $\mathcal{B}_t \subset \mathbb{R}^3$ with spatial coordinates $\mathbf{x} \in \mathcal{B}_t$, such that

$$\varphi_t := \begin{cases} \mathcal{B}_0 \times T \rightarrow \mathcal{B}_t \\ (\mathbf{X}, t) \mapsto \mathbf{x} = \varphi_t(\mathbf{X}), \end{cases} \quad (2.1)$$

as seen in Fig. 2.1. Accordingly, the material and spatial velocity of the material are given by

$$\mathbf{V}_0 = \dot{\varphi}_t(\mathbf{X}) := \frac{\partial}{\partial t} \varphi_t(\mathbf{X}) \quad \text{and} \quad \mathbf{v}_0 = \dot{\varphi}_t(\varphi_t^{-1}(\mathbf{x})). \quad (2.2)$$

The displacement of the material is $\mathbf{u} = \mathbf{x} - \mathbf{X}$. To describe local stretches and rotations, we make use of the deformation gradient \mathbf{F} defined by

$$\mathbf{F} = \frac{\partial \varphi_t}{\partial \mathbf{X}} = \frac{\partial \mathbf{x}}{\partial \mathbf{X}} = \text{Grad}(\mathbf{x}), \quad F_{ij} = \text{Grad}_j(x_i) = \frac{\partial x_i}{\partial X_j}. \quad (2.3)$$

The determinant $\mathbb{J} = \det \mathbf{F}$ thereby describes the mapping between material volume elements $dV \subset \mathcal{B}_0$ and their deformed spatial counterparts $dv \subset \mathcal{B}_t$, i.e.

$$\frac{dv}{dV} = \det \mathbf{F} =: \mathbb{J} > 0, \quad (2.4)$$

where the positivity constraint is required to avoid interpenetration of matter. The deformation gradient can be uniquely decomposed into a rotation and a stretch according to

$$\mathbf{F} = \mathbf{R}\mathbf{U}, \quad (2.5)$$

where \mathbf{R} is a orthogonal rotation tensor and \mathbf{U} is the right stretch tensor. The former describes rigid rotation ($\mathbf{R}^T \mathbf{R} = \mathbf{I}$) and the latter is positive definite, symmetric ($\mathbf{U} = \mathbf{U}^T$) and measures the local stretch (or contraction) along the orthogonal eigenvectors.

2.1.2 Volume and Surface Transformations

Note that all quantities and equations can be formulated both in the referential and the spatial setting. Since the physical interpretation is more intuitive in the spatial setting, we will usually formulate governing equations in the spatial form and transform them to the material formulation, which is the natural setting for a numerical treatment. From here on, whenever possible, we use lower case symbols for the spatial quantities (e.g. \mathbf{x} , c_α) and upper case symbols or diamond superscript (e.g. \mathbf{X} , c_α^\diamond) for the material quantities.

With the help of the deformation gradient \mathbf{F} , one can describe the mapping of tangential and normal vectors between material configuration (\mathbf{N}, \mathbf{T}) and spatial configuration (\mathbf{n}, \mathbf{t}) as

$$\mathbf{t} = \mathbf{FT} \quad \text{and} \quad \mathbf{n} = \mathbf{F}^{-T} \mathbf{N}, \quad (2.6)$$

see e.g. Holzapfel [98]. The integrals in the material and spatial configuration coincide for properly transformed quantities. The volume and the surface integrals (with spatial and material surface element $da \subset \partial\mathcal{P}_t$ and $dA \subset \partial\mathcal{P}_0$, respectively) thus are

$$\int_{\mathcal{P}_t} \mathbf{y} dv = \int_{\mathcal{P}_0} \mathbf{Y} dV \quad \text{and} \quad \int_{\partial\mathcal{P}_t} \tilde{\mathbf{y}} \cdot \mathbf{n} da = \int_{\partial\mathcal{P}_0} \tilde{\mathbf{Y}} \cdot \mathbf{N} dA, \quad (2.7)$$

where \mathbf{y} is a scalar or vector field defined on the domain \mathcal{P}_t and $\tilde{\mathbf{y}}$ a vector field defined on the boundary $\partial\mathcal{P}_t$, respectively. The corresponding material properties are

$$\mathbf{Y} = \mathbb{J} \mathbf{y} \quad \text{and} \quad \tilde{\mathbf{Y}} = \mathbb{J} \tilde{\mathbf{y}} \mathbf{F}^{-T}. \quad (2.8)$$

The latter is known as Nanson's relationship.

Now consider a scalar quantity \hat{y} defined on a deformed surface. Its scalar material counterpart \hat{Y} will differ because the effective size of the material area element dA is different to the spatial area element da . However, the identity

$$\int_{\partial\mathcal{P}_0} \hat{Y} dA = \int_{\partial\mathcal{P}_t} \hat{y} da \quad (2.9)$$

has to apply. To obtain a relation between \hat{y} and \hat{Y} , we insert $\mathbf{N} \cdot \mathbf{N} = 1$ on the left hand side and $\mathbf{n} \cdot \mathbf{n} = 1$ on the right hand side. We then use Eq. (2.7) and multiply both sides with \mathbf{N} to obtain

$$\hat{Y} = \mathbb{J} \mathbf{n} \mathbf{F}^{-T} \cdot \mathbf{N} \hat{y} = \frac{\mathbb{J}}{\mathbf{F} : (\mathbf{n} \otimes \mathbf{N})} \hat{y}. \quad (2.10)$$

The normals \mathbf{N} and \mathbf{n} are both normalized. Hence we have $\mathbf{n} \neq \mathbf{F}^{-T} \mathbf{N}$ and Eq. (2.10) cannot be simplified further.

Note that material points in \mathcal{P}_0 are usually associated with an undeformed material. Since \mathcal{P}_0 is a reference description, it is independent of time and thus the integral operator and time derivatives are interchangeable

$$\frac{d}{dt} \int_{\mathcal{P}_0} \mathbf{Y} dV = \int_{\mathcal{P}_0} \frac{d}{dt} \mathbf{Y} dV = \int_{\mathcal{P}_0} \dot{\mathbf{Y}} dV. \quad (2.11)$$

The property of Eq. (2.11) does not hold for an integral formulated in the spatial configuration.

2.2 Kinematics of Mobile Components

We describe the motion of mobile components with respect to a control volume associated to a host material in both spatial and material configurations. Fig. 2.2 gives an overview of the various transformation steps which will be discussed in the following.

2.2.1 Spatial Description

We assume that a species α is distributed as a continuum in a control volume $\mathcal{P}_t^\alpha \subseteq \mathcal{B}_t$. Postulating that \mathcal{P}_t^α coincides at time t with a control

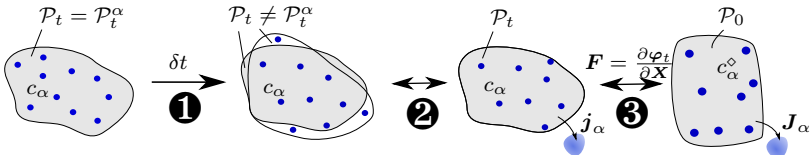


Figure 2.2: Transformation steps: ❶ Host domain \mathcal{P}_t and species domain \mathcal{P}_t^α underly a different motion during a timestep δt . ❷ With the Reynold's theorem, one considers the change of concentration within the host material in terms of a mass flux \mathbf{j}_α . ❸ All quantities can be expressed with respect to a material, undeformed configuration \mathcal{P}_0 .

volume \mathcal{P}_t associated to a host material moving at velocity $\mathbf{v}_0 = \dot{\varphi}_t$, volume and surface integrals coincide at time t :

$$\int_{\mathcal{P}_t^\alpha} \mathbf{y} dv_\alpha = \int_{\mathcal{P}_t} \mathbf{y} dv \quad \text{and} \quad \int_{\partial \mathcal{P}_t^\alpha} \tilde{\mathbf{y}} \cdot \mathbf{n} da_\alpha = \int_{\partial \mathcal{P}_t} \tilde{\mathbf{y}} \cdot \mathbf{n} da, \quad (2.12)$$

If the number of moles of species α in the control volume element dv is given by dN_α , we can define the spatial molar concentration as

$$c_\alpha = \frac{dN_\alpha}{dv}. \quad (2.13)$$

The spatial concentration c_α describes the amount of species of type α per deformed volume dv .

Now, let the species in \mathcal{P}_t^α move at velocity \mathbf{v}_α , which is in general different from \mathbf{v}_0 . If we consider the rates, we have to take the different time-dependencies of the integration domains \mathcal{P}_t^α and \mathcal{P}_t into account

(❶ in Fig. 2.2). To describe the relative motion as seen in ❷ of Fig. 2.2, we use Reynold's theorem

$$\begin{aligned} \frac{d}{dt} \int_{\mathcal{P}_t^\alpha} \mathbf{y} dv_\alpha &= \frac{d}{dt} \int_{\mathcal{P}_t} \mathbf{y} dv + \int_{\partial \mathcal{P}_t} \mathbf{y} ((\mathbf{v}_\alpha - \mathbf{v}_0) \cdot \mathbf{n}) da \\ &= \frac{d}{dt} \int_{\mathcal{P}_t} \mathbf{y} dv + \int_{\partial \mathcal{P}_t} \frac{1}{c_\alpha} \mathbf{y} (\mathbf{j}_\alpha \cdot \mathbf{n}) da, \end{aligned} \quad (2.14)$$

where we have introduced the quantity

$$\mathbf{j}_\alpha = c_\alpha (\mathbf{v}_\alpha - \mathbf{v}_0) \quad (2.15)$$

which will turn out to be the molar mass flux of species α . The second term on the right hand side of Eq. (2.14) denotes the influx of volume quantity \mathbf{y} into the host domain due to a relative velocity of the species with respect to the host.

2.2.2 Material Description

The third transformation in Fig. 2.2 is necessary to obtain a continuum description of the mobile components with respect to the referential configuration of the host material. Therefore, we define a material concentration similar to Eq. (2.13) and link it to the spatial concentration by Eq. (2.4), which yields

$$c_\alpha^\diamond = \frac{dN_\alpha}{dV} = \mathbb{J}c_\alpha. \quad (2.16)$$

Furthermore, we use Eq. (2.8) to transform the spatial quantity \mathbf{j}_α from Eq. (2.15) into the material configuration with

$$\mathbf{J}_\alpha = \mathbb{J}\mathbf{F}^{-1}\mathbf{j}_\alpha. \quad (2.17)$$

2.2.3 Reynolds Theorem in Finite Deformations

Combining Eq. (2.7) with Eq. (2.14) and using $\frac{\mathbf{y}}{c_\alpha} = \frac{\mathbb{J}\mathbf{y}}{\mathbb{J}c_\alpha} = \frac{\mathbf{Y}}{c_\alpha^\diamond}$ gives us the transformation to link moving species within a reference description of matter via

$$\frac{d}{dt} \int_{\mathcal{P}_t^\alpha} \mathbf{y} dv_\alpha = \int_{\mathcal{P}_0} \dot{\mathbf{Y}} dV + \int_{\partial\mathcal{P}_0} \frac{1}{c_\alpha^\diamond} \mathbf{Y} (\mathbf{J}_\alpha \cdot \mathbf{N}) dA. \quad (2.18)$$

The divergence theorem $\int_{\partial\mathcal{P}_0} \mathbf{Y} \cdot \mathbf{N} dA = \int_{\mathcal{P}_0} \text{Div}(\tilde{\mathbf{Y}}) dV$ with the definition of the divergence operator $\text{Div}(\tilde{\mathbf{Y}}) = \frac{\partial(\tilde{Y}_\alpha)_i}{\partial X_i}$. yields a fully volumetric description with

$$\begin{aligned} \frac{d}{dt} \int_{\mathcal{P}_t^\alpha} \mathbf{y} dv_\alpha &= \int_{\mathcal{P}_0} \dot{\mathbf{Y}} + \text{Div} \left(\frac{1}{c_\alpha^\diamond} \mathbf{Y} \otimes \mathbf{J}_\alpha \right) dV \\ &= \int_{\mathcal{P}_0} \dot{\mathbf{Y}} + \text{Grad} \left(\frac{1}{c_\alpha^\diamond} \mathbf{Y} \right) \mathbf{J}_\alpha + \frac{1}{c_\alpha^\diamond} \mathbf{Y} \text{Div}(\mathbf{J}_\alpha) dV, \end{aligned} \quad (2.19)$$

where we have applied the chain rule to obtain the second line. Eq. (2.19) relates the rate of change of a quantity \mathbf{y} in a moving domain \mathcal{P}_t^α to an undeformed reference state.

3 Theory of Ion Transport in a Binary Solid Electrolyte

Within this chapter, we establish a consistent model for ion transport in a deformable host. Based on the work of Ganser et al. [101], we exploit concepts of finite strain continuum mechanics, rigorously consider electrostatic influences and use standard notation of electrochemistry. With the help of the thermodynamic framework of Helmholtz energy and a series of consecutive steps deriving the physics and electrochemistry, a clear and consistent picture of the interdependencies of electrochemistry and mechanics is drawn, leading to a combination of ideas from multicomponent mass flow under the influence of an electric field with finite deformation theory for the mechanical response of the host. Both a treatment based on Gauss' law for a system containing unbalanced charges and an electroneutral version for a binary electrolyte are presented, thereby establishing a link to the well known concentrated solution

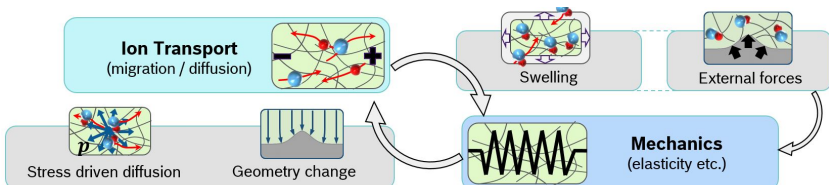


Figure 3.1: Representation of the coupling between multicomponent ion transport and mechanics in a solid state electrolyte. Mechanical response in the form of geometry changes and stresses is triggered by swelling or external forces. The ions are subject to this change of geometry and mechanical driving forces give rise to stress driven diffusion.

theory [53] similar to Monroe and Delacourt [102] by introducing local electroneutrality and by linking the commonly used transport parameters conductivity, transference number, diffusivity and thermodynamic factor to mobilities and chemical potentials. Non-idealities usually associated with a concentrated solution are thereby accounted for.

Throughout the derivation, specific care is taken in considering coupling mechanisms between ion transport and mechanics. In the spirit of Bucci et al. [68], we include coupling mechanisms such as swelling, stress driven diffusion and the change of geometry on which the transport takes place, see Fig. 5.3. Similar couplings between transport and mechanics are also present in hydrogels, where small molecules diffuse in a network of long fibers and where a change of local component concentration leads to heterogeneous swelling or shrinkage of the host material and consequently to mechanical stresses, which can in turn provide an additional driving force for diffusion [69]. Similar relations between swelling and transport are also found in the context of battery active materials [61–67].

In the following, we present the fundamentals of conservation laws in electro-chemo-mechanical systems, introduce Helmholtz energies and their relation to constitutive material properties, discuss the swelling mechanism and introduce thermodynamically consistent mass fluxes. Eventually, we conclude the chapter with a theory for binary solid electrolytes similar to those in concentrated solution theory [53] but extended by mechanical driving forces.

3.1 Field Variables

For the description of the fully coupled electro-chemo-mechanical system we distinguish between a solid host $\alpha = 0$ and N species with indices $\alpha = 1 \dots N$ that can move relative to the host. The electroneutral host

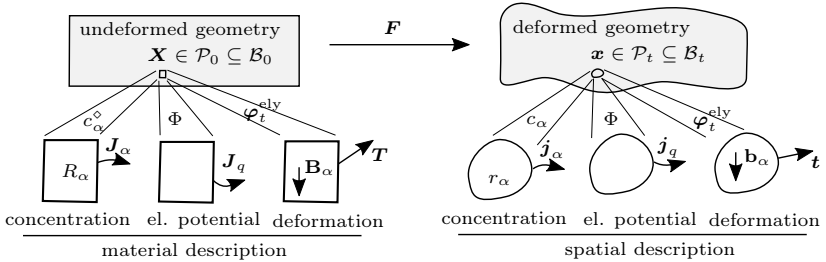


Figure 3.2: An undeformed geometry provides the material description where all balance equations are solved. The deformed geometry as well as spatial field variables are linked to material counterparts via the deformation gradient \mathbf{F} .

provides the mechanical strength whereas the (ionic) mobile components act as charge carrier.

As introduced in Section 2.1, we characterize the kinetics of the host with a mapping φ_t^{ely} , see Eq. (2.1). The deformation gradient \mathbf{F}^{ely} of Eq. (2.3) depicts local stretches and rotations. For the sake of simple notation, we will drop the index for the deformation gradient and continue with \mathbf{F} in this chapter. We emphasize that the host displacement with velocity $\dot{\varphi}_t^{\text{ely}} = \mathbf{v}_0$ will serve as reference to which the species transport will be defined.

Now we shift our attention to the solutes. We assume that N species are distributed each as a continuum in the solid matrix consistent with a mixture theory. If the number of moles of species α in an undeformed volume element dV is given by dN_α and its molar mass is M_α , we can define together with Eq. (2.16) the partial material densities as

$$\rho_\alpha^\diamond = \frac{dN_\alpha M_\alpha}{dV} = c_\alpha^\diamond M_\alpha \quad \forall \alpha = 1..N. \quad (3.1)$$

The spatial equivalent follows a similar definition and is linked to the spatial concentration by Eq. (2.13) and to the material density by Eq. (2.16), yielding

$$\rho_\alpha = \frac{dN_\alpha M_\alpha}{dv} = c_\alpha M_\alpha = \frac{\rho_\alpha^\diamond}{\mathbb{J}} \quad \forall \alpha = 1..N. \quad (3.2)$$

We assume that at each point of the host material, species α moves with velocity \mathbf{v}_α . Recall that the velocity of the host is defined via Eq. (2.2) and generally $\mathbf{v}_\alpha \neq \dot{\varphi}_t$. The overall densities of the mixture, including the host material in the undeformed and deformed configurations, respectively, are given by

$$\rho_{\text{tot}}^\diamond = \sum_{\alpha=0}^N \rho_\alpha^\diamond, \quad \rho_{\text{tot}} = \sum_{\alpha=0}^N \rho_\alpha. \quad (3.3)$$

Since species $\alpha = 1..N$ can carry charges, whereas the host material is assumed to be charge neutral, the material and spatial charge densities for each species are

$$\rho_{q_\alpha}^\diamond = F z_\alpha c_\alpha^\diamond, \quad \rho_{q_\alpha} = F z_\alpha c_\alpha, \quad (3.4)$$

where z_α is the charge number associated with ion α . The total charge density is computed via

$$\rho_q^\diamond = \sum_{\alpha=1}^N \rho_{q_\alpha}^\diamond, \quad \rho_q = \sum_{\alpha=1}^N \rho_{q_\alpha} \quad (3.5)$$

for the material and spatial configuration, respectively.

3.2 Balance Principles

3.2.1 Balance of Mass

For the balance of mass, we distinguish between the host ($\alpha = 0$) and the chemical species ($\alpha = 1 \dots N$). The host material is assumed to have constant mass which yields [98]

$$\dot{\rho}_0^\diamond = 0. \quad (3.6)$$

To derive the balance of mass for a single species α , we consider at time t an arbitrary control volume $\mathcal{P}_t^\alpha \subseteq \mathcal{B}_t$ with species velocity \mathbf{v}_α . The only change in mass of α in that volume occurs due to a mass source r_α associated with chemical reaction and we can write

$$\frac{d}{dt} \int_{\mathcal{P}_t^\alpha} c_\alpha dv_\alpha = \int_{\mathcal{P}_t^\alpha} r_\alpha dv_\alpha \quad \forall \alpha \neq 0. \quad (3.7)$$

To rewrite this in terms of the control volume \mathcal{P}_t tied to the motion of the host, we use the Reynolds theorem (2.14) and obtain

$$\frac{d}{dt} \int_{\mathcal{P}_t} c_\alpha dv + \int_{\partial \mathcal{P}_t} c_\alpha (\mathbf{v}_\alpha - \mathbf{v}_0) \cdot \mathbf{n} da = \int_{\mathcal{P}_t} r_\alpha dv \quad \forall \alpha \neq 0. \quad (3.8)$$

The second term on the left hand side denotes the mass flux $\mathbf{j}_\alpha = c_\alpha (\mathbf{v}_\alpha - \mathbf{v}_0)$ through the boundary $\partial \mathcal{P}_t$ as introduced in Eq. (2.15). Hence, we describe naturally the mass flux of a species relative to the velocity of the host \mathbf{v}_0 . That distinguishes our description from multi-component transport in liquids which usually utilizes the molar mixture velocity [103], barycentric velocity [104] or the solvent velocity [102].

Now, we apply a transformation to the material setting, the divergence and localization theorem, to obtain the local form of the balance of species mass and total mass, respectively, as

$$\dot{c}_\alpha^\diamond + \operatorname{Div}(\mathbf{J}_\alpha) = R_\alpha \quad \forall \alpha \neq 0 \quad \Rightarrow \quad \dot{\rho}_{\text{tot}}^\diamond + \operatorname{Div}(\mathbf{J}_{\text{tot}}) = 0. \quad (3.9)$$

The material species and total molar flux are $\mathbf{J}_\alpha = \mathbb{J}\mathbf{F}^{-1}\mathbf{j}_\alpha$, see Eq. (2.17), and $\mathbf{J}_{\text{tot}} = \sum_{\alpha=1}^N \mathbf{J}_\alpha$. The material concentration source is $R_\alpha = \mathbb{J}r_\alpha$ and since a chemical reaction does not produce mass, we have $\sum_{\alpha=1}^N R_\alpha = 0$, which gives the second equation.

3.2.2 Balance of Charge and Gauss' law

As we assume that charge is exclusively transported by ions without involvement of electrons, the balance of charge can be directly derived from the balance of mass

$$\dot{\rho}_{q_\alpha}^\diamond + \operatorname{Div}(\mathbf{J}_{q_\alpha}) = R_{q_\alpha} \quad \forall \alpha \quad \Rightarrow \quad \dot{\rho}_q^\diamond + \operatorname{Div}(\mathbf{J}_q) = 0, \quad (3.10)$$

with charge flux $\mathbf{J}_{q_\alpha} = Fz_\alpha \mathbf{J}_\alpha$ and source $R_{q_\alpha} = Fz_\alpha R_\alpha$. Since charge cannot be generated in reactions, we have $\sum_{\alpha=1}^N R_{q_\alpha} = 0$, which — together with the definition of current $\mathbf{J}_q = \sum_{\alpha=1}^N \mathbf{J}_{q_\alpha}$ — yields the total balance of charge on the right hand side. Note that Eq. (3.10) is not independent of the balance of mass as seen in Eq. (3.9). As a result, only $N - 1$ mass fluxes \mathbf{J}_α are independent for a given total current flux \mathbf{J}_q .

The Gauss law relates the spatial electric displacement \mathfrak{d} to the total charge density ρ_q . The spatial and material representations are

$$\operatorname{div}(\mathfrak{d}) = \rho_q \quad \Leftrightarrow \quad \operatorname{Div}(\mathbb{D}) = \rho_q^\diamond \quad (3.11)$$

with the material electric displacement $\mathbb{D} = \mathbb{J}\mathbf{F}^{-1}\mathfrak{d}$. Further we follow McMeeking and Landis [105] and introduce a surface charge $\omega^{\text{SC}} = [\mathbb{D}] \cdot \mathbf{N}$

as the jump of electric displacement. The electric field \mathbf{e} is related to the magnetic field by $\operatorname{curl}(\mathbf{e}) = \frac{d}{dt}\mathbf{b} = 0$ due to Maxwell's equations, where we have assumed that the change of magnetic field \mathbf{b} in time can be neglected. To satisfy Maxwell's equation¹, we define the electric potential Φ such that

$$\mathbf{e} = -\operatorname{grad}(\Phi) = -\mathbf{F}^{-T} \operatorname{Grad}(\Phi) = \mathbf{F}^{-T} \mathbb{E} \quad (3.12)$$

with $\mathbb{E} = -\operatorname{Grad}(\Phi)$ the material electric field. The electric field is related to the electric displacement by

$$\mathbf{d} = \epsilon_0 \mathbf{e} + \mathbf{p} = \epsilon_0 \epsilon_r \mathbf{e}, \quad (3.13)$$

where \mathbf{p} is the polarization. The quantities ϵ_0 and ϵ_r are the vacuum and relative permittivity, respectively. By inserting Eq. (3.12) in Eq. (3.11), we obtain the well known Poisson equation

$$-\operatorname{div}(\epsilon_0 \epsilon_r \operatorname{grad}(\Phi)) = \rho_q. \quad (3.14)$$

In the case of electroneutrality with $\rho_q = 0$ and in the absence of chemical and mechanical driving forces, the electric potential is decoupled from individual mobile components and Ohm's law

$$\mathbf{j}_q = \boldsymbol{\kappa} \mathbf{e} = -\boldsymbol{\kappa} \operatorname{grad}(\Phi) \quad (3.15)$$

in terms of the total current density \mathbf{j}_q becomes valid. In such circumstances the current is driven by an electric field through a conductivity $\boldsymbol{\kappa}$. An extended version of Eq. (3.15) that is valid for solid binary electrolytes will be presented in Section 3.5.

¹ Here we make use of the identity $\operatorname{curl}(\operatorname{grad}(\xi)) = 0 \quad \forall \xi$.

3.2.3 Balance of Linear Momentum

To state the balance of linear momentum, we sum the rates of the partial linear momenta of host and species and equate them with mechanical (e.g. gravity), electrical and chemical body forces of each species \mathbf{b}_α^M , \mathbf{b}_α^E , \mathbf{b}_α^C and effective tractions \mathbf{t}^M , \mathbf{t}^E , \mathbf{t}^C acting on the host material and obtain

$$\frac{d}{dt} \sum_{\alpha=0}^N \int_{\mathcal{P}_t^\alpha} \rho_\alpha \mathbf{v}_\alpha dv_\alpha = \sum_{\alpha=0}^N \int_{\mathcal{P}_t} \mathbf{b}_\alpha^M + \mathbf{b}_\alpha^E + \mathbf{b}_\alpha^C dv + \int_{\partial \mathcal{P}_t} \mathbf{t}^M + \mathbf{t}^E + \mathbf{t}^C da. \quad (3.16)$$

We now have to carefully apply the time derivative on the left hand side. Therefore, we apply Reynolds theorem in finite deformations (Eq. (2.19)) and obtain for the left hand side of Eq. (3.16)

$$\begin{aligned} \frac{d}{dt} \int_{\mathcal{P}_t^\alpha} \rho_\alpha \mathbf{v}_\alpha dv_\alpha &= \int_{\mathcal{P}_0} \frac{d}{dt} (\rho_\alpha^\diamond \mathbf{V}_\alpha) + \text{Div} (M_\alpha \mathbf{V}_\alpha \mathbf{J}_\alpha) dV \\ &= \int_{\mathcal{P}_0} \underbrace{\rho_\alpha^\diamond \dot{\mathbf{V}}_\alpha + \text{Grad} (M_\alpha \mathbf{V}_\alpha) \cdot \mathbf{J}_\alpha + M_\alpha \mathbf{V}_\alpha R_\alpha}_{\mathbf{B}_\alpha^V} dV, \end{aligned} \quad (3.17)$$

where we have utilized the balance of mass (Eq. (3.9)) for the second line. The body force \mathbf{B}_α^V corresponds to an inertia force of component α within the host material.

The total electric body force $\mathbf{B}_{\text{tot}}^E = \sum_{\alpha=0}^N \mathbb{J} \mathbf{b}_\alpha^E$ is expressed as a Piola-type Maxwell stress tensor $\mathbf{B}_{\text{tot}}^E := \text{Div} (\mathbf{P}^E)$. The same procedure is used for the chemical body forces. Further, we follow McMeeking and Landis

[105] and state that the mechanical, electric and chemical tractions are balanced via a jump in mechanical stress, yielding

$$\begin{aligned} \int_{\partial\mathcal{P}_t} \mathbf{t}^M + \mathbf{t}^E + \mathbf{t}^C da &= \int_{\partial\mathcal{P}_0} \mathbf{T}^M + \mathbf{T}^E + \mathbf{T}^C dA \\ &= - \int_{\partial\mathcal{P}_0} [\![\mathbf{P}^M]\!] \cdot \mathbf{N} dA \\ &= \int_{\mathcal{P}_0} \text{Div}(\mathbf{P}^M) dV. \end{aligned} \quad (3.18)$$

Consequently, an expression for the balance of momentum of the host material is

$$\rho_0^\diamond \ddot{\varphi}_t^{\text{ely}} = \mathbf{B}_{\text{tot}}^M + \text{Div} \left(\underbrace{\mathbf{P}^M + \mathbf{P}^E + \mathbf{P}^C}_{\mathbf{P}} \right) - \sum_{\alpha=1}^N \mathbf{B}_\alpha^V \quad (3.19)$$

where we have introduced the effective total mechanical body force

$$\mathbf{B}_{\text{tot}}^M = \sum_{\alpha=0}^N \mathbf{B}_\alpha^M = \sum_{\alpha=0}^N \mathbb{J} \mathbf{b}_\alpha^M \quad (3.20)$$

and the total Piola stress \mathbf{P} . The inertia, advection and reaction contribution of the mobile components can be regarded as an additional body force \mathbf{B}_α^V acting on the host material.

3.2.4 Balance of Angular Momentum

The balance of angular momentum

$$\frac{d}{dt} \mathcal{L} = \mathcal{M} \quad (3.21)$$

states that the rate of change of the angular momentum

$$\mathcal{L} = \sum_{\alpha=0}^N \int_{\mathcal{P}_t^\alpha} \mathbf{x} \times \rho_\alpha \mathbf{v}_\alpha dv_\alpha \quad (3.22)$$

is equal to the total torque

$$\mathcal{M} = \sum_{\alpha=0}^N \int_{\mathcal{P}_t^\alpha} \mathbf{x} \times \mathbf{b}^{\text{ECM}} + \mathbf{o}^{\text{EC}} dv_\alpha + \int_{\partial \mathcal{P}_t} \mathbf{x} \times \mathbf{t}^{\text{ECM}} da \quad (3.23)$$

with the body force $\mathbf{b}^{\text{ECM}} = \sum_{\alpha=0}^N \mathbf{b}_\alpha^E + \mathbf{b}_\alpha^C + \mathbf{b}_\alpha^M$ and traction force $\mathbf{t}^{\text{ECM}} = \mathbf{t}^M + \mathbf{t}^E + \mathbf{t}^C$. Further, an angular momentum due to dipoles has to be considered. Following McMeeking and Landis [105], we use $\mathbf{o}^E = o_i^E = \epsilon_{ijk} \sigma_{kj}^E$, where ϵ_{ijk} is the Levi-Civita symbol. Although a deviatoric contribution of the chemical stress is unlikely, we set $\mathbf{o}^C = \epsilon_{ijk} \sigma_{kj}^C$, and obtain by combination with the electrostatic contribution $\mathbf{o}^{\text{EC}} = \mathbf{o}^E + \mathbf{o}^C$.

The rate of angular momentum computes to

$$\begin{aligned} \frac{d}{dt} \mathcal{L} &= \sum_{\alpha=0}^N \int_{\mathcal{P}_0} \frac{d}{dt} (\mathbf{X} \times \rho_\alpha^\diamond \mathbf{V}_\alpha) + \text{Div} \left(\frac{1}{c_\alpha^\diamond} (\mathbf{X} \times \rho_\alpha^\diamond \mathbf{V}_\alpha) \otimes \mathbf{J}_\alpha \right) dV \\ &= \sum_{\alpha=0}^N \int_{\mathcal{P}_0} \epsilon_{ijk} X_j \left[\frac{d}{dt} (\rho_\alpha^\diamond V_k^\alpha) + \text{Div}_m (M_\alpha V_k^\alpha J_m) + M_\alpha \epsilon_{ijk} \delta_{jm} V_k^\alpha J_m^\alpha \right] dV, \end{aligned} \quad (3.24)$$

where we have used the index notation in the second line. The applied torque in index notation is

$$\begin{aligned} \mathcal{M} &= \sum_{\alpha=0}^N \int_{\mathcal{P}_t} \epsilon_{ijk} x_j b_k^{\text{ECM}} dv + \int_{\partial \mathcal{P}_t} \mathbf{x} \times (\boldsymbol{\sigma}^M \mathbf{n}) da + \int_{\mathcal{P}_t} \epsilon_{ijk} \sigma_{kj}^{\text{EC}} dv \\ &= \sum_{\alpha=0}^N \int_{\mathcal{P}_0} \epsilon_{ijk} X_j \left(B_k^{\text{ECM}} + \text{Div}_m (P_{km}^M) \right) + \epsilon_{ijk} \delta_{mj} P_{kl}^M F_{ml} + \epsilon_{ijk} P_{kl}^{\text{EC}} F_{jl} dV. \end{aligned} \quad (3.25)$$

Combining Eq. (3.24) and Eq. (3.25) gives

$$\begin{aligned} \sum_{\alpha=0}^N \int_{\mathcal{P}_0} \epsilon_{ijk} X_j \left[\frac{d}{dt} (\rho_\alpha^\diamond V_k^\alpha) + \operatorname{Div}_m (M_\alpha V_k^\alpha J_m) - B_k^{\text{ECM}} - \operatorname{Div}_m (P_{km}^M) \right] dV \\ = \sum_{\alpha=0}^N \int_{\mathcal{P}_0} \epsilon_{ijk} \left(P_{kl}^{\text{ECM}} F_{jl} - M_\alpha V_k^\alpha J_j^\alpha \right) dV. \end{aligned} \quad (3.26)$$

The left hand side is equal to zero due to the balance of linear momentum, see Eq. (3.17), and $\mathbf{B}^{\text{ECM}} = \mathbf{B}^M + \operatorname{Div}(\mathbf{P}^C + \mathbf{P}^E)$. The right hand side results in the symmetry condition

$$\mathbf{P} \mathbf{F}^T - \sum_{\alpha=1}^N M_\alpha \mathbf{J}_\alpha \otimes \mathbf{V}_\alpha = \mathbf{F} \mathbf{P}^T - \sum_{\alpha=1}^N M_\alpha \mathbf{V}_\alpha \otimes \mathbf{J}_\alpha. \quad (3.27)$$

Without component motion this reduces to

$$\mathbf{P} \mathbf{F}^T = \mathbf{F} \mathbf{P}^T, \quad (3.28)$$

which is the standard result for balance of angular momentum in finite strain solid mechanics.

3.2.5 Balance of Energy

Consider the balance of energy in an arbitrary volume $\mathcal{P}_t \subseteq \mathcal{B}_t$. The change of total internal energy E^{int} , as well as kinetic energy E^{kin} , is equal to the power supply in \mathcal{P}_t due to heat L^H , mechanics L^M and electricity L^E :

$$\frac{d}{dt} (E^{\text{int}} + E^{\text{kin}}) = L^H + L^M + L^E \quad (3.29)$$

The left hand side of Eq. (3.29) describes the rate of internal energy e_α and kinetic energy $\frac{1}{2}\rho_\alpha \mathbf{v}_\alpha \cdot \mathbf{v}_\alpha$ of each species

$$\begin{aligned} E^{\text{int}} &:= \sum_{\alpha=0}^N \int_{\mathcal{P}_t^\alpha} \rho_\alpha e_\alpha dv_\alpha, \\ E^{\text{kin}} &:= \sum_{\alpha=0}^N \int_{\mathcal{P}_t^\alpha} \frac{1}{2} \rho_\alpha \mathbf{v}_\alpha \cdot \mathbf{v}_\alpha dv_\alpha. \end{aligned} \quad (3.30)$$

Note since each component α moves with its own velocity \mathbf{v}_α , we have to again apply Reynolds transport theorem through Eq. (2.14) and obtain

$$\begin{aligned} \frac{d}{dt} E^{\text{int}} &= \sum_{\alpha=0}^N \left(\frac{d}{dt} \int_{\mathcal{P}_t} \rho_\alpha e_\alpha dv + \int_{\partial \mathcal{P}_t} \rho_\alpha e_\alpha (\mathbf{v}_\alpha - \mathbf{v}_0) \cdot \mathbf{n} da \right) \\ &= \sum_{\alpha=0}^N \int_{\mathcal{P}_0} \frac{d}{dt} (\rho_\alpha^\diamond e_\alpha) + M_\alpha \text{Grad}(e_\alpha) \cdot \mathbf{J}_\alpha + M_\alpha R_\alpha e_\alpha - M_\alpha \dot{c}_\alpha^\diamond e_\alpha dV, \end{aligned} \quad (3.31)$$

where we have used Eq. (2.19) together with Eq. (3.9) to obtain the second version, involving the transformation to the material configuration, the divergence theorem and balance of mass. The same procedure applies to the kinetic energy

$$\frac{d}{dt} E^{\text{kin}} = \sum_{\alpha=0}^N \int_{\mathcal{P}_0} \mathbf{B}_\alpha^V \cdot \mathbf{V}_\alpha - \frac{1}{2} \mathbf{V}_\alpha \cdot \mathbf{V}_\alpha M_\alpha R_\alpha dV, \quad (3.32)$$

where we recall the definition of \mathbf{B}_α^V in Eq. (3.17). On the right hand side of Eq. (3.29), we observe energy production due to heat sources

and heat fluxes. In terms of heat we treat host and components as one system and get the contribution

$$L^H := \int_{\mathcal{P}_t} r^H dv - \int_{\partial\mathcal{P}_t} \mathbf{j}^H \cdot \mathbf{n} da, \quad (3.33)$$

where we have introduced a homogenized heat flux \mathbf{j}^H and an external heat source r^H , e.g. an electromagnetic heating. Note that heat generated due to chemical reactions is an internal process of conversion within the internal energy. The reference description of Eq. (3.33) is

$$L^H = \int_{\mathcal{P}_0} R^H - \text{Div}(\mathbf{J}^H) dV. \quad (3.34)$$

The rate at which mechanical work is done on the host material and the species is

$$L^M := \sum_{\alpha=0}^N \int_{\mathcal{P}_t} (\mathbf{b}_\alpha^M \cdot \mathbf{v}_\alpha) dv + \int_{\partial\mathcal{P}_t} (\mathbf{t}^M \cdot \mathbf{v}_0) da, \quad (3.35)$$

where only the host material can support traction forces. The individual body forces act on the host material as well as on each mobile component. The result converts to

$$\begin{aligned} L^M &= \sum_{\alpha=0}^N \int_{\mathcal{P}_t} \mathbf{b}_\alpha^M \cdot (\mathbf{v}_\alpha - \mathbf{v}_0) dv + \sum_{\alpha=0}^N \int_{\mathcal{P}_t} \mathbf{b}_\alpha^M \cdot \mathbf{v}_0 dv + \int_{\partial\mathcal{P}_t} \mathbf{t}^M \cdot \mathbf{v}_0 da, \\ &= \int_{\mathcal{P}_0} \sum_{\alpha=0}^N \frac{1}{c_\alpha^\diamond} \mathbf{F}^T \mathbf{B}_\alpha^M \cdot \mathbf{J}_\alpha + (\mathbf{B}_{\text{tot}}^M + \text{Div}(\mathbf{P})) \cdot \mathbf{V}_0 + \mathbf{P} : \dot{\mathbf{F}} dV, \end{aligned} \quad (3.36)$$

where we have made use of Eq. (3.18), the divergence theorem and the notation of double contraction, meaning $\mathbf{A} : \mathbf{B} = A_{ij} B_{ij}$ to obtain the version with respect to the reference configuration.

The electrical energy supply due to transport of charged species at an electric potential Φ by means of a current \mathbf{j}_q reads

$$L^E := - \int_{\partial\mathcal{P}_t} \Phi \mathbf{j}_q \cdot \mathbf{n} da = \int_{\mathcal{P}_t} \mathbb{E} \cdot \mathbf{j}_q - \Phi \operatorname{div}(\mathbf{j}_q) dv. \quad (3.37)$$

Transformation to the reference formulation yields

$$\begin{aligned} L^E &= \int_{\mathcal{P}_0} \mathbb{E} \cdot \mathbf{J}_q + \Phi \operatorname{Div}(\dot{\mathbb{D}}) dV \\ &= \int_{\mathcal{P}_0} \mathbb{E} \cdot \mathbf{J}_q + \mathbb{E} \cdot \dot{\mathbb{D}} dV + \int_{\partial\mathcal{P}_0} \Phi [\dot{\mathbb{D}}] \cdot \mathbf{N} dA \end{aligned} \quad (3.38)$$

where we have used $\operatorname{Div}(\mathbf{J}_q + \dot{\mathbb{D}}) = 0$, a consequence of Eq. (3.10) and Eq. (3.11). The last term can be identified as a surface charge $\omega^{SC} = [\dot{\mathbb{D}}] \cdot \mathbf{N}$, see e.g. [105]. Since all free charges are carried by ions and the host is electroneutral, we assume that the change of surface charge is zero and hence $\dot{\omega}^{SC} = [\dot{\mathbb{D}}] \cdot \mathbf{N} = 0$ on $\partial\mathcal{P}_0$.

Combining Eq. (3.19), (3.32), (3.34), (3.36), (3.38), we obtain the local material form for the balance of energy

$$\begin{aligned} \frac{d}{dt} \sum_{\alpha=0}^N \rho_\alpha^\diamond e_\alpha &= R^H - \operatorname{Div}(\mathbf{J}^H) + \mathbf{P} : \dot{\mathbf{F}} + \mathbb{E} \cdot \dot{\mathbb{D}} + \mathbb{E} \cdot \mathbf{J}_q \\ &\quad + \sum_{\alpha=1}^N M_\alpha e_\alpha \dot{c}_\alpha^\diamond - \sum_{\alpha=1}^N \left(\tilde{\mathbf{B}}_\alpha + \operatorname{Grad}(M_\alpha e_\alpha) \right) \cdot \mathbf{J}_\alpha \\ &\quad - \sum_{\alpha=1}^N \left(M_\alpha e_\alpha - \frac{1}{2} M_\alpha \mathbf{V}_\alpha \cdot \mathbf{V}_\alpha \right) R_\alpha \end{aligned} \quad (3.39)$$

with the extended specific body force $\tilde{\mathbf{B}}_\alpha = -\frac{1}{c_\alpha^\diamond} \mathbf{F}^T (\mathbf{B}_\alpha^M + \mathbf{B}_\alpha^V)$. In addition to the thermal and mechanical contributions, we see a power supply due to electric interaction, e.g. Joule heating, species transport and chemical reaction.

3.2.6 Balance of Entropy

We proceed similarly with the balance of entropy and sum over the component entropies η_α . We locally assume equal absolute temperature $\Theta \equiv \Theta_\alpha$ for each constituent and obtain

$$\frac{d}{dt} \sum_{\alpha=0}^N \int_{\mathcal{P}_t^\alpha} \rho_\alpha \eta_\alpha dv_\alpha = \int_{\mathcal{P}_t} \frac{r^H}{\Theta} dv - \int_{\partial \mathcal{P}_t} \frac{\mathbf{j}^H}{\Theta} \cdot \mathbf{n} da + \int_{\mathcal{P}_t} \frac{\rho_0 \delta_V}{\Theta} dv \quad (3.40)$$

where δ_V is the dissipation density. Applying Reynold's theorem through Eq. (2.14) on the left hand side, divergence theorem on the right hand side and switching to the material frame gives

$$\begin{aligned} \frac{d}{dt} \sum_{\alpha=0}^N \rho_\alpha^\diamond \eta_\alpha &= \rho_0^\diamond \delta_V + \frac{1}{\Theta} \left[\left((R^H - \text{Div}(\mathbf{J}^H)) + \frac{1}{\Theta} \mathbf{J}^H \cdot \text{Grad}(\Theta) \right) \right. \\ &\quad \left. - \sum_{\alpha=1}^N [\text{Grad}(M_\alpha \eta_\alpha) \cdot \mathbf{J}_\alpha - M_\alpha \eta_\alpha \dot{c}_\alpha^\diamond + M_\alpha \eta_\alpha R_\alpha] \right] \end{aligned} \quad (3.41)$$

as an expression for the rate of total entropy.

3.3 2nd Law of Thermodynamics

We now introduce the total Helmholtz energies $\tilde{\psi}$ and the species Helmholtz energy ψ_α from the Legendre transforms of the internal energies e_α

$$\tilde{\psi}(\mathbf{F}, c_\alpha^\diamond, \Theta, \mathbb{D}) = \sum_{\alpha=0}^N \rho_\alpha^\diamond \psi_\alpha = \sum_{\alpha=0}^N \rho_\alpha^\diamond (e_\alpha - \Theta \eta_\alpha). \quad (3.42)$$

Combining Eq. (3.39) and Eq. (3.41), making use of Eq. (3.42) and solving for $\rho_0^\diamond \delta_V$, we obtain the so-called full dissipation inequality, also known as the Clausius-Planck inequality [98] as

$$\begin{aligned}
 \rho_0^\diamond \delta_V = & \left(- \sum_{\alpha=0}^N \eta_\alpha - \frac{\partial \tilde{\psi}}{\partial \Theta} \right) \dot{\Theta} + \left(\mathbf{P} - \frac{\partial \tilde{\psi}}{\partial \mathbf{F}} \right) : \dot{\mathbf{F}} \\
 & + \sum_{\alpha=1}^N \left(M_\alpha \psi_\alpha - \frac{\partial \tilde{\psi}}{\partial c_\alpha^\diamond} \right) \dot{c}_\alpha^\diamond + \left(\mathbb{E} - \frac{\partial \tilde{\psi}}{\partial \mathbb{D}} \right) : \dot{\mathbb{D}} \\
 & - \sum_{\alpha=1}^N \left[\tilde{\mathbf{B}}_\alpha + \text{Grad}(M_\alpha \psi_\alpha) + F z_\alpha \mathbb{E} - (M_\alpha \eta_\alpha) \text{Grad}(\Theta) \right] \cdot \mathbf{J}_\alpha \\
 & - \frac{1}{\Theta} \text{Grad}(\Theta) \cdot \mathbf{J}^H - \left(M_\alpha \psi_\alpha - \frac{1}{2} M_\alpha \mathbf{V}_\alpha \cdot \mathbf{V}_\alpha \right) R_\alpha \\
 & \geq 0.
 \end{aligned} \tag{3.43}$$

The left hand side has to be non-negative with $\rho_0^\diamond \delta_V \geq 0$ due to the second law of thermodynamics. Following the Coleman-Noll argument [106], we assume independence of the rates $\dot{\Theta}, \dot{\mathbf{F}}, \dot{c}_\alpha^\diamond, \dot{\mathbb{D}}$ and therefore require the parenthetical terms in Eq. (3.43) to vanish. This yields the consistency conditions

$$\begin{aligned}
 \sum_{\alpha=0}^N \eta_\alpha &= - \frac{\partial \tilde{\psi}}{\partial \Theta}, & \mathbf{P} &= \frac{\partial \tilde{\psi}}{\partial \mathbf{F}}, \\
 \mu_\alpha := M_\alpha \psi_\alpha &= \frac{\partial \tilde{\psi}}{\partial c_\alpha^\diamond}, & \mathbb{E} &= \frac{\partial \tilde{\psi}}{\partial \mathbb{D}},
 \end{aligned} \tag{3.44}$$

where we have introduced the chemical potential (per mole) as $\mu_\alpha := M_\alpha \psi_\alpha$ of species α , which is also sometimes referred to as the convective potential [107], a measure for the energy required to insert a mole of species α into a fixed volume dV . Consequently the total

Helmholtz energy of Eq. (3.42) is a combination of the host energy and the sum of the chemical potentials of the components

$$\tilde{\psi} = \rho_0^\diamond \psi_0 + \sum_{\alpha=1}^N c_\alpha^\diamond \mu_\alpha. \quad (3.45)$$

Further, since $\tilde{\psi}$ is composed from of the individual ψ_α , the definition in Eq. (3.44) has an implicit structure and can be resolved via

$$\begin{aligned} M_\alpha \psi_\alpha &= \frac{\partial}{\partial c_\alpha^\diamond} \sum_{\beta=0}^N \rho_\beta^\diamond \psi_\beta \quad \Leftrightarrow \quad \sum_{\beta=0}^N \rho_\beta^\diamond \frac{\partial \psi_\beta}{\partial c_\alpha^\diamond} = 0 \\ &\Leftrightarrow \quad \sum_{\beta=1}^N c_\beta^\diamond \frac{\partial \mu_\beta}{\partial c_\alpha^\diamond} = -\frac{\partial \psi_0}{\partial c_\alpha^\diamond}, \end{aligned} \quad (3.46)$$

where the last representation can be seen as a Gibbs-Duhem like equation at constant temperature and deformation.

We continue with the evaluation of the dissipation inequality (3.43). If all equations of Eq. (3.44) are fulfilled and Joules heating is reformulated to

$$\mathbb{E} \cdot \mathbf{J}_q = - \sum_{\alpha=1}^N \text{Grad}(\Phi) \cdot F z_\alpha \mathbf{J}_\alpha, \quad (3.47)$$

we can reduce Eq. (3.43) to

$$\begin{aligned} 0 \leq & - \sum_{\alpha=1}^N \left(\text{Grad} \left(\tilde{\mathbf{B}}_\alpha + \mu_\alpha + F z_\alpha \Phi \right) + M_\alpha \eta_\alpha \text{Grad}(\Theta) \right) \cdot \mathbf{J}_\alpha \\ & - \frac{1}{\Theta} \text{Grad}(\Theta) \cdot \mathbf{J}^H - \sum_{\alpha=1}^N \left(\mu_\alpha - \frac{1}{2} M_\alpha \mathbf{V}_\alpha \cdot \mathbf{V}_\alpha \right) R_\alpha. \end{aligned} \quad (3.48)$$

Eq. (3.48) constitutes a thermodynamic constraint for the molar fluxes \mathbf{J}_α (and therefore species velocities \mathbf{v}_α), the heat flux \mathbf{J}^H and the

reactions R_α . Under the assumption of each process being independent, the first term on the right hand side of Eq. (3.48) relates molar flux to chemo-electrical driving forces, inertial and body forces. Similarly, when independent of other terms, the second term leads to the well known Fourier's law of thermal conduction and the third term guides the direction of reactions.

Assuming uniform temperature ($\text{Grad}(\Theta) = 0$), quasistatic conditions for the host ($\dot{\varphi}_t^{\text{ely}} \approx 0$), the absence of body forces ($\mathbf{B}_\alpha^M \approx 0$) and further assuming that inertia related forces are small ($\mathbf{B}_\alpha^V \approx 0$), we obtain the thermodynamic constraints

$$0 \leq - \sum_{\alpha=1}^N \text{Grad}(\omega_\alpha) \cdot \mathbf{J}_\alpha \quad \text{and} \quad 0 \leq - \sum_{\alpha=1}^N \mu_\alpha R_\alpha, \quad (3.49)$$

where we have introduced the electrochemical potential

$$\omega_\alpha = \mu_\alpha + F z_\alpha \Phi. \quad (3.50)$$

The first of Eq. (3.49) provides a constraint for all mass fluxes \mathbf{J}_α as discussed in the upcoming sections. The second of Eq. (3.49) constitutes a requirement for chemical reactions within the bulk, e.g. degeneration of electrolyte. This will not play a role in the following sections, where $R_\alpha = 0$ will be assumed.

3.4 Material Description

To complete the electro-chemo-mechanical description of ion transport, we have to specify a material model for the solid electrolyte. Therefore, we will introduce the swelling mechanism, define the Helmholtz energy including mechanical, electrical and mechanical effects and derive the

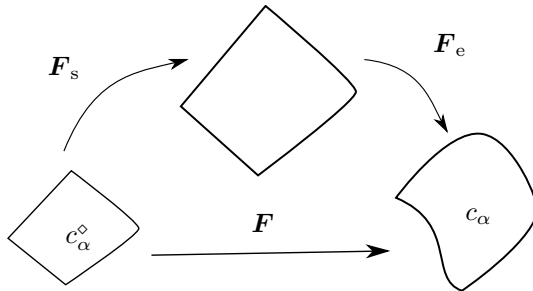


Figure 3.3: The deformation gradient is composed of purely isotropic swelling \mathbf{F}_s due to the pressure of ions and elastic deformation \mathbf{F}_e .

constitutive equations and prescribe thermodynamically consistent mass fluxes.

In the following, we use the a decomposition of the deformation gradient into swelling and elastic contributions as seen in Fig. 3.3 with the multiplicative split

$$\mathbf{F} = \mathbf{F}_e \mathbf{F}_s, \quad (3.51)$$

where \mathbf{F}_e describes the elastic response of the material and \mathbf{F}_s corresponds to a volumetric stress free expansion or compression due to swelling.

3.4.1 Swelling of the Host Material

The volumetric phenomenon of swelling occurs when species are inserted, removed or relocated in a host material. Although we will assume that swelling itself is stress free, it can eventually trigger an elastic response due to constraints from the boundary or adjacent material. Take for example a sponge. If it is clamped and cannot expand but additional species are inserted, then either the host or the species are compressed. The opposite effect is also possible when the host is already infiltrated

by species and is again clamped. If species are removed, then the host has to account for the missing material which eventually leads to tension forces.

Here, we assume an isotropic swelling. The deformation gradient of swelling then is

$$\mathbf{F}_s = \mathbb{J}_s^{\frac{1}{3}} \mathbf{I} \quad (3.52)$$

with the Jacobian $\mathbb{J}_s = \det \mathbf{F}_s$ as an unknown function of i.e. the concentration. With Eq. (2.4) we can deduce from a given material volume element dV the spatial volume element dv with

$$dv = \mathbb{J}_e \mathbb{J}_s dV = \mathbb{J} dV, \quad (3.53)$$

where $\mathbb{J}_e = \det \mathbf{F}_e$ is the Jacobian of elastic deformation. Each of the volume elements can be separated into a contribution from the host and from the mobile species α . The unswollen and undeformed state is defined by

$$dV = dV_0 + \sum_{\alpha=1}^N \Omega_\alpha dN_\alpha^{\text{ref}}, \quad (3.54)$$

where $dN_\alpha^{\text{ref}} = dV c_\alpha^{\text{ref}}$ denotes the amount of species α in dV and Ω_α is its molar volume, both defined in the initial, reference state. The swollen and deformed volume is

$$dv = dv_0 + \sum_{\alpha=1}^N \hat{\Omega}_\alpha dN_\alpha, \quad (3.55)$$

where we assume that the deformation of the host volume follows $dv_0 = \mathbb{J} dV_0$ and that the spatial molar volume of species α is given

by $\hat{\Omega}_\alpha$. Further, the amount of species dN_α in volume dv is determined from the concentration either in material or spatial configuration as

$$dN_\alpha = c_\alpha dv = c_\alpha^\diamond dV. \quad (3.56)$$

From Eq. (3.53), Eq. (3.55) and the knowledge that the host material deforms only elastically we obtain

$$\mathbb{J}_e \mathbb{J}_s dV = \mathbb{J}_e dV_0 + \sum_{\alpha=1}^N \hat{\Omega}_\alpha dN_\alpha. \quad (3.57)$$

Rearranging Eq. (3.57), using $dV_0 = dV - \sum_{\alpha=1}^N \Omega_\alpha c_\alpha^{\text{ref}} dV$ from Eq. (3.54) and with Eq. (3.56) then yields

$$\mathbb{J}_s = 1 + \sum_{\alpha=1}^N \left(\hat{\Omega}_\alpha \frac{1}{\mathbb{J}_e} c_\alpha^\diamond - \Omega_\alpha c_\alpha^{\text{ref}} \right) = \frac{1 - \sum_{\alpha=1}^N \Omega_\alpha c_\alpha^{\text{ref}}}{1 - \sum_{\alpha=1}^N \hat{\Omega}_\alpha c_\alpha}, \quad (3.58)$$

where the second equality is obtained with $\frac{1}{\mathbb{J}_e} = \frac{\mathbb{J}_s}{\mathbb{J}}$. An explicit model for the deformed molar volume $\hat{\Omega}_\alpha$ of species α is necessary to evaluate the swelling of a material as seen in Eq. (3.58). We consider two assumptions for the deformation of a species.

The first assumption is incompressibility of the inserted species such that $\hat{\Omega}_\alpha = \Omega_\alpha$. This gives

$$\mathbb{J}_s|_{\text{incompressible}} = \frac{1 - \sum_{\alpha=1}^N \Omega_\alpha c_\alpha^{\text{ref}}}{1 - \sum_{\alpha=1}^N \Omega_\alpha c_\alpha} \quad (3.59)$$

and implies an upper bound for the concentration with $\sum_{\alpha=0}^N c_\alpha \Omega_\alpha < 1$. The denominator reaches zero for $c_\alpha \rightarrow \frac{1}{\Omega_\alpha}$, which leads to an infinite swelling ($\mathbb{J}_s \rightarrow \inf$). The volume is completely occupied by the species α in this case and the host is compressed to zero volume.

	incompressible	incomp. (linearized)	compressible
\mathbb{J}_s	$\frac{1 - \sum_{\alpha=1}^N \Omega_\alpha c_\alpha^{\text{ref}}}{1 - \sum_{\alpha=1}^N \Omega_\alpha c_\alpha}$	$1 + \sum_{\alpha=1}^N \frac{\Omega_\alpha (c_\alpha - c_\alpha^{\text{ref}})}{1 - \Omega_\alpha c_\alpha^{\text{ref}}}$	$1 + \sum_{\alpha=1}^N \beta^s \Omega_\alpha (c_\alpha^\diamond - c_\alpha^{\text{ref}})$
λ^S	$\frac{\mathbb{J}_s}{1 - \sum_{\alpha=1}^N \Omega_\alpha c_\alpha}$	$\frac{1}{(1 - \sum_{\alpha=1}^N \Omega_\alpha c_\alpha^{\text{ref}}) \mathbb{J}}$	β^s

Table 3.1: The expressions for \mathbb{J}_s and λ^S for incompressible, linearized incompressible and compressible models of isotropic swelling.

Developing Eq. (3.59) with a Taylor expansion around $c_\alpha = c_\alpha^{\text{ref}}$ yields the linearized form

$$\mathbb{J}_s|_{\text{incompressible}} = 1 + \sum_{\alpha=1}^N \frac{\Omega_\alpha}{1 - \Omega_\alpha c_\alpha^{\text{ref}}} (c_\alpha - c_\alpha^{\text{ref}}) \quad (3.60)$$

which approximates swelling as a linear function of the spatial concentration.

The alternative assumption is compressibility of the inserted species with $\hat{\Omega}_\alpha = \beta^s \mathbb{J}_e \Omega_\alpha$. The molar volume increases or decreases proportional to the mechanical deformation of the host. The factor β^s thereby accounts for non-ideality in swelling and could be determined experimentally or by atomistic simulations [64]. Eq. (3.58) then yields

$$\mathbb{J}_s|_{\text{compressible}} = 1 + \beta^s \sum_{\alpha=1}^N \Omega_\alpha (c_\alpha^\diamond - c_\alpha^{\text{ref}}) \quad (3.61)$$

and aligns with models in literature [108, 109]. Using λ^S as defined in Tab. 3.1 we compute the derivative of \mathbb{J}_s with respect to the variable ξ as

$$\frac{\partial \mathbb{J}_s}{\partial \xi} = \lambda^S \Omega_\alpha \frac{\partial c_\alpha^\diamond}{\partial \xi}. \quad (3.62)$$

Tab. 3.1 sums up the expressions for \mathbb{J}_s and λ^S which follow from the three model assumptions of swelling. Note that the reference concentration

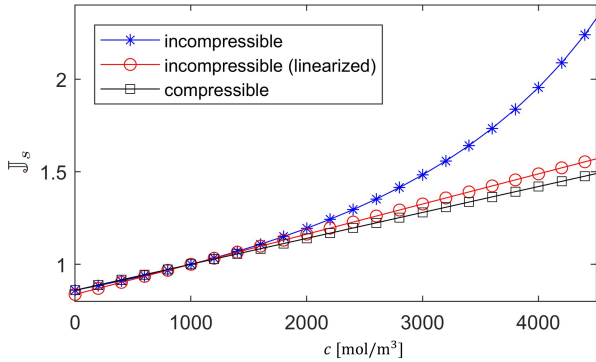


Figure 3.4: The graph illustrates the correlation of swelling and the concentration in a clamped system ($\mathbb{J} = 1$) infiltrated by a single species with concentration c with $c^{\text{ref}} = 1000 \frac{\text{mol}}{\text{m}^3}$ and $\Omega = 140 \frac{\text{cm}}{\text{mol}}$. The incompressible version of Eq. (3.59) diverges at $\frac{1}{\Omega} = 7143 \frac{\text{mol}}{\text{m}^3}$. No significant difference is observed for the compressible (Eq. (3.61) with $\beta^S = 1$) and the linearized incompressible case (Eq. (3.60)).

has to obey $\sum_{\alpha=1}^N \Omega_\alpha c_\alpha^{\text{ref}} < 1$ due to the requirement of $\mathbb{J}_s > 0$, for all of the three swelling assumptions. Fig. 3.4 illustrates the concentration dependencies of the two incompressible and the compressible version. The response is very similar around c^{ref} for all three assumptions. The effect of incompressibility is, however, significant for highly concentrated solutions. To reduce complexity, especially due to the factor λ^S , and to be in alignment with similar theories [68, 69], we will consider the compressible version of Eq. (3.61) in the upcoming sections.

3.4.2 Constitutive Helmholtz Energy

We assume that the Helmholtz free energy of the electro-chemo-mechanical system can be written as the sum of mechanical, electrical and chemical contributions as

$$\tilde{\psi}(\mathbf{F}, c_\alpha^\diamond, \mathbb{D}) = \tilde{\psi}^M(\mathbf{F}, c_\alpha^\diamond) + \tilde{\psi}^E(\mathbf{F}, \mathbb{D}) + \sum_{\alpha=1}^N \tilde{\psi}_\alpha^C(\mathbf{F}, c_\alpha^\diamond), \quad (3.63)$$

where we have chosen the Helmholtz free energy of the host at reference state to be zero.

Electrostatics

For the sake of simplicity, we use an isotropic formulation of electrostatics in the spatial domain consistent with Eq. (3.13), which leads to

$$\frac{\tilde{\psi}^E}{\mathbb{J}} := \frac{1}{2\epsilon_0\epsilon_r} \mathbf{d} \cdot \mathbf{d}. \quad (3.64)$$

The reference description is then given as

$$\tilde{\psi}^E = \frac{1}{2\epsilon_0} (\boldsymbol{\epsilon}_r^\diamond)^{-1} : (\mathbb{D} \otimes \mathbb{D}) \quad \text{with} \quad \boldsymbol{\epsilon}_r^\diamond = \mathbb{J} \mathbf{F}^{-1} \boldsymbol{\epsilon}_r \mathbf{F}^{-T}. \quad (3.65)$$

We introduce the material description of the relative electric permittivity as $\boldsymbol{\epsilon}_r^\diamond$ to keep the notation concise. With Eq. (3.65) we do not include dissipative materials [110] or anisotropic polarization [105] and assume a concentration independent permittivity.

Mechanics

In addition to the swelling of Eq. (3.52), we assume a Neo-Hookean material law for the description of the elastic response of the host. The

mechanical energy, which depends solely on $\mathbf{F}_e = \mathbf{F}\mathbf{F}_s^{-1}(c_\alpha^\diamond)$, then becomes

$$\begin{aligned}\tilde{\psi}^M(\mathbf{F}, c_\alpha^\diamond) &:= \tilde{\psi}_{\text{NH}}^{\text{etr}}(\mathbf{F}_e) \\ &= \frac{1}{2}\gamma_{\text{NH}}(\mathbb{I}_1 - 3) + \frac{1}{2}\lambda_{\text{NH}}(\log \mathbb{I}_3)^2 - \gamma_{\text{NH}} \log \mathbb{I}_3,\end{aligned}\quad (3.66)$$

with the Lamé constants γ_{NH} , λ_{NH} and the invariants

$$\mathbb{I}_1 = \text{tr}(\mathbf{F}_e^T \mathbf{F}_e), \quad \mathbb{I}_3 = \mathbb{J}_e = \det \mathbf{F}_e, \quad (3.67)$$

see e.g. Ogden [111]. Note that the Lamé constants can be converted from Young's modulus E or shear modulus G and the Poisson ratio ν by

$$\lambda_{\text{NH}} = \frac{E\nu}{(1+\nu)(1-2\nu)} = \frac{2G\nu}{1-2G} \quad \text{and} \quad \gamma_{\text{NH}} = \frac{E}{2(1+\nu)} = G. \quad (3.68)$$

Hereby, E , G and ν have their conventional meaning relating infinitesimal strain and change in stress.

Chemistry

The chemical contribution to the Helmholtz energy is assumed to be

$$\tilde{\psi}_\alpha^C = c_\alpha^\diamond \mu_\alpha^0 + R\Theta \int_{c_\alpha^{\text{ref}}}^{c_\alpha^\diamond} \ln\left(\frac{f_\alpha c_\alpha}{f_\alpha^{\text{ref}} c_\alpha^{\text{ref}}}\right) dc_\alpha^\diamond. \quad (3.69)$$

with the gas constant R and the standard chemical potential μ_α^0 which is independent of concentration and deformation. In concentrated solutions, a correction factor, the so called fugacity or activity coefficient f_α is introduced to incorporate non-idealities in the formulation [112, 113]. In dilute solutions, an ideal gas response is obtained with $f_\alpha = 1$.

Definition (3.69) is formulated very similarly to classical mixture theories in fluids and solids, but there are two features we want to highlight. In contrast to conventional usage in solids, where a vacancy motivated

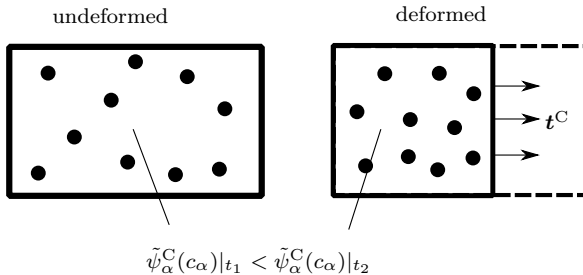


Figure 3.5: Consider an isolated system: The effective concentration c_{α} changes from the undeformed (t_1) to the deformed state (t_2). Therefore, the chemical energy increases and gives rise to chemical stresses t^C also known as osmotic stress or pressure.

chemical potential is a function of material concentration c_{α}^{\diamond} [63], we follow a concept used for fluids and postulate that the chemical energy depends on the amount of ions per deformed volume, i.e. on the spatial concentration c_{α} . Therefore, material compression leads to a decrease of spatial volume and hence an increase of effective spatial concentration (Fig. ??). The importance of this assumption and its implications will be illustrated in Example 4.5. The second feature is the integration domain of the integral in Eq. (3.69) which represents the entropic contribution to the chemical energy. We choose it to be zero at reference concentration c_{α}^{ref} . This will be beneficial for the description of the mechanical response in the upcoming section.

3.4.3 Constitutive Equations

Following Eq. (3.44), we can deduce the stress tensor, the chemical potential and the electric field from Eq. (3.65), Eq. (3.66) and Eq. (3.69). The Piola stress tensor then follows as

$$\mathbf{P} = \mathbf{P}^M + \mathbf{P}^E + \mathbf{P}^C \quad (3.70)$$

with the three contributions

$$\mathbf{P}^M = \mathbf{F}_s^{-1} : \left((\lambda_{NH} \log \mathbb{I}_3 - \gamma_{NH}) \mathbf{F}_e^{-T} + \gamma_{NH} \mathbf{F}_e \right), \quad (3.71)$$

$$\mathbf{P}^E = \mathbf{F}^{-T} \left(\mathbb{E} \otimes \mathbb{D} - \frac{1}{2} (\mathbb{E} \cdot \mathbb{D}) \mathbf{I} \right), \quad (3.72)$$

$$\mathbf{P}^C = \sum_{\alpha=1}^N -\mathbf{F}^{-T} R \Theta \int_{c_\alpha^{\text{ref}}}^{c_\alpha^\diamond} \left(1 + \frac{\partial \ln f_\alpha}{\partial \ln c_\alpha} \right) dc_\alpha^\diamond. \quad (3.73)$$

Note that the electric contribution \mathbf{P}^E is the Maxwell stress tensor as derived in [110] or [105]² and reduces to an electric body force in the material and spatial representations

$$\mathbf{B}_{\text{tot}}^E = \text{Div}(\mathbf{P}^E) = \rho_q^\diamond \mathbf{F}^{-T} \mathbb{E} \quad \Leftrightarrow \quad \mathbf{b}_{\text{tot}}^E = \rho_q \mathbf{e}. \quad (3.74)$$

The chemical contribution \mathbf{P}^C originates from the dependency of concentration on deformation in the chemical energy ($\mathbb{J}c_\alpha = c_\alpha^\diamond$). Its equivalent Cauchy stress

$$\boldsymbol{\sigma}^C = \sum_{\alpha=1}^N -R \Theta \left(c_\alpha - c_\alpha^{\text{ref}} + \int_{c_\alpha^{\text{ref}}}^{c_\alpha^\diamond} \frac{\partial \ln f_\alpha}{\partial \ln c_\alpha} dc_\alpha \right) \mathbf{I} \quad (3.75)$$

is purely hydrostatic. It corresponds to the osmotic pressure

$$p^C = -\frac{1}{3} \text{tr}(\boldsymbol{\sigma}^C), \quad (3.76)$$

which is typically introduced in the setting of a membrane permeable for a solution but not for a solvent. The jump in concentration across the membrane yields diffusion of solvent through it to minimize chemical energy. Diffusion through the membrane stops when a critical pressure

² McMeeking and Landis [105] formulate the mechanical response with Cauchy stresses $\boldsymbol{\sigma} = \frac{1}{\mathbb{J}} \mathbf{P} \mathbf{F}^T$.

across the membrane is reached that balances the chemical driving force [69]. An ideal solution with $f_\alpha = 1$ and $c_\alpha^{\text{ref}} = 0$ gives the familiar result for an ideal gas $p^C = \sum_{\alpha=1}^N R\Theta c_\alpha$ [113]. In contrast to the case of fluids, we formulate Eq. (3.69) such that a stress free state with $\sigma^C(c_\alpha^{\text{ref}}) = 0$ holds for the reference concentration, thereby avoiding further complexity with osmotic pressure having to be balanced in the reference configuration by a mechanical response.

Now we evaluate the chemical potential with Eq. (3.44) through

$$\mu_\alpha = \mu_\alpha^C + \mu_\alpha^M \quad \text{with} \quad \begin{cases} \mu_\alpha^C &= \frac{\partial \tilde{\psi}_\alpha^C}{\partial c_\alpha^\diamond} = \mu_\alpha^0 + R\Theta \ln \left(\frac{f_\alpha c_\alpha}{f_\alpha^{\text{ref}} c_\alpha^{\text{ref}}} \right) \\ \mu_\alpha^M &= \frac{\partial \tilde{\psi}_\alpha^M}{\partial c_\alpha^\diamond} = \mathbb{J}_e \lambda^S \Omega_\alpha p^M. \end{cases} \quad (3.77)$$

The mechanical part of the chemical potential therefore depends on the swelling assumption, see Tab. 3.1. We continue our analysis with the underlying assumption of compressibility which yields $\lambda^S = 1$. The chemical part μ_α^C is in alignment with standard chemical potentials with an energetic and an entropic contribution [53, 112]. The mechanical contribution μ_α^M due to the elastic part of the pressure $p^M = -\frac{1}{3} \text{tr} \left(\frac{1}{\mathbb{J}} \mathbf{P}^M \mathbf{F}^T \right)$ leads to stress assisted diffusion [114]. The factor \mathbb{J}_e is a consequence of large strain considerations. Concentration-dependent properties of elasticity and electrostatics would yield additional contributions to the chemical potential [64].

Finally we evaluate the electric field from Eq. (3.44) and get

$$\mathbb{E} = \frac{1}{\mathbb{J}\epsilon_0} (\epsilon_r^\diamond)^{-1} \mathbb{D}, \quad (3.78)$$

which gives together with Eq. (3.11) the Poisson equation

$$-\text{Div}(\epsilon_0 \epsilon_r^\diamond \text{Grad}(\Phi)) = \rho_q^\diamond. \quad (3.79)$$

The description in the material configuration of Eq. (3.79) aligns with the well known spatial Poisson equation, see Eq. (3.14).

3.4.4 Multicomponent Mass Flux in Finite Strain

Thermodynamically consistent transport models have to obey cross-relations between driving force/mass flux couples. The Onsager theory [115–117], the Maxwell-Stefan formalism [102, 103] or the Poisson-Nernst-Planck equation are different approaches to satisfy thermodynamic consistency. In our formulation this is equivalent to postulate, motivated by the requirement of the reduced dissipation inequality (3.49), a linear ansatz for the mass flux [68, 69, 118, 119] as

$$\mathbf{J}_\alpha = - \sum_{\beta=1}^N \mathbf{M}_{\alpha\beta}^\diamond \text{Grad}(\omega_\beta), \quad (3.80)$$

where we introduce a mobility matrix $\mathbf{M}_{\alpha\beta}^\diamond$, which we require to be positive semi-definite to guarantee non-negativity of Eq. (3.49). The mobility matrix

$$\mathbf{M}_{\alpha\beta}^\diamond := \left(\begin{array}{ccc} \mathbf{M}_{11}^\diamond & \mathbf{M}_{12}^\diamond & \dots \\ \mathbf{M}_{21}^\diamond & \mathbf{M}_{22}^\diamond & \dots \\ \vdots & \vdots & \ddots \end{array} \right) \Big|_{\alpha\beta} \quad (3.81)$$

with

$$(\mathbf{a}_\alpha \cdot \mathbf{M}_{\alpha\beta}^\diamond \cdot \mathbf{a}_\beta) \geq 0 \quad \forall \mathbf{a}_\alpha, \mathbf{a}_\beta \in \mathbb{R}^3 \quad (3.82)$$

consists of $N \times N$ entries where each entry can be again a $\mathbb{R}^{3 \times 3}$ tensor to represent anisotropic properties. A deeper discussion of the implementation of anisotropy within this theory can be found in Section 3.4.5. The

mobility matrix describes the influence of the driving force $\text{Grad}(\omega_\beta)$ on the mass flux \mathbf{J}_α . A low mobility is a result of high internal friction with respect to the host (on-diagonal terms) and with respect to component-component interaction (off-diagonal terms). They are related to drag coefficients and binary diffusion coefficients in the Maxwell-Stefan-diffusion model as discussed in Section 3.4.6.

We would like Eq. (3.80) to be consistent with the spatial relation

$$\mathbf{j}_\alpha = - \sum_{\beta=1}^N \mathbf{M}_{\alpha\beta} \text{grad}(\omega_\beta), \quad (3.83)$$

correlating the mass flux on the deformed geometry with a spatial gradient of the electrochemical potential and obtain ³

$$\mathbf{M}_{\alpha\beta}^\diamond = \mathbb{J} \mathbf{F}^{-1} \mathbf{M}_{\alpha\beta} \mathbf{F}^{-T}. \quad (3.84)$$

The property $\mathbf{M}_{\alpha\beta}$ is the spatial mobility matrix, a parameter closely related to measurable quantities and Eq. (3.84) effectively informs the material configuration of changes of transport paths due to deformation. Eventually, we solve the material mass flux in Eq. (3.80) with the material mobility of Eq. (3.84) which is equivalent to the desired spatial mass flux of Eq. (3.83). If the domain is deformed, the material mobility $\mathbf{M}_{\alpha\beta}^\diamond$ becomes anisotropic due to the conversion of Eq. (3.84), even if isotropic material properties are assumed. This anisotropy is solely related to deformation of transport paths. The requirement that the material mobility matrix has to obey a positive semi-definite structure leads along with Eq. (3.84) to the spatial mobility matrix having to be positive semi-definite. This property can be checked in the manner of Eq. (3.82)

³ We deduce from $\mathbf{j}_\alpha \cdot \mathbf{n} da = \mathbf{J}_\alpha \cdot \mathbf{N} dA$ the relation $\mathbf{J}_\alpha = \mathbb{J} \mathbf{F}^{-1} \mathbf{j}_\alpha$ [98]. Further, the material and spatial gradient operator are linked via $\text{Grad}(\cdot) = \frac{\partial \mathbf{x}}{\partial \mathbf{X}} \text{grad}(\cdot) = \mathbf{F} \text{grad}(\cdot)$.

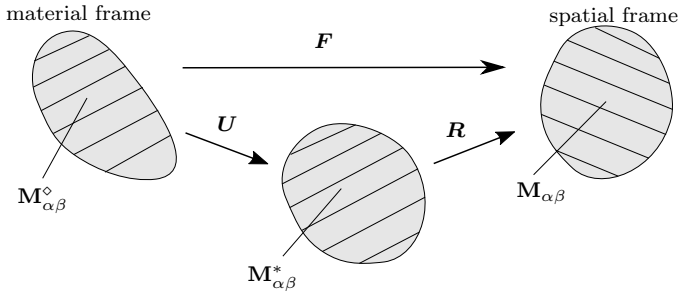


Figure 3.6: $\mathbf{M}_{\alpha\beta}^*$ is defined on an intermediate configuration, where the orientation is linked to the material frame but the stretches and hence the length of the effective transport paths are linked to the spatial frame.

or by the eigenvalues which are required to be non-negative. Furthermore, we can conclude that the determinant of $\mathbf{M}_{\alpha\beta}$ has a non-negative value.

3.4.5 Modeling Anisotropy in Solid Electrolytes

In order to include anisotropic material properties as found e.g. in laminar structures [37, 57] in our transport framework, we link transport paths with the material configuration and use properties like the effective length of a transport path from the deformed configuration. For illustration purposes, imagine a set of parallel lines on a material which are associated with the material points. Their shape and length will change with deformation. Now consider an ion traveling through the material without being able to cross the lines. The ion then has to follow the material structure (the lines are borders) but needs to move the spatial length of these lines (deformed geometry). To implement this in our framework, we decompose the deformation gradient into $\mathbf{F} = \mathbf{R}\mathbf{U}$ with a right stretch tensor \mathbf{U} and a rotation tensor \mathbf{R} , see Eq. (2.5). This defines an intermediate configuration, where the material is stretched with \mathbf{U} but

not rotated. It serves for the definition of the transport properties, e.g. anisotropic mobility matrix $\mathbf{M}_{\alpha\beta}^*$. If the structure rotates, the effective spatial mobility $\mathbf{M}_{\alpha\beta}$ does so via

$$\mathbf{M}_{\alpha\beta} = \mathbf{R} \mathbf{M}_{\alpha\beta}^* \mathbf{R}^T. \quad (3.85)$$

We get with Eq. (3.84) the material mobility matrix as

$$\mathbf{M}_{\alpha\beta}^\diamond = \mathbf{U}^{-1} \mathbf{M}_{\alpha\beta}^* \mathbf{U}^{-T}. \quad (3.86)$$

The material mobility matrix is ultimately influenced only by stretches. The mass flux stated in the material frame takes length changes of the transport path into account, the orientation, however, is governed by a path associated with the material.

If an electrolyte is isotropic, we can reduce the formulation by the introduction of an isotropic mobility $\mathbf{M}_{\alpha\beta}^* = M_{\alpha\beta} \mathbf{I}$, which results in

$$\mathbf{M}_{\alpha\beta} = M_{\alpha\beta} \mathbf{R} \mathbf{R}^T = M_{\alpha\beta} \mathbf{I} \quad \text{and} \quad \mathbf{M}_{\alpha\beta}^\diamond = \mathbb{J} (\mathbf{F}^T \mathbf{F})^{-1} M_{\alpha\beta} \quad (3.87)$$

Therefore, the spatial mobility matrix coincides with the intermediate definition. Nevertheless, the material mobility behaves anisotropic due to deformation. This anisotropy is required because of the nature of finite deformation where the partial differential equations are solved in the undeformed configurations.

3.4.6 Relation to Maxwell-Stefan Theory

From Eq. (3.83), we can directly deduce the Maxwell-Stefan diffusion model [103], which is also the foundation of Newman's derivation [53, 102, 120]. For simplicity, we restrict ourselves to isotropic mobilities

$\mathbf{M}_{\alpha\beta} = \mathbf{M}_{\alpha\beta} \mathbf{I}$. Recalling Eq. (3.83), inserting Eq. (2.15) and multiplying both sides with $c_\beta \mathbf{M}_{\alpha\beta}^{-1}$ yields

$$c_\beta \operatorname{grad}(\omega_\beta) = \sum_{\alpha=1}^N \tilde{\mathbf{K}}_{\alpha\beta} (\mathbf{v}_\alpha - \mathbf{v}_0) = \sum_{\alpha=0}^N \mathbf{K}_{\alpha\beta} (\mathbf{v}_\alpha - \mathbf{v}_\beta), \quad (3.88)$$

with the definition

$$\tilde{\mathbf{K}}_{\alpha\beta} = -c_\beta \mathbf{M}_{\alpha\beta}^{-1} c_\alpha \quad \text{with} \quad \mathbf{M}_{\alpha\beta}^{-1} = \left(\begin{array}{ccc} \mathbf{M}_{11} & \mathbf{M}_{12} & \cdots \\ \mathbf{M}_{21} & \mathbf{M}_{22} & \cdots \\ \vdots & \vdots & \ddots \end{array} \right)^{-1} \Big|_{\alpha\beta} \quad (3.89)$$

where we identify $\mathbf{K}_{\alpha\beta}$ as the drag coefficient as introduced e.g. in [53]. The transformations between the two drag coefficient matrices are

$$\tilde{\mathbf{K}}_{\alpha\beta} = \begin{cases} -\sum_{\gamma \neq \alpha=0}^N \mathbf{K}_{\alpha\gamma} & \alpha = \beta \\ \mathbf{K}_{\alpha\beta} & \alpha \neq \beta \end{cases} \quad (3.90)$$

$$\mathbf{K}_{\alpha\beta} = \begin{cases} 0 & \alpha = \beta \\ -\sum_{\gamma \neq 0=0}^N \tilde{\mathbf{K}}_{\alpha\gamma} & \alpha \neq \beta = 0 \\ -\sum_{\gamma \neq 0=0}^N \tilde{\mathbf{K}}_{\gamma\beta} & \beta \neq \alpha = 0 \\ \tilde{\mathbf{K}}_{\alpha\beta} & \text{else.} \end{cases} \quad (3.91)$$

Note that $\mathbf{K}_{\alpha\beta} \in \mathbb{R}^{N+1 \times N+1}$ considers friction with the host but no self or background friction. The matrices $\tilde{\mathbf{K}}_{\alpha\beta} \in \mathbb{R}^{N \times N}$ and $\mathbf{M}_{\alpha\beta} \in \mathbb{R}^{N \times N}$ have non-zero diagonal elements. These diagonal elements correspond to interactions with the underlying media. All reformulations maintain the symmetry of the matrices. The transformation of drag coefficients to

mobilities is $M_{\alpha\beta} = c_\alpha c_\beta \tilde{K}_{\alpha\beta}^{-1}$. The Maxwell-Stefan diffusion coefficients $\mathcal{D}_{\alpha\beta}$ are related to the second drag coefficients with

$$K_{\alpha\beta} = R\Theta \frac{c_\alpha c_\beta}{c_T \mathcal{D}_{\alpha\beta}}, \quad (3.92)$$

where $c_T = \sum_{\alpha=0}^N c_\alpha$ is the total concentration. Further, a host concentration c_0 is necessary within this description. For dilute solutions with no component-component interaction ($M_{\alpha\beta} = 0 \quad \forall \alpha \neq \beta$), we obtain the correlation $M_{\beta\beta} = \frac{c_T c_\beta}{R\Theta c_0} \mathcal{D}_{0\beta} \quad \forall \beta = 1..N$. The Maxwell-Stefan diffusion coefficients are similar to self-diffusion coefficients obtained by experiments [57, 120] or MD simulations [121]. If cross dependencies are present, the conversion within the concepts of mobilities and Maxwell Stefan coefficients is not as trivial and we refer to Section 3.5.5 for a binary electrolyte.

3.4.7 Ionic Current and Mass Fluxes

The driving force for mass transport in Eq. (3.80) is partially due to the chemical potential and partially driven by gradients of the electric potential, see Eq. (3.50). We now split the mass flux into a chemical and an electrical contribution with

$$\mathbf{J}_\alpha = \mathbf{J}_\alpha^C + \mathbf{J}_\alpha^E \quad \text{with} \quad \begin{cases} \mathbf{J}_\alpha^C &= -\sum_{\beta=1}^N \mathbf{M}_{\alpha\beta}^\diamond \text{Grad}(\mu_\beta) \\ \mathbf{J}_\alpha^E &= -\boldsymbol{\kappa}_\alpha^\diamond \text{Grad}(\Phi), \end{cases} \quad (3.93)$$

where we have introduced the mass conductivity

$$\boldsymbol{\kappa}_\alpha^\diamond = F \sum_{\beta=1}^N \mathbf{M}_{\alpha\beta}^\diamond z_\beta, \quad (3.94)$$

which defines the impact of the electric field on mass transport.⁴ A similar split for the electric current $\mathbf{J}_q = \sum_{\alpha=1}^N F z_\alpha \mathbf{J}_\alpha$ from Eq. (3.10) can be obtained by a rearrangement of the summation terms

$$\mathbf{J}_q = \mathbf{J}_q^C + \mathbf{J}_q^E \quad \text{with} \quad \begin{cases} \mathbf{J}_q^C &= -\sum_{\alpha=1}^N \boldsymbol{\kappa}_\alpha^\diamond \text{Grad}(\mu_\alpha) \\ \mathbf{J}_q^E &= -\boldsymbol{\kappa}^\diamond \text{Grad}(\Phi). \end{cases} \quad (3.95)$$

We can identify the mass conductivity of Eq. (3.94) in the chemical part of the current density and introduce the ionic conductivity

$$\boldsymbol{\kappa}^\diamond = \sum_{\alpha=1}^N F z_\alpha \boldsymbol{\kappa}_\alpha^\diamond, \quad (3.96)$$

which relates analog to Ohm's law (Eq. (3.15)) the electric part of the current density with the electric field. Together with Eq. (3.94) we observe that the ionic conductivity $\boldsymbol{\kappa}^\diamond$ is directly related to the mobilities. Further, we introduce a so-called transference number t_α^\diamond with

$$t_\alpha^\diamond \mathbf{J}_q^E = F z_\alpha \mathbf{J}_\alpha^E \quad \Rightarrow \quad t_\alpha^\diamond \boldsymbol{\kappa}^\diamond = F z_\alpha \boldsymbol{\kappa}_\alpha^\diamond \quad \Leftrightarrow \quad t_\alpha^\diamond = F z_\alpha \boldsymbol{\kappa}_\alpha^\diamond (\boldsymbol{\kappa}^\diamond)^{-1}, \quad (3.97)$$

as also introduced e.g. in [122, 123] for binary systems. Physically, the transference number t_α^\diamond represents the fraction of the overall current transported by species α in case of pure migration with no diffusion mechanism present ($\text{Grad}(\mu_\alpha) = 0$) [124]. The transference number in Eq. (3.97) is therefore a representation of mobilities and thus a well defined material property. Note that transference numbers are in general anisotropic, their sum is the identity tensor ($\sum_{\alpha=1}^N t_\alpha^\diamond = \mathbf{I}$) and, based on our derivation, we find that there is no thermodynamic

⁴ In the case of uncharged species—as found e.g. in active particles [63]—the conductivities from Eq. (3.93) are zero. Consequently, the electric portion \mathbf{J}_α^E drops out and only mass transport due to chemo-mechanics remains.

restriction demanding positivity of the transference number. In fact, negative entries in t_α^\diamond are possible when one component is more strongly affected by the chemical potential of another species, i.e. the component under consideration is dragged along by one or more other components. Recent experimental work [56, 123] confirms this theoretical result. We also refer to Section 3.5.6 which gives further insights on how to test thermodynamic consistency of the transport parameters.

In the following we assume that at least one species is charged ($z_\alpha \neq 0$). In such systems, the conductivity and transference number are measurable characteristic parameters and we can rewrite the current density of Eq. (3.95) with the last term in Eq. (3.97) as

$$\mathbf{J}_q = -\kappa^\diamond \sum_{\alpha=1}^N \frac{1}{Fz_\alpha} t_\alpha^\diamond \text{Grad}(\mu_\alpha) - \kappa^\diamond \text{Grad}(\Phi). \quad (3.98)$$

Next, we rewrite the electric part of the mass flux of Eq. (3.98) as

$$\mathbf{J}_\alpha^E = \frac{1}{Fz_\alpha} t_\alpha^\diamond (\mathbf{J}_q - \mathbf{J}_q^C), \quad (3.99)$$

which gives us the possibility of decomposing the species mass flux into three components

$$\mathbf{J}_\alpha = (\mathbf{I} - \mathbf{t}_\alpha^\diamond) \mathbf{J}_\alpha^C - \mathbf{t}_\alpha^\diamond \sum_{\beta \neq \alpha=1}^N \frac{z_\beta}{z_\alpha} \mathbf{J}_\beta^C + \frac{1}{Fz_\alpha} t_\alpha^\diamond \mathbf{J}_q \quad (3.100)$$

namely, a self diffusion, a drag diffusion and a migration portion, respectively. Note that Eq. (3.98) and Eq. (3.100) are generic versions of Newman type equations for transport in concentrated solutions [53].

Care has to be taken when evaluating the gradient of the chemical potential of Eq. (3.77). With $c_\alpha \stackrel{(2.13)}{=} c_\alpha^\diamond/\mathbb{J} \stackrel{(3.51)}{=} c_\alpha^\diamond/(\mathbb{J}_e \mathbb{J}_s)$ due to the effect of compression this gives rise to

$$\text{Grad}(\mu_\alpha) = \xi_\alpha^c \frac{\partial \mu_\alpha^C}{\partial c_\alpha} \text{Grad}(c_\alpha^\diamond) + \xi^P \Omega_\alpha \text{Grad}(p^M) + \xi_\alpha^{\mathbb{J}_e} \text{Grad}(\mathbb{J}_e) \quad (3.101)$$

with the prefactors

$$\begin{aligned} \xi_\alpha^c &= \frac{1}{\mathbb{J}} \left(1 - \frac{\partial \ln \mathbb{J}_s}{\partial \ln c_\alpha^\diamond} \right), \\ \xi^P &= \mathbb{J}_e \beta^s, \\ \xi_\alpha^{\mathbb{J}_e} &= \beta^s \Omega_\alpha p^M - \frac{c_\alpha^\diamond}{\mathbb{J}_e \mathbb{J}} \frac{\partial \mu_\alpha^C}{\partial c_\alpha}. \end{aligned} \quad (3.102)$$

The first term on the right hand side of Eq. (3.101) drives classical diffusivity, the center term is the mechanical driving force due to pressure gradients, whereas the last term specifies a second order effect due to volume change. In other words, if the volume changes due to elastic deformation, the ions are packed closer and the chemical energy increases. If the elastic deformation is inhomogeneous, the third driving force in Eq. (3.101) originates.

3.5 Binary Electrolyte

Ionic charge in binary electrolyte systems is carried by a positively charged cation and a negatively charged anion which we denote by $\alpha = \{+, -\}$. As we consider Lithium based binary electrolytes, we apply $z_+ = 1$ and $z_- = -1$ henceforth. In solid electrolytes, these ions are embedded in a solid host material, whose kinematics are described by the deformation

map φ_t ; this is fundamentally different from liquids where a third mobile component, the solvent, is present. Therefore, we have only two mobile species and obtain the binary mobility matrix

$$\{\mathbf{M}_{\alpha\beta} | \alpha, \beta = \{+, -\}\} = \begin{bmatrix} \mathbf{M}_+ & \mathbf{M}_\pm \\ \mathbf{M}_\pm & \mathbf{M}_- \end{bmatrix}, \quad (3.103)$$

with three independent mobilities (which can each be functions of concentration, stress, etc.). The diagonal contains the cation mobility \mathbf{M}_+ and the anion mobility \mathbf{M}_- . The off-diagonal term \mathbf{M}_\pm in addition to the fugacity stems from the non-ideality of concentrated solutions and can be associated with the motion of clusters of both cations and anions with unlike charge that cause the constituting cations to be influenced by the anion potential and vice versa. In the settings of ion-exchange polymer-metal composites (IPMC) [125] for sensing and actuation, this effect is known as electro-osmosis drag where water is shuttled along with hydrogen [126, 127]. Another motivation for the off-diagonal term is a counting argument. There are four constitutive quantities, namely the chemical potential and the three mobilities. This is the same number of parameters as for the standard parametrization of binary ion transport [53], see Section 3.5.5.

In the following, we will present three approaches to compute the motion of the mobile species $\{c_+, c_-, \rho_q\}$. The first is a straight forward application of the previously derived theory for binary electrolytes. The second approach is a reformulation introducing the balance of charge and serves as the transition to the third, the electroneutral version that constitutes simplifications of the first two. All of these formulations describe transport and, hence, the underlying structure of the mechanics with the Piola stress tensor \mathbf{P} from Eq. (3.70), the material mobilities $\mathbf{M}_{\alpha\beta}^\diamond$ from Eq. (3.84) and swelling from Eq. (3.61), is unaffected and remains the same in all versions.

3.5.1 Full Formulation

For the full formulation in terms of $\{\varphi_t, c_+^\diamond, c_-^\diamond, \Phi\}$, we state the balance of linear and angular momentum, add mass conservation for positive and negative ions derived from Eq. (3.83) and include Gauss' law as

$$\begin{aligned}
 \dot{c}_+^\diamond + \operatorname{Div}(\mathbf{J}_+) &= 0 \\
 \mathbf{J}_+ &= -\mathbf{M}_+^\diamond \operatorname{Grad}(\omega_+) - \mathbf{M}_\pm^\diamond \operatorname{Grad}(\omega_-) \\
 \dot{c}_-^\diamond + \operatorname{Div}(\mathbf{J}_-) &= 0 \\
 \mathbf{J}_- &= -\mathbf{M}_\pm^\diamond \operatorname{Grad}(\omega_+) - \mathbf{M}_-^\diamond \operatorname{Grad}(\omega_-) \\
 \operatorname{Div}(\mathbf{P}) &= 0, \quad \mathbf{P}\mathbf{F}^T = \mathbf{F}\mathbf{P}^T \\
 \operatorname{Div}(\mathbb{D}) &= \rho_q^\diamond, \quad \mathbb{D} = -\epsilon_0 \epsilon_r^\diamond \operatorname{Grad}(\Phi)
 \end{aligned} \tag{3.104}$$

where the electrochemical potentials are given by

$$\omega_+ = \mu_+ + F\Phi \quad \text{and} \quad \omega_- = \mu_- - F\Phi. \tag{3.105}$$

The equations in formulation (3.104) constitute the system of field equations necessary for the solution for the fields $\{\varphi_t, c_+^\diamond, c_-^\diamond, \Phi\}$. The initial boundary value problem requires initial conditions for $c_+^\diamond, c_-^\diamond$ and boundary conditions (BC) for $\varphi_t, c_+^\diamond, c_-^\diamond$ and Φ . Typical electrochemical boundary values (BV) are those for blocking electrodes given by

$$-\mathbf{N} \cdot \mathbf{J}_+|_{\partial\mathcal{B}_0} = -\mathbf{N} \cdot \mathbf{J}_-|_{\partial\mathcal{B}_0} = 0, \quad \Phi|_{\partial\mathcal{B}_0} = \tilde{\Phi}, \tag{3.106}$$

where $\tilde{\Phi}$ is a prescribed, position dependent electrical potential on the boundary. Also typical are galvanostatic BC specified by

$$-\mathbf{N} \cdot \mathbf{J}_+|_{\partial\mathcal{B}_0} = \frac{J^{\text{app}}}{F}, \quad -\mathbf{N} \cdot \mathbf{J}_-|_{\partial\mathcal{B}_0} = 0, \tag{3.107}$$

where a boundary current per undeformed area J^{APP} is applied and only cations leave the system. The boundary current is usually given by reaction kinetics such as the Butler-Volmer equation [128]. Note that for global electroneutrality, it is necessary that $\int_{\partial\mathcal{B}_0} J^{\text{APP}} = 0$, where $\partial\mathcal{B}_0$ denotes the boundary of the electrolyte. To within an additive constant the electric potential is fully described due to its coupling to ion transport.

3.5.2 Towards Balance of Charge

To reformulate Eq. (3.104), we recall the cation mass flux from Eq. (3.100) and use its binary form as

$$\begin{aligned}\mathbf{J}_+ &= \mathbf{t}_- \mathbf{J}_+^C + \mathbf{t}_+ \mathbf{J}_- + \frac{\mathbf{t}_+^\diamond}{F} \mathbf{J}_q \\ &= -(\mathbf{t}_-^\diamond \mathbf{M}_+^\diamond + \mathbf{t}_+^\diamond \mathbf{M}_\pm^\diamond) \operatorname{Grad}(\mu_+) \\ &\quad - (\mathbf{t}_+^\diamond \mathbf{M}_-^\diamond + \mathbf{t}_-^\diamond \mathbf{M}_\pm^\diamond) \operatorname{Grad}(\mu_-) + \frac{\mathbf{t}_+^\diamond}{F} \mathbf{J}_q,\end{aligned}\tag{3.108}$$

where we identify an ambipolar mobility matrix as mentioned e.g. in [119] as

$$\begin{aligned}\mathbf{M}_{\text{amb}}^\diamond &:= \mathbf{t}_-^\diamond \mathbf{M}_+^\diamond + \mathbf{t}_+^\diamond \mathbf{M}_\pm^\diamond = \mathbf{t}_+^\diamond \mathbf{M}_-^\diamond + \mathbf{t}_-^\diamond \mathbf{M}_\pm^\diamond \\ &= F^2 \left(\mathbf{M}_+^\diamond \mathbf{M}_-^\diamond - \mathbf{M}_\pm^\diamond {}^2 \right) \boldsymbol{\kappa}^{\diamond-1}.\end{aligned}\tag{3.109}$$

Note that in contrast to the treatment in [53], all concentration dependencies are hidden in the mobilities. Further, we exchange the anion concentration c_-^\diamond with the field variable total charge density ρ_q via $c_-^\diamond = c_+^\diamond - \frac{\rho_q^\diamond}{F}$ and obtain from Eq. (3.98) a statement for the charge flux

$$\mathbf{J}_q = -\frac{\boldsymbol{\kappa}^\diamond}{F} [\mathbf{t}_+^\diamond \operatorname{Grad}(\mu_+) - \mathbf{t}_-^\diamond \operatorname{Grad}(\mu_-)] - \boldsymbol{\kappa}^\diamond \operatorname{Grad}(\Phi).\tag{3.110}$$

From Eq. (3.104) we deduce with

$$\begin{aligned}\dot{\rho}_q^\diamond &= Fz_+ \dot{c}_+^\diamond + Fz_- \dot{c}_-^\diamond \\ &= \operatorname{Div}(Fz_+ \mathbf{J}_+) + \operatorname{Div}(Fz_- \mathbf{J}_-) = \operatorname{Div}(\mathbf{J}_q),\end{aligned}\quad (3.111)$$

the electric potential $\Phi = \frac{\omega_+}{F} - \frac{\mu_+}{F}$ and some rearrangements the second set of transport equations

$$\begin{aligned}\dot{c}_+^\diamond + \operatorname{Div}(\mathbf{J}_+) &= 0 \\ \mathbf{J}_+ &= -\mathbf{M}_{\text{amb}}^\diamond \operatorname{Grad}(\mu_+ + \mu_-) + \frac{\mathbf{t}_+}{F} \mathbf{J}_q \\ \dot{\rho}_q^\diamond + \operatorname{Div}(\mathbf{J}_q) &= 0 \\ \mathbf{J}_q &= -\frac{\boldsymbol{\kappa}^\diamond}{F} ((\mathbf{t}_+^\diamond - \mathbf{I}) \operatorname{Grad}(\mu_+ + \mu_-)) \\ &\quad - \frac{\boldsymbol{\kappa}^\diamond}{F} \operatorname{Grad}(\omega_+) \\ \operatorname{Div}(\mathbf{P}) &= 0, \quad \mathbf{P} \mathbf{F}^T = \mathbf{F} \mathbf{P}^T \\ \operatorname{Div}(\mathbb{D}) &= \rho_q^\diamond \quad \mathbb{D} = -\epsilon_0 \epsilon_r^\diamond \operatorname{Grad}(\Phi)\end{aligned}\quad (3.112)$$

where the current density is driven by the electrochemical potential of the cation, see Eq. (3.105). With respect to the BC, we exchange the anion flux in Eq. (3.107) with a boundary current with

$$-\mathbf{N} \cdot \mathbf{J}_q = J^{\text{app}} \quad (3.113)$$

consistent with the cation flux of Eq. (3.107).

3.5.3 Electroneutral Description

Ion polarization occurs only in the double layer close to interfaces and results in strong electric potential gradients. The width of this domain can be approximated by the Debye length [104] and is usually of the order

of nanometers. Away from this region, electrostatic forces are dominant, drawing unlike charges together, and therefore electroneutrality prevails. The relationship

$$c_+^\diamond \approx c_-^\diamond \quad (3.114)$$

is an adequate approximation for simplifying the transport equations and the individual concentrations c_+^\diamond and c_-^\diamond can be both replaced by a salt concentration $c_\pm^\diamond = c^\diamond$. Consequently, the charge density becomes zero $\rho_q^\diamond = 0$ everywhere and Poisson's law decouples from mass transport [116]. Besides the replacement of c_+^\diamond and c_-^\diamond by c^\diamond , it is beneficial to replace Φ by the electrochemical potential of the cations

$$\omega_+ = \mu_+ + Fz_+\Phi, \quad (3.115)$$

because it is directly accessible in probe measurements [53]. Consequently, we reduce the set of field variables $\{\varphi_t, c_+^\diamond, c_-^\diamond, \Phi\}$ to $\{\varphi_t, c^\diamond, \omega_+\}$. Conservation of charge, as given in the form of an extended Ohm's law in Eq. (3.112), then serves as the governing equation for the electrochemical potential.

Besides eliminating a field variable and thus saving computational effort, another advantage of the electroneutrality assumption is the reduction in the number of required parameters. This is significant especially since individual ion properties are very difficult to measure. With the molar

volume of the salt $\Omega_{\pm} = \Omega_+ + \Omega_-$, the chemical potential of the salt $\mu_{\pm}^C := \mu_+^C + \mu_-^C$ [53] and considering Eq. (3.101), we obtain

$$\begin{aligned}
 \dot{c}^\diamond + \text{Div}(\mathbf{J}_+) &= 0 \\
 \mathbf{J}_+ &= -\mathbf{D}^\diamond \text{Grad}(c^\diamond) + \frac{\mathbf{t}_+^\diamond}{F} \mathbf{J}_q \\
 &\quad - \xi^p \Omega_{\pm} \mathbf{G}^\diamond \text{Grad}(p^M) - \xi_{\pm}^{\mathbb{J}_e} \mathbf{G}^\diamond \text{Grad}(\mathbb{J}_e) \\
 \text{Div}(\mathbf{J}_q) &= 0 \\
 \mathbf{J}_q &= \mathbf{D}_q^\diamond \text{Grad}(c^\diamond) - \frac{\boldsymbol{\kappa}^\diamond}{F} \text{Grad}(\omega_+) \\
 &\quad + \xi^p \Omega_{\pm} \mathbf{G}_q^\diamond \text{Grad}(p^M) + \xi_{\pm}^{\mathbb{J}_e} \mathbf{G}_q^\diamond \text{Grad}(\mathbb{J}_e) \\
 \text{Div}(\mathbf{P}) &= 0, \quad \mathbf{P} \mathbf{F}^T = \mathbf{F} \mathbf{P}^T
 \end{aligned} \tag{3.116}$$

with contributions of diffusion, migration, stress-assisted diffusion and volumetric effects. The prefactors are given by

$$\begin{aligned}
 \mathbf{D}^\diamond &= \xi_{\pm}^c \mathbf{M}_{\text{amb}}^\diamond \frac{\partial \mu_{\pm}^C(c)}{\partial c}, \\
 \mathbf{G}^\diamond &= \mathbf{M}_{\text{amb}}^\diamond = \frac{1}{\xi_{\pm}^c} \left(\frac{\partial \mu_{\pm}^C(c)}{\partial c} \right)^{-1} \mathbf{D}^\diamond, \\
 \mathbf{D}_q^\diamond &= \frac{\xi_{\pm}^c}{F} (\mathbf{I} - \mathbf{t}_+^\diamond) \frac{\partial \mu_{\pm}^C(c)}{\partial c} \boldsymbol{\kappa}^\diamond, \\
 \mathbf{G}_q^\diamond &= \frac{1}{F} (\mathbf{I} - \mathbf{t}_+^\diamond) \boldsymbol{\kappa}^\diamond,
 \end{aligned} \tag{3.117}$$

with the Fickian diffusion coefficient \mathbf{D}^\diamond formulated in the material setting. Choosing the chemical potential μ_{\pm}^C to be of the form of Eq. (3.77) with mean salt fugacity $f_{\pm} = \sqrt{(f_-)(f_+)}$ as introduced in Eq. (3.69), we obtain

$$\frac{\partial \mu_{\pm}^C(c)}{\partial c} = \frac{2R\Theta}{c} \left(1 + \frac{\partial \ln f_{\pm}(c)}{\partial \ln c} \right), \tag{3.118}$$

where the expression in brackets is usually called the thermodynamic factor.

The set (3.116) thereby constitutes an extended version of the classical Newman theory [53, 129] with which it coincides for the case of $\varphi_t = \mathbf{X}$ (no deformation) and $\Omega_{\pm} = 0$ (no swelling). Under these conditions the last two terms on the right-hand side of the mass and current flux in Eq. (3.116) drop out.

The osmotic stress in Eq. (3.75) becomes

$$p^C = 2R\Theta \int_{c^{\text{ref}}}^{c_{\alpha}} \left(1 + \frac{\partial \ln f_{\pm}}{\partial \ln c} \right) dc, \quad (3.119)$$

and thus is solely depended on the thermodynamic factor.

Other than the parameters associated with swelling in Eq. (3.61) due to the salt molar volume, i.e. Ω_{\pm} and the reference salt concentration c^{ref} , no further properties than the standard electrochemical parameters $\{\mathbf{D}^{\diamond}, \kappa^{\diamond}, t_+^{\diamond}, 1 + \frac{\partial \ln f_{\pm}(c)}{\partial \ln c}\}$ are required to couple mechanics and ion transport in this formulation.

3.5.4 Steady State Current in a Binary Electrolyte

Charging and discharging a battery involves cation shuttling through the solid electrolyte. During this process, a concentration gradient of the salt builds up, see discussion in Section 4.4. When the steady state is reached, the concentration gradient has the highest slope eventually determining a steady state conductivity. The steady state conductivity property is important to judge the performance of an electrolyte and is also easy to access in measurements.

Since the anions are restricted to the electrolyte domain and are, unlike the cations, not inserted and extracted during operation, their dynamics determine the steady state. In other words, when the driving forces for anions are in equilibrium and their mass flux vanishes, i.e. $\mathbf{J}_{-} = 0$,

then the system is in steady state. From the mass fluxes in formulation (3.104), where we eliminate ω_- in the expression for \mathbf{J}_+ , we obtain with $(\mathbf{J}_q)^{\text{SS}} = F \mathbf{J}_+$ an expression of a steady state Ohm's law as

$$(\mathbf{J}_q)^{\text{SS}} = -(\boldsymbol{\kappa}^\diamond)^{\text{SS}} \text{Grad} \left(\frac{\omega_+}{F} \right) \quad (3.120)$$

with the steady state conductivity

$$(\boldsymbol{\kappa}^\diamond)^{\text{SS}} = F^2 \left(\mathbf{M}_+^\diamond - \mathbf{M}_\pm^\diamond (\mathbf{M}_-^\diamond)^{-1} \mathbf{M}_\pm^\diamond \right). \quad (3.121)$$

Expression (3.121) shows the importance of off-diagonal mobilities. The steady state conductivity would only be governed by the cation mobility if \mathbf{M}_\pm^\diamond is assumed to be zero. It is worth noting that effects from mechanics and the chemical potential do not enter the calculation explicitly. In the case of an isotropic system ($\mathbf{M}_{\alpha\beta} = M_{\alpha\beta} \mathbf{I}$), we can deduce requirements on the entries of the binary mobility matrix from Eq. (3.103) from a positive steady state conductivity. To do so, we write the steady state conductivity in the spatial form as

$$(\kappa^{\text{iso}})^{\text{SS}} = \frac{1}{J} \mathbf{F} (\boldsymbol{\kappa}^\diamond)^{\text{SS}} \mathbf{F}^T = \frac{1}{M_-} (M_+ M_- - M_\pm^2) \mathbf{I}. \quad (3.122)$$

The expression in brackets is the determinant of the spatial mobility matrix. Since both the determinant and the steady state conductivity are non-negative, we conclude $M_- \geq 0$. Due to the structure of the determinant, one can further conclude that M_+ has to be non-negative, too.

Alternatively, one can follow Balsara and Newman [130] and use the formulation (3.112) to derive the steady state conductivity. It is reached when

$$\mathbf{J}_- = -\mathbf{M}_{\text{amb}}^\diamond \text{Grad} (\mu_+ + \mu_-) - \frac{t_-}{F} \mathbf{J}_q^{\text{SS}} \stackrel{!}{=} 0. \quad (3.123)$$

and gives a correlation between the steady state current \mathbf{J}_q^{SS} and the chemical potential. Rearrangement yields

$$(\mathbf{J}_q)^{SS} = \frac{1}{Ne} \left(-\mathbf{t}_-^\diamond \frac{\boldsymbol{\kappa}^\diamond}{F} \text{Grad}(\mu_+ + \mu_-) \right), \quad (3.124)$$

where we have introduced the so called Newman number

$$Ne = \frac{(t_-^{\text{iso}} \kappa^{\text{iso}})^2}{F^4 \det M_{\alpha\beta}} = \frac{(M_- - M_\pm)^2}{\det M_{\alpha\beta}} = \xi^c \frac{\kappa^{\text{iso}} t_-^{\text{iso}}}{F^2 D^{\text{iso}}} \frac{\partial \mu_\pm}{\partial c}. \quad (3.125)$$

Here we have used Eq. (3.109) for M_{amb}^\diamond and assumed isotropic transport properties. Eq. (3.125) is in alignment with the work of Balsara and Newman [130]. The Newman number is non-negative due to the thermodynamic constraint $\det M_{\alpha\beta} \geq 0$. The right hand side of Eq. (3.124) corresponds to the diffusion part of the electric current in Eq. (3.112). Consequently, we obtain

$$(\mathbf{J}_q)^{SS} = -(\boldsymbol{\kappa}^\diamond)^{SS} \text{Grad} \left(\frac{\omega_+}{F} \right) \quad \text{with} \quad (\boldsymbol{\kappa}^\diamond)^{SS} = \frac{\boldsymbol{\kappa}^\diamond}{1 + Ne} \quad (3.126)$$

which is consistent with the result of Eq. (3.120).

3.5.5 Conversion of Transport Parameters

Binary electrochemical systems are usually characterized by macroscopic measurements yielding isotropic transport parameter $\{\kappa^{\text{iso}}, t_+^{\text{iso}}, D^{\text{iso}}, 1 + \frac{\partial \ln f_\pm(c)}{\partial \ln c}\}$. We now want to correlate these parameters to the mobilities and drag coefficients introduced in Section 3.4.4 and Section 3.4.6 as

these give an idea of the interaction of the anions and cations in the solid electrolyte. With Eq. (3.96), Eq. (3.97) and Eq. (3.117) we obtain

$$\begin{aligned}\kappa^{\text{iso}} &= F^2 (M_+ + M_- - 2M_\pm), \\ t_+^{\text{iso}} &= \frac{M_+ - M_\pm}{M_+ + M_- - 2M_\pm} \\ D^{\text{iso}} &= \frac{M_+ M_- - M_\pm^2}{M_+ + M_- - 2M_\pm} \frac{2R\Theta\xi_\pm^c}{c} \left(1 + \frac{\partial \ln f_\pm(c)}{\partial \ln c} \right).\end{aligned}\quad (3.127)$$

The spatial properties transform into the material description with

$$\boldsymbol{\kappa}^\diamond = \mathbb{J} \left(\mathbf{F}^T \mathbf{F} \right)^{-1} \boldsymbol{\kappa}^{\text{iso}}, \quad \mathbf{t}_+^\diamond = t_+^{\text{iso}} \mathbf{I}, \quad \mathbf{D}^\diamond = \mathbb{J} \left(\mathbf{F}^T \mathbf{F} \right)^{-1} \mathbf{D}^{\text{iso}}.\quad (3.128)$$

Taking the inverse of Eq. (3.127), we deduce mobilities from measured parameters as

$$\begin{aligned}M_\gamma &= \frac{D^{\text{iso}} c}{2R\Theta\xi_\pm^c \left(1 + \frac{\partial \ln f_\pm(c)}{\partial \ln c} \right)} + \kappa^{\text{iso}} \frac{t_\gamma^{\text{iso}}}{F^2}, \quad \gamma = \{+, -\} \\ M_\pm &= \frac{D^{\text{iso}} c}{2R\Theta\xi_\pm^c \left(1 + \frac{\partial \ln f_\pm(c)}{\partial \ln c} \right)} - \kappa^{\text{iso}} \frac{t_+^{\text{iso}} t_-^{\text{iso}}}{F^2}.\end{aligned}\quad (3.129)$$

The first part in Eq. (3.129) describes the influence of diffusion, the second equation reveals the diffusion and migration contributions to the mobility. The ratio of both for the anion mobility M_- is given by the Newman number, see Eq. (3.125).

Further, if we assume $f_\pm = f_+ = f_-$, we can compute from the fugacity the thermodynamic factor by integration as

$$f_\pm(c^*) = \exp \left(\int_0^{c^*} \frac{\partial \ln f_\pm(c)}{\partial \ln c} \frac{1}{c} dc \right).\quad (3.130)$$

Eq. (3.129) and Eq. (3.130) therefore yield the transformation rules to convert transport properties used in formulation (3.116) to the properties used in Eq. (3.104). Using Eq. (3.90) with the inverse of Eq. (3.89) gives the correlation between binary drag and diffusion coefficients for a binary system as

$$\begin{pmatrix} M_+ & M_\pm \\ M_\pm & M_- \end{pmatrix} = \frac{1}{c^2 (K_{0+} K_{0-} + K_\pm (K_{0+} + K_{0-}))} \begin{pmatrix} K_{0-} + K_\pm & K_\pm \\ K_\pm & K_{0+} + K_\pm \end{pmatrix} \quad (3.131)$$

The on-diagonal mobilities $M_{\alpha\alpha}$ stem from a complex interplay between friction of host as well as the adjacent component. If the drag coefficients are positive then the mobilities are also positive. Combining Eq. (3.127), Eq. (3.131) and Eq. (3.92) provides us with

$$\begin{aligned} \kappa^{\text{iso}} &= \frac{F^2 (K_{0+} + K_{0-})}{c^2 (K_{0+} K_{0-} + K_\pm (K_{0+} + K_{0-}))} \\ t_+^{\text{iso}} &= \frac{K_{0-}}{K_{0+} + K_{0-}} = \frac{\mathcal{D}_{0+}}{\mathcal{D}_{0+} + \mathcal{D}_{0-}} \\ M_{\text{amb}}^{\text{iso}} &= \frac{c^2}{K_{0+} + K_{0-}} = \frac{c_T c}{R \Theta c_0} \frac{\mathcal{D}_{0+} \mathcal{D}_{0-}}{\mathcal{D}_{0+} + \mathcal{D}_{0-}} =: \frac{c_T c}{R \Theta c_0} \mathcal{D} \end{aligned} \quad (3.132)$$

where we have linked the isotropic ambipolar mobility $M_{\text{amb}}^{\text{iso}}$ from Eq. (3.109) and the thermodynamic diffusivity $\mathcal{D} = \frac{\mathcal{D}_{0+} \mathcal{D}_{0-}}{\mathcal{D}_{0+} + \mathcal{D}_{0-}}$ [53, 120]. It is worth noting that only the conductivity depends on the component-component friction K_\pm . Further, the transference number can only be negative if one of the drag coefficients K_{0-} or K_{0+} is negative.

It is important to note that measurements of electrochemical transport parameters do not usually take the mechanical response into account. As seen in the derivations, conductivity and transference number are not influenced by mechanics. The steady state conductivity from Eq. (3.122) is another measurable parameter without direct impact of mechanics.

The diffusion coefficient is, however, usually identified by experiments where quite large concentration gradients occur. In such measurements, we expect a strong influence of mechanical driving forces which assist the diffusion. The measured relaxation time can be then only associated to an effective diffusion coefficient. An alternative approach to gain diffusion coefficients without contributions of stress driven diffusions might be atomistic simulations [131].

Finally, we want to point out that a third component would introduce three new transport parameters due to the non-diagonal entries. In general, having N species requires $N(N+1)/2+1$ independent measurable parameters to account for all possible interactions between ions and the chemical potential.

3.5.6 Thermodynamically Consistent Parameters

It is important to use thermodynamically consistent parameters in order not to violate the fundamental second law of thermodynamics. Obviously, this has to hold for both the formulation with mobilities (Eq. (3.104)) and the parameters of the concentrated solution theory (Eq. (3.116)). For the former, we have concluded that the mobility matrix $\mathbf{M}_{\alpha\beta}$ has to be positive semi-definite, see Eq. (3.81). The eigenvalues, therefore, can be checked for validation. In binary isotropic electrolytes, an easier assessment is possible. From Eq. (3.109), (3.117) and (3.118) we deduce that the determinant is positive for positive conductivity, diffusivity and thermodynamic factor. In isotropic systems, this reads

$$\det(\mathbf{M}_{\alpha\beta}) = D^{\text{iso}} \kappa^{\text{iso}} \frac{c}{2R\Theta\xi_{\pm}^c} \left(1 + \frac{\partial \ln f_{\pm}(c)}{\partial \ln c}\right)^{-1}. \quad (3.133)$$

Note that a positive determinant does not necessarily yield a positive definite matrix. However, we know that the diagonal elements are positive due to positive steady state conductivity in Eq. (3.122). If the symmetric

mobility matrix has a strongly diagonally dominant structure, it has a positive definite form. This feature is given with $0 < t_+^{\text{iso}} < 1$ as seen in Eq. (3.127). Therefore, we can conclude that

$$\begin{aligned} 0 < \kappa^{\text{iso}}, \quad 0 < (\kappa^{\text{iso}})^{\text{SS}}, \quad 0 < D^{\text{iso}}, \\ 0 < t_+^{\text{iso}} < 1, \quad 0 < 1 + \frac{\partial \ln f(c)}{\partial \ln c}, \end{aligned} \tag{3.134}$$

is sufficient to fulfill the second law of thermodynamics. If not, the eigenvalues of $M_{\alpha\beta}$ have to be computed and checked for non-negativity. Therefore, the transference number t_+^{iso} cannot just independently take any real value as proposed by Monroe and Delacourt [102].

3.6 Summary

In this chapter, we have presented a rigorous formulation of ion transport in a solid electrolyte. Using the concept of finite strain, the Coleman-Noll procedure and the Helmholtz energy, we derived in a consistent manner the driving forces for species transport, the mechanical response of the host material and their coupling mechanisms. We thereby chose the transport description in the deformed geometry but solve it—as common in continuum mechanics—in a reference description. The influence of mechanics turned out to be broad. Most notable is the consideration of ion size by means of swelling and eventually stress driven diffusion. Further, we considered the effect of the change of geometry on mass flux and in the chemical potential. The former was also discussed for an anisotropic material and the latter gives rise to an osmotic pressure and is closely related to the thermodynamic factor. Using electroneutrality assumptions for a binary electrolyte, we have derived an extended version of concentrated solution theory [53] taking

diverse mechanical coupling mechanisms into account. We identified the connections to the Maxwell-Stefan theory and presented the correlation of mobilities, drag coefficients and transport parameters by means of conductivity, diffusivity, transference number and thermodynamic factor from concentrated solution theory. Further, the relation to the steady state current was shown and thermodynamic consistency of transport parameters was discussed. The off diagonal terms of the mobility matrix and hence the anion-cation interaction were found to be significant.

4 Understanding Ion Transport in a Binary Solid Electrolyte

In this chapter, we complement the theoretical description of the coupled electro-chemo-mechanical modeling of a binary solid electrolyte with numerical studies as shown in Ganser et al. [101]. We utilize simulations to highlight the coupling mechanisms between electrochemistry and mechanics in solid electrolytes and some of their implications on battery performance. Whenever possible and meaningful, we utilize full sets of measured, concentration-dependent transport properties. Three studies with polymer electrolytes and thus mobile anions and cations are shown. In particular, we examine the influence of the changes of the mechanical material properties on the response of the electrolyte, while keeping the electrochemical properties fixed.

4.1 Simulation Environment

We utilize the finite element solver COMSOL Multiphysics® [132]. Poisson equation (from Eq. (3.104)), conservation of mass (from Eq. (3.104) and Eq. (3.116), respectively) and balance of charge (from Eq. (3.116)) were implemented as partial differential equations in the "general form" and discretized with quadratic Lagrange elements. Since no theory development was done in the mechanical part of the transport theory in Chapter 3, we were able to use the COMSOL modules "structural mechanics" and "nonlinear structural materials" to solve the deformation field

with cubic Lagrange elements. All equation were solved in a fully coupled manner and all field variables involved were normalized to optimize accuracy and convergence.

4.2 Material Data

The most common polymer electrolyte is poly(ethylene oxide) (PEO) which shows sufficient transport and chemical stability. However, PEO creeps rapidly at elevated temperatures and its mechanical response then comes closer to that of a liquid than to that of a solid. Composite systems such as the block copolymers PS-PEO are under investigation to combine the transport property of PEO with enhanced mechanical properties of polystyrene (PS). However, besides improving mechanical properties, such compositing strategies generally reduce the volume fraction of the conducting phase and thus lead to reduced transport properties. This means that improving, e.g., mechanical stiffness generally negatively impacts electrochemical transport. In the following studies where the influence of mechanics is investigated, we keep the electrochemical parameters constant and thus do not account for these competing effects as we are interested in highlighting the effect of mechanics on electrochemistry. This is easier to study if electrochemical properties remain unchanged.

4.2.1 Electrochemical Transport Parameters

Only very few complete electrochemical characterizations are reported for polymer electrolytes. We utilize a set of concentration-dependent parameters for sodium salt (NaCF_3SO_3) in a PEO polymer electrolyte [55] and a recently published work [56] with lithium salt (LiTFSi). Furthermore, we take data from Timachova et al. [57] for the PS-PEO polymer with the lithium salt LiTFSi. In all cases, we assume a homogeneous material and

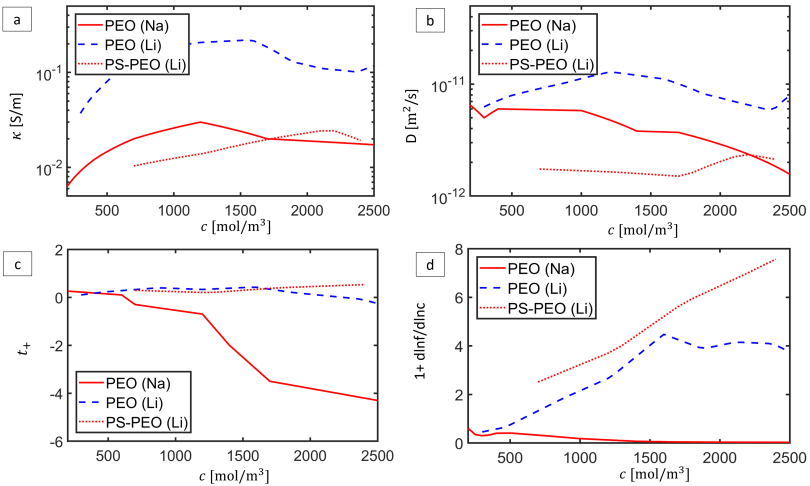


Figure 4.1: Transport properties data of PEO with sodium salt [55], with lithium salt [56] and PS-PEO with lithium salt [57]: (a) ionic conductivity, (b) diffusivity, (c) transference number and (d) thermodynamic factor.

define the concentration with respect to the overall PEO and PS-PEO volume, respectively.

The concentration-dependent transport parameters are shown in Fig. 4.1. In general, we can observe that the conductivity of PS-PEO is almost one order of magnitude lower compared to that of the two PEO electrolytes. The diffusivity of the sodium system varies almost one order of magnitude depending on the concentration. In contrast to that, PEO with lithium salt has an almost constant diffusivity of $D^{\text{iso}} \approx 1 \times 10^{-11} \frac{\text{m}^2}{\text{s}}$, which is much higher than the PS-PEO system. The transference number as shown in Fig. 4.1c is strongly negative for high concentrations of sodium salt while the other two lithium systems show very similar response, where only t_+^{iso} of PEO with LiTFSi is slightly negative for higher salt concentrations. The strong deviation of the sodium system compared to the lithium systems might be either a

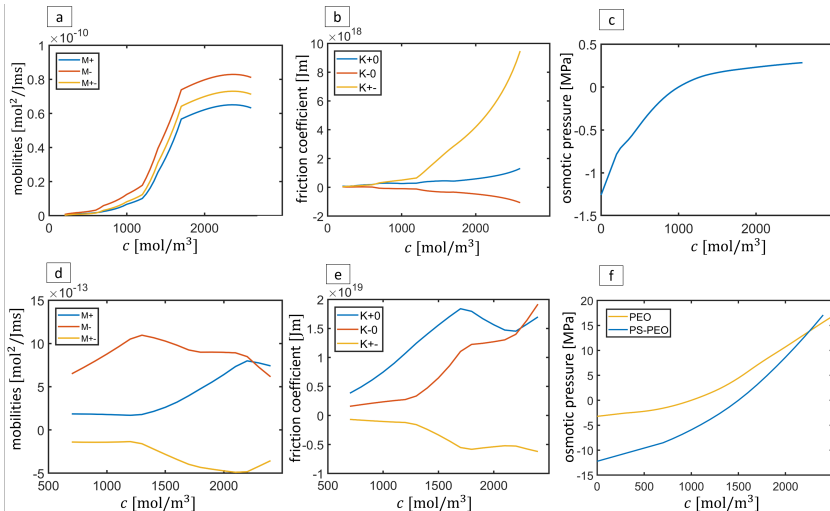


Figure 4.2: The graphs in the first row show the converted mobilities (a), drag coefficients (b) and chemical stresses (c) from PEO polymer electrolyte with sodium salt [55]. The graphs in the second row show the converted mobilities (d), drag coefficients (e) and osmotic pressure (f) converted from PS-PEO block-copolymer electrolyte [57]. Fig. (f) shows also the osmotic pressure from PEO with lithium salt [56].

consequence of the different material or simply due to a different evaluation method: Both Pesko et al. [56] and Timachova et al. [57] utilize the recently introduced concept of the Newman number, see Section 3.5.4, to measure transport properties. The thermodynamic factor is similar for the lithium salt systems and increases almost linearly with concentration. The sodium system on the other hand shows a very small thermodynamic factor.

We now take the measured transport properties of Fig. 4.1 and convert them into mobilities and drag coefficients. We do this for PEO with NaCF_3SO_3 and for PS-PEO with LiTFSi salt. The mobilities of the former are shown in Fig. 4.2a and were computed with Eq. (3.129).

It can be observed that anions are slightly more mobile than cations throughout the concentration range. Strong cross interactions between the ions are present due to the high off-diagonal mobility M_{\pm} . This is confirmed by the drag coefficient K_{\pm} in Fig. 4.2b obtained with Eq. (3.90). The negative drag coefficient K_{-0} is a consequence of the negative transference number. Although the negative sign is non-intuitive, one can show by an eigenvalue analysis that the system is still thermodynamically consistent, see Section 3.5.6.

The resulting mobilities of the PS-PEO/LiTFSi system are depicted in Fig. 4.2d and show a low cation mobility in the concentration range of interest. The mobile anion has a small drag coefficient (Fig. 4.2e). The negativity of the off-diagonal mobility goes along with a negative drag coefficient between anion and cation. Note that this negative mobility is not related to a negative transference number. Again, these data are admissible from a thermodynamic point of view, see Eq. (3.134).

4.2.2 Mechanical Properties

Measurements of mechanical properties of polymer electrolytes are challenging due to several reasons. The electrolyte layers used in batteries are very thin, the operating temperature range is usually elevated and an inert atmosphere is required. The few available characterization access mostly the elastic properties, although mechanically irreversible and time-dependent behavior is strongly expected. In the following, we will leave the Young's moduli as design parameters and disregard inelastic effects due to a lack of information. The orders of magnitudes are as follows: PEO provides a stiffness of roughly $E = 10 \text{ MPa}$ at room temperature [133, 134]. However, its ability to resist deformation at elevated temperatures decreases rapidly [48]. The mechanical properties for PS-PEO are dominated by the PS-phase, leading to roughly $E = 150 \text{ MPa}$ [45, 48] at operation temperatures of 80°C . We assume a Poisson ratio of $\nu = 0.4$.

for all electrolytes as found for e.g. polystyrene [135] and an isotropic response throughout the work.

The reference value of the molar volume is $\Omega_{\pm} = 140 \frac{\text{m}^3}{\text{mol}}$ for LiTFSi [136] and $\Omega_{\pm} = 80 \frac{\text{m}^3}{\text{mol}}$ for NaCF₃SO₃ [137]. Note that the ions are assumed to be compressible in the swelling model used in this work, see Section 3.4.1. The reference salt concentration for which swelling is assumed to be zero is set to be $c^{\text{ref}} = 1000 \frac{\text{mol}}{\text{m}^3}$ for PEO (both salts) and $c^{\text{ref}} = 1500 \frac{\text{mol}}{\text{m}^3}$ for PS-PEO. Fig. 4.2c and f shows the osmotic pressure of Eq. (3.75) as a function of salt concentration. With values up to 2 MPa for PEO with sodium salt it is small but not negligible. The chemical stress in a PS-PEO electrolyte is an order of magnitude higher compared to PEO with sodium salt and in the same order as PEO with lithium salt. The similarities of the lithium salt systems come either from the same salt or can be traced back to the experimental assessment of the thermodynamic factor.

4.3 Double Layer in a Solid Electrolyte

In the first example we want to show the capabilities of the full model as given by Eq. (3.104) that treats anions and cations separately and can thus be applied to situations where electroneutrality cannot be assumed everywhere and where the ions behave differently such as in a double layer. This effect is characterized by local anion/cation polarization and is most pronounced in the case of blocking electrodes. Related studies are found for liquid electrolyte systems [104, 138], solid electrolytes with fixed anions [139] and references cited therein. Double layer properties can be obtained experimentally e.g. via impedance spectroscopy measurements [140].

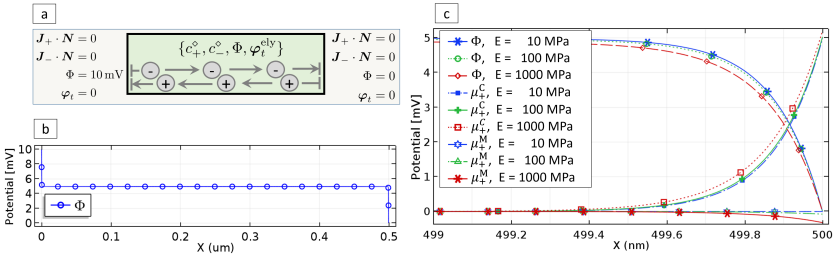


Figure 4.3: (a): Setup of the boundary value problem for blocking electrodes solved with Eq. (3.104). (b) illustrates the drop of electric potential over the whole domain and (c) zooms into the double layer regions where the electric potential decreases and the chemical potential increases. In systems with a high elastic modulus, mechanics has an influence on the result.

4.3.1 Material

We will restrict our investigation to the impact of mechanics on the ion distributions in a solid binary electrolyte. Note that concentration-independent material parameters are used in this study since the available parametrization as discussed in the previous section resolves the concentration dependency only with respect to the salt and does not distinguish between anion and cation concentrations. With $\kappa^{\text{iso}} = 0.01 \frac{\text{s}}{\text{m}}$, $D^{\text{iso}} = 5 \times 10^{-12} \frac{\text{m}^2}{\text{s}}$, $t_+^{\text{iso}} = 0.3$ a system similar to PS-PEO is utilized. We assume an ideal mixture such that $f_+ = f_- = 1$, see Eq. (3.69). These parameters transform with Eq. (3.129) to $M_+ = 1.1 \times 10^{-12} \frac{\text{mol}^2}{\text{mJ s}}$, $M_- = 1.5 \times 10^{-12} \frac{\text{mol}^2}{\text{mJ s}}$ and $M_\pm = 7.6 \times 10^{-13} \frac{\text{mol}^2}{\text{mJ s}}$, showing that the anion is more mobile than the cation. The electric permittivity is set to $\epsilon_r = 10$ [141], the molar volume of the salt is $\Omega_\pm = 140 \frac{\text{cm}^3}{\text{mol}}$ [136]. Although ion sizes for some non-aqueous solvents are reported [142], there is a lack of such information for solid state electrolytes and therefore we assume $\Omega_- = 10\Omega_+$. The reference concentration is assumed to be $c_\alpha^{\text{ref}} = 1000 \frac{\text{mol}}{\text{m}^3}$. As the influence of mechanics is the focus of this work, we vary Young's modulus in the range 10 MPa to 1000 MPa.

4.3.2 Boundary Value Problem

We consider a blocking electrode (Fig. 4.3a) of width $L = 0.5\text{ }\mu\text{m}$ with no-flux conditions for anions and cations on the boundaries. We assume that the right boundary is electrically grounded ($\Phi_r = 0$) and on the left boundary subject to $\Phi_l = 10\text{ mV}$. The system is mechanically fixed on both sides.

4.3.3 Results

A stationary solution exhibiting a double layer is reached within 1 ms. Fig. 4.3b shows a constant electric potential for most of the domain. The potential drops occur very locally at the two electrodes within the double layer (Fig. 4.3c) which extends to a width of 0.5 nm, comparable to the results in [139] and the Debye length of $\lambda_D = 0.1\text{ nm}^1$.

Fig. 4.4a shows the related concentration profiles of anions and cations within this double layer. Away from the electrode, the concentrations are basically equal which confirms electroneutrality for the inner part of the electrolyte. In the region close to the negative electrode the concentration of anions decreases whereas the cations accumulate. The concentration of cations is such that their chemical potential gradient balances the electric field (Fig. 4.3c). Comparison of the results with different Young's moduli reveals that the anion concentration depends strongly on the mechanical stiffness: The higher the material stiffness, the more pronounced is the non-symmetric response of the ions (Fig. 4.4a). The reason for this is that the large size of the anions leads to swelling that cannot be countered by depletion of the smaller cations. Consequently, a pressure gradient builds up and increases the mechanical contribution to the chemical potential (Fig. 4.3c). Although both ions are affected by this driving force, the

¹ The Debye length represents the length scale of the diffuse layer and is given by $\lambda_D = \sqrt{\frac{\epsilon_r \epsilon_0 \Theta}{F^2 c}}$ [138].

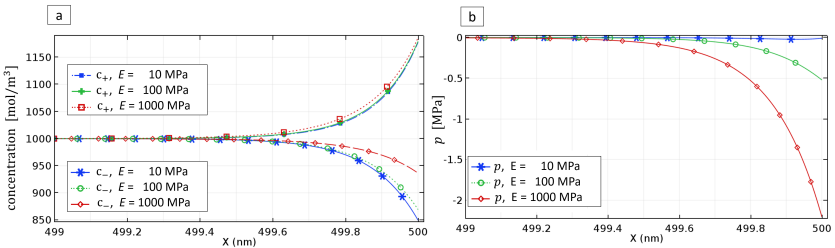


Figure 4.4: The figures show the concentration (a) and the pressure profiles (b) in the double layer for various material stiffnesses. The higher the elastic modulus, the more pronounced is the pressure gradient which acts as a mechanical driving force and yields a lower concentration of the anions. The impact on the smaller cations is less.

influence on bigger ions outweighs that on smaller ones and results in a considerably lower increase of anion concentration at the electrode for high Young's moduli. The cation concentration, however, increases slightly as the modulus is increased. This is a result of the lower drop of the anion concentration. The size of the double layer region stays nearly the same when the modulus is varied.

4.3.4 Discussion

In summary we see that the suggested full model of Eq. (3.104) is well suited to describe double layers and can also predict the influence of the mechanical properties of the electrolyte on the related electrochemical phenomena. Note that of course mechanical effects on the double layer are more pronounced in solid electrolytes than in liquid electrolytes, where the solvent is mobile and can relax the constraints in liquids.

Finally we point out that the electroneutral transport model from Eq. (3.116) cannot capture the potential drop associated with blocking electrodes, since only a full model with dedicated Poisson equation and separate concentration fields for anions and cation such as given by Eq. (3.104) can accurately describe the situation, specifically at the

boundaries. However, in contrast to the case of blocking electrodes, charge separation is negligible when flux boundary conditions are used such as for galvanostatic charge and discharge (see Example 4.4). In this situation, the discontinuities in electric potential adjacent to the electrode are features of the redox reactions occurring at the interfaces between the electrolyte and the electrodes. As such they are accounted for by models like Butler-Volmer reaction kinetics (see Chapter 5) or Tafel equations. As a result, the electroneutral model serves as an appropriate approximation when flux BC are invoked. The blocking electrode BC is therefore the condition that most strongly requires an approach that accounts for local charge separation.

4.4 Galvanostatic Charging

When a battery is charged, cations pass from the positive electrode (cathode) to the negative electrode (anode) through the electrolyte. When this process occurs at a given current density it is referred to as galvanostatic charging. In a binary electrolyte, both anions and cations act as carriers of charge, but only one kind of ion (usually the cation) enters and leaves the system. The other (usually the anion) accumulates against what are effectively blocking electrodes. The cation is locally attracted to the polarizing anions due to strong electrostatic forces (leading to effective local electroneutrality) and eventually a salt concentration gradient builds up. These profiles dictate the performance of a battery and are thus one of the classical tasks for electrochemical simulations to predict. Locally low concentrations are not favorable due to their influence in slowing reaction kinetics on the interfaces, while locally high concentrations can lead to phase separation, e.g. depletion of lithium. The concentration gradient is usually governed by the diffusion coefficient, the transference number and the thermodynamic factor. In this study, we emphasize

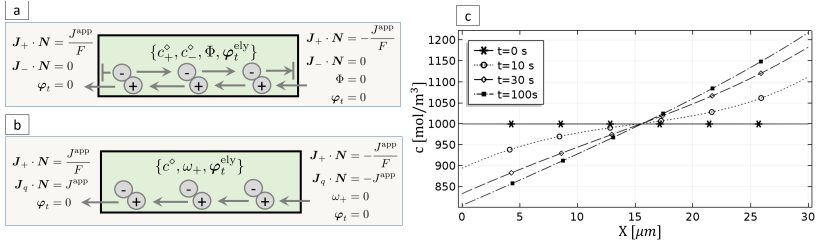


Figure 4.5: Setup of the boundary value problem of galvanostatic charging for (a) the full model, Eq. (3.104) and (b) the reduced model, Eq. (3.116). (c): A concentration gradient builds up during charging for $E = 10 \text{ MPa}$. Both, model (3.104) and model (3.116) lead to the same result.

that mechanical properties can also be important in controlling the salt concentration gradient and thus the performance of the electrolyte. We utilize isotropic parameters of the PEO polymer with NaCF_3SO_3 salt [55] at 85°C operating temperature, see Section 4.2.1. We will vary the Young's modulus in the range of 10 MPa to 500 MPa . For the full description as given in Eq. (3.104), we utilize $\epsilon_r = 10$, $f_+ = f_-$ and $\Omega_- = 10\Omega_+$.

4.4.1 Boundary Value Problem

We use both the full model without electroneutrality from Eq. (3.104) and the extended Newman model from Eq. (3.116) to study the complex interplay of electrostatics, chemistry and mechanics. The charging process can be treated as a 1D problem where we assume a separator thickness of $L = 30 \mu\text{m}$. We apply a current of $J^{\text{app}} = 0.5 \frac{\text{mA}}{\text{cm}^2}$ and set $\Phi = 0 \text{ V}$ for the full and $\omega_+ = 0 \text{ V}$ for the electroneutral model on the right, see Fig. 4.5. Again, we fix the left and the right boundary mechanically.

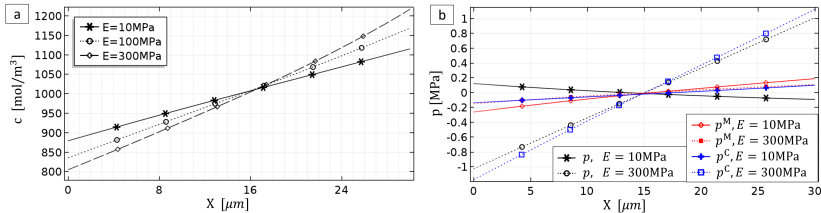


Figure 4.6: (a): Steady state concentration gradient which occurs during charging for three different Young's moduli. (b): Mechanical pressure p^M , osmotic pressure p^C and total pressure p within the electrolyte.

4.4.2 Results - General Remarks

Focusing first on the electrochemical response, we carry out a simulation with fixed Young's modulus of $E = 10 \text{ MPa}$. From the results we see that a concentration gradient builds up due to migration of anions in the first 100 s, see Fig. 4.5c. A stationary state is reached when the chemical driving forces on the anions equal the electric driving forces and hence $\mathbf{J}_- = 0$. Comparison of the extended Newman model and the full formulation yield the same concentration and electrochemical potential profile within numerical accuracy. In the full formulation, only a small double layer develops with differences in anion and cation concentration of $\leq 0.01 \frac{\text{mol}}{\text{m}^3}$. Note that spatial and material quantities are almost identical in this example because mechanical deformation is small.

4.4.3 Results from the Full Model

To gain further understanding on the coupling mechanism, it is instructive to investigate the driving forces for the ions $\text{grad}(\omega_\alpha)$ within the solid electrolyte and their chemical, mechanical and electrical components. The first order approximation of the gradient, e.g. $\text{grad}(\omega_\alpha) \approx \frac{\Delta\omega_\alpha}{L}$,

enables us to access the driving force by measuring $\Delta\omega_\alpha = \omega_\alpha^{\text{right}} - \omega_\alpha^{\text{left}}$.² For $E = 10 \text{ MPa}$, we measure $\Delta\omega_+ = 13.2 \text{ mV}$ for the cations and $\Delta\omega_- = -8.2 \text{ mV}$ and hence a relatively high potential drop for the anions although the mass flux \mathbf{j}_- vanishes in steady state. This can be confirmed by using $\mathbf{j}_- = 0$ in Eq. (3.104) which gives

$$\text{grad}(\omega_-) = \frac{M_\pm}{M_+ M_- - M_\pm^2} j_+^{ss}. \quad (4.1)$$

The cation mass flux $\|j_+^{ss}\| = J^{\text{app}}/F$ is constant for a 1D-problem and consequently, even though the anion flux vanishes in steady state ($\mathbf{j}_- = 0$) the gradient of the anionic electrochemical potential can only be zero for $M_\pm = 0$.

To understand the influence of mechanics, we repeat the simulations with $E = 100 \text{ MPa}$ and $E = 300 \text{ MPa}$. We observe that concentration gradients are less pronounced with increasing mechanical stiffness E , see Fig. 4.6a. In general, the concentration polarization has two effects on mechanics: (1) The osmotic pressure p^C increases slightly for an increase of salt concentration and (2) the swelling mechanism leads to a pressure gradient (Fig. 4.6b). The mechanical pressure p^M thereby shows different characteristics for different moduli. It has a reversed slope with respect to the concentration polarization for $E = 10 \text{ MPa}$. This is a consequence of the osmotic pressure p^C which couples with the mechanical stress via $\text{Div}(\mathbf{P}^M + \mathbf{P}^C) = 0$. For high moduli such as $E = 300 \text{ MPa}$, the picture changes such that the sign of the pressure gradient follows the sign of the concentration gradient because the swelling mechanism becomes dominant. Local volume change is observed to be small with $J = 1 \pm 0.025$.

Fig. 4.7a shows the potential drops with respect to the mechanical moduli E . The electrochemical potential for the cation $\Delta\omega_+$ is composed

² We use the spatial description to motivate the findings and avoid therefore the formal material anisotropy as discussed in Eq. (3.84).

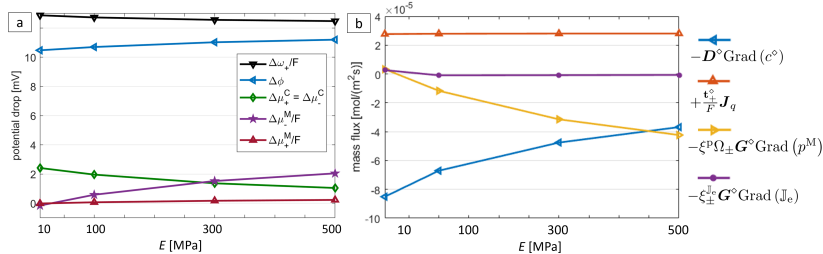


Figure 4.7: (a): Potential drops across the electrolyte of the individual contributions for various Young's moduli computed with Eq. (3.104). (b): The cation mass flux \mathbf{J}_+ for different stiffnesses at $\mathbf{X} = \frac{1}{2}\mathbf{L}$ is composed of diffusion (blue), migration (red), stress driven diffusion (yellow) and a volume change contribution (purple), see Eq. (3.116).

of $\Delta\Phi$, $\Delta\mu_{\pm}^C$ and $\Delta\mu_{\pm}^M$. The chemical contributions $\Delta\mu_{\pm}^C$ for both ions decrease with increasing stiffness. Note that the increased stiffness also leads to a less pronounced salt concentration polarization, see Fig. 4.6a. The mechanical contribution $\Delta\mu_{\pm}^M$ and $\Delta\mu_{\pm}^M$ is in tandem with the mechanical pressure as shown in Fig. 4.6b. However, due to the small size of the cation, $\Delta\mu_{\pm}^M$ and therefore its contribution to the electrochemical potential is small. The effect on the anion is substantially more pronounced, see Fig. 4.7a.

There is a small decrease of $\Delta\omega_+$, which comes from the concentration dependencies of the mobilities. Integrating the left equation in Eq. (4.1) we find that

$$\Delta\omega_+ = \int_{\mathcal{P}_t} \text{grad}(\omega_+) dv = \mathbf{j}_+ \int_{\mathcal{P}_t} \frac{\mathbf{M}_-}{\mathbf{M}_+\mathbf{M}_- - \mathbf{M}_{\pm}^2} dv, \quad (4.2)$$

where the mobilities are concentration dependent. The integral can be interpreted as a macroscopic steady state resistance. Using the concentration profile from Fig. 4.6a we obtain a smaller value from the integral and therefore a smaller $\Delta\omega_+$ for an increase of E . Further, we see a small

increase of $\Delta\Phi$ for increasing E in Fig. 4.7a. To explain this behavior, we consider the case of constant mobilities and therefore get from Eq. (3.83) the estimation

$$\underbrace{j_+}_{const.} \sim \underbrace{\text{grad}(\omega_+)}_{const.} = \text{Grad}(\mu_+^C) + \underbrace{\text{Grad}(\mu_+^M)}_{\sim 0} + F\text{Grad}(\Phi) \quad (4.3)$$

The gradient in electric potential has to compensate the gradient of the chemical potential.

4.4.4 Results from the Extended Newman Formalism

Now, we move our focus to the solution using the extended Newman formalism as given in Eq. (3.116) and probe the contribution on the mass fluxes in the middle of the separator ($X = \frac{1}{2}L$). The cation mass flux of $-5.2 \frac{\text{mol}}{\text{m s}^2}$ is composed of diffusion, migration, stress driven diffusion and a contribution from the effect of volume change, see Fig. 4.7b. The fractions due to migration and the effect of volume change stay almost constant for the range of investigated moduli. The stress driven contribution gains importance for higher material stiffness and, therefore, the diffusion contribution is less pronounced. The latter can be seen from the smaller gradient of concentration in Fig. 4.6a. Note that probing at a fixed location with varying concentration introduces an additional contribution due to the concentration-dependence of the transport properties. Positivity of the migration originates from the negative transference number (Fig. 4.1c).

4.4.5 Discussion

This example illustrates several aspects of the complex mechanisms occurring during galvanostatic charging. Both models, Eq. (3.104) and

Eq. (3.116), align and no pronounced double layer effects are observed. The parametrization [55] shows strong interactions between anions and cations by means of cross mobilities M_{\pm} . They have a direct influence on the steady state current of Eq. (3.120) and potential drop of Eq. (4.1) and yield $\text{Grad}(\omega_-) \neq 0$ although $\mathbf{J}_- = 0$. Young's modulus has a great impact on the concentration profile. The decrease of chemical potential drop with increasing Young's modulus goes together with an increase of electric potential drop. The mechanical contribution μ_+^M is found to be small. Overall, the electrochemical potential drop $\Delta\mu_+$ is barely influenced by a change of Young's modulus.

The mechanical driving forces in Eq. (3.116) due to swelling show a pronounced influence on ion transport. Especially for stiffer systems, the influence of stress driven diffusion is on the order of the diffusion mechanism and must be accounted for. Although we see a strong impact on the concentration distribution in the simulation, the absolute value of mechanical stress is small and therefore not in the regime of inelastic deformation. For soft materials, osmotic pressure leads to small strains and stresses which induce (small) transport contributions in the direction opposing the concentration increase. On the other hand, for stiffer materials, the importance of osmotic pressure is negligible for the parameter set investigated. Transport effects due to volume change are small in all cases.

4.5 Mechanically Deformed Electrolyte

For the last example in this chapter, we study a two dimensional problem where the solid electrolyte undergoes an inhomogeneous external deformation. This can be caused for example by inhomogeneous deposition on a metal interface on one side of the electrolyte layer, i.e. the growth of an intrusion penetrating the separator. The change of effective transport

paths is an obvious outcome, but also a stress field in the host will build up which couples with ion transport. With this example, we want to demonstrate the importance of the large deformation formalism for correctly predicting ion transport in a deformed solid electrolyte and we want to show that external deformation has a strong influence on the concentration distribution within a solid electrolyte.

4.5.1 Setup

We use the the full model as given in Eq. (3.104) to solve this problem. The formulation includes various aspects of coupling between mechanical deformation and electrochemistry. An analysis of the different contributions in the fully coupled system is difficult since all effects interplay with each other. Therefore, in addition to the full model, we consider two simplifications to isolate specific effects and to investigate the importance of the individual coupling mechanisms:

<i>Setting A</i>	$\beta^s = 0$	(No swelling)	$\mu^C(c^\circ)$	(No spatial diffusion)
<i>Setting B</i>	$\beta^s = 0$	(No swelling)	$\mu^C(c)$	(Spatial diffusion)
<i>Setting C</i>	$\beta^s = 1$	(With swelling)	$\mu^C(c)$	(Spatial diffusion)

Both *Settings A* and *B* exclude the swelling mechanism and therefore consider no contribution of stress driven diffusion. In addition to this simplification, *Setting A* excludes the contribution of the change of volume to the chemical energy with $\mu^C(c^\circ)$ such that e.g. no osmotic pressure is present. Therefore, Eq. (3.116) simplifies with $\xi_\alpha^c = 1$ and $\xi_\alpha^p = \xi_\alpha^{J_e} = 0$ and only the change of transport path due to deformation is taken into account. On the other end of the spectrum, *Setting C* includes all features. For this calculation we use the electrochemical data measured for a PS-PEO block-copolymer with LiTFSi [57], see Section 4.2.1, and $E = 300 \text{ MPa}$.

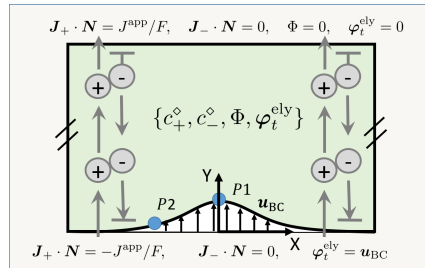


Figure 4.8: Boundary conditions for Example 4.5. Mechanical deformation with displacement BC is applied at *Phase 3*. P1 and P2 mark the probe points for Fig. 4.9.

4.5.2 Boundary Value Problem

We consider a rectangular domain of size $50 \mu\text{m} \times 30 \mu\text{m}$ with periodic BC left and right, see Fig. 4.8, and apply plain strain conditions. The top edge is fixed in space and grounded ($\Phi = 0$). The bottom edge will be deformed into a Gaussian-like shape with $\mathbf{u}_{\text{BC}} = [X, A^P w(X/R^P)]$, where we utilize the Wendland function

$$w(r) = (1 - \|r\|)^4(1 + 4\|r\|) \quad \forall r \leq 1 \quad (4.4)$$

with amplitude A^P and radius R^P to define the protrusion with compact support of size $2R^P$. The amplitude is chosen to be $A^P = 5 \mu\text{m}$ and the radius is $R^P = 20 \mu\text{m}$. Further, we impose a current density J^{APP} on the top and bottom edges. To highlight the results of our theory, we will successively apply varying boundary conditions in six phases:

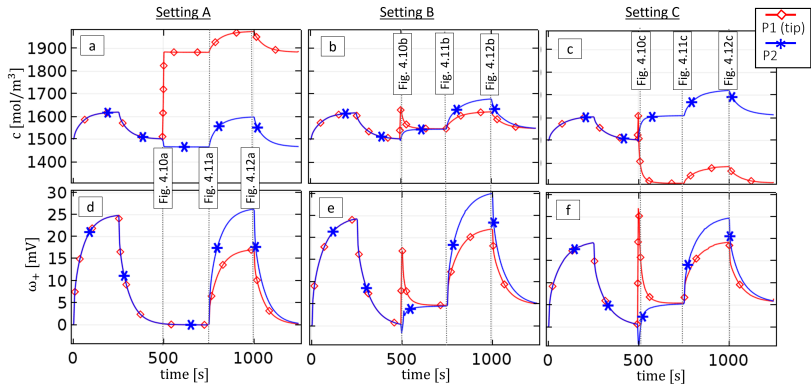


Figure 4.9: Spatial concentration c and electrochemical potential ω_+ measured at the tip (P1) and the flank (P2).

<i>Phase 1</i>	Current flow	$t = [0, 250]s$	$J^{\text{app}} = 0.175 \frac{\text{mA}}{\text{cm}^2}$	undeformed
<i>Phase 2</i>	Relaxation	$t = [250, 500]s$	$J^{\text{app}} = 0$	undeformed
<i>Phase 3</i>	Deformation	$t = [500, 505]s$	$J^{\text{app}} = 0$	
<i>Phase 4</i>	Relaxation	$t = [505, 750]s$	$J^{\text{app}} = 0$	deformed
<i>Phase 5</i>	Current flow	$t = [750, 1000]s$	$J^{\text{app}} = 0.175 \frac{\text{mA}}{\text{cm}^2}$	deformed
<i>Phase 6</i>	Relaxation	$t = [1000, 1250]s$	$J^{\text{app}} = 0$	deformed

Phase 1 serves as a comparison datum for a current flow on the deformed geometry in *Phase 5*. The relaxation *Phase 2* is used to obtain a steady state subsequent to a transient phase. In *Phase 3*, we apply a deformation much faster than the diffusion time to highlight the effect of mechanics. Since we obtain via the next relaxation in *Phase 4* a steady state once more, the features in *Phase 5* and *Phase 6* are independent of the rate of deformation as long as a purely elastic response is considered. The outcome would coincide with a slowly penetrating protrusion.

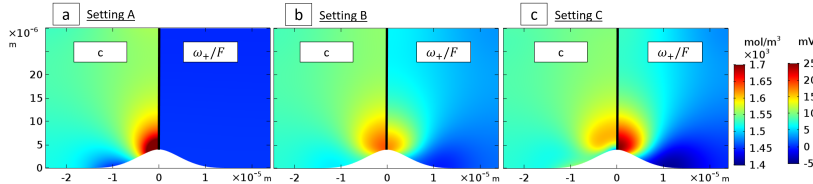


Figure 4.10: Color contour plots showing the salt concentration and the electrochemical potential in the electrolyte immediately after deformation (end of *Phase 3*). The spatial concentration shows a peak close to the protrusion tip. The electrochemical potential shows no gradient for *Setting A*, small effect for *Setting B* and a strong one for *Setting C*.

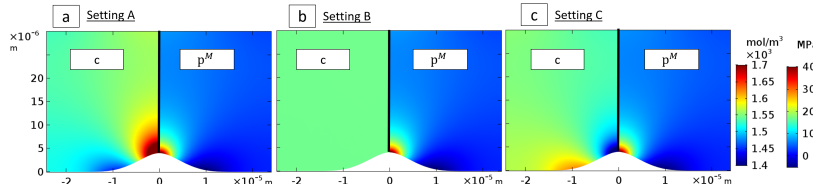


Figure 4.11: Color contour plots showing the salt concentration and mechanical pressure in the deformed electrolyte for the relaxed state in equilibrium (end of *Phase 4*). The concentration in *Setting A* does not relax, *Setting B* shows complete relaxation and in *Setting C* the ions are pushed away from high pressure regions.

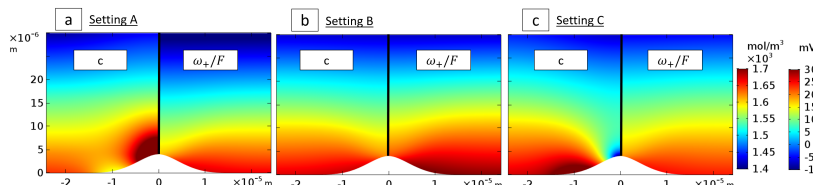


Figure 4.12: Color contour plots showing the salt concentration and the electrochemical potential in the electrolyte during galvanostatic charging (*Phase 5*). *Setting A* still shows a peak at the concentration tip, an almost linear concentration polarization occurs in *Setting B* and *Setting C* shows, even during concentration polarization, a depletion of salt at the tip.

4.5.3 Results

Fig. 4.9 shows the evolution of electrochemical potential ω_+ and spatial concentration c at two probes attached to the boundary of the material. One probe is associated with the tip of the protrusion ($\mathbf{X}_{P1} = [0, 0]$) and the other is on the flank ($\mathbf{X}_{P2} = [-15 \mu\text{m}, 0]$), see Fig. 4.8.

During application of current in *Phase 1*, a concentration gradient builds up. Therefore, the concentration at probes P1 and P2 increases in all settings, see Fig. 4.9. Since there is no deformation, the results for tip probe P1 and the flank probe P2 coincide. The concentration gradient is not as pronounced if stress-driven diffusion is taken into account and, therefore, *Setting C* has the least increase of salt concentration. The electrochemical potential is linked to the salt concentration and hence has the same characteristics. Afterwards, in *Phase 2*, the salt distribution relaxes to the reference concentration c^{ref} for all settings.

In *Phase 3*, the volume above the tip (P1) is compressed with $J_e \approx 0.8$, where swelling effects are small ($J_s \approx 1$) due to the fast deformation process. Therefore, the same amount of ions is located in a smaller (compressed) volume. Fig. 4.10 shows contour plots of the salt concentration and electrochemical potential immediately after deformation. If no swelling is considered, the salt concentration increases to a value of $c \approx \frac{1}{0.8}c^{\text{ref}} = 1.25c^{\text{ref}}$. Indeed, this happens in *Setting A* (Fig. 4.9a), but the electrochemical potential stays constant because of its material description (Fig. 4.10a). For the other two settings, this value is not reached. The diffusion mechanism due to increased chemical potential counteracts the concentration build-up from the beginning of the deformation. The peak of salt concentration at P1 in Fig. 4.9b increases only up to $c \approx 1.08c^{\text{ref}}$. The mechanical pressure locally reaches 50 MPa and therefore, in *Setting C*, stress driven diffusion plays a major role, increases ω_+ locally and therefore $\text{grad}(\omega_+)$ dramatically, and squeezes ions away from the tip immediately. The snapshot, Fig. 4.10c, taken

directly after deformation, shows depletion in the region of high pressure. An opposite effect can be seen in P2. This region experiences a small tension and thus an increase of volume ($J_e \approx 1.02$). Therefore, the ions occupy more space and the concentration decreases.

During relaxation after deformation (*Phase 4*, Fig. 4.11), no change of salt concentration occurs in *Setting A* since the chemical potential defined with respect to the material concentration is "not aware" of the deformation. Its value stays constant as seen in Fig. 4.9a and consequently the gradient, which drives transport, is zero. *Setting B*, in contrast, equilibrates the concentration profile to a value slightly above c^{ref} . This is a consequence of the no-flux-boundary conditions and conservation of mass in the deformed computational domain. Since Φ is prescribed on the top boundary, the change of $50 \frac{\text{mol}}{\text{m}^3}$ also affects the electrochemical potential which increases to 5 mV. The time constant to reach steady state is comparable to *Phase 2*. The response in *Setting C* shows again a gradient in salt concentration throughout the electrolyte. The salt concentration decreases at the tip with $c \approx 0.87c^{\text{ref}}$ (Fig. 4.11c) and therefore goes even below the reference concentration. The high pressure in this region makes the tip an energetically less favorable place for the ions. On the other hand, the region of negative pressure experiences a small increase of concentration.

In *Phase 5*, we solve for galvanostatic charging on the deformed geometry (Fig. 4.12). All of the three settings account for the deformed transport path associated with Eq. (3.84), i.e. the electrochemical potential at the tip (P1) needed for transport is 6 to 9 mV less than to that at P2 (Fig. 4.9). A concentration polarization with less salt accumulation on the tip (P1) and more ion accumulation on the flank (P2) originates and, roughly speaking, is superposed to the steady state of Fig. 4.11. Therefore, the very high concentration in *Setting A* is observed. *Setting B* -on the other hand- shows a moderate increase of salt concentration at P1, an effect of the shorter transport path (Fig. 4.12b). The gradient of

concentration in the electrolyte is almost homogeneous and therefore, one finds the highest concentration in the region furthest away from the counter electrode, i.e. in P2. *Setting C* shows a similar increase of concentration at both probes, P1 and P2, but the squeezing effect is still dominant and the concentration difference between P1 and P2 remains at $300 \frac{\text{mol}}{\text{m}^3}$. Nevertheless, due to the additional contribution of pressure in the electrochemical potential, the difference of ω_+ between P1 and P2 is smaller compared to the other two settings.

4.5.4 Discussion

These examples lay out the complex coupling mechanisms for ion transport in an inhomogeneously deformed solid electrolyte and illustrate the various contributions to the coupling in our model. Each setting (the simplified *Settings A* and *B* as well as the full *Setting C*) with their different assumptions shows not only qualitative, but also quantitative differences in terms of the mechanical and electrochemical response to a given penetration. The missing relaxation mechanism after deformation in *Setting A* is not compatible with the understanding of mobile ions within an electrolyte. Similarly, *Setting B* neglects the property of ion volume and thus omit the energetic unfavorability of salt in high pressure regions. Only *Setting C* provides a consistent coupling including considerations of the change of transport path, appropriate relaxation and stress driven diffusion. Therefore, we can predict a concentration and electrochemical potential profile along a deformed separator.

4.6 Summary

Three examples illustrated the impact of mechanics on ion transport by using both a transport model distinguishing cations and anions with

full considerations of electrostatics and one that only describes the salt concentration by assuming electroneutrality. Only the first is capable of resolving the double layer at a blocking electrode. In the case of galvanostatic charging, the electroneutrality condition holds throughout the domain and both models align. Maxwell stresses therefore are negligible. Also the osmotic pressure was found to be small for relatively stiff materials. Using electrochemical transport parameters from PEO based electrolytes and extending them by mechanical stiffness gave us the possibility of investigating the impact of Young's modulus on double layers (in blocking electrodes) as well as the salt concentration profile and electrochemical potential (galvanostatic charging). The salt concentration profile is strongly affected by the stiffness of the host material although only small pressure gradients occur. The electrochemical potential, however, alters only little. Finally we have studied the response of a deformed electrolyte. Only the comprehensive mechanical considerations of the fully coupled model enabled us to obtain reasonable simulation results. External deformation thereby influences the electrochemical transport significantly. The concentration profile along the interface varies strongly and suggests that a depletion of salt occurs in the region of highest intrusion.

With a constant boundary current we have excluded interface effects in these examples to analyze solely the bulk transport. Reaction kinetics at the electrode-electrolyte interface and their coupling with the bulk transport need to be described thoroughly for a comprehensive model of charge and discharge and will be discussed in the upcoming chapter.

5 Extended Butler-Volmer Interface Kinetics

Interface kinetics are a subject of non-equilibrium thermodynamics and describe the speed of a reduction / oxidation process as given e.g. in the context of reaction (1.2). Its generalized form is the monovalent reactions, i.e.



where an atom M reacts to a cation M^+ and an electron e^- . The reduction-oxidation processes are influenced by electric fields and, potentially, configurational entropy and mechanics. In analogy to the transport theory of Chapter 3, we approach the interface kinetics on a macroscopic level since the micro-structure of the interface is either barely understood, as in the case of the composition of the so-called solid-electrolyte-interphase (SEI) layer, or too difficult to treat computationally, e.g. requiring the atomistic structure to be resolved.

This chapter follows Ganser et al. [128] and discusses in the first section the state of the art of modeling reaction kinetics. We then use transition state theory from a purely energetic point of view and derive the generic form of the Butler-Volmer equation. This is then specialized to various combinations of different types of electrode and electrolyte, putting the presented theory in the context with commonly used formulas. A special emphasis will thereby be placed on the impact of mechanical stress and mechanics as they play varying roles depending on the specific combination of electrode and electrolyte considered. The mechanisms

behind deposition and stripping of a metal electrode will be discussed in detail. In the course of our formulation of the electro-chemo-mechanical reaction kinetics at the interface we suggest a new form of the Butler-Volmer equation for describing the influence of mechanics.

5.1 State of the Art

The Nernst equation and the Butler-Volmer equation are two widely used formulae for describing interface electrochemistry. The Nernst equation—an equilibrium description—correlates the difference between the energetic states of the adjacent materials, usually described by their activities, and the difference in their electric potentials [143]. The Butler-Volmer equation [70] on the other hand constitutes a non-equilibrium description that links the current flux at the interface to the electric potential drop across it via Arrhenius kinetics. If chosen consistently, the Butler-Volmer equation should thus yield the same result in conditions of equilibrium as stated by the Nernst equation. The Butler-Volmer equation is therefore the more general formulation.

Different approaches have been used to derive Butler-Volmer reaction kinetics. A prominent one is transition state theory, which is also our choice in this work. Our derivation is, however, slightly different to the derivations documented in literature so far. The basic idea of e.g. Bockris et al. [143], Hamann and Vielstich [144] and Newman and Thomas-Alyea [53] is as follows: The current density across the interface between an electrode and an electrolyte is governed by three quantities, namely concentration-independent reaction rate constants (k^{etr} , k^{ely}) determining the frequency of activation, the concentrations of the species present at the interface (c_M , c_+) specifying the amount of species which can react, and a contribution due to the activation energy, adjusted by the drop in electric potential across both sides of the interface $\Phi^{\text{etr}} - \Phi^{\text{ely}}$, where

Φ^{etr} , Φ^{ely} denote the electric potentials at the surface of the electrode and the surface of the electrolyte, respectively. Following this approach, the net current density then reads

$$j^{\text{BV}} = k^{\text{etr}} c_M \exp\left(\frac{-\overrightarrow{\Delta G}_{\text{ref}} + (1 - \beta)F(\Phi^{\text{etr}} - \Phi^{\text{ely}})}{R\Theta}\right) - k^{\text{ely}} c_+ \exp\left(\frac{-\overleftarrow{\Delta G}_{\text{ref}} - \beta F(\Phi^{\text{etr}} - \Phi^{\text{ely}})}{R\Theta}\right). \quad (5.2)$$

where j^{BV} is the current density across the interface, defined to be positive for ions moving from the electrode to the electrolyte, $\overrightarrow{\Delta G}_{\text{ref}}$ is the activation energy barrier for the forward reaction, $\overleftarrow{\Delta G}_{\text{ref}}$ is the activation barrier for the reverse reaction (both defined at reference state), F is the Faraday constant, β is the symmetry factor, R is the universal gas constant and Θ is the absolute temperature. Several authors [71, 145, 146] use Eq. (5.2) as a starting point for deriving an extended Butler-Volmer equation (e.g. to incorporate mechanics) - but each with a slightly different model and outcome. In addition, most of the derived theories are formulated in a way that makes their application to relevant problems very cumbersome. For example, Bockris et al. [143] refer to surface concentrations (i.e. moles per unit area) in the prefactors of Eq. (5.2), whereas usually volume concentrations are utilized in its application (i.e. moles per unit volume). Such volume concentrations are commonly utilized in applications of the Butler-Volmer equations because they are directly accessible from the theory of volumetric bodies.¹ Furthermore, only the dilute version of the Nernst equation can be derived from Eq. (5.2), as activity coefficients do not appear in its formulation.

¹ To avoid issues with units, some authors simply define the rate constant as a reaction velocity, see e.g. Christensen and Newman [61] or Hamann and Vielstich [144]. Other authors set bulk and surface concentration equal [147] or leave inconsistencies in their derivation [119].

Bazant and coworkers resolve this issue by extending the reference Gibbs energy by a non-ideality contribution, which is denoted as an excess chemical potential [112, 148, 149]. The comprehensive work of Bazant [112] describes various interfaces under non-ideal conditions with a special emphasis on phase transition materials such as LiFePO₄ in the framework of non-equilibrium thermodynamics.

Other aspects of the formulation of electrochemical kinetics at interfaces and their relationships to the Butler-Volmer equation have been addressed and shall be outlined in the following. As an alternative approach to transition state theory, one can use the law of mass action [150] to derive the Butler-Volmer equation, as seen in Latz and Zausch [151]. A rigorous asymptotic analysis was deployed by Dreyer et al. [152] to motivate the jump of electric potential in the interface region. Yang [147] extends the Nernst equation to the non-equilibrium condition and considers (surface) stresses in the overpotential via a Taylor expansion. Lai and Ciucci [122] propose an exponential relation between the current and the electrochemical potential drop across the interface. However, this drop is not modeled as an energy landscape with an activation energy to be overcome. We note that all the derivations mentioned above lead to the same overall form of the Butler-Volmer equation. However, they yield slightly different prefactors, especially when mechanical contributions are of interest.

A somewhat more sophisticated formulation is the electron transfer theory by Marcus and Hush, which assumes that the charge transfer kinetics are dominated by a reorganization of the solutes in the adjacent layers due to a change of charge. Well defined experiments on surface-bound redox couples showed that the electron transfer theory is superior to the Butler-Volmer equation, though both theories align for small current densities [153]. Further extensions are possible including effects such as electron tunneling in metal electrodes [153, 154], N-shaped free energy landscapes in intercalation materials [155] or proton-electron

interactions [156] to increase accuracy. A quantum mechanical approach for the description of reaction kinetics provided by the Marcus theory is also used e.g. in [112, 157–159]. Finally, we mention that the diffusive layer at the interface can be explicitly resolved through a Poisson-Nernst-Planck formalism. In this way only the remaining Stern layer needs to be modeled by a Butler-Volmer equation [65, 160]. However, we will restrict our analysis to the Butler-Volmer equation as it is commonly used and parameterized in the field of energy storage, especially in contexts where influences of mechanics are important such as solid state batteries.

5.2 General Framework

Following Bockris et al. [143], we utilize transition state theory to describe the reaction kinetics on an electrode-electrolyte interface. We restrict our considerations to a monovalent reaction, see Eq. (5.1). Intercalation, de-intercalation, deposition and stripping of lithium serve as concrete examples. As seen in Fig. 5.1, the material state changes from the electrode phase on the left hand side (in this case a metal electrode) to the electrolyte phase at the right hand side. This process follows a specific energy landscape along reaction coordinates. Note that these coordinates are a theoretical construct and are not necessarily related to spatial dimensions. Proceeding along the reaction coordinate may thereby describe various processes such as adsorption, electron transfer, transport through an SEI layer, passivation etc. The energetic states of the reactants in their reduced form G^{etr} (in the electrode) and in their oxidized form (in the electrolyte) G^{ely} are specified by Gibbs energies which consist of enthalpic, entropic and mechanical contributions. At this point, we assume the absence of an electric potential and postpone consideration of electrostatics. In the following, we use the notion of partial molar

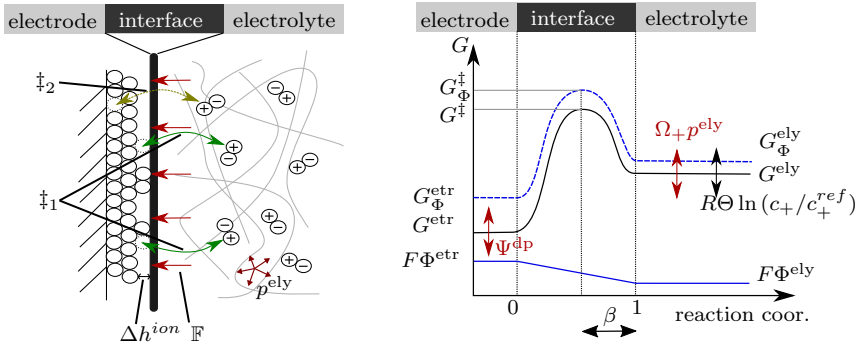


Figure 5.1: (a): Illustration of a metal electrode-electrolyte interface with a mechanical contribution due to electrolyte pressure and normal stress at the interface. The energy barrier G^\ddagger is associated with the most likely deposition/stripping reaction \ddagger_1 involving the first atomic layer of the electrode. Reactions into hidden layers, e.g. reaction in the second layer \ddagger_2 are not considered. (b): Energy landscape for a reaction involving the first layer at the interface between an electrode and electrolyte without an electric contribution (black) and with an electric contribution (blue). The double headed arrows indicate that the energetic level of electrode and electrolyte can change e.g. by deposition Ψ^{dp} , swelling $\Omega + p^{\text{ely}}$ or configurational entropy $R\Theta \ln(c_+/c_+^{\text{ref}})$.

Gibbs energy instead of chemical potentials as it is commonly used in the context of reaction kinetics.

5.2.1 Gibbs Energies of Electrode and Electrolyte

The most prominent representatives of electrolytes are binary ion conducting systems as discussed in Chapter 3. We assume an additive split of the Gibbs energy of the atoms in the electrolyte, in energy per mole,

$$G^{\text{ely}} = \sum_{k \in I^{\text{ely}}} G_k^{\text{ely}}, \quad I^{\text{ely}} = \{\text{ref, conf, ni, mech, V, ...}\}, \quad (5.3)$$

where the different contributions I^{ely} such as reference value, configurational entropy, non-idealities and mechanics are dependent on the chosen electrolyte. Note that electrical effects are excluded.

Recalling the chemical potential of a solid electrolyte of Eq. (3.77), and noting that for pure substances the partial molar Gibbs energy equals the chemical potential, we define the different contributions

$$G_{\text{conf}}^{\text{ely}} = R\Theta \ln(c_+/c_+^{\text{ref}}), \quad (5.4)$$

$$G_{\text{ni}}^{\text{ely}} = R\Theta \ln(f_+/f_+^{\text{ref}}), \quad (5.5)$$

$$G_{\text{mech}}^{\text{ely}} = \Omega_+ p^{\text{ely}}, \quad (5.6)$$

in addition to the reference value of the Gibbs energy per mole $G_{\text{ref}}^{\text{ely}}$ defined at standard pressure and at a reference value of concentration of the cation. If the concentration c_+ deviates from c_+^{ref} , one has to take the configurational entropy $G_{\text{conf}}^{\text{ely}}$ into account. The contribution of Eq. (5.4) holds for dilute solutions. Eq. (5.5) describes non-idealities, as usually present in concentrated solutions, see Section 3.4.2. The mechanical contribution of Eq. (5.6) in a binary solid electrolyte is a consequence of swelling and shrinkage of the electrolyte due to local change of salt concentration. Note that we describe the reaction kinetics in the spatial configuration and for simplicity we assume volume change in Eq. (3.77) with $\mathbb{J}_e \lambda^S = 1$ in this chapter.

Electrodes in battery applications are often aggregates of active particles where the ions are intercalated and de-intercalated in a host material, or metal electrodes where the ions are deposited and stripped layer by layer. We will consider four representative situations — a metal electrode with mechanical effects neglected, a metal electrode with mechanical effects taken into account, an active intercalation particle in the limit of

dilute concentrations of stored cations without mechanics and an intercalation particle with a high concentration of stored cations and with mechanics taken into consideration.

Similar to the electrolyte, we define an additive split of the Gibbs energy of the atoms in the electrode, without considering electrical effects, in energy per mole,

$$G^{\text{etr}} = \sum_{k \in I^{\text{etr}}} G_k^{\text{etr}}, \quad I^{\text{etr}} = \{\text{ref, conf, mech, ...}\}, \quad (5.7)$$

where the different contributions in I^{etr} such as a reference value, configurational entropy and mechanics are dependent on the kind of electrode.

The contribution $G_{\text{ref}}^{\text{etr}}$ is a reference value of the Gibbs energy per mole. If we assume that the electrode is at standard temperature and pressure, then $G_{\text{ref}}^{\text{etr}}$ is the standard Gibbs energy per mole. The reference values are specific for a system, i.e. we denote $G_{\text{ref}}^{\text{etr}|M}$ for a lithium metal electrode (M) and $G_{\text{ref}}^{\text{etr}|AP}$ for an active particle (AP). It is also related to a reference concentration c_M^{ref} , in moles per volume, of intercalated atoms. The configurational entropy is important if the atom concentration c_M deviates from c_M^{ref} :

$$G_{\text{conf}}^{\text{etr}} = R\Theta \ln(c_M/c_M^{\text{ref}}). \quad (5.8)$$

For higher atom concentration c_M in the active storage particle, one has to take the maximum capacity of the storage particle in moles per unit volume into account. Each spot is either occupied by an intercalated atom or a vacancy. The latter has a concentration c_V and the concentration of total sites is given by $c_M^{\text{max}} = c_M + c_V$. The reaction (5.1) is then



Since the vacancies appear in the reaction as oxidation products, their Gibbs energy

$$G_V^{\text{ely}} = R\Theta \ln \left(\left(c_M^{\max} - c_M \right) / c_M^{\text{ref}} \right), \quad (5.10)$$

is added to the electrolyte energy G^{ely} of Eq. (5.3). A mechanical contribution can be found in both active storage particle and metal electrode. The former is

$$G_{\text{mech}}^{\text{etr}}|^{\text{AP}} = \Omega_M p^{\text{etr}}, \quad (5.11)$$

where Ω_M is the partial molar volume of the intercalated atoms in the storage particle, and p^{etr} is the pressure in the storage particle minus standard pressure [63]. For a metal electrode, we have

$$G_{\text{mech}}^{\text{etr}}|^{\text{ME}} = \Psi^{\text{dp}}, \quad (5.12)$$

where the contribution Ψ^{dp} to the Gibbs energy due to deposition and stripping will be discussed in Section 5.3.

5.2.2 Reaction Kinetics

Now consider the reaction and the path it takes, still in a setting where the electric potential is zero everywhere so that electrostatics need not be considered. The reaction itself is a complex and nonlinear phenomenon with different multidimensional reaction paths possible. We choose the most likely path and associate a reaction coordinate between 0 and 1 to the process, as shown in Fig. 5.1. The reaction coordinate is not necessarily associated with a spatial length but, obviously, 0 corresponds to conditions in the electrode and an energy per mole for the cation equal to G^{etr} and 1 to conditions in the electrolyte and an energy per mole for the cation equal to G^{ely} . Somewhere between 0 and 1 on the reaction

coordinate axis there is an energetic barrier G^\ddagger which is the highest point in the energy landscape as seen in Fig 5.1.² The higher the barrier, the less likely is the successful completion of the reaction for each attempt.

Within transition state theory it is difficult to link a clear material state to the reaction coordinate and consequently it is not trivial to model the energetic state of the barrier. In analogy to the Bronsted-Evans-Polanyi principle (used e.g. in Huang et al. [161] and Bazant [112]) one can assume that the barrier has a relationship with the states of the electrode and electrolyte such that the barrier energy can be fully dependent, partially dependent, or completely independent of the energies of the cation in the electrode and the electrolyte. We therefore introduce the barrier energy, in energy per mole of the cation, as

$$G^\ddagger = G_{\text{ref}}^\ddagger + \sum_{k \in I^{\text{ely}}} \delta_k^{\text{ely}} G_k^{\text{ely}} + \sum_{k \in I^{\text{etr}}} \delta_k^{\text{etr}} G_k^{\text{etr}} \quad (5.13)$$

where G_{ref}^\ddagger is independent of the reduced (electrode) and oxidized (electrolyte) states and the prefactors δ_k^{etr} and δ_k^{ely} account for the relationship between the barrier energy and that of the cation in the electrode and the electrolyte. Eq. (5.13) can be regarded as an extension of Bazant [112], who applies the Bronsted-Evans-Polanyi principle solely to the reference energies. The prefactors have, as yet, an undetermined character, but possible choices for them will be discussed and utilized below. In general, the barrier can be expressed in terms of a transition state activity coefficient and it is explicitly dependent on the chemical or mechanical state of the activated complex, see e.g. Bazant [112]. However, these properties of the activated complex are not easily accessible. In the absence of electric potential, $G^\ddagger - G^{\text{etr}}$ is the energy barrier height standing in the way of a successful anodic reaction (oxidation). Similarly, in the absence

² The energy barrier corresponds to the state of an activated complex.

of electric potential, $G^\ddagger - G^{\text{ely}}$ is the energy barrier height standing in the way of a successful cathodic reaction (reduction).

We now consider the energy landscape in the presence of an electric potential. It changes if we consider charged species and electric potentials Φ^{etr} on the electrode and Φ^{ely} on the electrolyte.³ The Gibbs energies for the electrode and electrolyte for monovalent reactions, including the effects of electric potentials, are then, in energy per mole of cations,

$$G_\Phi^{\text{etr}} = G^{\text{etr}} + F\Phi^{\text{etr}}, \quad G_\Phi^{\text{ely}} = G^{\text{ely}} + F\Phi^{\text{ely}}, \quad (5.14)$$

where the second term is equivalent to the electrochemical potential of Eq. (3.115). Since the bulk properties of the interface regions (e.g. an SEI layer) are unknown, classical bulk theories for electrostatics like the Gauss law cannot be used to resolve the exact spatial distribution of the electric potential. Nevertheless, we know that the electric potential has to change continuously from the electrode to the electrolyte. Therefore, we make the assumption that the electric potential varies linearly along the reaction coordinates. Note that this assumption is tantamount to use of the value of the potential as a reaction coordinate. The energetic state of the barrier, due to electric potential, then becomes

$$G_\Phi^\ddagger = G^\ddagger + F(\Phi^{\text{ely}} + \beta(\Phi^{\text{etr}} - \Phi^{\text{ely}})), \quad (5.15)$$

where β , the symmetry factor, expresses the position of the peak value of energy in the energy landscape, i.e. the position of G^\ddagger on the reaction coordinate, see Fig. 5.1. Marcus-Hush theory indicates that $\beta = 0.5$ and aligns with several experimental findings on symmetric reactions [153]. However, more recent studies have revealed cases of asymmetric

³ Most authors we found use only the electric potential drop instead of the absolute values. We will see that only the drop is relevant and the absolute values do not affect the reaction rates.

heterogeneous electron transfer processes which do not allow an accurate parameterization in terms of Marcus-Hush theory unless one assumes unequal force constants for the solvent reorganization in reduced and oxidized state [162, 163]. We will proceed with the symmetry factor as a parameter.

If an ion is "sitting" on the electrode and attempts to jump into the electrolyte (anodic reaction) or is "sitting" in the electrolyte and attempts to jump onto the electrode (cathodic reaction), it has to overcome the activation energies

$$\overrightarrow{\Delta G}_\Phi = G_\Phi^\ddagger - G_\Phi^{\text{etr}}, \quad \overleftarrow{\Delta G}_\Phi = G_\Phi^\ddagger - G_\Phi^{\text{ely}} \quad (5.16)$$

for the forward (anodic) and backward (cathodic) reactions, respectively.⁴ Use of Eq. (5.13), (5.14) and (5.15) yields

$$\begin{aligned} \overrightarrow{\Delta G}_\Phi &= G_{\text{ref}}^\ddagger + \sum_{k \in I^{\text{etr}}} (\delta_k^{\text{etr}} - 1) G_k^{\text{etr}} + \sum_{k \in I^{\text{ely}}} \delta_k^{\text{ely}} G_k^{\text{ely}} \\ &\quad + (\beta - 1) F (\Phi^{\text{etr}} - \Phi^{\text{ely}}), \\ \overleftarrow{\Delta G}_\Phi &= G_{\text{ref}}^\ddagger + \sum_{k \in I^{\text{etr}}} \delta_k^{\text{etr}} G_k^{\text{etr}} + \sum_{k \in I^{\text{ely}}} (\delta_k^{\text{ely}} - 1) G_k^{\text{ely}} \\ &\quad + \beta F (\Phi^{\text{etr}} - \Phi^{\text{ely}}). \end{aligned} \quad (5.17)$$

Having established the activation energy barriers, we can now compute the rates of the reactions taking place at the interface. For this purpose,

⁴ Bockris et al. [143] use the opposite definition of the arrows. The right arrow in their publication describes electronation which is a cathodic reaction.

we use the Eyring theory [113] where the rates are determined from the activation energy through

$$\begin{aligned}\vec{r} &= \frac{k_B\Theta}{h} \exp\left(-\frac{\overrightarrow{\Delta G}_\Phi}{R\Theta}\right), \\ \overleftarrow{r} &= \frac{k_B\Theta}{h} \exp\left(-\frac{\overleftarrow{\Delta G}_\Phi}{R\Theta}\right),\end{aligned}\tag{5.18}$$

where \vec{r} it is the success frequency for the forward (anodic) reaction, k_B is Boltzmann's constant, h is Planck's constant and \overleftarrow{r} is the success frequency for the reverse (cathodic) reaction⁵. Note that the configurational entropy contribution in $\overrightarrow{\Delta G}_\Phi$ and $\overleftarrow{\Delta G}_\Phi$ yields a concentration dependency of \vec{r} and \overleftarrow{r} . Excluding the configurational entropy, one can identify the remainder of Eq. (5.18) with classical rate constants. The Boltzmann factor, for the forward reaction $\exp\left(-\frac{\overrightarrow{\Delta G}_\Phi}{R\Theta}\right)$ with temperature Θ and universal gas constant R gives the probability of the ion successfully accomplishing the jump, from the electrode to the electrolyte, with an equivalent Boltzmann factor for the reverse reaction. The coefficient $\frac{k_B\Theta}{h}$ is the attempt frequency for such jumps, see. e.g. Bockris et al. [143].

Full consistency of Eq. (5.18) with Eyring theory requires the exclusion of the dependency of G_Φ^\ddagger on the configurational entropy of the reactants by setting

$$\delta_{\text{conf}}^{\text{etr}} = \delta_{\text{conf}}^{\text{ely}} = \delta_V^{\text{ely}} = 0.\tag{5.19}$$

This choice is based on the understanding that Gibbs energies of reactants naturally depend on their concentrations, while a transition state only exists at a single point in time and, in this instance, is not an ensemble of states. We emphasize that values for $\delta_{\text{conf}}^{\text{ely}}$, δ_V^{ely} and $\delta_{\text{conf}}^{\text{etr}}$ other than

⁵ The transmission coefficient occurring in the Eyring theory is assumed to be one.

zero would lead to invalid kinetic rate laws even for simple chemical reactions independent of electrical potential. See also Savèant [156] for a critical discussion of previous studies that used invalid assumptions in the context of electron transfer processes.

To obtain an interface current from the success frequencies in Eq. (5.18), we introduce an area density c^S , in moles per unit area, of active surface sites. This property is independent of the actual amount of cations in the electrolyte and atoms in the electrode. In the case of a metal electrode this might be associated to the amount of atoms per area at the interface. For a sufficiently smooth surface the density c^S is directly related to the lattice constant and therefore a material constant. Implicit in this choice is the concept that only the outer layer (see \ddagger_1 in Fig. 5.1) is able to react with rate \vec{r} ; the reaction in hidden layers (e.g. \ddagger_2) are unlikely to occur because their energy barrier is much higher than G_{Φ}^{\ddagger} , and so their reaction rates will be negligible. Therefore, for a metal electrode, as shown in Fig. 5.1, the anodic reaction (stripping) then gives rise to a current density

$$\vec{j} = Fc^S \vec{r}. \quad (5.20)$$

We now argue that the same area density, c^S , controls the reverse (cathodic deposition) reaction. Consider an attempted jump of an ion from the electrolyte to the electrode. If the target site of that jump is already occupied by an atom (e.g. of an inner layer), there exists an additional energy barrier for completion of the jump in the form of repulsion from that site. Thus the success rate for such a jump will be negligible. Successful jumps are therefore only possible to sites on the surface whose area density on the metal electrode is given by c^S . Therefore, the current density associated to the reverse (cathodic deposition) reaction is

$$\overleftarrow{j} = Fc^S \overleftarrow{r}. \quad (5.21)$$

A similar argument holds for non-metallic active storage particles but with the area density c^S associated with the intercalation sites at the interface. Note that the entropic energy contribution and not c^S causes the forward or backward current density to vanish if the volume concentration approaches zero. For example, Eq. (5.8) and Eq. (5.4), respectively, yield

$$\begin{aligned} c_M \rightarrow 0 &\Rightarrow G^{\text{etr}} \rightarrow -\infty \Rightarrow \overrightarrow{\Delta G}_\Phi \rightarrow \infty \Rightarrow \overrightarrow{r} \rightarrow 0 \\ c_+ \rightarrow 0 &\Rightarrow G^{\text{ely}} \rightarrow -\infty \Rightarrow \overleftarrow{\Delta G}_\Phi \rightarrow \infty \Rightarrow \overleftarrow{r} \rightarrow 0. \end{aligned} \quad (5.22)$$

In the case of a metal electrode, the anodic current density cannot vanish since a reaction partner is always available on the surface. Surface passivation, however, can decrease the amount of active surface sites c^S and limit the overall current density. But such aspects of the behavior are outside the scope of this work.

Combining Eq. (5.20) and (5.21) with Eq. (5.16) and (5.18) yields the anodic and cathodic current densities

$$\begin{aligned} \overrightarrow{j} &= j_{00} \exp \left(-\frac{G_{\text{ref}}^\ddagger + \sum_{k \in I^{\text{etr}}} (\delta_k^{\text{etr}} - 1) G_k^{\text{etr}} + \sum_{k \in I^{\text{ely}}} \delta_k^{\text{ely}} G_k^{\text{ely}}}{R\Theta} \right) \\ &\quad \exp \left(\frac{(1 - \beta)F(\Phi^{\text{etr}} - \Phi^{\text{ely}})}{R\Theta} \right), \\ \overleftarrow{j} &= j_{00} \exp \left(-\frac{G_{\text{ref}}^\ddagger + \sum_{k \in I^{\text{etr}}} \delta_k^{\text{etr}} G_k^{\text{etr}} + \sum_{k \in I^{\text{ely}}} (\delta_k^{\text{ely}} - 1) G_k^{\text{ely}}}{R\Theta} \right) \\ &\quad \exp \left(-\frac{\beta F(\Phi^{\text{etr}} - \Phi^{\text{ely}})}{R\Theta} \right), \end{aligned} \quad (5.23)$$

where the prefactor is given by

$$j_{00} = \frac{k_B\Theta}{h} F c^S. \quad (5.24)$$

We note that Eq. (5.2) and Eq. (5.23) differ in that independent reaction rates and cation concentrations appear as coefficients of the anodic and cathodic current densities in Eq. (5.2), whereas they are identical in Eq. (5.23). The concept that the forward and reverse current densities are not explicitly a function of electrode and electrolyte cation concentrations is also applied by Gutman [150] who derives the current densities via the kinetic law of mass action.

Before evaluating the effective current densities, it is beneficial to consider a steady state where forward and reverse current densities are equal, and thus the net current density is zero. Under these conditions, the electric potential difference equals the equilibrium or open circuit potential $V_\Phi^{eq} = (\Phi^{etr} - \Phi^{ely})^{eq}$. The individual anodic and cathodic current densities prevailing at this equilibrium potential difference are then called the exchange current densities and read

$$\begin{aligned} j_0 &= j_{00} \exp \left(- \frac{G_{ref}^\dagger + \sum_{k \in I^{etr}} (\delta_k^{etr} - 1) G_k^{etr} + \sum_{k \in I^{ely}} \delta_k^{ely} G_k^{ely}}{R\Theta} \right) \\ &\quad \exp \left(\frac{(1 - \beta) F V_\Phi^{eq}}{R\Theta} \right) \\ &= j_{00} \exp \left(- \frac{G_{ref}^\dagger + \sum_{k \in I^{etr}} \delta_k^{etr} G_k^{etr} + \sum_{k \in I^{ely}} (\delta_k^{ely} - 1) G_k^{ely}}{R\Theta} \right) \\ &\quad \exp \left(- \frac{\beta F V_\Phi^{eq}}{R\Theta} \right). \end{aligned} \quad (5.25)$$

We deduce from the equality of the two lines in Eq. (5.25) a general version of the Nernst equation between the electrode and electrolyte as

$$\boxed{FV_{\Phi}^{\text{eq}} = G^{\text{ely}} - G^{\text{etr}},} \quad (5.26)$$

in agreement with Bockris et al. [143] who derive the Nernst equation from consideration of thermodynamic equilibrium.

We emphasize that the result connecting Eq. (5.25) and (5.26) is a consequence of the equality of the prefactor j_{00} in Eq. (5.25) for forward and reverse reactions. If the anodic and cathodic terms in Eq. (5.25) had coefficients that differ from each other and that are not both equal to j_{00} , the prefactors would enter Eq. (5.26) as exponents and a conventional Nernst equation would be unattainable. Note that the equilibrium potential in Eq. (5.26) is independent of the barrier height, the symmetry factor and the coefficients δ_k^{etr} and δ_k^{ely} .

Using Eq. (5.26) we rewrite the exchange current density from Eq. (5.25) as

$$\begin{aligned} j_0 = & j_{00} \exp \left(\frac{-G_{\text{ref}}^{\ddagger}}{R\Theta} \right) \exp \left(\frac{\sum_{k \in I^{\text{etr}}} (\beta - \delta_k^{\text{etr}}) G_k^{\text{etr}}}{R\Theta} \right) \\ & \exp \left(\frac{\sum_{k \in I^{\text{ely}}} (1 - \beta - \delta_k^{\text{ely}}) G_k^{\text{ely}}}{R\Theta} \right). \end{aligned} \quad (5.27)$$

It is not surprising that the exchange current density depends on the energetic states of electrode and electrolyte. The consequence of this will be discussed in the upcoming section. Note that the open circuit potential (Eq. (5.26)) and the exchange current density (Eq. (5.27)) are both determined by the same energetic states of the electrode and electrolyte and thus are not thermodynamically independent [112].

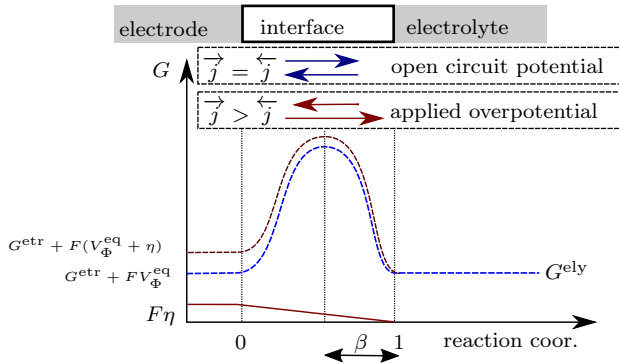


Figure 5.2: The energy landscape at open circuit conditions (blue) attains an equal level at electrode and electrolyte. In the case of an anodic reaction ($\eta > 0$), the equilibrium of forward and reverse reactions are violated and a positive net interface current arises.

Now we consider the non-equilibrium case where $\vec{j} \neq \vec{j}^\leftarrow$. The net current density in the direction from the electrode on the left side of the interface to the electrolyte on the right is defined as

$$j^{\text{BV}} = \vec{j} - \vec{j}^\leftarrow. \quad (5.28)$$

and is therefore anodic if positive and cathodic if negative. With the help of Eq. (5.23) and Eq. (5.27), we obtain the well known Butler-Volmer equation

$$\boxed{j^{\text{BV}} = j_0 \left[\exp \left((1 - \beta) \frac{F}{R\Theta} \eta \right) - \exp \left(-\beta \frac{F}{R\Theta} \eta \right) \right]} \quad (5.29)$$

where we have introduced the surface overpotential

$$\eta = \Phi^{\text{etr}} - \Phi^{\text{ely}} - V_\Phi^{\text{eq}} \quad (5.30)$$

as a function of the open circuit potential V_Φ^{eq} given in Eq. (5.26). Note that only the exchange current density j_0 in Eq. (5.29) depends on the barrier, and the term in the brackets does not. If the overpotential is positive, the equilibrium given by the Nernst equation (5.26) is violated, the Gibbs energy of the electrode increases and consequently, the anodic current density \overrightarrow{j} dominates the cathodic current density \overleftarrow{j} (see Fig. 5.2). The net current density is then positive. If the overpotential is smaller than zero, a negative current density prevails.

5.3 Mechanical Energy of Deposition

In the previous section we presented a generic concept to link the energetic state of the electrode and electrolyte to the interface reactions which are usually accessible from bulk theories. Active storage particles [63] and solid binary electrolytes [101] have shown a strong coupling mechanism between mechanical stresses and electrochemical transport due to a swelling mechanism. Each ion inserted or removed displaces surrounding material, i.e. the host, due to its molar volume. Consideration of these concepts for solid electrolytes and for intercalation storage particles yield the mechanical effects accounted for in Eq. (5.6) or Eq. (5.11). We note that experimental verification for the influence of mechanical stresses on electrochemical response has been obtained, for example, for silicon active particles [164] and energy harvesting applications [76]. The work of Pannikat and Raj [165] on the correlation of mechanical stress and equilibrium potential of a platinum-zirconium interface also proves that mechanics influences reaction kinetics.

In contrast, deposition on and stripping from metal electrodes is qualitatively different from intercalation, de-intercalation and solid solution in electrolytes. The stress free size of the electrode grows/shrinks atom layer by atom layer at the oxidation/reduction process and thus cannot

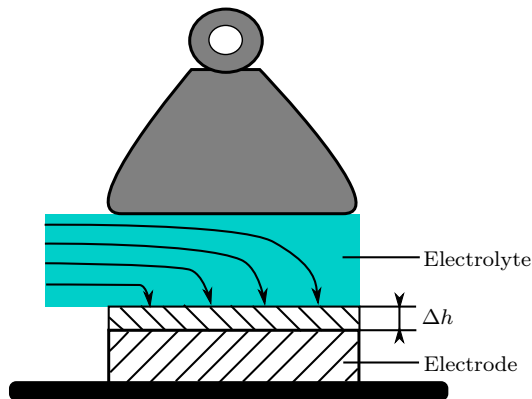


Figure 5.3: A sketch of a solid state half cell loaded by a dead load \mathbb{F} . The weight is lifted by Δh during deposition.

be treated as a volumetric swelling process. This change of geometry is likely to cause deformation and therefore contributes to the overall energetic state of the metal electrode. In this section we consider the mechanics of deposition on and stripping from metal electrodes and its implications for electrochemistry.

5.3.1 Macroscopic Motivation

Imagine a half-cell consisting of an ion conducting solid electrolyte and a metal electrode that rest on a rigid support. The electrolyte is connected to a second electrode which serves as an ion supply. Furthermore, the electrolyte is assumed to have very good transport properties such that a homogeneous deposition on the metal electrode takes place when a current is applied. A weight is placed on the solid electrolyte and consequently a force \mathbb{F} acts on the electrolyte. As the material is deposited on the

electrode with a current density j^{BV} , the thickness of the metal electrode increases by

$$\Delta h = \frac{\Omega_M}{F} j^{\text{BV}} \Delta t \quad (5.31)$$

for each time increment Δt , where Ω_M is the molar volume (defined in the undeformed state). As a consequence, the weight is lifted by this amount and therefore, the potential energy of the weight rises by

$$\Delta W_1 = \mathbb{F} \Delta h = \mathbb{F} \frac{\Omega_M}{F} j^{\text{BV}} \Delta t. \quad (5.32)$$

Obviously, the potential energy decreases in the case of stripping. To capture the full mechanical response, we also have to take into account the mechanical deformation within the newly deposited material. In the case of a linear elastic response, we can use a spring model. The stiffness is thereby $k = E^{\text{ME}} A / h$ with Young's modulus of the electrode E^{ME} , electrode thickness h and area A . The material will be compressed following Hooke's law

$$\mathbb{F} = ku \quad \Leftrightarrow \quad u = \mathbb{F}/k, \quad (5.33)$$

by the displacement u . The new height of the metal is then $\tilde{h} = h - u$ and the generated energy due to deposition is composed of potential energy and elastic energy

$$\Delta W_2 = \mathbb{F} \Delta \tilde{h} + \frac{1}{2} k u^2 = \mathbb{F} (\Delta h - \frac{1}{2} u) = \mathbb{F} \Delta h \left(1 - \frac{1}{2} \frac{\sigma_n^{\text{etr}}}{E^{\text{ME}}} \right). \quad (5.34)$$

In cases where $\frac{\sigma_n^{\text{etr}}}{E^{\text{ME}}}$ is small (i.e. if forces are small and stiffness high), only the mechanical energy due to the displacement as in Eq. (5.32) is relevant.

Now move attention to the impact on the electrochemistry at the cell level. To store the electrochemical energy ΔE by depositing a certain amount of ions, one has to apply the voltage U . The energy supply in the half cell is then $j^{\text{BV}}AU\Delta t$ and splits to electrochemical and mechanical energy

$$\Delta E + \Delta W_1 = j^{\text{BV}}AU\Delta t. \quad (5.35)$$

Consequently, to store electrochemical energy ΔE at current density j^{BV} requires

$$\Delta E = \left(U - \mathbb{F} \frac{\Omega_M}{AF} \right) j^{\text{BV}} A \Delta t. \quad (5.36)$$

Hence, in order to store the same electrochemical energy in the cell, the applied voltage must be higher if the electrolyte is loaded by a weight.

5.3.2 Deposition on Ion Scale

In the previous section we have motivated the fact that the mechanics of deposition and stripping, have an effect on electrochemistry. We now want to transfer our macroscopic insights to resolve the local energy contribution due to mechanics that is required for transition state theory. Assume a planar interface, where one layer of atoms is deposited on a surface with area A . There are N_M moles of atoms with volume Ω_M necessary to create this layer on the metal electrode and the interface then moves by

$$\Delta h^{\text{ion}} = \frac{N_M \Omega_M}{A}. \quad (5.37)$$

We also assume a mechanical force \mathbb{F} in the normal direction acting on the interface with area A . The energetic contribution due to the deposition of N_M moles of atoms is then

$$W_{N_M} = \Delta h^{\text{ion}} \mathbb{F} = \frac{N_M \Omega_M}{A} \mathbb{F}. \quad (5.38)$$

The molar energy generated by displacing the interface is

$$\boxed{\Psi^{\text{dp}} = \frac{W_{N_M}}{N_M} = \frac{\Omega_M}{A} \mathbb{F} = -\Omega_M \sigma_n^{\text{etr}}} \quad (5.39)$$

where the normal compressive stress $\sigma_n^{\text{etr}} = \mathbf{n}^T \boldsymbol{\sigma} \mathbf{n}$ in the normal direction \mathbf{n} to the interface and $\boldsymbol{\sigma}$ is the Cauchy stress tensor evaluated at the metal electrode interface. Note that the amount of atoms drops out in Eq. (5.39) and the concept of discrete atom layers changed to a continuous setting. As obvious from Eq. (5.34), we can neglect the elastic strain energy contributions for $\frac{\sigma_n^{\text{etr}}}{E^{\text{ME}}} < 1$.

The result of Eq. (5.39) is comparable with, for example, the findings of Monroe and Newman [71] and Ma et al. [145] if making a few strong assumptions. For example, we can assume we are dealing with a solid that behaves like a fluid with $\sigma_n^{\text{etr}} = -p^{\text{etr}}$. We then obtain

$$\Psi^{\text{dp}} = \Omega_M p^{\text{etr}}, \quad (5.40)$$

where the mechanical contribution is identical to that arising from the process of swelling during intercalation in an active particle [63].

5.4 Examples

The Butler-Volmer equation derived in Eq. (5.29) is independent of the specific (interface) material system. However, the corresponding exchange

current density and overpotential need to be adjusted accordingly. We will do this for a selection of representative interface systems in the following. In all upcoming equations the definition

$$j_{00}^{\text{ref}}|_Z^Y = j_{00} \exp \left(\frac{-G_{\text{ref}}^{\ddagger} + (1 - \beta - \delta_{\text{ref}}^{\text{ely}})G_{\text{ref}}^{\text{ely}}|_Y + (\beta - \delta_{\text{ref}}^{\text{etr}})G_{\text{ref}}^{\text{etr}}|_Z}{R\Theta} \right) \quad (5.41)$$

is used, where j_{00} is defined by Eq. (5.24). The quantity j_{00}^{ref} corresponds to a reference state and hence is independent of changes in volume concentrations of electrode and electrolyte and mechanical state. The index Y represents the class of electrolyte and Z the class of electrode. We further define

$$\begin{aligned} \overrightarrow{\Delta G}_{\text{ref}}|_Z^Y &= G_{\text{ref}}^{\ddagger} - \delta_{\text{ref}}^{\text{etr}} G_{\text{ref}}^{\text{etr}}|_Z \\ \overleftarrow{\Delta G}_{\text{ref}}|_Y^Y &= G_{\text{ref}}^{\ddagger} - \delta_{\text{ref}}^{\text{ely}} G_{\text{ref}}^{\text{ely}}|_Y \end{aligned} \quad (5.42)$$

as the activation energy barriers in the forward and reverse reaction, respectively, at reference state and

$$\Delta G_{\text{ref}}|_Z^Y = G_{\text{ref}}^{\text{ely}}|_Y - G_{\text{ref}}^{\text{etr}}|_Z \quad (5.43)$$

as the difference of standard Gibbs energy between electrolyte and electrode.

5.4.1 Dilute Electrolyte | Storage Particle (ideal)

With above framework at hand, we first investigate the reaction kinetics between two ideal systems, namely an ideal active particle (Z=AP), using contribution of Eq. (5.8) and a dilute binary ion conducting electrolyte solution (Y=BIC), using contribution of Eq. (5.4) where in both materials non-idealities and mechanics are neglected. Thus, we

have $I^{\text{etr}} = \{\text{ref}, \text{conf}\}$ and $I^{\text{ely}} = \{\text{ref}, \text{conf}\}$. Making use of Eq. (5.23) together with Eq. (5.28), we write the current density as

$$j^{\text{BV}} = k^{\text{etr}} c_{\text{M}} \exp \left(\frac{-\overrightarrow{\Delta G}_{\text{ref}}|^{\text{AP}} + (1 - \beta)F(\Phi^{\text{etr}} - \Phi^{\text{ely}})}{R\Theta} \right) - k^{\text{ely}} c_{+} \exp \left(\frac{-\overleftarrow{\Delta G}_{\text{ref}}|^{\text{BIC}} - \beta F(\Phi^{\text{etr}} - \Phi^{\text{ely}})}{R\Theta} \right) \quad (5.44)$$

with the two rate constants

$$\begin{aligned} k^{\text{etr}} &= \frac{j_{00}}{c_{\text{M}}^{\text{ref}}} \exp \left(-\frac{\sum_{k \in I^{\text{etr}}} \delta_k^{\text{etr}} G_k^{\text{etr}} + \sum_{k \in I^{\text{ely}}} \delta_k^{\text{ely}} G_k^{\text{ely}}}{R\Theta} \right), \\ k^{\text{ely}} &= \frac{j_{00}}{c_{+}^{\text{ref}}} \exp \left(-\frac{\sum_{k \in I^{\text{etr}}} \delta_k^{\text{etr}} G_k^{\text{etr}} + \sum_{k \in I^{\text{ely}}} \delta_k^{\text{ely}} G_k^{\text{ely}}}{R\Theta} \right). \end{aligned} \quad (5.45)$$

With that, we have determined the exact form of the rate constants in Eq. (5.2) from the introduction. Linear reaction theory implies concentration independent rate constants which is in line with the finding that the barrier is not affected by the configurational entropy of the adjacent regions as discussed in connection with Eq. (5.19). Therefore, we use Eq. (5.19) in Eq. (5.45) and henceforth throughout this work.

Eventually, we obtain for the Butler-Volmer equation (5.29) the open circuit potential with respect to the electric potential Φ via Eq. (5.26) as

$$V_{\Phi}^{\text{eq}} = \frac{1}{F} \left[\Delta G_{\text{ref}}|^{\text{BIC}}_{\text{AP}} + R\Theta \ln \left(\frac{c_{+}/c_{+}^{\text{ref}}}{c_{\text{M}}/c_{\text{M}}^{\text{ref}}} \right) \right]. \quad (5.46)$$

The exchange current density from Eq. (5.27) computes to

$$j_0 = j_{00}^{\text{ref}}|^{\text{BIC}}_{\text{AP}} \left(\frac{c_{+}}{c_{+}^{\text{ref}}} \right)^{(1-\beta)} \left(\frac{c_{\text{M}}}{c_{\text{M}}^{\text{ref}}} \right)^{\beta}. \quad (5.47)$$

The Butler-Volmer equation together with Eq. (5.46) and Eq. (5.47) reassembles the form as derived in, for example, Newman and Thomas-Alyea [53] and Bockris et al. [143]. Although we arrive at the same outcome, we point out that we made the specific assumptions of a dilute electrolyte and an ideal active particle. Therefore, if non-ideal systems are of interest one has to adjust the formulation of the open circuit potential and the exchange current density accordingly.

5.4.2 Dilute Electrolyte | Metal Electrode (w/o mechanics)

Another idealized electrochemical system is an electrolyte at dilute concentration of cations, see Eq. (5.4), together with a pure metal electrode ($Z=ME$), again without considering mechanics. Thus we have $I^{ely} = \{\text{ref}, \text{conf}\}$ and $I^{etr} = \{\text{ref}\}$. We obtain from Eq. (5.27) and (5.30) with Eq. (5.19) the open circuit potential with respect to the electric potential and exchange current density as

$$V_{\Phi}^{\text{eq}} = \frac{1}{F} \left[\Delta G_{\text{ref}}|_{\text{ME}}^{\text{BIC}} + R\Theta \ln \left(\frac{c_+}{c_+^{\text{ref}}} \right) \right], \quad (5.48)$$

$$j_0 = j_{00}|_{\text{ME}}^{\text{BIC}} \left(\frac{c_+}{c_+^{\text{ref}}} \right)^{(1-\beta)}. \quad (5.49)$$

Thus we obtain the commonly used form of the Butler-Volmer equation for metal electrodes [60].

5.4.3 Concentrated Electrolyte | Storage Particle

If we consider a high concentration of atoms intercalated in active storage particles, we have to take the Gibbs energy of the vacancies into account, see Eq. (5.10). This energy contributes to the electrolyte Gibbs energy, as given in Eq. (5.4) and Eq. (5.5). Together with the Gibbs

energy of the active particle, using Eq. (5.8) and (5.11) and taking mechanical effects into account we then have $I^{\text{ely}} = \{\text{ref}, \text{conf}, \text{ni}, \text{mech}, V\}$, $I^{\text{etr}} = \{\text{ref}, \text{conf}, \text{mech}\}$ and can derive the open circuit potential with respect to the electric potential as

$$V_{\Phi}^{\text{eq}} = \frac{1}{F} \left[\Delta G_{\text{ref}}|_{\text{AP}}^{\text{BIC}} + R\Theta \ln \left(\frac{c_+ f_+ (c_M^{\max} - c_M)}{c_+^{\text{ref}} f_+^{\text{ref}} c_M} \right) + \Omega_+ p^{\text{ely}} - \Omega_M p^{\text{etr}} \right]. \quad (5.50)$$

Accordingly, applying Eq. (5.27), the exchange current density is given by

$$j_0 = j_{00}|_{\text{AP}}^{\text{BIC}} \left(\frac{c_+}{c_+^{\text{ref}}} \right)^{(1-\beta)} \left(\frac{f_+}{f_+^{\text{ref}}} \right)^{(1-\beta-\delta_{\text{ni}}^{\text{ely}})} \left(\frac{c_M^{\max} - c_M}{c_{\text{ref}}} \right)^{(1-\beta)} \left(\frac{c_M}{c_{\text{ref}}} \right)^{\beta} \exp \left(\frac{(\beta - \delta_{\text{mech}}^{\text{etr}})}{R\Theta} \Omega_M p^{\text{etr}} \right) \exp \left(\frac{(1 - \beta - \delta_{\text{mech}}^{\text{ely}})}{R\Theta} \Omega_+ p^{\text{ely}} \right), \quad (5.51)$$

where we have already applied Eq. (5.19). The dependence of the exchange current density on the fugacity f_+ of the electrolyte and intercalation concentration in the active storage particles aligns with the currently available literature on the subject in regard to modeling if $\delta_{\text{ni}}^{\text{ely}} = 0$ is assumed [54, 63, 149, 166]⁶. The decline of the exchange current density for fully charged ($c_M = c_M^{\max}$) and fully discharged ($c_M = 0$) particles as predicted by Eq. (5.51) has been shown to occur for LiFePO₄ [167].

Next, we turn our attention to mechanical effects. The mechanical contribution for an active storage particle in Eq. (5.50) aligns with results of Stein et al. [168]. The exchange current density depends on both the pressure in the active particle p^{etr} and the pressure in the electrolyte p^{ely} .

⁶ Note that [149] and [166] treat the configurational entropy of the vacancies within the activated state and thus differ from the treatment in Eq. (5.9). The symmetry coefficient in the fourth expression of Eq. (5.51) then drops out.

These pressures can be significantly different in magnitude. In liquid electrolyte systems the pressure in the fluid is usually small. On the other hand, active storage particles can experience high mechanical stress magnitudes during the intercalation process [62, 63]. Thus the difference in pressure between the electrode and the electrolyte must be taken into account, see Eq. (5.50).

5.4.4 Concentrated Electrolyte | Metal Electrode

The study of pure metal electrode systems which are, for example, present in solid state batteries requires, comprehensive consideration of electrochemistry and mechanics. Therefore, for a metal electrode subject to mechanical stress we use the energy as defined in Eq. (5.39) and consider a binary ion conducting electrolyte (e.g. a polymer) with utilization of the energy contributions of Eq. (5.4), (5.5) and (5.6). Hence we have $I^{\text{ely}} = \{\text{ref}, \text{conf}, \text{ni}, \text{mech}\}$ and $I^{\text{etr}} = \{\text{ref}, \text{mech}\}$. The result in Eq. (5.26) then gives, together with Eq. (5.39),

$$V_{\Phi}^{\text{eq}} = \frac{1}{F} \left[\Delta G_{\text{ref}}|_{\text{ME}}^{\text{BIC}} + R\Theta \ln \left(\frac{c_+ f_+}{c_+^{\text{ref}} f_+^{\text{ref}}} \right) + \Omega_+ p^{\text{ely}} + \Omega_M \sigma_n^{\text{etr}} \right]. \quad (5.52)$$

Making use of Eq. (5.19), the exchange current density follows

$$j_0 = j_{00}^{\text{ref}}|_{\text{ME}}^{\text{BIC}} \left(\frac{c_+}{c_+^{\text{ref}}} \right)^{(1-\beta)} \left(\frac{f_+}{f_+^{\text{ref}}} \right)^{(1-\beta-\delta_{\text{ni}}^{\text{ely}})} \exp \left(-\frac{(\beta - \delta_{\text{mech}}^{\text{etr}})}{R\Theta} \Omega_M \sigma_n^{\text{etr}} \right) \exp \left(\frac{(1 - \beta - \delta_{\text{mech}}^{\text{ely}})}{R\Theta} \Omega_+ p^{\text{ely}} \right) \quad (5.53)$$

and is consequently a function of the entropic state of the electrolyte and the mechanical states of both the electrolyte and the electrode.

To discuss the influence of deviatoric stresses, we split the normal stress into a hydrostatic and a deviatoric portion with

$$\sigma_n^{\text{etr}} = \sigma_{n,d}^{\text{etr}} - p^{\text{ely}} \quad \text{with} \quad \sigma_{n,d}^{\text{etr}} = \mathbf{n} \cdot \boldsymbol{\sigma}^d \cdot \mathbf{n} \quad (5.54)$$

where $\boldsymbol{\sigma}^d$ is the deviatoric stress tensor. If the molar volumes of the cation in the salt and the metal electrode are such that $\Omega_+ \approx \Omega_M$, then Eq. (5.52) simplifies to

$$V_\Phi^{\text{eq}} = \frac{1}{F} \left[\Delta G_{\text{ref}}|_{\text{ME}}^{\text{BIC}} + R\Theta \ln \left(\frac{c_+ f_+}{c_+^{\text{ref}} f_+^{\text{ref}}} \right) + \Omega_+ \sigma_{n,d}^{\text{etr}} \right]. \quad (5.55)$$

The open circuit potential V_Φ^{eq} is therefore independent of mechanical contributions if $\sigma_{n,d}^{\text{etr}}$ is small. This follows because G_Φ^{ely} and G_Φ^{etr} increase and decrease in the same magnitude if $p^{\text{ely}} > 0$ and $p^{\text{ely}} < 0$, respectively. The difference of the energies remains constant. Note that, although the mechanical stresses drop out in Eq. (5.55) if $\sigma_{n,d}^{\text{etr}} = 0$, a gradient in mechanical stress induces a change of concentration due to stress driven diffusion and thus implicitly influences the open circuit potential. The exchange current density reads

$$j_0 = j_{00}^{\text{ref}} \left(\frac{c_+}{c_+^{\text{ref}}} \right)^{(1-\beta)} \left(\frac{f_+}{f_+^{\text{ref}}} \right)^{(1-\beta-\delta_{\text{ni}}^{\text{ely}})} \exp \left(\frac{(1 - \delta_{\text{mech}}^{\text{ely}} - \delta_{\text{mech}}^{\text{etr}}) \Omega_+ p^{\text{ely}}}{R\Theta} \right) \exp \left(\frac{-(\beta - \delta_{\text{mech}}^{\text{etr}}) \Omega_+ \sigma_{n,d}^{\text{etr}}}{R\Theta} \right). \quad (5.56)$$

For small $\sigma_{n,d}^{\text{etr}}$, the mechanical contribution in Eq. (5.56) is independent of the symmetry factor β . Depending on the choice of prefactors, the mechanical contribution in Eq. (5.56) may vanish ($\delta_{\text{mech}}^{\text{ely}} + \delta_{\text{mech}}^{\text{etr}} = 1$), decrease the exchange current density as the pressure increases ($\delta_{\text{mech}}^{\text{ely}} + \delta_{\text{mech}}^{\text{etr}} > 1$) or increase the exchange current density as the pressure in

the electrolyte increases ($\delta_{\text{mech}}^{\text{ely}} + \delta_{\text{mech}}^{\text{etr}} < 1$). The latter is a consequence of a decrease in activation energies.

5.5 Application within Concentrated Solution Theory

Recall that the Butler-Volmer equation obtained in the previous section, Eq. (5.29), is derived via a difference in electric potentials. In the context of concentrated solution theory [53], the field variable in the electrolyte is, however, the electrochemical potential

$$\omega_+ = F\Phi^{\text{ely}} + G^{\text{ely}}, \quad (5.57)$$

see Eq. (3.115), and is therefore not directly compatible with the definition of the overpotential of Eq. (5.30). With the help of Eq. (5.57) and the Nernst equation (5.26), we rewrite the overpotential from Eq. (5.30) as

$$\boxed{\eta = \Phi^{\text{etr}} - \frac{1}{F}\omega_+ - V_{\omega_+}^{\text{eq}}}, \quad (5.58)$$

where we have introduced the open circuit potential with respect to ω_+ as

$$V_{\omega_+}^{\text{eq}} = -\frac{1}{F}G^{\text{etr}}. \quad (5.59)$$

This overpotential is independent of the energetic state of the electrolyte G^{ely} , i.e. its cation concentration or mechanical condition. Note that the exchange current density (e.g. Eq. (5.27)) is not a function of the electric potential, thus remains unchanged and, as before, is a function of G^{ely} .

Open circuit potentials can be accessed by measurement in an equilibrium state, i.e. in the absence of concentration gradients [169]. Both

definitions of the open circuit potential, $V_{\omega_+}^{\text{eq}}$ and V_{Φ}^{eq} , differ only by the additive constant $G_{\text{ref}}^{\text{ely}}$ in the equilibrium and stress free state. Concentrated solution theory as discussed in Chapter 3 considers implicitly the electrolyte energy state in the field variable ω_+ and thus only requires knowledge of the electrode in the parametrization of the open circuit potential $V_{\omega_+}^{\text{eq}}$.

At this point, let us briefly recall selected examples of Section 5.4 with respect to a formulation with the electrochemical potential as electrolyte field variable. Recall that the exchange current densities (Eq. (5.49), Eq. (5.51) and Eq. (5.53)) remain unchanged. The metal electrode in combination with a dilute electrolyte (Section 5.4.2) yields

$$V_{\omega_+}^{\text{eq}} = -\frac{1}{F} G_{\text{ref}}^{\text{etr}}|^{\text{ME}}. \quad (5.60)$$

In experiments it is beneficial to select one material as datum and measure only potential differences with respect to this material. This is achieved in our formulation by setting $G_{\text{ref}}^{\text{etr}}|^{\text{ME}} = 0$. The open circuit potential $V_{\omega_+}^{\text{eq}}$ for the metal electrode then vanishes. This concept is in agreement with, for example, Newman and Thomas-Alyea [53] who use the metal electrode as the reference potential. We emphasize that the specific choice of zero open circuit potential is different to the notion of standard Gibbs energy and further does not take mechanical effects into account. The system of Section 5.4.4 with the electrode energy contributions $I^{\text{etr}} = \{\text{ref}, \text{mech}\}$ (see Eq. (5.7) and Eq. (5.39)) yields the open circuit potential with respect to the electrochemical potential as

$$V_{\omega_+}^{\text{eq}} = \frac{1}{F} \left(-G_{\text{ref}}^{\text{etr}}|^{\text{M}} + \Omega_{\text{M}} \sigma_n^{\text{etr}} \right), \quad (5.61)$$

with the stress dependency arising due to normal stresses. Eq. (5.59) gives for the system of Section 5.4.3 that describes the combination of

concentrated electrolyte and active particles with mechanics (Eq. (5.8), Eq. (5.10) and Eq. (5.11)), the open circuit potential

$$V_{\omega_+}^{\text{eq}} = -\frac{1}{F} \left(G_{\text{ref}}^{\text{etr}}|^{\text{AP}} + R\Theta \ln \left(\frac{c_M}{c_M^{\max} - c_M} \right) + \Omega_M p^{\text{etr}} \right). \quad (5.62)$$

The exchange current density is given by Eq. (5.51). Eq. (5.62) provides a clear correlation of $V_{\omega_+}^{\text{eq}}$ and c_M based on the electrode model with energy contributions of Eq. (5.8), Eq. (5.10) and Eq. (5.11). However in battery application, direct measurements of $V_{\omega_+}^{\text{eq}}$ as a function of c_M (state of charge) are feasible. Therefore one usually relies on the measured open circuit potential instead of using e.g. Eq. (5.62) although the theoretical formulation is able to resolve the mechanical contribution. We note that Bohn et al. [63] and Christensen and Newman [61] have considered deviations from ideal conditions in storage particles by inclusion, inter alia, of an excess Gibbs energy for the intercalated cations.

5.6 Influence of Mechanics

We have defined a generic form of the energy barrier with respect to the energy states of the adjacent electrode and electrolyte in Eq. (5.13). The way that the parameters δ_k^{etr} and δ_k^{ely} are chosen has a strong impact on the exchange current density. Recall that the overpotential (Eq. (5.30)) is independent of the barrier and is therefore not affected by δ_k^{ely} and δ_k^{etr} . We have assumed that the energy barrier is independent of the configurational entropy of the adjacent layers. In the following, we focus on the mechanical contribution and discuss four assumptions for $\delta_{\text{mech}}^{\text{etr}}$ and $\delta_{\text{mech}}^{\text{ely}}$ as given in Table 5.1 and relate them to literature.

Before doing so, we note that $G_{\text{ref}}^{\ddagger}$, as introduced in Eq. (5.13), might also be stress dependent. In general, it is difficult to determine the mechanical contribution to the activated state $G_{\text{ref}}^{\ddagger}$ due to its unknown

$\delta_{\text{mech}}^{\text{etr}}$	$\delta_{\text{mech}}^{\text{ely}}$	<i>implication on the barrier</i>	<i>similar work</i>
0	0	barrier is independent	[112, 145]
$1 - \alpha^M$	α^M	linear drop of Gibbs energies	[71]
β	$1 - \beta$	equivalent to electric potential	[71, 146, 161, 170]
0	1	only electrolyte affects barrier	[71, 72]

Table 5.1: Different assumptions for the influence of mechanics in the electrode and electrolyte energies on the energy barrier.

location on the reaction coordinate. Therefore we will not consider the stress dependency of G_{ref}^\ddagger in the following.

A barrier which is independent of the mechanical state of the electrolyte and electrode is given by $\delta_{\text{mech}}^{\text{ely}} = \delta_{\text{mech}}^{\text{etr}} = 0$. Mechanical stress influences the exchange current density in this case, but not due to the Bronsted-Evans-Polanyi idea, where the barrier height itself is a function of stress. Here, mechanical stress stems from the stress-dependency of the open circuit potential (see Eq. (5.62) and (5.61)). Ma et al. [145] follow the concept of a fixed barrier, with both $\delta_{\text{mech}}^{\text{etr}}$ and $\delta_{\text{mech}}^{\text{ely}}$ equal to zero, but come to a slightly different Butler-Volmer formulation than we do since they define the open circuit potential to be zero and thus independent of stress. It also aligns with Bazant [112] where the Bronsted-Evans-Polanyi principle is applied solely to the reference energies of oxidized and reduced states.

A second assumption is to propose a linear drop of the mechanical part of the Gibbs energy between the electrode and electrolyte with $\delta_{\text{mech}}^{\text{etr}} = 1 - \alpha^M$ and $\delta_{\text{mech}}^{\text{ely}} = \alpha^M$ where we have introduced a second symmetry factor α^M , again restricted to the interval between 0 and 1.

The exchange current density of Eq. (5.27) as a function of electrode and electrolyte energies then reads

$$j_0 = j_{00} \exp\left(\frac{-G_{\text{ref}}^{\ddagger}}{R\Theta}\right) \exp\left(\frac{(\alpha^M - (1 - \beta))(G^{\text{etr}} - G^{\text{ely}})}{R\Theta}\right) \quad (5.63)$$

and, for the specific case of a metal electrode and a solid electrolyte (see Eq. (5.53)), takes the form

$$j_0 = j_{00}^{\text{ref}}|_{\text{M}}^{\text{BIC}} \left(\frac{c_+}{c_+^{\text{ref}}}\right)^{(1-\beta)} \left(\frac{f_+}{f_+^{\text{ref}}}\right)^{(1-\beta-\delta_{\text{ni}}^{\text{ely}})} \quad (5.64)$$

$$\exp\left(\frac{(\alpha^M - (1 - \beta))(-\Omega_M \sigma_n^{\text{etr}} - \Omega_+ p^{\text{ely}})}{R\Theta}\right). \quad (5.65)$$

This structure with symmetry factors is similar to that of Monroe and Newman [71], but with only mechanical effects taken into account.⁷

Motivated by the idea that mechanics should solely affect the equilibrium potential, Monroe and Newman [71] assume in a second step that $\alpha^M = 1 - \beta$ (which translates in our formulation to $\delta_{\text{mech}}^{\text{etr}} = \beta$ and $\delta_{\text{mech}}^{\text{ely}} = 1 - \beta$). Another motivation for this choice is the idea that the difference in the mechanical part of the Gibbs energy along the reaction coordinates parallels the difference in electric potential, see Eq. (5.17). This approach is utilized e.g. by Lu et al. [146], Huang et al. [161] and Joos [170].

A second simplification of the derivation used by Monroe and Newman [71] is to set $\alpha^M = 1$, leading to $\delta_{\text{mech}}^{\text{etr}} = 0$ and $\delta_{\text{mech}}^{\text{ely}} = 1$. This assumption is, for example, used in [72] and several subsequent publications studying the interface stability of a metal electrodes in solid state batteries. Here,

⁷ Monroe and Newman [71] introduces the term $\Delta\mu_{e^-}^{\alpha, \alpha'}$ as the change of the mechanical energy drop at the interface between undeformed and deformed state. This is equivalent to $G_{\text{mech}}^{\text{etr}} - G_{\text{mech}}^{\text{ely}}$ in our formulation.

only the energetic state of the electrolyte influences the energy barrier and implies a non-symmetric influence of electrode and electrolyte state on the reaction.

Since all assumptions in Table 5.1 are thermodynamically consistent from a theoretical point of view, only experimental validation will enable comprehensive understanding of reaction kinetics and clarify which assumption is most appropriate regarding the energy barrier. Until better knowledge is available, we suggest the use of the simplest model with $\delta_{\text{mech}}^{\text{ely}} = \delta_{\text{mech}}^{\text{etr}} = 0$ because no further assumptions, such as the same linear drop of energies between electrode and electrolyte, is required. Furthermore, with a theory for the thermodynamics of the adjacent components in hand, see Chapter 3, it seems to us more appropriate to treat mechanical effects in the same manner as entropic ones. In Eq. (5.19) we have seen that $\delta_{\text{conf}}^{\text{etr}} = \delta_{\text{conf}}^{\text{ely}} = 0$ and thus we conclude the mechanical parameter to be $\delta_{\text{mech}}^{\text{ely}} = \delta_{\text{mech}}^{\text{etr}} = 0$.

5.7 Interface Properties

We now want to deduce the interface properties of a polymer electrolyte adjacent to a metal electrode. Within the formulation of the extended concentrated solution theory with electrochemical potential as field variable, we utilize the equilibrium potential from Eq. (5.61), choose lithium metal as reference and thus set $G_{\text{ref}}^{\text{etr}|M} = 0$ under standard stress conditions. Regarding the exchange current density, the interface resistivity R_{BV} can be experimentally measured by, for example, impedance spectroscopy. The correlation to the exchange current density is given by linearization of the Butler-Volmer equation (5.29) yielding

$$j^{\text{BV}} = j_0 \frac{F}{R\Theta} \eta, \quad (5.66)$$

where the symmetry factor β drops out. With the knowledge of Ohm's law $\eta = R_{\text{BV}} j^{\text{BV}}$ we obtain with

$$j_0 = \frac{R\Theta}{F} \frac{1}{R_{\text{BV}}} \quad (5.67)$$

the correlation of exchange current density and the interface resistance. Experimental data for an interfaces between lithium metal and a polymer electrode, for example, showed an interface resistance in the range of $6.7 \Omega \text{ cm}^2$ and $27 \Omega \text{ cm}^2$ [171]. Under the assumption that the measurements were done in a stress free environment, Eq. (5.67) then yields an exchange current densities between $1.1 \frac{\text{mA}}{\text{cm}^2}$ and $4.5 \frac{\text{mA}}{\text{cm}^2}$. These measurements, however, do not take concentration dependencies into account. To resolve that, we recall Eq. (5.53), use the electroneutrality condition $c = c_+$ and choose a symmetric reaction with $\beta = 0.5$. We then obtain

$$j_0 = K^{\text{BV}} c^{0.5} \exp\left(-\frac{\Omega_M \sigma_n^{\text{etr}}}{2R\Theta}\right) \exp\left(\frac{\Omega_+ p^{\text{ely}}}{2R\Theta}\right), \quad (5.68)$$

where we have introduced $K^{\text{BV}} = j_{00}^{\text{ref}}|_{\text{ME}} \left(\frac{f_+}{f_+^{\text{ref}} c^{\text{ref}}} \right)^{0.5}$. Eq. (5.68) is similar to [58, 60] but extended by mechanical effects. Neglecting the mechanical contribution and assuming an ideal solution with $c = 1000 \frac{\text{mol}}{\text{m}^3}$ yields for the before mentioned interface resistances values for K^{BV} between $0.356 \frac{\text{A}}{\sqrt{\text{m mol}}}$ and $1.437 \frac{\text{A}}{\sqrt{\text{m mol}}}$. For the upcoming investigation, we will use with $K^{\text{BV}} = 0.589 \frac{\text{A}}{\sqrt{\text{m mol}}}$ an intermediate value which is also used in [58, 60]⁸.

⁸ Note that the exchange current density in [58, 60] miss the Faraday constant. Therefore, one has to multiply the rate constant by the Faraday constant to achieve the values presented in our work.

5.8 Summary

This chapter dealt with a consistent derivation of the Butler-Volmer equation including mechanics and together with the transport theory of Chapter 3, it completes the electro-chemo-mechanical model for a solid state electrolyte adjacent to a metal electrode.

We have used the Gibbs energies of cations in electrode and electrolyte bulk and an energy barrier based on the Bronsted-Evans-Polanyi idea to define activation energies for reaction kinetics. The reaction rates are then related to a surface concentration of cations at the interface, which is the same for both the forward and reverse reactions. This yields a generic Nernst equation and resolves discrepancies between surface and volume concentrations that are present in the literature. It also suggests that interface kinetics depend strongly on the thermodynamic states of the adjacent bulk materials, i.e. the coupling of open circuit potential, the exchange current density and the chemical potential of active particles. We have embedded the Butler-Volmer equation in concentrated solution theory, where the electrochemical potential is used instead of the electric potential as the field variable in the electrolyte.

We have additionally discussed the energetic contribution of the mechanics of deposition and stripping at a metal electrode, which is conceptually different from that of intercalation and de-intercalation processes. The normal stress, not the hydrostatic pressure, is shown to be the variable of interest for the thermodynamics of deposition and stripping, with an impact on both the open circuit potential and the exchange current density. We have elaborated the link between our very generic formulation and other modified Butler-Volmer equations discussed in literature, with an emphasis on mechanical stress. Although not definitive, we suggest independence of the energy barrier from the Gibbs energy in the electrolyte and electrode. This is a simple assumption but, with mechanics taken into account, constitutes a new form of the Butler-Volmer equation.

We now recapitulate the thoroughly derived reaction kinetics for a metal electrode adjacent to a solid binary electrolyte which we are going to apply in the morphological interface stability analysis in the upcoming chapters. The Butler-Volmer equation for this system reads

$$\boxed{\begin{aligned} j^{\text{BV}} &= j_0 \left[\exp\left(\frac{F\eta}{2R\Theta}\right) - \exp\left(-\frac{F\eta}{2R\Theta}\right) \right] \\ \eta &= \Phi^{\text{etr}} - \frac{1}{F} (\omega_+ + \Omega_M \sigma_n^{\text{etr}}), \\ j_0 &= K^{\text{BV}} c^{0.5} \exp\left(-\frac{\Omega_M \sigma_n^{\text{etr}}}{2R\Theta}\right) \exp\left(\frac{\Omega_+ p^{\text{ely}}}{2R\Theta}\right), \end{aligned}} \quad (5.69)$$

where we have repeated the Butler-Volmer equation (5.29), the overpotential of Eq. (5.58) with the mechanical contribution of a metal electrode (Eq. (5.61)) and the exchange current density of Eq.(5.68).

6 Morphological Stability: A Quasi Static Analysis

After carefully deriving an electro-chemo-mechanical battery model in the previous chapters, we now present our first assessment of morphological stability of a metal electrode in a solid state battery. Recall that the mechanisms by which lithium dendriting and intrusion into solid electrolytes may be suppressed are not fully understood. For example, an open question concerning a polymer electrolyte such as PS-PEO is whether there is a composition that provides reasonable transport properties and, at the same time, achieves sufficient mechanical stiffness and strength to suppress intrusions. Other polymer systems struggle with the same trade-off. It is widely believed that a stiffer electrolyte is more likely to keep the lithium metal under control, but a full understanding is still missing. Mechanical properties alone cannot explain morphological stability because polymers under consideration have Young's moduli that are an order of magnitude lower than that of lithium. Therefore, it can be inferred that coupling between electrochemistry and mechanics in the battery plays a key role in any possible suppression mechanism.

To understand possible suppression mechanisms, we utilize the rigorous formulation of coupled electro-chemo-mechanics for bulk ion transport as introduced in Chapter 3 and for reaction kinetics as derived in Chapter 5. Our approach allows us to utilize a full set of measured electrochemical parameters and to solve for the ion transport in the deformed geometry caused by lithium protrusion. The model is used to numerically analyze the interface current density at a given deformation state. If the current

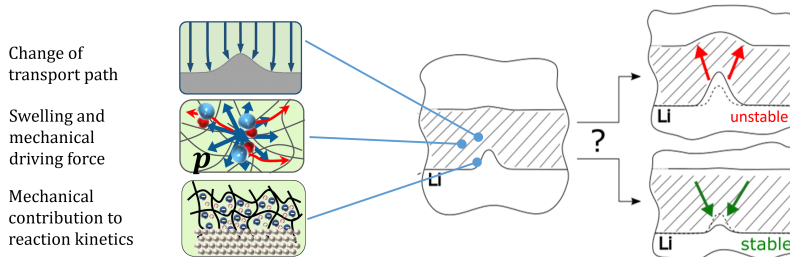


Figure 6.1: The comprehensive simulation model in this study considers electro-chemo-mechanical interaction in the electrolyte bulk as well as at the interface in order to determine morphological interface stability of a metal electrode.

density is higher at the tip of the protrusion than at an undisturbed region, we expect an unstable behavior and growth of the protrusion. Otherwise, we expect stable behavior, see Fig. 6.1. Note that the basic definition of stability used here is somewhat similar to that used by Monroe and Newman [72] even though the further considerations and results differ considerably. With the stability criterion at hand, we ultimately aim for a morphological stability map.

6.1 The Boundary Value Problem

A protrusion of a metal electrode into a solid electrolyte stems either from an initial geometry (surface roughness), from inhomogeneous electro-chemical deposition or a combination of both. In this study, we prescribe a pre-existing protrusion and study the response of the interface kinetics without specifically identifying the source of deformation. For such a protrusion, we can conclude that if the current density at the tip is higher than a reference value on an undisturbed region, then the tip will grow faster than the surrounding, indicating an unstable system.

We consider a similar setup to Section 4.5 with a two dimensional geometry of the solid electrolyte at plain strain, see Fig. 6.2a. The electrolyte has a thickness of $L^{\text{ely}} = 30 \mu\text{m}$ [33] and the width of the computational domain is chosen to be $W = 100 \mu\text{m}$. While the top side of the separator is assumed to be held fixed, symmetry boundary conditions are applied on the sides. The bottom boundary is deformed with a Gaussian shaped protrusion. The displacement is $\mathbf{u}_{\text{BC}} = [X, A^P w(X/R^P)]$, where we utilize the Wendland function of Eq. (4.4). We choose an amplitude $A^P = 4 \mu\text{m}$ and radius $R^P = 15 \mu\text{m}$ for the deformation. The metal electrode is assumed to be very stiff compared to the electrolyte and hence only the separator undergoes mechanical deformation. Furthermore, we know that lithium has a much higher electric conductivity compared to the ionic conductivity of the electrolyte and therefore we set the electrode electric potential as $\Phi^{\text{etr}} = 0$ along the bottom interface of the separator. Other than in Section 4.5 where we have assigned a fixed current density for the top and bottom interface, we now apply a constant current of $J^{\text{app}} = 0.5 \frac{\text{mA}}{\text{cm}^2}$ only at the top of the solid electrolyte, see Fig. 6.2a, and use the Butler-Volmer equation to determine the interface current density on the bottom electrolyte-electrode interface. The current density at the electrolyte-electrode interface is therefore the consequence of coupled bulk and interface transport described by the extended concentrated solution theory, see Eq. (3.116,) and reaction kinetics, see Eq. (5.69). All upcoming results correspond to the steady state solution.

Polymer solid electrolytes are the main scope of this investigation. We hence utilize two recently published sets of parametrization, one for PEO [56], and one of the composite material PS-PEO [57], each with the salt LiTFSi. The latter host material has a higher Young's modulus, dependent on the ratio of PS to PEO phase. The polystyrene phase (PS) enhances stiffness but also degrades the electrochemical transport properties since less ion conducting PEO material is available. Fig. 4.1 shows the concentration-dependent transport parameters. The

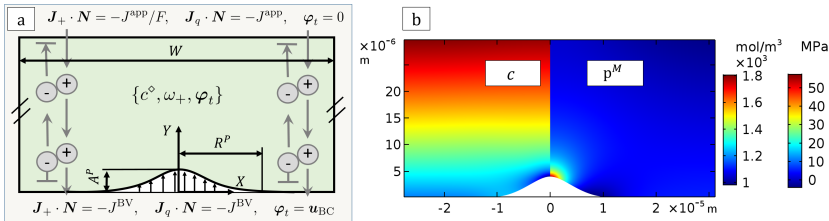


Figure 6.2: (a) Boundary value problem of the deformed solid electrolyte. (b) Color contour plots showing the salt concentration and the mechanical part of the hydrostatic pressure in the case of a PS-PEO electrolyte with $E = 100 \text{ MPa}$.

operating temperature is set to $\Theta = 353 \text{ K}$. The interface conductivity is $K^{BV} = 0.589 \frac{\text{A}}{\sqrt{\text{m mol}}}$. We assume a Poisson ratio of $\nu = 0.4$ and will vary the Young's modulus E .

As in Chapter 4, the simulations are carried out with the finite element tool COMSOL Multiphysics® 5.3a. All field variables are carefully scaled to improve conditioning of the system matrix and thus gain appropriate numerical convergence. The non-linear equations of mass transport, balance of charge, mechanics and the non-linear boundary conditions by means of the Butler-Volmer equation are solved in a fully coupled, direct scheme. The outcome shows insensitivity to the width of the computational domain and to mesh resolution for the fine meshes used in the numerical analysis.

6.2 Effect of Deformation on Interface Current Density

Fig. 6.2b shows the steady state solution for the deformed electrolyte during galvanostatic charging in terms of the salt concentration and the hydrostatic pressure for one exemplary system (PS-PEO and $E = 100 \text{ MPa}$).

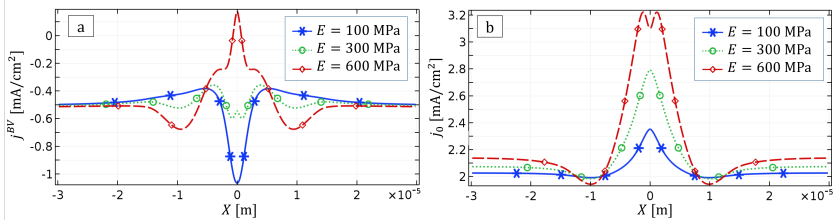


Figure 6.3: The graphs show the response of the interface subjected to lithium protrusion for selected Young's moduli: (a) Current density j_{BV} ; (b) Exchange current density j_0 . There is a qualitative change of the current density for increasing Young's moduli suggesting morphological stability.

The electro-chemo-mechanical coupling in the bulk is the superposition of two mechanisms. First there is a vertical salt-concentration gradient along the height of the separator due to the nature of the binary salt, see also the discussion in Section 4.4. Recall that the electric field acts on both the negatively charged anions and the positively charged cations. However, anions are restricted to the electrolyte and cannot leave or enter it. They then accumulate at the electrode where the cation enter the electrolyte and become dilute at the other such that, at steady state, diffusion equalizes the electrically driven transport.

The second effect is mainly driven by the external deformation. As discussed in Chapter 4, a stress field builds up with a pressure peak close to the tip. The hydrostatic stress causes a depletion of the salt concentration due to the stress driven diffusion mechanism. The perimeter shows the opposite response. We observe tension on the shoulders due to the fact that the relatively stiff separator wants to follow the deformation of the tip, but is constraint by the given displacement of the boundary condition since we do not allow delamination. The increase in tension leads to tensile stresses as also predicted by Harry et al. [31] and yields an increase of the salt concentration. The findings show that the ion

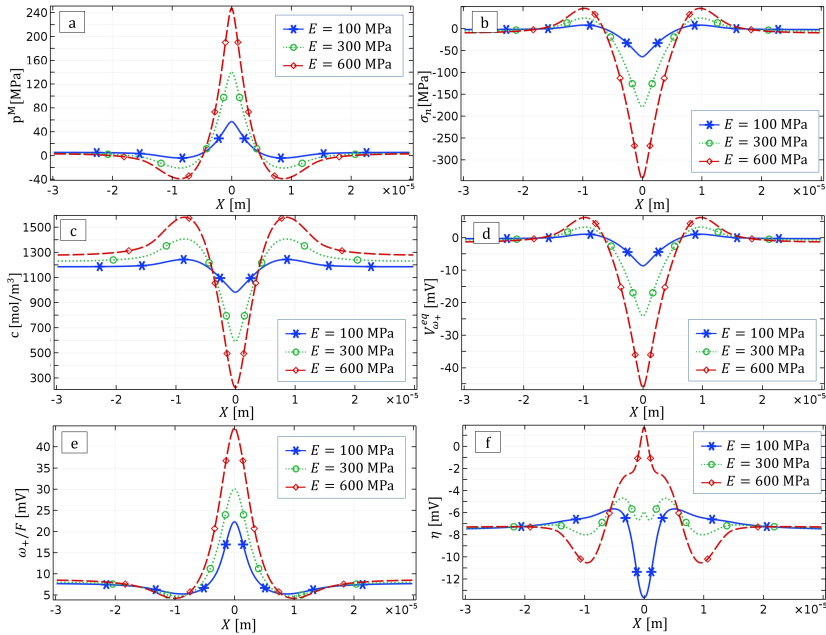


Figure 6.4: The graphs show the response of the interface under protrusion for selected Young's moduli: (a) mechanical contribution of hydrostatic pressure, (b) the surface stress, (c) salt concentration, (d) open circuit potential, (e) electrochemical potential in the electrolyte, (f) overpotential.

transport in the electrolyte is also strongly coupled with interface kinetics, especially in the case of inhomogeneous deformation.

We now consider PS-PEO parameter values for the transport properties and three Young's moduli, namely $E = \{100, 300, 600\}$ MPa. Fig. 6.3a shows the current density at the interface for the three stiffnesses at steady state. For a relatively small elastic modulus ($E = 100$ MPa), a two times higher current density can be observed at the protrusion peak compared to the flatter region. This changes when the Young's modulus is increased leading to a current density at the protrusion tip that is

almost equal to ($E = 300 \text{ MPa}$) and smaller than ($E = 600 \text{ MPa}$) the current density in the flatter, undisturbed region. With $E = 100 \text{ MPa}$ the simulation shows a faster deposition process at the tip which therefore means an unstable surface. The opposite occurs for $E = 600 \text{ MPa}$. The qualitative change of current density for different Young's moduli is an indication of morphological stability and we will rely on this idea for the upcoming analysis. Before proceeding, we wish to discuss the origin of the change of current density distribution when the Young's modulus is varied.

For the analysis of the current density at the electrolyte-electrode interface we recall the Butler-Volmer equation from Eq. (5.69)

$$j^{\text{BV}} = j_0 \left[\exp \left((1 - \beta) \frac{F}{R\Theta} \eta \right) - \exp \left(-\beta \frac{F}{R\Theta} \eta \right) \right] \quad (6.1)$$

as a function of the exchange current density j_0 and the overpotential $\eta = -\frac{1}{F}\omega_+ - V_{\omega_+}^{\text{eq}}$ with $V_{\omega_+}^{\text{eq}} = \frac{1}{F}\Omega_M \sigma_n^{\text{etr}}$. The interface current density is therefore dependent on the electro-chemo-mechanical state of the cation in the solid electrolyte and the stress state of the electrode. In the following, we systematically investigate the different contributions.

We first focus on the bulk transport in the solid electrolyte. The protrusion leads to a positive hydrostatic pressure p^M at the protrusion tip as seen in Fig. 6.4a. The hydrostatic stress increases for higher mechanical stiffness. We also observe a state of tension at the perimeter of the protrusion. Fig. 6.4c shows the spatial salt concentration at the interface for the three investigated Young's moduli. There is a depletion of salt concentration at the protrusion peak due to the effect of stress driven diffusion as it is also observed in Fig. 6.2b. Recall that the driving

force of the electrolyte for the reaction at the interface is the cationic electrochemical potential

$$\omega_+ = \mu_+^0 + R\Theta \ln \left(\frac{c_+}{c_+^{\text{ref}}} \right) + R\Theta \ln \left(\frac{f_+}{f_+^{\text{ref}}} \right) + \mathbb{J}_e \Omega_+ p^M + F\Phi, \quad (6.2)$$

which has been derived in Eq. (3.115) and (3.77). This field variable is plotted in Fig. 6.4e and stems from a superposition of mechanical (Fig. 6.4a) and entropic effects (Fig. 6.4c). We see that the mechanical contribution dominates. For a change of Young's modulus, we observe that ω_+/F increases from 20mV (for $E = 100 \text{ MPa}$) and up to 45mV (for $E = 600 \text{ MPa}$) at the protrusion tip compared to the flatter region with a constant value of roughly 7mV.

We now investigate mechanical influences on the open circuit potential $V_{\omega_+}^{\text{eq}}$ and exchange current density which enters the reaction kinetics. Fig. 6.4b shows the normal stress at the interface for the three different Young's moduli. We observe a compression at the protrusion peak which is more pronounced for higher stiffnesses, but also some tension at the perimeter. The form is similar to the hydrostatic pressure in the solid electrolyte (Fig. 6.4a), but the absolute values are a bit higher. The open circuit potential $V_{\omega_+}^{\text{eq}}$ scales linearly with the normal stress due to Eq. (5.52), which yields the values of $V_{\omega_+}^{\text{eq}}$ at the interface in Fig. 6.4d. While the open circuit potential is close to zero at the undeformed regions, we see values of $V_{\omega_+}^{\text{eq}}$ from -7 mV (for $E = 100 \text{ MPa}$) up to -46 mV (for $E = 600 \text{ MPa}$). Positive values of $V_{\omega_+}^{\text{eq}}$ are present at the perimeter.

The overpotential η at the interface for different Young's moduli as seen in Fig. 6.4f is computed using Eq. (5.58) from the electrochemical potential (Fig. 6.4d) and the open circuit potential (Fig. 6.4e). Recall that the electric potential of the electrode is assumed to be constant along the interface. The surface overpotential as shown in Fig. 6.4f is strongly negative (anodic reaction) at the tip for $E = 100 \text{ MPa}$ and

positive (cathodic reaction) for $E = 600$ MPa. The intermediate modulus $E = 300$ MPa shows some oscillation but is overall fairly uniform over the protrusion surface.

The second variable that is necessary to compute the current density and that is influenced by mechanics is the exchange current density, see Eq. (5.69). The mechanical stresses at the tip of the protrusion cause an increase in j_0 as seen in Fig. 6.3b. The exchange current density at the tip is a factor of 1.5 higher than that in the flatter region for $E = 600$ MPa. In contrast to the overpotential, which the normal stress and electrolyte bulk stress enter with opposite signs, the mechanical influences add up together and therefore increase j_0 as the Young's modulus increases. Note that there is a small dip for $E = 600$ MPa due to a strong depletion of the salt concentration.

Ultimately, the distribution of the current density in Fig. 6.3a broadly follows that of the overpotential η in Fig. 6.4f. The increase of the exchange current density in Fig. 6.3b with the increase of stress is especially pronounced for materials that are quite stiff. The current density at the tip is at $-1 \frac{\text{mA}}{\text{cm}^2}$ approximately twice as high in magnitude as the applied current density for $E = 100$ MPa and much less for $E = 300$ MPa. For $E = 600$ MPa, it even changes from deposition to depletion due to high mechanical stresses. The exchange current density has only a small impact on the overall current density in our example. The current density for materials with higher Young's modulus decreases at the protrusion tip and thus aligns with experimental findings of Harry et al. [31]. Another aspect observed by the experimental study is an increase of current density on the perimeter of the protrusion. Our simulations also show this effect for a high Young's modulus material (Fig. 6.3a).

To summarize the analysis, we see that a deformation of the solid electrolyte triggers stabilizing and destabilizing effects for the growth of a protrusion. Three contributions are competing. A positive hydrostatic

pressure p^M increases the electrochemical potential of the electrolyte, thus promotes a faster deposition and is therefore destabilizing. The effect of stress driven diffusion yields a depletion of salt concentration which lowers the electrochemical potential of the electrolyte as well as the exchange current density and thus decreases the current density at the protrusion tip (stabilizing). The third effect is the open circuit potential, which eventually lowers the current density at the peak of the protrusion for higher normal stresses and is also stabilizing. Depending on the transport parameter and mechanical properties, either the stabilizing or the destabilizing effects dominate. Therefore, we will develop a morphological stability map dependent on these factors in the next section.

6.3 Morphological Stability Map

The findings of the previous section, which showed a qualitative change of current density along the deformed interface due to a variation of Young's modulus of the electrolyte, suggest a morphological stability criterion for solid polymer electrolytes. The idea is that there is a critical Young's modulus, for which the current density at the peak of the protrusion becomes smaller than that on the undeformed interface. Our aim is to find this critical modulus as a function of material properties, geometry, interface conductivity and applied current density.

6.3.1 Definition of Morphological Stability

To avoid influence of the small oscillation in results between the peak of the protrusion (see e.g. Fig. 6.4a), we use a weighted average current

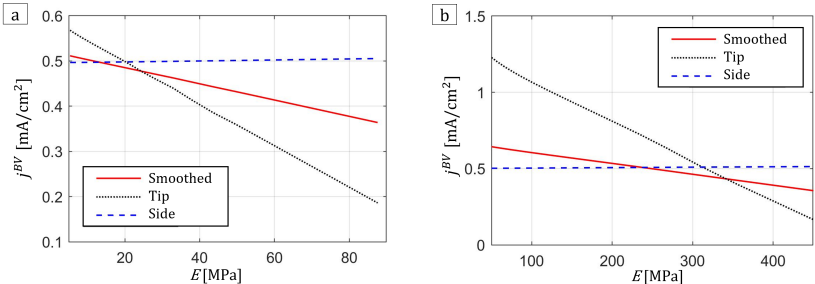


Figure 6.5: The current density evaluated at the side, the tip and with the smoothing scheme of Eq. (6.3) for (a) PEO and (b) PS-PEO. The crossing point between evaluation at the side (dashed line) and smoothed evaluation scheme (straight line) determines the critical Young's modulus and is in the same region compared to the tip evaluation (dotted line).

density over the protrusion instead of a single value and compare it to the current density at the side of the computational domain. This yields

$$\left(\left[\frac{\int_{-W/2}^{W/2} j^{\text{BV}}(X) w(X/R^P) dx}{\int_{-W/2}^{W/2} w(X/R^P) dx} \right] - \left[j^{\text{BV}}|_{\text{side}} \right] \right) \begin{cases} > 0 & \text{unstable} \\ \leq 0 & \text{stable,} \end{cases} \quad (6.3)$$

where the Wendland function w is defined by Eq. (4.4) as for the protrusion itself. The contribution of the current density adjacent to the peak of the protrusion is therefore smoothed out, and the current density in the regions where it oscillates is given less weight.

Our intent is to find the smallest Young's modulus where Eq. (6.3) changes from a stable to an unstable interface. We denote this value as the critical Young's modulus E^{crit} and we will see that this value strongly depends on the properties of both the bulk material and the interface.

The concept of the stability criterion of Eq. (6.3) is thereby similar to the one used by Monroe and Newman [72] who compare current

density at the peak of the protrusion to the current density at the lowest point in the valleys. Fig. 6.5 shows the difference of the two evaluation schemes for PEO and PS-PEO for the setup herein. The current densities are evaluated at the side $j^{\text{BV}}(0.5W)$, at the tip $j^{\text{BV}}(0)$ and with the smoothing scheme of Eq. (6.3) as a function of Young's modulus. The values from the side remain almost constant over the Young's moduli range and thus serve as a reference in the stability criterion (6.3). The current density at the tip crosses the reference in a similar range of the Young's modulus compared to the values obtained by the smoothing scheme. This is 14 MPa (smoothed) and 20 MPa (tip) for PEO and 230 MPa (smoothed) and 310 MPa (tip) for PS-PEO. Since protrusion growth is usually not a local effect but a process along the perturbed interface (see Fig. 1.3b) we find the smoothed scheme in stability criterion (6.3) more appropriate than the tip evaluation. Nevertheless, we want to emphasize that this is not conservative since the tip evaluation indicates up to 40% higher requirements to the electrolyte stiffness.

6.3.2 Influence of the Protrusion Height

First, we investigate the influence of the amplitude of the protrusion on the critical Young's modulus. The stability-instability boundaries for PEO and PS-PEO are shown in Fig. 6.6a as a function of the protrusion amplitude A^P . This boundary is the locus of points for which the term in parenthesis in Eq. (6.3) is equal to zero. Above the lines, the interfaces are predicted to be stable for the respective materials and below to be unstable in the sense that the height of the protrusion will grow. We varied the amplitude between 0.1 μm and 4 μm . The results in Fig. 6.6a show that the critical Young's moduli for stability are dependent on the amplitude of the protrusion. However, the critical Young's modulus does not change much for both PEO, where it varies from 13 to 28 MPa, and PS-PEO, where it ranges from 246 to 330 MPa. Although the results of

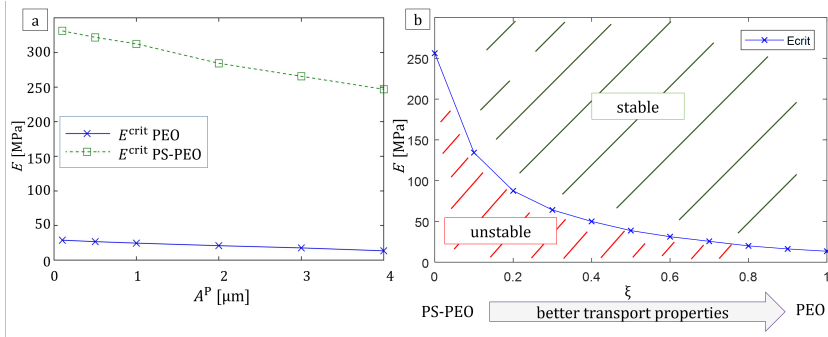


Figure 6.6: (a) The critical Young's modulus separating stability from instability decreases only slightly as the amplitude of the protrusion is increased. (b) Morphological stability map for protrusion amplitude $A^P = 4 \mu\text{m}$. The critical Young's modulus (blue line) is plotted as a function of a measure of how good the transport properties of a material are. Above the blue line there is a stable electrolyte in the sense that the protrusion is predicted not to grow. Below the blue line the electrolyte is unstable and the protrusion will grow.

the critical Young's modulus should be understood more qualitatively, the order of magnitude corresponds quite well to experimental findings. The polymer electrolyte PS-PEO with a Young's modulus of approximately 150 MPa [48] showed stable behavior with lithium metal anodes. On the other hand, the soft polymer electrolyte PEO that is usually operated above the glass transition temperature has a high likelihood for protrusion growth.

6.3.3 Variation between PEO and PS-PEO

We have already seen that the PEO material with relatively good transport properties (see Fig. 4.2) requires a much lower stiffness to ensure stability compared to the PS-PEO material, see Fig. 6.6a. To broaden our insights and to more generally consider the trade-off between interface stability, elastic modulus and lithium transport, we interpolate between

the sets of transport properties for PEO and PS-PEO by use of the parameter ξ , that is equal to 0 for PS-PEO and 1 for PEO. This parameter can be thought of as characterizing a family of composites with different amounts of PS present compared to PEO. With such a parameter we interpolate between the electrochemical properties of PEO and PS-PEO by use of

$$\Upsilon = \xi \Upsilon^{\text{PEO}} + (1 - \xi) \Upsilon^{\text{PS-PEO}}, \quad \xi \in [0, 1], \quad (6.4)$$

where ξ is the interpolation parameter and $\Upsilon \in \{\kappa, D, t_+, \frac{\partial \ln f_{\pm}(c)}{\partial \ln c}, c^{\text{ref}}\}$ are the transport parameter. We carry out a series of stability simulations using the values of transport parameters produced by various values of ξ in Eq. (6.4). We assume $\nu = 0.4$ for both materials throughout this analysis.

The results are shown in Fig. 6.6b where the critical elastic modulus is plotted against the interpolation parameter ξ . The blue line indicates the boundary between stability and instability for the protrusion growth, see Eq. (6.3). As shown in Fig. 6.6b, the stability regime is above the blue line and the unstable regime is below it. We note that there is a monotonic decay in the value of the critical Young's modulus required for stability of the protrusion as one ranges through composites from PS-PEO to PEO.

6.3.4 Variation of Selected Parameter for PS-PEO

We now study the correlation of the critical Young's modulus with respect to selected parameters. We use PS-PEO as reference material system and modify only one parameter per each analysis. Fig. 6.7a shows the correlation of conductivity and critical Young's modulus E^{crit} . We see that a higher conductivity is beneficial for stability. Especially a decrease of the ionic conductivity has a strong impact, e.g. if it is two orders

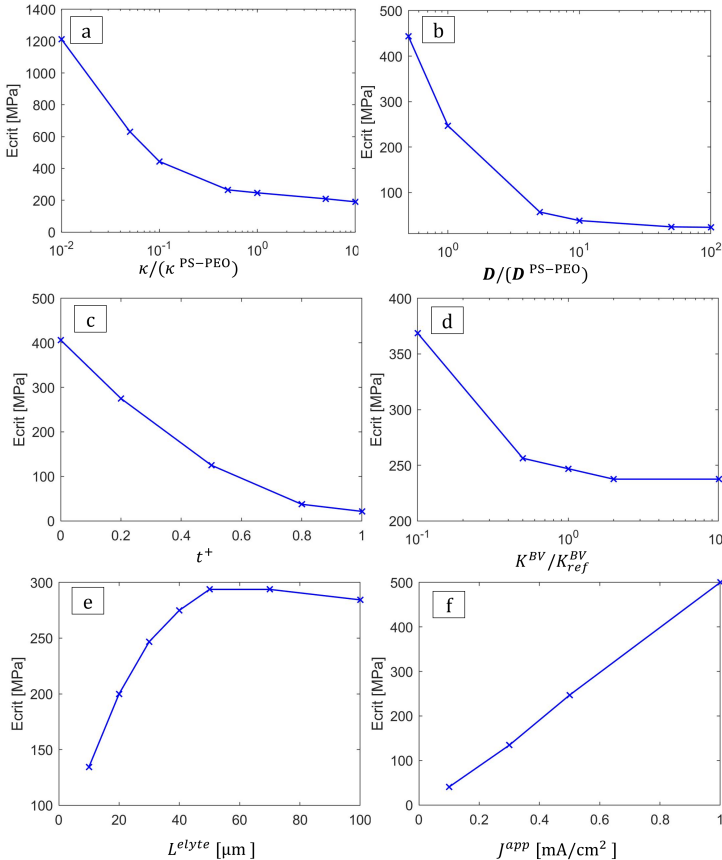


Figure 6.7: Parameter study of the critical Young's moduli with PS-PEO as reference material. The following parameters are varied separately while keeping all others fixed: (a) ionic conductivity; (b) diffusivity; (c) transference number; (d) interface conductivity; (e) separator thickness; (f) applied current.

of magnitude lower than PS-PEO then a Young's modulus of up to $E = 1200$ MPa is required. If the diffusivity is increased, the value of E^{crit} drops significantly, see Fig. 6.7b. A strong benefit with respect

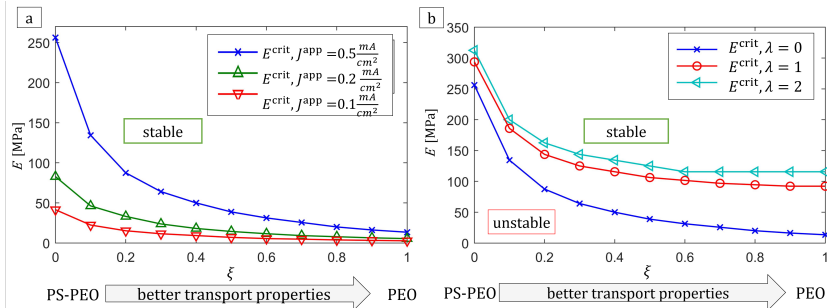


Figure 6.8: The graphs show the critical Young's moduli for stability of the protrusion as a function of ξ from Eq. (6.4), a measure of how good the transport properties of a material are. (a) Results are shown for three charging rates indicating that the protrusion is less stable at higher charging rate. (b) Results are shown for two non-uniform and a uniform value of K^{BV} . As can be seen, non-uniformity causes the protrusion to be less stable because it enhances the interface conductivity at the peak.

to morphological stability is already obtained for the relatively small increase of diffusivity by a factor of five. Smaller diffusivities lead to a complete depletion of salt and thus a termination of the simulation. Fig. 6.7c shows the impact of the transference number. Note that we set the transference number constant in this study. For $t_+^{iso} = 0$ and $t_+^{iso} = 1$ we obtain $E^{crit} = 400$ MPa and 21 MPa, respectively. The intermediate values scale almost linearly. Next, we study the impact of the interface conductivity which enters the simulation model in Eq. (5.69). Fig. 6.7d indicates that degrading the interface conductivity is harmful for stability since a higher E is required. However, there is a saturation limit, which is in the case of PS-PEO at about 240 MPa. The relation of E^{crit} to the thickness of the separator is presented in Fig. 6.7e. We see that a very thin separator is beneficial for the morphological stability.¹ Values higher than $L^{ely} = 50 \mu\text{m}$, however, are equally stable with $E^{crit} \sim 300$ MPa.

¹ Note that we assume a stiff cathode. However, for very thin separators, a deformation of the cathode is more likely and thus should resolve to increase accuracy.

Next, we study the influence of current density. Experimental findings and theoretical model formulations indicate that a higher charging rate supports the growth of an intrusion [32]. The result of a corresponding analysis is shown in Fig. 6.8a. Three sets of calculations, with $0.1 \frac{\text{mA}}{\text{cm}^2}$, $0.2 \frac{\text{mA}}{\text{cm}^2}$ and $0.5 \frac{\text{mA}}{\text{cm}^2}$, are carried out for composites with a range of transport parameters as characterized in Eq. (6.4). Fig. 6.8a indicates that higher charging rates demand higher Young's moduli. Furthermore, we see in Fig. 6.7f a linear correlation between applied current and critical Young's modulus for PS-PEO. This outcome holds also for PEO and the intermediate values, see Fig. 6.8a.

6.3.5 Heterogeneous Interface Conductivity

One explanation for the source of protrusions is a heterogeneous interface conductivity, e.g. triggered by the presence of an inhomogeneous SEI or defects in the metal electrode [50], see the discussion in Chapter 8. These inhomogeneities are assumed to decrease activation energies and therefore to increase the exchange current density locally. We model this phenomenon by applying a factor to the standard exchange current density and use the Gaussian like function $w(r)$ defined in Eq. (4.4) as the perturbation. The modified interface parametrization then reads

$$K^{\text{BV}}|^{\text{SEI}} = (1 + \lambda w(X/R^P)) K^{\text{BV}}, \quad (6.5)$$

where λ defines the amplitude of heterogeneity and X is the horizontal coordinate of the interface. Therefore, e.g. for $\lambda = 1$, the region of highest protrusion has an interface conductivity twice that prevailing in the valleys on either side of the protrusion.

Simulations are carried out at an applied charging rate of $0.5 \frac{\text{mA}}{\text{cm}^2}$ for $\lambda = 0$ (uniform), $\lambda = 1$ and $\lambda = 2$ and the results are shown in Fig. 6.8b. The results are plotted versus ξ and show that the non-uniform interface

conductivity causes the protrusion to be less stable and more likely to grow. This occurs because the non-uniform interface conductivity has a higher value at the peak of the protrusion and therefore more lithium is deposited there than on the shoulders adjacent. PEO demands an almost ten times higher stiffness for stability of the protrusion when the non-uniformity in the interface conductivity is present, whereas the necessary increase of E^{crit} for PS-PEO is not as pronounced. For PS-PEO the critical value of Young's modulus that ensures protrusion stability increases only by $\sim 20\%$ to roughly 300 MPa for $\lambda = 2$. Fig. 6.8b shows also, that the requirement on the stiffness is overall similar for $\lambda = 1$ and $\lambda = 2$.

6.3.6 Discussion

The morphological stability analysis of the deformed solid electrolyte with the fully coupled electro-chemo-mechanical model indicates a strong correlation of the material stiffness and local deposition current density while protrusion growth. Although we assume the worst case scenario, an infinitely stiff metal electrode, a growth of the protrusion can be suppressed if the electrode material has a certain mechanical stiffness. This is contrary to analyses such as that of Monroe and Newman [72], who find a relationship between material properties of the metal electrode and solid electrolyte. It further contradicts the simple purely mechanical consideration that the electrolyte has to provide a certain stiffness such that the lithium protrusion is suppressed by "pushing it down".

By using a full continuum description of transport and interface, we are able to show that the electrolyte transport properties correlate strongly with the stability of the interface. The better the transport properties are, the lower are the requirements on a "stable" separator's Young's modulus. The stability map from Fig. 6.6b indicates that even a mechanically soft material such as PEO has almost the capabilities to suppress protrusion

growth. Material modifications like cross-linking [39, 40] or using a gel electrolyte with a double polymer network ($E = 44 \text{ MPa}$ [42]) are possible paths to successfully suppress protrusion growth. Of course, these materials cannot be directly associated to a specific ξ in the interpolation scheme of Eq. (6.4), but they are most certainly closer to PEO and thus do not require as high stiffness as PS-PEO does. The critical Young's modulus for PS-PEO is in the same order of magnitude compared to its measured mechanical properties and therefore aligns with experimental findings of stable deposition. If the glass transition temperature of PS is exceeded, then PS-PEO loses its stiffness and therefore its capabilities to suppress the growth of protrusions [172].

Furthermore, we varied several parameter of PS-PEO as shown in Fig. 6.7. The outcome confirms the correlation of transport properties and stability: If the transport parameters of PS-PEO are degenerated, then the requirements on the separator are higher. We see an almost linear correlation between the applied current density J^{app} and E^{crit} . Note that with the values of J^{app} in our simulations we are below the limiting current density of approximately $2.7 \frac{\text{mA}}{\text{cm}^2}$ for PS-PEO as predicted e.g. by [30, 32, 77] who correlate dendrite growth with a full depletion of salt at the SEI. A pronounced likelihood of a complete depletion of salt at the SEI is given by a lower ionic conductivity, diffusivity and transference number. Fig. 6.7a-c agrees with this understanding as it shows that a higher stiffness is required when the transport parameters are degraded. A higher transference number showed to be beneficial for stability as already suggested by Tikekar et al. [88, 89]. The interface conductivity also has a strong influence on stability, especially for small interface conductivities, which aligns with the observations of Liu et al. [173]. A thinner separator is also beneficial for stability. The trend of higher requirements on the separator stiffness for higher current densities, lower transport properties and larger separator width align with the idea of a depletion triggered dendrite growth [30, 32, 77].

If we solely consider the analysis of an interface with homogeneous transport properties, we can conclude that increasing the stiffness by sacrificing good transport properties is not necessarily helpful for the morphological stability. Obviously, this is good news in fulfilling the demands of high charging rate performances for batteries since a material design that optimizes transport properties can also be beneficial for morphological stability.

Furthermore, it is worth to consider the inhomogeneities of the interface with a local increase of interface conductivity. We then see that the mechanically weak PEO is far away from the stable region. This is different for PS-PEO where the impact of locally increased interface conductivity is relatively small. The finding highlights the importance of homogeneous interfaces, especially for mechanically weak separator materials. We have further seen an almost linear correlation between charging rate and critical Young's modulus no matter which material. This is a problematic feature of polymer electrolyte battery systems especially for fast charging applications.

6.4 Summary

This chapter discussed a quasi-static analysis of morphological stability of a metal electrode in contact to a binary solid polymer electrolyte based on a rigorous electro-chemo-mechanical description of the bulk and reaction kinetics. We utilized measured transport parameters of the polymer electrolytes PEO and PS-PEO. Analysis of the current density at a deformed interface showed that the normal stress dependency of the equilibrium potential, the mechanical influence onto the electrochemical potential in the electrolyte bulk as well as the value of the exchange current density are equally relevant. The current density at the protrusion tip showed a clear dependency on the Young's modulus of the electrolyte.

This effect is present even though the metal electrode is assumed infinitely stiff - which is in agreement with the fact that the Young's modulus of a polymer electrolyte is at least one order of magnitude lower than pure lithium. The simulation is able to quantitatively reproduce the experimental findings of Harry et al. [31], i.e. the increase of current density at the protrusion perimeter.

The analysis showed a correlation between required stiffness and transport properties. PEO demands only a fraction of the critical Young's modulus compared to PS-PEO electrolyte, yielding in a plausible range although some drastic model assumptions were made (i.e. elastic behavior). The study suggests that it is important to find the right trade-off between the electrochemical and mechanical properties of the solid electrolyte. It is not necessarily better to increase the mechanical stiffness if this increases is accompanied by a decrease of transport properties.

We further find that the charging rates and local modifications of interface conductivities alter the morphological stability plot. The required stiffness scales linearly with the charging rate and therefore suggests upper bounds for the charging rate for a given Young's modulus for fast charging applications. Local defects experimentally showed a strong impact on the likelihood of protrusion growth. Again, this could be rationalized by the presented calculations. Especially electrolytes with good transport properties such as pure PEO require a much higher mechanical stiffness if interface inhomogeneities are present.

The presented methodology is therefore an attractive tool to predict the "sweet spot" of a solid polymer electrolyte which has sufficient transport properties by obeying at the same time the mechanical stiffness requirements for morphologically stable lithium/polymer interfaces.

7 The Metal Electrode

Metal electrodes, in particular lithium metal electrodes, and their usage within batteries are an interesting modeling subject for several reasons. The first and most obvious property of metal electrodes is their ability to conduct electrons. Secondly and most importantly, the oxidation and reduction process of cations (i.e. lithium) at the interface to the electrolyte leads to a deposition and stripping of material. The mass and therefore the stress free volume of the electrode thus changes due to an applied current. The third modeling subject is the mechanical response of lithium itself.

This chapter focuses on the kinematics of material deposition and stripping. This includes the volume description, the interface compatibility and the growth rate. We will also briefly discuss the material properties of lithium metal such as elasticity and electric conductivity.

7.1 Kinematics of Material Deposition

The stress free growth of lithium during deposition (charge) and shrinkage during stripping (discharge) is associated to the current density at the metal electrode-solid electrolyte interface. Assuming no significant surface migration of ions [174], one can deduce the boundary velocity $\|\mathbf{v}^{\text{dep}}\|$ in analogy to Ferrese and Newman [60] at a specific point by counting ions passing the interface. We obtain

$$\|\mathbf{v}^{\text{dep}}\| = \frac{\Omega_{\text{Li}}}{F} j^{\text{dep}}, \quad (7.1)$$

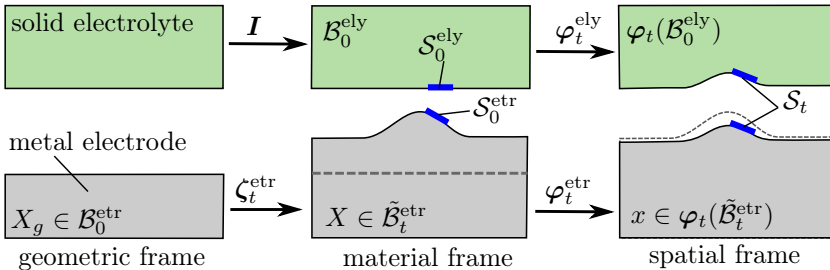


Figure 7.1: Illustration of the two mappings necessary to describe deposition or stripping and deformation: The geometry frame describes the metal electrode at initial state. Deposition is modeled with the mapping ζ_t^{etr} which yields the undeformed material frame. With the mappings of the electrolyte φ_t^{ely} and the electrode φ_t^{etr} , we obtain the deformed state, where the interface shapes S_t of electrode and electrolyte coincide.

where j^{dep} is the current density at the interface i.e. obtained by the Butler-Volmer equation (5.69), Ω_{Li} is the molar volume of lithium atoms in the lattice structure and F is the Faraday constant.

Eq. (7.1) is usually utilized in liquid electrolyte systems [58, 79], where the liquid solvent can be easily displaced during inhomogeneous deposition. In contact with a solid electrolyte, however, the newly deposited material on the metal electrode is able to generate mechanical stresses in both electrode and electrolyte, which will lead to local deformations. Therefore, we describe the dynamics of deposition and stripping at the metal electrode together with the mechanical coupling to the solid electrolyte, and we do so within the concept of finite strains.

7.1.1 Volume Description

In Chapter 2, we have introduced the idea of finite strain continuum mechanics that distinguishes between a material and a spatial configuration due to deformation. Recall that the process of deformation underlies

the conservation of mass. Deposition and stripping, however, change the mass of a given, undeformed (material) electrode domain $\tilde{\mathcal{B}}_t^{\text{etr}}$ and are therefore dependent on time $t \in T$, see Fig. 7.1. To depict the temporal dependency, we introduce a third configuration $\mathcal{B}_0^{\text{etr}}$ independent of time and which we refer to as geometry configuration. This domain might be associated to the initial shape of the metal electrode. Each point $\mathbf{X}_g \in \mathcal{B}_0^{\text{etr}}$ can be uniquely mapped to $\mathbf{X} \in \tilde{\mathcal{B}}_t^{\text{etr}}$ by

$$\zeta_t^{\text{etr}} := \begin{cases} \mathcal{B}_0^{\text{etr}} \times T \rightarrow \tilde{\mathcal{B}}_t^{\text{etr}} \\ (\mathbf{X}_g, t) \mapsto \mathbf{X} = \zeta_t^{\text{etr}}(\mathbf{X}_g, t). \end{cases} \quad (7.2)$$

The geometry displacement field $\mathbf{d} = \mathbf{X}_g - \mathbf{X}$ describes the geometry change in the metal electrode due to deposition or removal of mass. In addition, we characterize the mechanical deformation by the deformation map

$$\varphi_t^{\text{etr}} := \begin{cases} \tilde{\mathcal{B}}_t^{\text{etr}} \times T \rightarrow \varphi_t(\tilde{\mathcal{B}}_t^{\text{etr}}) \\ (\mathbf{X}, t) \mapsto \mathbf{x} = \varphi_t^{\text{etr}}(\mathbf{X}, t). \end{cases} \quad (7.3)$$

which is equivalent to Eq. (2.1). The displacement field $\mathbf{u} = \mathbf{X} - \mathbf{x}$ is determined by the balance equations, the constitutive material model and the boundary condition.

Here we have to turn to the numerical treatment to fully describe the methodology used. Describing only a deformation process, the associated discretization (grid points) in the interior of the domain is usually associated to the material body description and therefore are displaced in a physically meaningful way by the deformation map φ_t^{etr} . This is different for the deposition and stripping process ζ_t^{etr} , where the material in the interior and the associated discretization points are not physically altered. The newly generated material is therefore not adequately resolved by the discretization and, even worse, mesh entities can disappear if the removal

of material is greater than the mesh size. To avoid this problem, we equally redistribute the mesh in the interior domain φ_t^{etr} with a Laplace smoothing [132] in every time step

$$\text{Div}_{X_g}(\text{Grad}_{X_g}(\mathbf{X})) = 0, \quad (7.4)$$

where the operators $\text{Div}_{X_g}(\cdot) = \frac{\partial(\cdot)_i}{\partial(X_g)_i}$ and $\text{Grad}_{X_g}(\cdot) = \frac{\partial(\cdot)_j}{\partial(X_g)_i}$ are defined with respect to the geometric coordinates \mathbf{X}_g . Note that the choice of the Laplace operator is not physically motivated and therefore not the only option. Since it showed reasonable results for our application we will use Eq. (7.4) henceforth.¹

Solving the Laplace smoothing of Eq. (7.4) requires appropriate boundary conditions. The geometric boundary displacement \mathbf{d} is zero for surfaces which are not affected by material deposition and stripping. The other boundaries are determined by the growth rate and will be discussed in the upcoming section.

7.1.2 Interface Compatibility

It is obvious that electrochemical reactions require interfacial contact between metal electrode and solid electrolyte. If an interface region delaminates, the reduction and oxidation reactions (5.1) are most likely blocked and no further deposition and stripping of material can take place. It was shown that polymer electrolytes are able to maintain adhesion to the lithium electrode [48]. This finding is supported by X-ray microtomography images [50] which do not show delamination effects of PS-PEO electrolyte and lithium metal at a protrusion while depositing. The same holds for PEO [30]. What is not known from these image

¹ Other smoothing methods provided by COMSOL Multiphysics® are computationally more expensive and have not shown an improvement of the smoothing quality Multiphysics [132].

techniques is whether a tangential slip along the interface occurs during deposition and stripping or not. Measurements of friction coefficients have not been conducted yet, and therefore, we will describe two extreme situations, one where the interfaces are perfectly glued together and the second where tangential slip is not constrained.

The kinematics of a perfectly aligned interface are as follows. We denote the interface of the metal electrode and solid electrolyte as

$$\mathcal{S}_t = \varphi_t(\mathcal{B}_0^{\text{ely}}) \cap \varphi_t(\tilde{\mathcal{B}}_t^{\text{etr}}), \quad (7.5)$$

given in the spatial configuration (Fig. 7.1 right). Recall Section 3.1 for the kinematics of the electrolyte such as the deformation map φ_t^{ely} . The interface \mathcal{S}_t is either computed from the electrode $\mathcal{S}_t = \varphi_t^{\text{etr}}(\zeta_t^{\text{etr}}(\mathcal{S}_0^{\text{etr}}))$ or from the electrolyte side $\mathcal{S}_t = \varphi_t^{\text{ely}}(\mathcal{S}_0^{\text{ely}})$. The shape of the interface is therefore determined by three contributions: the deformation in the electrolyte φ_t^{ely} , the deformation in the electrode φ_t^{etr} as well as the geometry change ζ_t^{etr} .

Note that the interfaces of electrode and electrolyte do not align in the material configuration (Fig. 7.1 center):

$$(\varphi_t^{\text{etr}})^{-1}(\mathcal{S}_t) \neq (\varphi_t^{\text{ely}})^{-1}(\mathcal{S}_t). \quad (7.6)$$

We therefore have to apply special treatment for the growth of material since the material boundary conditions defined on the electrolyte (such as the current density) have to be converted to obtain consistent boundary conditions for the metal electrode.

To obtain the perfect contact given by Eq. (7.5), we have to couple the mechanical response of the electrode-electrolyte interface. Let's assume that the interfaces align in the initial state, i.e. $\mathcal{S}_0^{\text{etr}} = \mathcal{S}_0^{\text{ely}}$. The assumption of perfect compatibility is then fulfilled if and only if the boundary displacement of each interface point of the electrolyte \mathbf{u}^{ely} is

equal to the combined geometry change \mathbf{d}^{etr} and the deformation of the metal electrode \mathbf{u}^{etr} . To couple both, we demand pointwise

$$\mathbf{u}|_{\mathcal{S}_0^{\text{ely}}} = \mathbf{d}|_{\mathcal{S}_0^{\text{etr}}} + \mathbf{u}|_{\mathcal{S}_0^{\text{etr}}}, \quad (7.7)$$

which is also used by Tikekar et al. [89]. Note that the compatibility condition of Eq. (7.7) does not allow any tangential slip or in other words, the boundaries are glued together.

Alternatively, one obtains a transition condition with perfect contact together with tangential slip by imposing equal boundary velocities in the spatial normal direction to the interface. The boundary condition then reads for each point on the interface \mathcal{S}_t

$$(\mathbf{v} \cdot \mathbf{n})|_{\mathcal{S}_t}^{\text{ely}} = -(\mathbf{v} \cdot \mathbf{n})|_{\mathcal{S}_t}^{\text{etr}} \quad (7.8)$$

with the electrolyte velocity $\mathbf{v}|_{\mathcal{S}_t}^{\text{ely}} = \frac{d}{dt} \varphi_t^{\text{ely}}(\mathbf{X})$, the electrode velocity $\mathbf{v}|_{\mathcal{S}_t}^{\text{etr}} = \frac{d}{dt} (\varphi_t^{\text{etr}}(\zeta_t^{\text{etr}}(\mathbf{X}_g)))$ and spatial normal vector \mathbf{n} that points in opposite direction for the electrode and electrolyte.

7.1.3 Growth Rate

We now derive the relation of current density and interface velocity taking the geometric changes of the interface during deposition and stripping into account and therefore generalize Eq. (7.1). The current density j^{BV} is computed with respect to the deformed geometry with area element da and normal direction \mathbf{n} whereas the deposition is defined on the material configuration with area element dA and normal direction \mathbf{N} .

We make use of the fundamental law of conservation of mass to resolve the growth rate of the interface between electrolyte and electrode. It is given by

$$\frac{d}{dt}m_{\text{Li}} + \int_{S_t} M_{\text{Li}} \frac{j^{\text{dep}}}{F} da = 0 \quad (7.9)$$

and states that the rate of change of (lithium) metal electrode mass m_{Li} is equivalent to the material with molar mass M_{Li} deposited or stripped due to the current density j^{dep} . Note that the current density is defined on the deformed interface as it specifies the active area for electrochemical reactions. The mass of the electrode m_{Li} can be written in terms of the density, yielding

$$\frac{d}{dt}m_{\text{Li}} = \frac{d}{dt} \int_{\varphi_t(\tilde{\mathcal{B}}_t^{\text{etr}})} \rho_{\text{Li}} dv \quad (7.10)$$

with the mass density ρ_{Li} . In order to exchange the integral and the temporal derivative, we switch from the spatial via the material to the geometry configuration and thus use the time-independent integral domain $\mathcal{B}_0^{\text{etr}}$. With the help of Reynold's theorem (Eq. (2.14)), we take the moving boundary due to deposition into account and obtain

$$\frac{d}{dt}m_{\text{Li}} = \frac{d}{dt} \int_{\tilde{\mathcal{B}}_t^{\text{etr}}} \rho_{\text{Li}}^\diamond dV = \underbrace{\int_{\tilde{\mathcal{B}}_t^{\text{etr}}} \frac{d}{dt} \rho_{\text{Li}}^\diamond dV}_{=0} + \int_{S_0^{\text{etr}}} \rho_{\text{Li}}^\diamond \mathbf{v}^{\text{dep}} \cdot \mathbf{N} dA, \quad (7.11)$$

where the first term on the right hand side drops out due the balance of mass of an undeformed medium, see Eq. (3.6), and $\mathbf{v}^{\text{dep}} = \frac{d}{dt} \zeta_t^{\text{etr}}(\mathbf{X}_g)|_{S_0^{\text{etr}}}$ is the unknown interface velocity for deposition and stripping defined in the material configuration. Note that this velocity is different to the one in Eq. (7.8) because it takes only deposition but no deformation

into account. Using Eq. (2.8) we obtain the spatial representation of the boundary integral

$$\frac{d}{dt}m_{\text{Li}} = \int_{S_t} \rho_{\text{Li}} \mathbf{v}^{\text{dep}} \cdot \mathbf{F}^T \mathbf{n} da \quad (7.12)$$

Inserting Eq. (7.12) into Eq. (7.9) and postulating that material deposition and stripping are local effects gives

$$\frac{M_{\text{Li}} j^{\text{dep}}}{F} = -\rho_{\text{Li}} \mathbf{v}^{\text{dep}} \cdot \mathbf{F}^T \mathbf{n}. \quad (7.13)$$

We are now interested in the normal velocity of the boundary in the material configuration. We thus multiply Eq. (7.13) with the material normal \mathbf{N} and get with $\mathbf{N} \cdot \mathbf{F}^T \mathbf{n} = \mathbf{F} : (\mathbf{n} \otimes \mathbf{N})$ the normal velocity as

$$\mathbf{v}^{\text{dep}} \cdot \mathbf{N} = -\frac{M_{\text{Li}}}{F \rho_{\text{Li}}^\diamond} J^{\text{dep}} = -\frac{M_{\text{Li}}}{F \rho_{\text{Li}}^\diamond} \frac{\mathbb{J}}{\mathbf{F} : (\mathbf{n} \otimes \mathbf{N})} j^{\text{dep}}, \quad (7.14)$$

where the scaling factor between J^{dep} and j^{dep} is taken from Eq. (2.10). Note that all properties in Eq. (7.14) such as the deformation gradient \mathbf{F} are associated with the metal electrode.

7.2 Material Properties of Lithium Metal

In the past, mechanical response of pure lithium has received little attention due to its very reactive nature and limited fields of application. Studies on anti-proton sources [11, 12] provided first measurements on mechanical stiffness with $E = 1.9 - 4 \text{ GPa}$ [11, 12] and non-elastic behavior such as the mechanical strength with about 1 MPa [12]. Due to the rise of solid state batteries with lithium metal anodes, the material properties of lithium got into the focus of research. Microindentation [15], compression experiments [14] and nanoindentation [175–177] showed higher yield

strength with up to 105 MPa, size effects and anisotropy due to the grain structure of lithium metal. Due to its low melting point of 180.6 °C and for an application at elevated temperatures (e.g. 80 °C) such as necessary for polymer battery systems [50], there is also a high likelihood that the material starts to creep. This might influence long term applications in battery systems. Recently, Narayan and Anand [178] published an elastic-viscoplastic material model which describes the complex response of lithium.

In this work, however, we put our focus on the electrochemical response with a simple mechanical description. Therefore, we apply the same level of complexity as we have used for the solid electrolyte in Chapter 3 and assume purely elastic behavior. We also note that by omitting non-elastic effects, we model a material which is more prone against deformation. This assumption is therefore conservative with respect to a morphological interface stability analysis.

7.2.1 Material Model

Despite the knowledge of non-elastic effects of lithium as stated before, we reduce complexity by the assumption that the full deformation as described by the deformation gradient \mathbf{F} is purely elastic. This assumption is especially true for small strains. Similar to the solid electrolyte, we assume an isotropic hyperelastic Neo-Hookean material model [111], but without considering swelling effects (see Eq. (3.66)). The strain energy is then given by

$$\tilde{\psi}_{\text{NH}}^{\text{etr}}(\mathbf{F}) = \frac{1}{2}\gamma_{\text{NH}}(\mathbb{I}_1 - 3) + \frac{1}{2}\lambda_{\text{NH}}(\log \mathbb{I}_3)^2 - \gamma_{\text{NH}} \log \mathbb{I}_3, \quad (7.15)$$

with the Lamé constants γ_{NH} , λ_{NH} and the invariants

$$\mathbb{I}_1 = \text{tr}(\mathbf{F}^T \mathbf{F}), \quad \mathbb{I}_3 = \mathbb{J} = \det \mathbf{F}. \quad (7.16)$$

The elastic material model helps us to understand the basic electro-chemo-mechanical response and is in analogy to the works of e.g. [15, 71, 86]. This approach of using solely an elastic model also circumvents questions whether newly deposited material "inherits" some history of the pre-existing material such as strain hardening, etc. Considering in-elasticity also requires a mapping of history variables such as plastic strain or hardening parameters to the geometric configuration and not to the material configuration as it is usually done.

7.2.2 Ohm's law

Electronic conduction in a metal electrode is governed by the balance of charge where the current density is deduced by Ohm's law. It states a linear relationship between electric current density \mathbf{J}_q and voltage drop. Recall Eq. (3.15) for the differential form

$$\operatorname{div}(\mathbf{j}_q) = 0 \quad \text{with} \quad \mathbf{j}_q = -\kappa^{\text{etr}} \operatorname{grad}(\Phi), \quad (7.17)$$

where the conductivity of the metal electrode is κ^{etr} is equal to the inverse of the resistivity. Lithium metal, for example, has a conductivity of $\kappa^{\text{etr}} = 10.6 \times 10^6 \frac{\text{S}}{\text{m}} \mathbf{I}$ [179] which is almost ten orders of magnitude higher compared to the one of a polymer electrolyte (see Section 4.2.1) since the small electrons can more easily be transported compared to the bulky ions of the salt. Hence, small gradients of the electric potential already yield a very high electric current. Since the length of the electron path between current collector and electrolyte is small, roughly $\approx 100 \mu\text{m}$, the drop in electric potential in the electrode is expected to be small.

For the consistent implementation of Ohm's law on a deformed geometry, we again use the formulation of finite strains and solve the partial

differential equation in the material configuration.² The electric field in the metal electrode then is computed by

$$\operatorname{Div}(\mathbf{J}_q) = 0 \quad \text{with} \quad \mathbf{J}_q = -\mathbb{J}\mathbf{F}^{-1}\boldsymbol{\kappa}^{\text{etr}}\mathbf{F}^{-T}\operatorname{Grad}(\Phi), \quad (7.18)$$

where the electric conductivity is transformed in analogy to Eq. (3.84) into the material configuration. Appropriate boundary conditions such as Cauchy or Neumann condition, respectively, are

$$\Phi|_{\partial\tilde{\mathcal{B}}_t^{\text{etr}}} = \tilde{\Phi}, \quad -\mathbf{N} \cdot \mathbf{J}_q|_{\partial\tilde{\mathcal{B}}_t^{\text{etr}}} = -J^{\text{dep}}. \quad (7.19)$$

The boundary conditions are defined in the undeformed geometry and we apply Eq. (2.10) to convert the current density of deposition J^{dep} to j^{dep} to take the deformation of the interface length into account.

7.3 Summary

This chapter dealt with the description of the metal electrode in a solid state battery. Two mechanisms lead to a change of geometry. One process is related to deposition and stripping, which adds and removes material from the electrode. Mechanical deformation of the electrode is the second process that has to be modeled. We derived a consistent formulation within the finite strain framework by utilizing in addition to the commonly used displacement field (deformation) a geometric displacement field (for deposition and stripping). We postulated interface compatibility between electrode and electrolyte motivated by experimental findings. Furthermore, we presented material properties of lithium metal concerning elastic response and its capability to conduct electrons.

² We use the capabilities of COMSOL Multiphysics® 5.3a which automatically maps the material to geometric configurations correctly if no history variables are involved.

8 Morphological Stability: A Transient Analysis

This chapter deals with a second approach to describe the morphological stability of a solid electrolyte - metal electrode interface. In addition to the scope of the first study in Chapter 6, we now model the metal electrode and the growth of material during charging explicitly.

The study utilizes the electro-chemo-mechanical model of ion transport in a solid polymer electrolyte (Chapter 3), the extended Butler-Volmer reaction kinetics by means of mechanics (Chapter 5) and describes explicitly the lithium electrode and its growth and shrinkage due to deposition and stripping (Chapter 7).

One of the few explicit treatments of lithium metal growth in battery applications on the continuum scale was presented by Ferrese et al. [58] who describe the ion transport by using the classical concentrated solution theory [53] but disregard any mechanical influences. The follow-up works [59, 60] also treat mechanics, including non-elastic effects, describing the redistribution of lithium within the metal foil due to inhomogeneous deposition. However, the mechanisms of swelling and stress driven diffusion and the effect of reduction of transport paths due to deformation are not considered.

In our analysis, we first investigate trigger mechanisms in order to understand possible reasons for inhomogeneous material deposition leading to damaging of the solid electrolyte. The calculations provide insight into the mechanisms dominating interface evolution during deposition

and are capable of predicting protrusion branching. The idea of protrusion branching thereby stems from the current density distribution of the analysis of Section 6, which suggest elevated current density at the perimeter of a protrusion. We then put our focus on the morphological interface stability for PEO and PS-PEO electrolytes and compare the outcome with the results of Chapter 6. We will see that inhomogeneity of interface conductivity is a likely reason to cause protrusion growth and therefore we develop an analytical network model to depict a correlation of interface and bulk properties on morphological stability. We conclude this chapter with a recap of coupling mechanisms in protrusion growth.

8.1 The Boundary Value Problem

In this analysis, we model the negative metal electrode and the solid electrolyte and substitute the cathode by a current density and mass flux at the top side of the electrolyte, see Fig. 8.1. Again, we assume an isothermal system at 80 °C in two dimensions at plane strain. The electrode and the electrolyte are 20 µm and 30 µm thick, respectively. The width of the computation domain is set to 100 µm.

A linear elastic material model is assumed for the lithium metal electrode, see Eq. (7.15). At elevated temperature, lithium has a Young's modulus of approx 4 GPa [12] and the Poisson ratio $\nu = 0.34$. Its electronic conductivity is $\kappa^{\text{etr}} = 10.6 \frac{\text{S}}{\text{m}} \mathbf{I}$ [179]. The coupled system of ion transport and mechanics in the solid electrolyte is described by the extended concentration solution theory of Eq. (3.116) considering migration, diffusion and stress-assisted diffusion of the ions. It takes also hyperelasticity and swelling of the host material into account. We again utilize the electrochemical parametrizations of PEO [56] and PS-PEO [57] with LiTFSi salt introduced in Section 4.2.1 and the interface properties discussed in Section 5.7 i.e. a symmetric reaction with the exchange

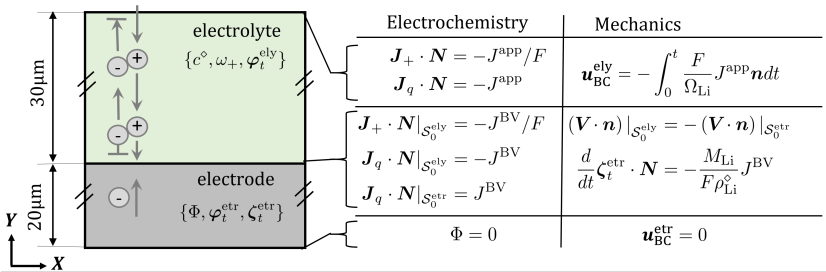


Figure 8.1: The boundary value problem of the second stability analysis deals with a metal electrode at the bottom and the electrolyte on the top.

current density given by Eq. (5.68) with $K^{BV} = 0.589 \frac{A}{\sqrt{m \text{ mol}}}$. The Poisson ratio is assumed to be $\nu = 0.4$ for both PEO and PS-PEO and the Young's modulus of PEO and PS-PEO will be varied to gain more understanding of the system behavior.

The boundary and transition conditions of the metal electrode and solid electrolyte are summarized in Fig. 8.1. Symmetry boundary conditions are applied on the left and right side. Therefore we enforce continuity of the electrochemical properties $\{\omega_+, c^\circ\}$ and zero horizontal displacement for $\{\varphi_t^{\text{ely}}, \varphi_t^{\text{etr}}, \zeta_t^{\text{etr}}\}$. It is assumed that the lithium metal is attached to a highly conductive and stiff current collector at the bottom interface and thus we have $\Phi = 0$ (electrically grounded) and $u_{\text{BC}}^{\text{etr}} = 0$ (no deformation). The lithium electrode is attached to the solid electrolyte. Between the metal electrode and electrolyte, we assume compatibility in normal direction and allow tangential slip according to Eq. (7.8). The interface current density is computed by the Butler-Volmer equation (5.69) as a function of $\{\omega_+, c_+, \Phi, \sigma_n^{\text{etr}}\}$, which determines the growth of the lithium metal interface, see Eq. (7.14), the electrical current at the electrode, and the current and mass flux of the electrolyte. The cathode is not explicitly modeled and thus we relate the mass and current flux to the applied current density J^{app} . We further mimic a second metal

electrode at the top where lithium is homogeneously stripped with a boundary displacement proportional to J^{app} .

We simulate one charging step and deposit $4\mu\text{m}$ of lithium with $J^{\text{app}} = 0.5 \frac{\text{mA}}{\text{cm}^2}$ on the metal electrode. This leads to a charging time of 5936 s. Afterwards, we apply a relaxation phase of 3000 s where J^{app} is zero.

Again, we use COMSOL Multiphysics[®] to solve the coupled system of partial differential equations. We scale the field variables to improve conditioning of the system matrix and therefore increase numerical accuracy. The transition condition (7.14) and (7.8) are enforced with the concept of Lagrange multipliers [132], where scaling is done automatically by the simulation tool. We utilize a staggered solver and thus separate the transport equations from the deposition process. The first step solves for $\{\omega_+, c_+^\diamond, \varphi_t^{\text{ely}}, \Phi\}$ and the second for $\{\varphi_t^{\text{ely}}, \zeta_t^{\text{etr}}\}$ including the Lagrange multiplier. The mechanics for the electrolyte is considered in both steps because it influences the ion-transport as well as the purely mechanical interaction with the electrode. If not otherwise stated, we use a structured grid with quadrilateral elements, where the nodes on the interface between electrode and electrolyte align at time $t = 0$. Approximately one hundred thousand degrees of freedom were solved with the direct solver MUMPS in each time step. The backward differential method showed best performance for the numerical integration with respect to time. The integration order is automatically varied between one and five. The time steps are freely chosen by the simulation tool, but are restricted to a maximum time step Δt^{\max} . Numerical tests showed that $\Delta t^{\max} = 10$ s provides a good accuracy in a reasonable computing time.

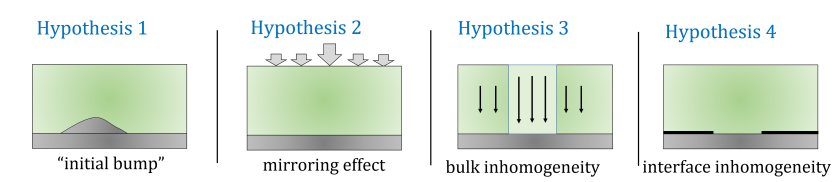


Figure 8.2: Illustration of four hypotheses of trigger mechanism which might lead to inhomogeneous deposition.

8.2 Analysis of Instability Triggers

With the comprehensive description of electrode and electrolyte at hand, we now explore the growth of lithium metal during charging. Obviously, a planar interface as depicted in Fig. 8.1 in combination with homogeneous transport properties yields homogeneous material deposition and stripping. To break the homogeneity, a trigger needs to be introduced. Fig. 8.2 illustrates four hypotheses to be investigated in this context. Note that we will provide only a qualitative comparison based on educated guesses of the parameter variations. A one-to-one comparison as done in non-dimensionalized settings, see e.g. [180], is not feasible in our case because variation of geometry, bulk properties, interface properties and boundary conditions are of different kind and cannot be easily related by one non-dimensionalized parameter.

8.2.1 Four Hypothesis on Trigger Mechanisms

Hypothesis 1 postulates an initial protrusion, e.g. due to surface roughness, as reason for a harmful protrusion growth into the separator. It influences the transport paths: The shorter the path, the higher the effective conductivity and the more likely an increased deposition process. In analogy to Chapter 6 we consider a Gaussian like protrusion, see Eq. (4.4), with an amplitude of $A^P = 4 \mu\text{m}$. We chose a support of

$R^P = 15 \mu\text{m}$ throughout this study. Other than in Chapter 6, we assumed the electrolyte to be stress free in the initial state. To resolve the curved shape, we utilize an unstructured grid with triangular mesh elements.

Hypothesis 2 assumes an inhomogeneous ion supply at the cathode. Recall that the cathode is a porous composite with active storage particles. For example, particles close to the solid electrolyte that have lost their connection to the positive current collector are not functional, block the ion transport and thus increase the current density in the adjacent regions.¹ The morphology of the positive electrode is then mirrored on the negative electrode, due to local changes of current entering the solid electrolyte. We model this effect by

$$(J^{\text{app}})^{\text{trigger}} = (1 + w(X/R^{\text{deg}})) J^{\text{app}}. \quad (8.1)$$

and thus double the applied current density at the center of the computation domain. The support of the degraded zone is $R^{\text{deg}} = 15 \mu\text{m}$.

Protrusion growth can also be triggered by inhomogeneities in transport properties, either in the bulk (*Hypothesis 3*) or at the interface (*Hypothesis 4*). Better transport properties in a region yield a higher deposition rate compared to the neighboring region and thus lead to instability. For *Hypothesis 3*, we increase the ionic conductivity and the diffusivity of the bulk with

$$\{\kappa, D\}^{\text{trigger}} = (1 + 9w(X/R^{\text{deg}})) \{\kappa, D\}. \quad (8.2)$$

by one order of magnitude in the center of the computational domain. *Hypothesis 4* is similar to the adjustments of Eq. (6.5) and reads

$$(K^{\text{BV}})^{\text{trigger}} = (1 + 2w(X/R^{\text{deg}})) K^{\text{BV}}. \quad (8.3)$$

¹ Active particles usually have a diameter of several micrometers [167, 181] which is the same order of magnitude as we use for the support in Eq. (8.1).

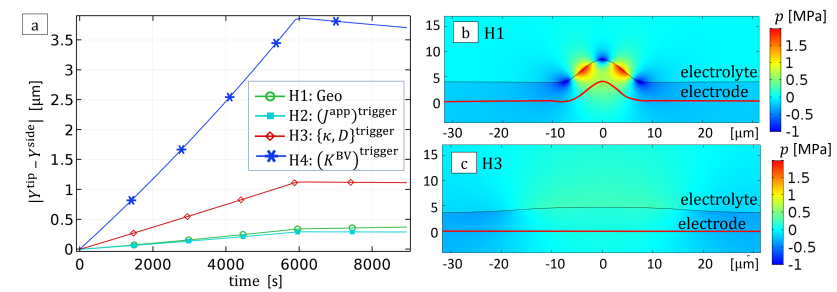


Figure 8.3: Four trigger mechanism for protrusion growth are investigated: (a) shows the protrusion height over time for the four hypotheses of Fig. 8.2. (b) and (c) show the contour plot of hydrostatic pressure for hypotheses 1 and 3. The red lines indicate the initial interface shape.

The exchange current density or, in other words, the interface conductivity is increased by a factor of three in the center of the interface and gradually declining to reference sideways.

8.2.2 Results and Discussion

For this study, we use the solid polymer electrolyte PEO with a Young's modulus of $E = 10 \text{ MPa}$ and transport properties as given in Section 4.2.1. Recall that this material showed a high likelihood for morphological instability in the previous study of Chapter 6.

Fig. 8.3a shows the growth of the protrusion height over time. We subtract the displacement measured at the side of the computational domain from total displacement of the electrolyte at the center in order to remove the translation of the interface due to homogeneous material deposition.

The initial protrusion (*Hypothesis 1*) yields only a very small growth although the initial height of the protrusion is already significant. Therefore, one can conclude that an initial protrusion is not the main cause

of morphological instability. Nevertheless, we use this setup to understand material growth normal to the interface. The region close to the protrusion tip is under tension, see Fig. 8.3b, and the shoulder is under compression. This behavior is due to the broadening of the protrusion in the in-plane direction and results in quite strong compressive normal forces in the shoulder region and consequently pushes the separator up. In order to preserve compatibility, the perimeter as well as the tip have to pull on the electrolyte and are therefore under tension. The small pressure jump between electrode and electrolyte is due to the compatibility condition of Eq. (7.8) which requires only the normal traction force to align but not the lateral traction forces. Although the stress state with tension at the tip will always be present when a protrusion is growing, it is of second order when a planar interface is used as initial condition.

Hypothesis 2 with an inhomogeneous current supply also shows only small protrusion growth. Ion transport in the in-plane direction smooths out the local current spike (J_{app})_{trigger}. We note that this might change if either the separator thickness is reduced² or the transport properties of the polymer are degraded.

Fig. 8.3c illustrates the interface for *Hypothesis 3*. Locally enhanced transport properties do not yield a pronounced protrusion growth. The modification of the interface conductivity (*Hypothesis 4*) results, however, in a significant increase of local deposition (Fig. 8.3a). With 4 µm the tip grows almost twice as fast as the neighboring regions. The growth speed even accelerates over time, meaning that the tip velocity increases the higher the protrusion is. This can be explained by the shortening of the transport paths. The effect of *Hypothesis 1* and *Hypothesis 4* then superpose.

Fig. 8.3a shows another interesting effect. There is a reorganization of lithium in the relaxation phase which yields to a decrease of the protrusion

² Note that Rosso et al. [35] measured protrusion growth for much thicker electrolytes.

height for *Hypothesis* 2-4 and a small increase for *Hypothesis* 1. Although no external current is applied, there is a small stripping current density at compression regions and a deposition current density at regions under tension. As discussed later, ions at the metal electrode prefer to be on a low pressure region. Since an ion as well as an electron conduction path is provided, there is no hurdle for a reorganization of the ions. The overpotential is, however, much smaller compared to doing charging which yields only a small decrease of protrusion height over time.

The analysis of the trigger mechanisms suggests that *Hypothesis* 1-3 are very unlikely to cause harmful protrusion growth, although the single influences were perturbed quite significantly. *Hypothesis* 4 with a perturbation of the interface conductivity has proven to be a likely candidate for instability. We do not claim that this is exclusive since purely chemical reactions might also contribute but are not depicted in our continuum description. Nevertheless, also experimental studies align with our outcome that the cause has to be related to the electrode-polymer interface. For example, Harry et al. [50] were able to correlate a protrusion growth to an impurity at the lithium surface. The impurity might increase the surface conductivity. Although this has not been experimentally proven, we will continue with *Hypothesis* 4 for the upcoming second stability analysis.

8.3 Stability Analysis

In the previous section, it was observed that an inhomogeneous interface conductivity, see Eq. (8.3), is the most likely trigger for protrusion growth. In the following study we stick to this trigger mechanism, vary the Young's modulus and investigate the response of the resulting interface amplitude. We apply the analysis to both PEO and PS-PEO.

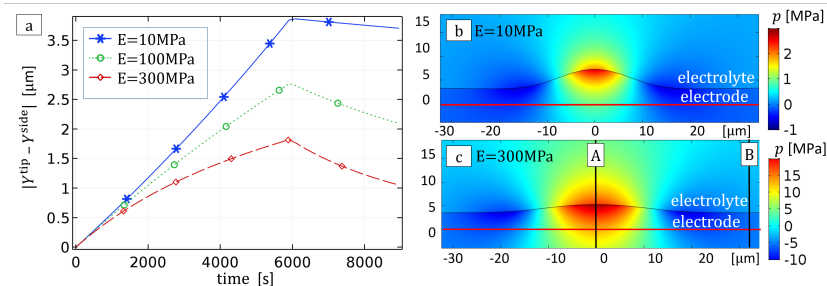


Figure 8.4: (a) The evolution of the protrusion height depending on the Young's modulus for a PEO polymer. The contour plots on the right show the hydrostatic pressure in the electrode and electrolyte for (b) $E = 10$ MPa and (c) $E = 300$ MPa at $t = 5900$ s. The red line indicates the initial surface at $t = 0$ s and the lines A and B are cross sections used to evaluate Fig. 8.7. Note that B is evaluated at the side of the computational domain.

8.3.1 Lithium Metal and PEO Electrolyte

We first analyze the PEO polymer electrolyte and vary the Young's modulus between $E = 10$ MPa and $E = 300$ MPa. Fig. 8.4a shows the protrusion growth over time. Note that the results for $E = 10$ MPa are equivalent to *Hypothesis 4* in Fig. 8.3a and recall that the protrusion growth velocity increases with time due to the shortening of the transport path. Fig. 8.4b shows the interface at $t = 5900$ s. The tip experiences compression and the perimeter tension, similar to the study of Section 4.5. The hydrostatic pressure goes up to 3 MPa and is thus not very pronounced. If the Young's modulus is increased, the effective protrusion height decreases significantly as seen in Fig. 8.4a. The rate of growth is identical in the beginning, but the more material is deposited, the slower is the protrusion growth for a higher Young's modulus. The case of $E = 300$ MPa indicates an asymptotic behavior of the growth with a maximum protrusion height and therefore morphological stability. That means that even though the local interface conductivity is increased,

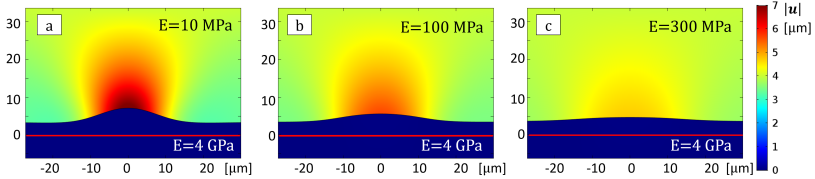


Figure 8.5: The contour plots show the displacement of the electrode (bottom) and solid electrolyte for (a) $E = 10 \text{ MPa}$, (b) $E = 100 \text{ MPa}$ and (c) $E = 300 \text{ MPa}$. The red lines indicate the initial states of the interface. Note that the displacement of the electrolyte takes also translation due to deposition processes into account.

the local stress state compensate this modification and yield to a homogeneous deposition process. Again, we observe an amplitude decrease at the relaxation phase which is more pronounced the stiffer the material is.

To understand the underlying effect of the decrease of protrusion height for increasing Young's moduli, we first consider the mechanical response. Fig. 8.5 illustrates the displacement of the electrode and the electrolyte. Note that the displacement of the solid electrolyte takes the translation due to deposition into account which explains the displacement of $3.2 \mu\text{m}$ for $E = 10 \text{ MPa}$ up to $3.6 \mu\text{m}$ for $E = 300 \text{ MPa}$ at the perimeter and $t = 5900 \text{ s}$. The difference between desired deposition ($4 \mu\text{m}$) and actual translation is explained by the protrusion growth. It requires additional material to create the protrusion which can not deposited onto the adjacent area. The displacement of the electrode is almost negligible for all three cases, especially if it is compared to the amplitudes of the protrusions. A simple push-down effect of the electrode based on elastic deformation to stabilize the interface can thus be excluded.

We can explain the different protrusion heights with a change of the interface current densities. The current densities do not differ significantly for the three considered Young's moduli at time $t = 200 \text{ s}$, see Fig. 8.6.

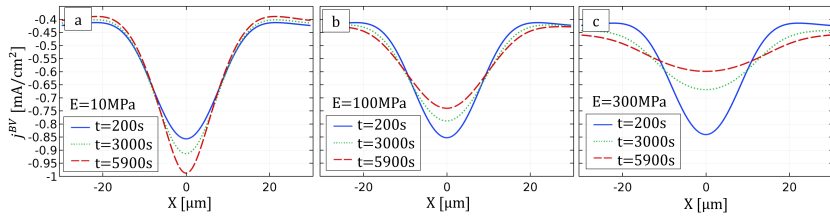


Figure 8.6: The current density at the electrode-electrolyte interface at the beginning, in the middle and at the end of the charging process for (a) $E = 10 \text{ MPa}$, (b) $E = 100 \text{ MPa}$ and (c) $E = 300 \text{ MPa}$.

The Gaussian like shape of the current densities with a maximum of $0.85 \frac{\text{mA}}{\text{cm}^2}$ comes from the modified exchange current density. When time passes and more material is deposited, we observe that for $E = 10 \text{ MPa}$ the current density increases with time, most likely due to the decrease of the related transport path. Contrary to that, the current density decreases for $E = 100 \text{ MPa}$ and even more for $E = 300 \text{ MPa}$ as seen in Fig. 8.6b and 8.6c. The smaller amplitudes of the current density explain the smaller protrusion growth for a higher Young's modulus.

Fig. 8.7a shows the electrochemical potential ω_+ in the electrolyte and the electric potential Φ in the electrode in the cross section along the Y-axis at $X = 0$ (line A in Fig. 8.4c) and $X = 0.5W$ (line B in Fig. 8.4c). The potentials at the side basically coincide for the three stiffnesses thus we plot only the value for $E = 10 \text{ MPa}$. We observe that ω_+^{tip} is very similar for the three considered Young's moduli but differs strongly from ω_+^{side} . The electric potential is almost constant in the electrode. We note that the drop of electrochemical potential in the electrolyte is in the same order of magnitude compared to the potential jump along the interface with roughly $\eta = 6 \text{ mV}$. The concentration of the salt, again in the cross-section along the Y-axis at $X = 0$ (line A in Fig. 8.4c) and $X = 0.5W$ (line B in Fig. 8.4c) at $t = 1000 \text{ s}$ for the three different moduli, is shown in Fig. 8.7b. We observe a

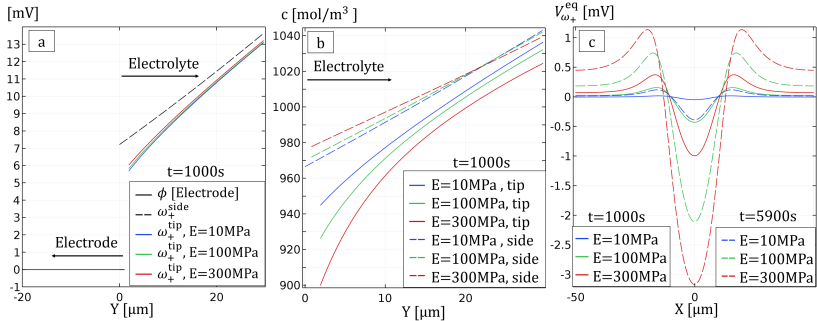


Figure 8.7: The electro-chemo-mechanical response of PEO during charging at $t = 1000\text{s}$ for three Young's moduli: (a) Electric and electrochemical potential. Note that influence of E onto Φ and ω_+^{side} is negligible and therefore not shown. (b) Concentration profile along cross section A (tip) and B (side), see Fig. 8.4c. (c) Open circuit potential along the interface, here also for $t = 5900\text{s}$.

concentration polarization in the out-of-plane direction along the Y-axis. At the perimeter, an increase of Young's modulus leads to a decrease of the concentration gradient. On the other hand, there is an increase of the concentration gradient or depletion of salt at the tip for an increasing Young's modulus due to stress driven diffusion. For a further discussion of these effects we refer to Section 4.5. The open circuit potential $V_{\omega_+}^{\text{eq}}$ is shown in Fig. 8.7c for the three different Young's moduli at $t = 1000\text{s}$ and $t = 5900\text{s}$. The tip value of $V_{\omega_+}^{\text{eq}}$ decreases with respect to time and also with respect to the Young's modulus. In this case, a negative open circuit potential provokes a decrease of the interface current density. This effect is especially significant for $E = 300\text{ MPa}$ at $t = 5900\text{s}$ with $V_{\omega_+}^{\text{eq}} = -3\text{ mV}$ and explains the reduction of interface current in Fig. 8.6.

In the relaxation phase at $t > 5900\text{s}$, we observe a decreasing protrusion height, see Fig. 8.4a. This is most pronounced for the solid electrolyte with $E = 300\text{ MPa}$. Fig. 8.8a reveals the current density during relaxation at $t = 6500\text{s}$, $t = 7500\text{s}$ and $t = 8500\text{s}$. There is a stripping current at

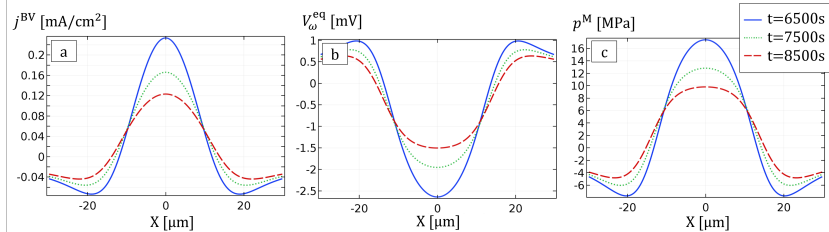


Figure 8.8: The figures show the relaxation process for PEO with $E = 300 \text{ MPa}$ for three different snapshots. (a): Interface current density, (b): open circuit potential and (c): hydrostatic mechanical pressure p^M .

the tip ($j^{\text{BV}} > 0$) and a deposition current ($j^{\text{BV}} < 0$) at the perimeter. This is triggered by the open circuit potential $V_{\omega+}^{\text{eq}}$, see Fig. 8.8b, which is negative at the peak of the protrusion and positive at the side. Fig. 8.8c shows the hydrostatic stress p^M for the three Young's moduli along the electrode-electrolyte interface. There is compression at the tip yielding a negative value of $V_{\omega+}^{\text{eq}}$ (and thus stripping) and mechanical tension away from the protrusion (and thus deposition). The process is slow but will eventually yield to a completely flat surface in case if non-elastic effects are neglected.

8.3.2 Lithium Metal and PS-PEO Electrolyte

We redo the previous study, but now with the parametrization of a PS-PEO electrolyte, see Section 4.2.1. All other parameters are kept the same. In addition, we investigate a second system where we decrease the interface conductivity or exchange current density, respectively, by a factor of ten along the interface ($K^{\text{BV}} = 0.0589 \frac{\text{A}}{\sqrt{\text{m mol}}}$). As we have discussed in Section 6, the PS-PEO electrolyte requires higher stiffnesses for stability compared to PEO, therefore, we have chosen three Young's moduli between $E = 100 \text{ MPa}$ and $E = 1000 \text{ MPa}$.

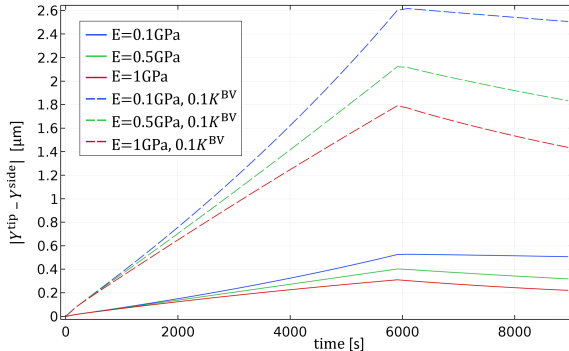


Figure 8.9: The penetration depth over time for PS-PEO for three Young's moduli and two interface conductivities.

We observe a similar trend in the protrusion growth as observed for PEO in Fig. 8.9. The higher the stiffness, the smaller the protrusion height. However, the protrusion height for the reference interface conductivity has values between $0.4\text{ }\mu\text{m}$ and $0.6\text{ }\mu\text{m}$ and is therefore very small for all investigated Young's moduli at the end of the charging process. Numerical studies showed that moderate changes of charging rate J^{app} and the amplitude of the interface conductivity disturbance in Eq. (8.3), did not increase the instability significantly. By adjusting the prefactor of the interface conductivity K^{BV} , we again observe a strong impact of the Young's modulus on the protrusion height. Degrading the surface by dividing K^{BV} by a factor of ten and therefore increasing the interface resistance by one order of magnitude yields a significant protrusion growth with values between $2.3\text{ }\mu\text{m}$ and $3.2\text{ }\mu\text{m}$, see Fig. 8.9. In both cases, the influence of the mechanical stiffness is not as pronounced as for the PEO electrolyte.

Fig. 8.10 reveals a detailed analysis of the electrochemical potential for $E = 100\text{ MPa}$ at $t = 1000\text{ s}$ for the two prefactors of the interface conductivity K^{BV} and $0.1K^{\text{BV}}$. The graphs in Fig. 8.10c and 8.10d are

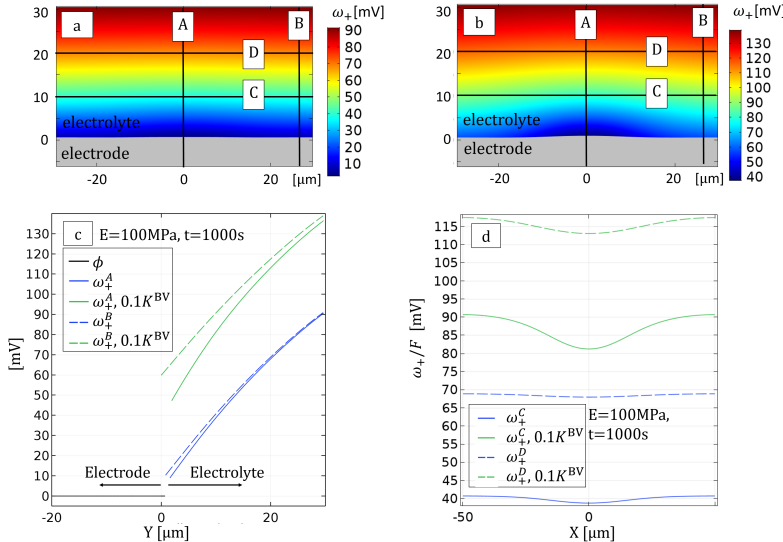


Figure 8.10: The electrochemical potential for PS-PEO with $E = 100 \text{ MPa}$ at $t = 1000 \text{ s}$ for two interface conductivities. (a) Contour plot of ω_+ for reference K^{BV} . (b) Contour plot of ω_+ for $0.1K^{\text{BV}}$. The lines A-D indicate cross sections. Note that B is evaluated at the side of the computational domain. (c) Cross section in the direction A and B. (d) Cross section in the direction C and D. Note that the figures (a) and (b) are truncated to highlight the region around the protrusion growth.

defined by the cross sections A, B, C and D, as depicted in Fig. 8.10a and Fig. 8.10b. Recall that the gradient of the electrochemical potential ω_+ is a major driving force for ion flux and is therefore a good indicator for the current in the electrolyte.

In Fig. 8.10, we see that the electrochemical potentials in the out-of-plane direction are shifted by roughly 50 mV if the interface conductivity is smaller but the slopes are similar. On the other hand, there are strong differences in the variation of ω_+ in the in-plane direction, see Fig. 8.10d. For the standard interface conductivity, only a very small drop of ω_+ is observed in the center region (cross section C). Further away from

the electrode-electrolyte interface (cross section D) we observe an almost constant ω_+ in the in-plane direction. This is different for the second case with $0.1K^{BV}$, where cross sections C and D show a notable drop of ω_+ in the region where the interface conductivity is increased.

8.3.3 Discussion

The results of protrusion growth at a metal electrode adjacent to a PEO and a PS-PEO electrolyte, respectively, extend the first study of Chapter 6 and give new insights into the morphological stability. Contrary to the first study with a given deformation, the protrusion growth now has to be triggered with the help of an inhomogeneous interface conductivity. The two approaches are therefore not directly comparable, although the study of Section 6.3.5 with its modification of the interface conductivity is based on similar assumptions.

We first point out that the shape and size of the protrusion chosen in Section 6 align with the outcome of the dynamic protrusion growth from this study. A bifurcation of the protrusion as indicated by the current density distribution of Fig. 6.3a with the highest deposition rate at the perimeter to each side of the protrusion is not observed. This confirms the idea that the build-up of secondary tips is suppressed due to the electro-chemo-mechanical coupling and aligns with experiments which have shown no morphology change of the protrusion during charging [50, 182].³

The PEO material obeys a strong dependency of the growth speed on mechanical stiffness. This is in agreement with the results of Chapter 6 (Fig. 6.8b), where we have seen a characteristic change in stability at approximately $E = 100$ MPa. If the Young's modulus is smaller than $E = 100$ MPa, then the growth accelerates, if it is larger, then an

³ Note that repeated stripping and deposition can yield a porous structure in polymer electrolytes [50].

asymptotic limit will be reached eventually. Both the modification of the interface conductivity and the shortening of the transport path will then be balanced by the mechanical stress at the protrusion peak.

The deposition current has a maximum at the peak of the protrusion for all calculations and is hence different to the study of Chapter 6, which has shown a strong drop of the current density, partially even a stripping current, at the tip for high Young's moduli (see Fig. 6.3). The mechanical stresses in the soft electrolyte ($E = 10 \text{ MPa}$) are small and not able to lower the effective current density at the tip although the stress increases with protrusion depth. In fact, when the protrusion grows, the current densities increases at the peak of the protrusion, see Fig. 8.6a, which eventually leads to an acceleration of growth as seen e.g. in Fig. 8.4a for PEO and Fig. 8.9 for PS-PEO. If a Young's modulus above a critical value is chosen, then the variation of current density decreases while the protrusion is growing. This indicates a maximum height of the protrusion. The deposition rate at the tip equals the deposition rate at the flatter regions in this state. The protrusion growth is then stopped and a morphological stability is reached.

PS-PEO has this pattern at around $E = 500 \text{ MPa}$, which is slightly higher than the outcome of Chapter 6. However, the overall growth is small without a modification of K^{BV} , even for small Young's moduli, and a failure of the battery is not likely. This behavior changes when the electrochemical interface property such as K^{BV} is degraded. PS-PEO then shows a similar amplitude of the protrusion as the PEO electrolyte without interface degradation. This indicates that a decrease of bulk transport and an increase of interface properties decrease the likelihood of protrusion growth. The correlation of bulk and interface properties with respect to morphological stability will be analyzed in the next section.

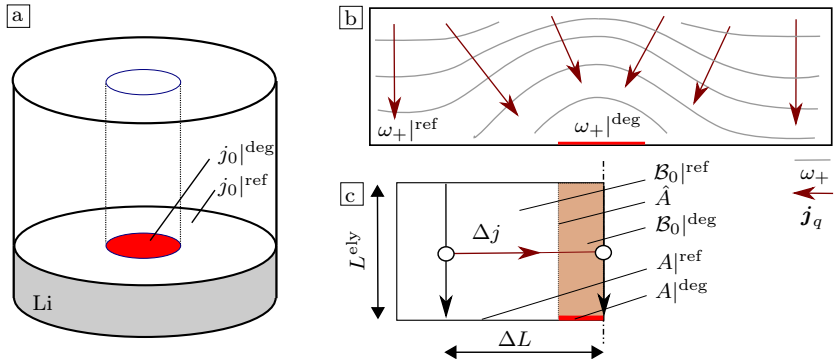


Figure 8.11: Problem description of the network model: (a) Axis symmetric section of an undeformed electrolyte-electrode system. The red area denotes a degraded interface between the electrode and electrolyte. (b) Sketch of the electrochemical potential ω_+ (isolines) and the current density in an electrolyte with degraded interfaces. (c) Idealized setting of ion transport in an electrolyte within a network model. The ions from the top are either transported directly through the bulk (vertical) or in-plane (horizontal) to the electrode.

8.4 An Analytical Assessment of Morphological Stability

We now want to rationalize the findings of the previous simulations such as the correlation of bulk and interface properties with the help of an analytical network model. We restrict the analysis to an undeformed geometry as shown in Fig. 8.11, where the exchange current density is degraded locally at the electrode-electrolyte interface (red area, see also Hypothesis 4 in Section 8.2.1). The undeformed geometry corresponds to the initial state of the deposition process in Section 8.3. In this state, mechanical effects such as stress driven diffusion or change of length of transport paths due to deformation are negligible and will not be taken into account.

Fig. 8.11b illustrates isolines of the electrochemical potential in the solid electrolyte as observed previously in Fig. 8.10b. The mass flux follows the gradient of ω_+ and is therefore perpendicular to the isolines. It is obvious that the in-plane contribution of the mass flux is directly related to the protrusion growth. The higher the current density in the in-plane direction, the more ions are transported into the degraded area and are thus deposited. This leads to the inhomogeneous growth and eventually to morphological instability. In the following, we approximate the continuous model of ion transport by a network model, separate the mass flux into a through-plane and an in-plane contribution in the region of the degraded area, see Fig. 8.11c, and deduce an expression for the harmful in-plane mass flux.

8.4.1 Network Model of Ion Transport

To derive an analytical expression for the in-plane contribution of the ion flux, we consider an electrolyte with a locally degraded interface to the metal electrode. The domain of the electrolyte above the degraded zone is denoted as $\mathcal{B}_0|^{\text{deg}}$ and the surrounding domain as $\mathcal{B}_0|^{\text{ref}}$, see Fig. 8.11c. A constant current density j^{app} is applied at the top (cathode side) and the current densities at the interface are denoted as $j^{\text{BV}}|^{\text{deg}}$ and $j^{\text{BV}}|^{\text{ref}}$ for the degraded and non-degraded areas, respectively. Due to the degradation, we postulate a current density in in-plane direction Δj which is defined to be positive in the direction from $\mathcal{B}_0|^{\text{ref}}$ to $\mathcal{B}_0|^{\text{deg}}$. Using the network model of Fig. 8.11c, we can now apply conservation of mass in the nodes and get

$$\begin{aligned} j^{\text{BV}}|^{\text{deg}} A|^{\text{deg}} &= j^{\text{app}} A|^{\text{deg}} + \hat{A} \Delta j \\ j^{\text{BV}}|^{\text{ref}} A|^{\text{ref}} &= j^{\text{app}} A|^{\text{ref}} - \hat{A} \Delta j \end{aligned} \tag{8.4}$$

with the degraded interface area $A|^{\text{deg}}$, the remaining interface area $A|^{\text{ref}}$ and the area of the cylindrical surface of $\mathcal{B}_0|^{\text{deg}}$ as \hat{A} . Eliminating the in-plane current $\hat{A}\Delta j$ in Eq. (8.4) yields

$$j^{\text{BV}}|^{\text{deg}} + aj^{\text{BV}}|^{\text{ref}} = j^{\text{app}}(1+a) \quad (8.5)$$

where $a = \frac{A|^{\text{ref}}}{A|^{\text{deg}}} = \frac{A|^{\text{tot}}}{A|^{\text{deg}}} - 1$. To obtain expressions for $j^{\text{BV}}|^{\text{deg}}$ and $j^{\text{BV}}|^{\text{ref}}$, we utilize a linearized version of the Butler-Volmer equation such as Eq. (5.66). The degraded interface has an exchange current density $j_0|^{\text{deg}}$. Otherwise, the exchange current density is $j_0|^{\text{ref}}$ which is proportional to K^{BV} , see Eq. (5.68). The electric potential of the electrode is given by $\Phi \approx 0$ (grounded). Furthermore, we consider a stress free state and thus have $V_{\omega_+}^{\text{eq}} = 0$. Eq. (5.69) then yields $\eta|^{\text{deg}} = -\omega_+|^{\text{deg}}$ and $\eta|^{\text{ref}} = -\omega_+|^{\text{ref}}$ and the two linearized Butler-Volmer equations are

$$\begin{aligned} j^{\text{BV}}|^{\text{deg}} &= -bj_0|^{\text{deg}}\omega_+|^{\text{deg}}, \\ j^{\text{BV}}|^{\text{ref}} &= -bj_0|^{\text{ref}}\omega_+|^{\text{ref}}, \end{aligned} \quad (8.6)$$

with $b = \frac{F}{R\Theta}$. They give a linear relationship between current densities and electrochemical potentials ω_+ . Combining Eq. (8.5) and Eq. (8.6) yields

$$j_0|^{\text{deg}}\omega_+|^{\text{deg}} + aj_0|^{\text{ref}}\omega_+|^{\text{ref}} = -j^{\text{app}}\frac{1+a}{b}. \quad (8.7)$$

Subtraction of $j_0|^{\text{deg}}\omega_+|^{\text{ref}}$ on both sides then gives

$$j_0|^{\text{deg}}(\omega_+|^{\text{deg}} - \omega_+|^{\text{ref}}) = -j^{\text{app}}\frac{1+a}{b} - (j_0|^{\text{deg}} + aj_0|^{\text{ref}})\omega_+|^{\text{ref}}. \quad (8.8)$$

In the next step we combine Eq. (8.4), Eq. (8.8) and the linearized Butler-Volmer equation (8.6) and obtain

$$\omega_+|^\text{deg} - \omega_+|^\text{ref} = \frac{1}{bj_0|^\text{ref}} \left(\chi j^\text{app} - (1 + (1 - \chi) a) \frac{\hat{A}}{A|^\text{ref}} \Delta j \right) \quad (8.9)$$

with $\chi = 1 - \frac{j_0|^\text{ref}}{j_0|^\text{deg}}$ as a measure for the interface inhomogeneity. For example, if the interface conductivity in the degraded zone is higher compared to the side, then $\chi > 0$. In the next step, we assume a linear potential drop in the in-plane direction of the electrolyte bulk and compute the in-plane current density as

$$\Delta j = -\kappa^\text{eff} \frac{\omega_+|^\text{ref} - \omega_+|^\text{deg}}{F\Delta L} \quad (8.10)$$

where κ^eff is the bulk conductivity and ΔL is a characteristic length between the $B_0|^\text{ref}$ and $B_0|^\text{deg}$. Inserting Eq. (8.9) in Eq. (8.10) yields

$$\Delta j = \frac{\kappa^\text{eff}}{F\Delta L b j_0|^\text{ref}} \left(\chi j^\text{app} - (1 + (1 - \chi) a) \frac{\hat{A}}{A|^\text{ref}} \Delta j \right). \quad (8.11)$$

Solving the implicit equation for Δj then yields

$$\boxed{\Delta j = \frac{\chi}{\frac{F\Delta L}{R\Theta} \frac{j_0|^\text{ref}}{\kappa^\text{eff}} + \frac{\hat{A}}{A|^\text{ref}} + \frac{\hat{A}(1-\chi)}{A|^\text{deg}}} j^\text{app}} \quad (8.12)$$

and thus gives the in-plane current Δj as a function of geometric properties, the interface conductivity $j_0|^\text{ref}$, the bulk conductivity κ^eff and the ratio $\chi = 1 - \frac{j_0|^\text{ref}}{j_0|^\text{deg}}$. Assuming a circular degraded zone of radius R^deg and

a height of the electrolyte of L^{ely} one can deduce $\frac{\hat{A}}{A|^{\text{deg}}} = \frac{2\pi R^{\text{deg}} L^{\text{ely}}}{\pi(R^{\text{deg}})^2} = \frac{2L^{\text{ely}}}{R^{\text{deg}}}$ and together with $\Delta L = dR^{\text{deg}}$ with $d > 1$ we finally obtain

$$\Delta j = \frac{\chi}{\frac{F}{R\Theta} R^{\text{deg}} d \frac{j_0|^{\text{ref}}}{\kappa^{\text{eff}}} + \frac{\hat{A}}{A|^{\text{ref}}} + \frac{2L^{\text{ely}}(1-\chi)}{R^{\text{deg}}}} j^{\text{app}} \quad (8.13)$$

as a second approximation of the in-plane current density.

8.4.2 Discussion

Eq. (8.12) is a first order approximation of the in-plane current density which describes the material transport into the degraded zone. In general, morphological instability is found for $\chi > 0$ which is equivalent to $j_0|^{\text{deg}} > j_0|^{\text{ref}}$. If the exchange current density is homogeneous, then a stable deposition is expected. If the degraded interface has a much higher interface conductivity, i.e. $\chi \rightarrow 1$, then protrusion growth is strongly promoted. In general, the higher the difference between the exchange current densities, the larger the protrusion growth. The applied current density j^{app} enters linearly and indicates higher morphological instability issues for higher current densities. The linear correlation aligns with the findings of the numerical study in Section 6.3.4.

Eq. (8.12) indicates a smaller in-plane flux for decreasing bulk conductivity κ^{eff} which is thus beneficial for morphological stability. Qualitatively speaking, a small bulk conductivity penalizes in-plane ion transport. Note that this finding does not contradict the result of Section 6.3.3, where an electrolyte with higher bulk conductivity showed lower requirements for mechanical stiffness (see e.g. Fig. 6.6). The study in Section 6.3.3 correlates bulk transport properties with mechanical properties on a deformed geometry, whereas the analysis of Eq. (8.12) deals with the initiation process. In other words, Eq. (8.12) determines the deposition growth at time $t = 0$ (e.g. the initial slope in Fig. 8.4) and not the growing pattern when a protrusion builds up ($t > 0$). However, both are

not decoupled as discussed in Section 6.3.5 (Fig. 6.8b), where a change of interface conductivity at the degraded interface also changes the requirements on mechanical stiffness. The analytical model and the simulations agree that a degraded zone with $j_0|^\text{deg} > j_0|^\text{ref}$ promote instability. Furthermore, the network models aligns with the numerical studies with the prediction that electrolytes with poorer electrochemical transport properties such as PS-PEO are more robust against inhomogeneous interface conductivities.

Another way to stabilize the system is to increase the reference interface conductivity $j_0|^\text{ref}$. In this case, the drop in electrochemical potential along the interface is smaller and thus the driving force for the in-plane current decreases. The ratio $\frac{j_0|^\text{ref}}{\kappa_\text{eff}}$ that is found in the denominator of Eq. (8.12) aligns with the findings of Section 8.3.2. In this study, we have observed almost the same protrusion growth for a system with PS-PEO (and an exchange current density decreased by a factor of ten) and for a system with PEO, which has roughly ten times better transport properties (see. Fig. 4.2.1). The analytical expression (8.12) confirms therefore that interface properties and bulk properties cannot be decoupled in a morphological stability analysis.

We further note that Eq. (8.13) indicates a decrease of Δj for thick electrolytes. This effect, although not very pronounced, was observed in the parameter study of Section 6.3.3 for $h > 50 \mu\text{m}$. For small thicknesses, the mechanical effects dominate. We further note that the in-plane current density vanishes for a small degraded area ($R^\text{deg} \rightarrow 0$) and a large degraded area ($R^\text{deg} \rightarrow \infty$).

8.5 Recap of the Coupling Mechanisms

The previous studies have shown several mechanisms which contribute to protrusion growth of a metal electrode in a solid state battery. In

what follows, the driving forces for protrusion growth are summarized and discussed.

In Section 6.2, we have seen that the overpotential η at the SEI is a key ingredient in understanding the difference in deposition rates along an interface. Recall from Eq. (5.58) and Eq. (5.61) that the overpotential consists of three components: the electrode potential Φ , the electrolyte potential ω_+ and the open circuit potential $V_{\omega_+}^{\text{eq}}$. The electrode potential, however, can be assumed to be constant due to the high electronic conductivity in the metal electrode. We assume that the electrode is grounded and thus set to $\Phi = 0$. The overpotential then reads

$$\eta = -(\omega_+^{\text{ely}} + V_{\omega_+}^{\text{eq}}). \quad (8.14)$$

Recall that a negative overpotential yields a deposition current. We emphasize that both the exchange current density j_0 and the overpotential determine the current density. In the following, we neglect the effect of the mechanical dependency of the exchange current density as we have seen in Section 6.2 that the overpotential is the dominant mechanism for inhomogeneous deposition. As shown in Fig. 8.7a and Fig. 8.10c, the electrochemical potential is almost constant at the counter electrode ($Y = L^{\text{ely}}$) although a protrusion growth is triggered. Therefore, we assume that the electrochemical potential at the separator-cathode interface $\omega_+|^{\text{top}}$ remains equal during protrusion growth. This also implies a constant current density $j^{\text{app}}|^{\text{top}}$.

Fig. 8.12 summarizes the effects which influence the overpotential and shall be discussed in the following. We consider the electrochemical and mechanical contributions on both ω_+ and $V_{\omega_+}^{\text{eq}}$. Quantitative statements with absolute values of the single effects would require knowledge of the material system, mechanical state, charging rate, etc. Therefore, this discussion shall serve as a qualitative study to gain an overview of the different mechanism and of which kind (stabilizing, destabilizing)

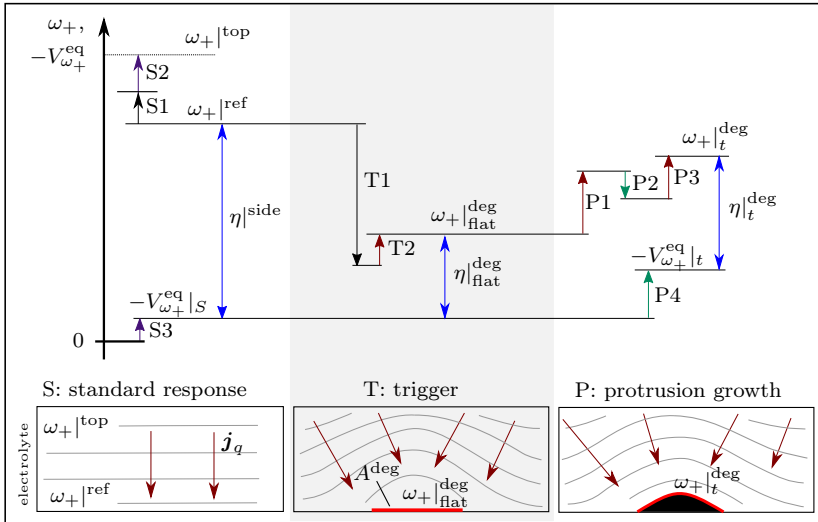


Figure 8.12: Processes that changes the electrochemical potential ω_+ and open circuit potential $V_{\omega+}^{eq}$ at the electrolyte-electrode interface clustered in three categories: Standard response (no inhomogeneity) in form of bulk conductivity (S1), concentration polarization in the bulk (S2) and at the interface (S3); Trigger mechanisms due to locally increased interface properties at area A^{deg} (T1) and in-plane current flux (T2); Protrusion growth yields pressure in the electrolyte (P1), stress driven diffusion (P2), change of transport paths (P3) and normal stress at the interface (P4). The color code of the arrows is as follows: Black (initial response when current is applied), purple (changes due to concentration polarization), red (destabilizing process), green (stabilizing process) and blue (overpotential of each condition).

they are. We cluster the effects in standard processes (S) specified by homogeneous ion transport, intermediate effects due to a trigger (T) and effects while protrusion growth (P).

We start with the standard processes due to ion-transport in a homogeneous electrolyte:

- S1: At the initial state after applying a current, there is a drop in electrochemical potential in the electrolyte due to Ohm's law inversely proportional to the ionic conductivity κ .
- S2: A concentration polarization occurs for a galvanostatic current as discussed in Section 4.4. The ionic conductivity then decreases (see discussion in Section 3.5.4), which increases the drop in electrochemical potential in the bulk.
- S3: The change of concentration also has an impact on swelling and osmotic pressure which eventually lead to mechanical stress. The open circuit potential $-V_{\omega_+}^{\text{eq}}|_S$ is therefore not zero anymore.

Note that these steps occur regardless whether the interface is degraded or not and are therefore not relevant to the considerations of morphological stability. This state now defines the overpotential $\eta|^{\text{side}}$ at a flat, not degraded interface.

As a trigger mechanism, we follow the previous findings and degrade the interface A^{deg} with an increase of interface conductivity:

- T1: A lower electrochemical potential is necessary to transfer the same amount of current (see discussion in Section 8.4).
- T2: The drop in ω_+ leads to a change of the ion transport path, see Fig. 8.10a. Following the highest decent, more ions will enter the area of A^{deg} , which ultimately leads to an increase of the current density in this region, see Eq. (8.12). The increase of current density results, however, in an increase of the overpotential, see e.g. Eq. (5.66). We denote this overpotential as $\eta|_{\text{flat}}^{\text{deg}}$ if the interface is still flat.

The increased current density at the degraded zone compared to side regions then leads to a protrusion growth, which affects the overpotential as follows:

- P1: The protrusion growth yields mechanical stresses in the solid electrolyte. The hydrostatic pressure p^M increases ω_+ due to Eq. (3.77) and influences the overpotential such that more deposition takes place at A^{deg} .
- P2: The hydrostatic pressure also has the effect that the ions are depleted in the region around the protrusion tip (see Section 4.5), which decreases ω_+ and therefore stabilizes the interface current density.
- P3: If the protrusion grows, the effective bulk conductivity increases due to a shorter transport path, which then promotes instability (see e.g. Fig. 8.8a).
- P4: Similar to the hydrostatic pressure of the electrolyte, we obtain positive normal stresses at the metal electrode. This lowers the open circuit potential $V_{\omega_+}^{\text{eq}}$, decreases the overpotential and is therefore a stabilizing effect.

Ultimately, if the material properties of a solid electrolyte are chosen such that $\eta|_t^{\text{deg}}$ at time t decreases with protrusion height, than the deposition current will also decrease and morphological stability might be reached. Ideally, only a small or even infinitesimal protrusion is required to equilibrate stabilizing and non-stabilizing effects. That might be the case for ceramic electrolytes, which are single-ion conductors. They do not feature the effects P1 and P2 due to the missing swelling mechanism. The stabilizing effect of P4 is then dominating even for small deformations.⁴ We refer to McMeeking et al. [91] and Klinsmann et al.

⁴ Ceramic electrolytes struggle, however, with lithium growth in grain boundaries.

[93] for a more detailed study of stability in ceramic electrolytes. The coupling mechanism in polymer electrolytes is, however, more complicated and showed to be very sensitive to small changes in mechanical stiffness as discussed in Section 6. Deducing morphological stability maps for these systems require therefore a comprehensive electro-chemo-mechanical formulation as presented in this thesis.

8.6 Summary

With the help of the comprehensive model of coupled ion transport, reaction kinetics, deposition and electrode response, we were able to model the growth of a protrusion in a binary solid electrolyte. We investigated within our continuum mechanical framework four different trigger mechanism which can cause harmful protrusion growth. The analysis indicates that a heterogeneous interface conductivity (modeled by a local increase of the exchange current density) is most likely to initiate a protrusion growth with a deposition rate big enough to penetrate the solid electrolyte. We studied the impact of the Young's modulus on the protrusion growth for the two parameterizations of the polymer electrolytes PEO and PS-PEO. Both showed a characteristic change of protrusion growth at $E = 100 \text{ MPa}$ and $E = 500 \text{ MPa}$, respectively, and align quite well with the results of Section 6.3.5. Below this value, we have seen an acceleration of growth whereas an asymptotic limit is indicated for higher Young's moduli. We have confirmed that the suppression mechanisms do not stem from a deformation of lithium but from a decrease of the interface current density for higher Young's moduli. Furthermore, the model indicates a self healing effect due to residual stresses after penetration. The influence of the mechanical stress on the open-circuit potential of the electrode-electrolyte interface leads to a

stripping current at the protrusion tip and deposition at the perimeter. This effect is more pronounced the higher the Young's modulus is. The simulation offered insights into the correlation of bulk transport properties and interface properties. With the reference interface conductivity used in this work, we observed only a small protrusion growth for PS-PEO. With a decrease of the interface conductivity, we could trigger a harmful protrusion growth again. This response could be confirmed by an analytical network model, which describes a required in-plane current density for protrusion growth as a function of inhomogeneity, geometry, applied current, bulk conductivity and exchange current density. According to this model, a low applied current, a low bulk conductivity, a high exchange current and a homogeneous exchange current density are all stabilizing. This aligns with the findings of Section 6.3.5, which states that PS-PEO is more robust against interface imperfections compared to PEO and of Section 6.3.4 which indicates a linear correlation of applied current and mechanical stiffness. Finally, we summarized the influence of the different coupling mechanism in a binary solid electrolyte on the morphological stability.

9 Conclusion and Outlook

The scope of this work was the development of a model for a polymer based solid state battery with a metal electrode in order to get insights into the morphological interface stability that is a major concern in this kind of next generation energy storage system. We presented therefore

- a transport theory tailored for binary solid electrolytes,
- a theory for reaction kinetics including mechanical effects,
- a description of deposition and stripping for metal electrodes.

The novel transport model combines the idea of finite strain continuum mechanics and the widely utilized electrochemical description of batteries, namely the concentrated solution theory. Herein, both anions and cations are mobile and, during charge and discharge, form a concentration gradient along the electrolyte. Besides migration and diffusion, we considered stress driven diffusion in the binary solid electrolyte, a direct consequence of swelling of the host material. Using the electroneutral limit we identified the required input parameter by those accessible by experiments. The electro-chemo-mechanical coupling mechanism were discussed using several exemplary simulations.

Another important aspect of this work is the assessment of the influence of mechanics on the reaction kinetics between a solid electrolyte and a metal electrode. Following the concept of transition state theory, we elaborated the influence of mechanical stress on the electrochemical equilibrium (Nernst equation) and non-equilibrium (Butler-Volmer equation). The generic concept using energetic states of electrode, electrolyte and energy barrier is able to describe a broad range of interface combinations consistent with literature. We put a special focus on a metal electrode

where the normal stress, not the hydrostatic stress, was shown to be the variable of interest for the thermodynamics of deposition and stripping.

The third aspect required to model a solid state battery is a consistent description of the metal electrode. Cations are deposited on and stripped from the metal electrode and therefore we introduced (in addition to the deformation map) a second mapping describing the stress free change of material shape. With the formulation of a compatible interface between solid electrolyte and metal electrode, we have gathered all elements to describe a solid state battery.

In this work, we have carefully analyzed the morphological stability of a binary solid state battery to determine the impact of transport properties and mechanical stiffness on the likelihood of undesired protrusion growth. We were able to conclude that

- an electrolyte with higher mechanical stiffness is in general more prone to morphological stability.
- at the same time, an electrolyte with better bulk transport properties has less requirement on the Young's modulus.
- the influence of mechanical stress on electrochemistry causes stability and not, as widely believed, a purely mechanical push down.
- instabilities are most likely caused by inhomogeneous interface properties such as the interface conductivity.
- materials with better bulk transport properties are more sensitive to inhomogeneous interface properties.

We executed two studies on morphological interface stability. The first assessment assumed an infinitely stiff electrode penetrating the solid electrolyte. Varying the Young's modulus led to a characteristic change of the current density along the deformed interface. Above a critical Young's modulus, the current density at the tip was below average which we interpreted as stable. Several parameter studies showed that an increase of transport parameters (by means of diffusivity, conductivity or

transference number) lowers the requirement on the mechanical stiffness. The predictions of the required Young's moduli for PEO and PS-PEO electrolytes align with experimental findings.

With the second study on morphological interface stability, we explicitly modeled the material deposition during charging. We found that protrusion growth is most likely caused by an inhomogeneous interface conductivity. Again, we observed a lower deposition rate for stiffer electrolytes. This is caused by a decrease of the interface current density rather than a push down effect of the metal electrode. There is a transition of accelerated to decelerated growth at approximately the same Young's modulus as predicted by the first study. Furthermore, we rationalized findings of the numerical simulations with an analytical network model namely that solid electrolytes with poor transport properties are more robust against inhomogeneous interface conductivity.

In conclusion, we have seen that a polymer based electrolyte with a certain balance of stiffness and electrochemical transport properties in combination with a sufficiently homogeneous interface conductivity is a promising concept to enable stable lithium metal electrodes.

The presented model of a solid state battery can be extended by various aspects. One should overcome the assumption of pure elastic response and use an elastic-visoplastic material model as recently parametrized for lithium metal [178]. In the same course, an adequate material model for the solid electrolyte going beyond an elastic stability analysis is needed. Further, anisotropy of electrolytes such as PS-PEO with a laminar structure [45, 57] and the metal electrodes [14] should be examined. Depending on the charge-discharge profiles, different protrusion morphologies were observed by Harry et al. [50] and should be investigated further.

A Nomenclature

Kinematics

[material frame; spatial frame; unit; first appearance; description]

t	s	Eq. (2.1)	time
T	s	Eq. (2.1)	time domain
φ_t	m	Eq. (2.1)	mapping from material to spatial frame
V_0	$\frac{m}{s}$	Eq. (2.2)	host velocity
V_α	$\frac{m}{s}$	Eq. (2.14)	velocity of species α
\mathbf{X}	\mathbf{x}	m	spatial coordinate
$\text{Grad}(\cdot)$	$\text{grad}(\cdot)$	$\frac{1}{m}$	gradient operator
$\text{Div}(\cdot)$	$\text{div}(\cdot)$	$\frac{1}{m}$	divergence operator
\mathbf{N}	\mathbf{n}	1	normal vector
\mathbf{T}	\mathbf{t}	1	tangent vector
dV	dv	m^3	volume element
dV_0	dv_0	m^3	volume element of the host
dA	da	m^2	area element
\mathcal{P}_0	\mathcal{P}_t	Eq. (2.7)	control volume w.r.t. to the host
	\mathcal{P}_t^α	Eq. (2.12)	control volume w.r.t. species α
$\partial\mathcal{P}_0$	$\partial\mathcal{P}_t$	Eq. (2.7)	surface of control volume \mathcal{P}_0
\mathcal{B}_0	\mathcal{B}_t	Eq. (2.1)	body of the host material
	\mathbf{u}	m	displacement vector
\mathbf{F}	1	Eq. (2.3)	deformation gradient
\mathbf{R}, \mathbf{U}	1	Eq. (2.5)	rotation and right stretch tensor
\mathbb{J}	1	Eq. (2.4)	Jacobian of deformation gradient
$\mathbf{F}_e, \mathbf{F}_s$	1	Eq. (3.51)	elastic and swelling part of \mathbf{F}
$\mathbb{J}_e, \mathbb{J}_s$	1	Eq. (3.52)	elastic and swelling part of \mathbb{J}

Kinematics

[material frame; spatial frame; unit; first appearance; description]

Y	y	Eq. (2.7)	scalar or vector field
\tilde{Y}	\tilde{y}	Eq. (2.7)	vector field defined on a surface
\hat{Y}	\hat{y}	Eq. (2.9)	scalar quantity defined on a surface
I	1		identity matrix
w	1	Eq. (4.4)	Wendland function

Kinematics of Deposition and Stripping

[symbol; unit; first appearance; description]

ζ_t^{etr}	m	Eq. (7.2)	mapping from geometry to material frame
X_g	m	Eq. (7.2)	geometric coordinate
d	m	Page 163	geometry displacement field
\tilde{B}_t^{etr}		Eq. (7.2)	body describing geometry change but no deformation
S_t		Eq. (7.5)	deformed interface between electrode and electrolyte

Fields [Mechanics]

[material frame; spatial frame; unit; first appearance; description]

\mathbf{B}_α^M	\mathbf{b}_α^M	$\frac{\text{N}}{\text{m}^3}$	Eq. (3.16)	mechanical body forces
\mathbf{B}_α^E	\mathbf{b}_α^E	$\frac{\text{N}}{\text{m}^3}$	Eq. (3.16)	electrical body forces
\mathbf{B}_α^C	\mathbf{b}_α^C	$\frac{\text{N}}{\text{m}^3}$	Eq. (3.16)	chemical body forces
\mathbf{B}_α^V		$\frac{\text{N}}{\text{m}^3}$	Eq. (3.17)	body force w/r to component inertia
$\tilde{\mathbf{B}}_\alpha$		$\frac{\text{N}}{\text{m}^3}$	Page 38	extended specific body force
\mathbf{T}^M	\mathbf{t}^M	$\frac{\text{N}}{\text{m}^2}$	Eq. (3.16)	mechanical traction force
\mathbf{T}^E	\mathbf{t}^E	$\frac{\text{N}}{\text{m}^2}$	Eq. (3.16)	electrical traction force
\mathbf{T}^C	\mathbf{t}^C	$\frac{\text{N}}{\text{m}^2}$	Eq. (3.16)	chemical traction force

Fields [Mechanics]

[material frame; spatial frame; unit; first appearance; description]

\mathbf{P}	$\boldsymbol{\sigma}$	$\frac{\text{N}}{\text{m}^2}$	Eq. (3.19)	total Piola & Cauchy stress tensor
\mathbf{P}^M		$\frac{\text{N}}{\text{m}^2}$	Eq. (3.19)	mechanical Piola stress tensor
\mathbf{P}^E		$\frac{\text{N}}{\text{m}^2}$	Eq. (3.70)	Maxwell stress tensor
\mathbf{P}^C	$\boldsymbol{\sigma}^C$	$\frac{\text{N}}{\text{m}^2}$	Eq. (3.70)	stress tensor due to chemical forces
	σ_n^{etr}	$\frac{\text{N}}{\text{m}^2}$	Eq. (5.39)	normal compressive Cauchy stress
	$\boldsymbol{\sigma}^d$	$\frac{\text{N}}{\text{m}^2}$	Eq. (5.54)	deviatoric Cauchy stress tensor
	p	$\frac{\text{N}}{\text{m}^2}$	Page 50	total hydrostatic pressure
	p^M	$\frac{\text{N}}{\text{m}^2}$	Eq. (3.77)	pressure due to mechanical strain
	p^C	$\frac{\text{N}}{\text{m}^2}$	Eq. (3.119)	osmotic pressure
	\mathcal{L}	$\frac{\text{J}}{\text{m}^2}$	Eq. (3.21)	angular momentum
	\mathcal{M}	$\frac{\text{N}}{\text{m}}$	Eq. (3.21)	total torque
$\mathbb{I}_1, \mathbb{I}_2, \mathbb{I}_3$		1	Eq. (3.66)	invariants of \mathbf{F}
$\xi_\alpha^c, \xi_\alpha^p, \xi_\alpha^{J_c}$		1	Eq. (3.101)	prefactors defined in Eq. (3.102)
λ^S		1	Eq. (3.62)	parameter from swelling model
Θ		K	Eq. (3.40)	absolute temperature

Fields [Electrochemistry]

[material frame; spatial frame; unit; first appearance; description]

N_α	mol		Eq. (2.13)	amount of atoms of species α
N	1		Page 27	number of species
c_α^\diamond	c_α	$\frac{\text{mol}}{\text{m}^3}$	Eq. (2.13)	concentration of species α
ρ_α^\diamond	ρ_α	$\frac{\text{kg}}{\text{m}^3}$	Eq. (3.1)	partial mass density
ρ_{tot}^\diamond	ρ_{tot}	$\frac{\text{kg}}{\text{m}^3}$	Eq. (3.3)	total mass density
$\rho_{q_\alpha}^\diamond$	ρ_{q_α}	$\frac{\text{As}}{\text{m}^3}$	Eq. (3.4)	partial charge density
ρ_q^\diamond	ρ_q	$\frac{\text{As}}{\text{m}^3}$	Eq. (3.5)	total charge density
\mathbf{J}_α	\mathbf{j}_α	$\frac{\text{mol}}{\text{m}^2 \text{s}}$	Eq. (2.15)	total molar flux of species α

Fields [Electrochemistry]

[material frame; spatial frame; unit; first appearance; description]

$\mathbf{J}_{q\alpha}$		$\frac{\text{A}}{\text{m}^2}$	Eq. (3.10)	charge flux of species α
$\mathbf{J}_\alpha^E, \mathbf{J}_\alpha^C$		$\frac{\text{mol}}{\text{m}^2 \text{s}}$	Eq. (3.93)	electric and chemical part of \mathbf{J}_α
\mathbf{J}_{tot}	\mathbf{j}_{tot}	$\frac{\text{mol}}{\text{m}^2 \text{s}}$	Eq. (3.9)	total mass flux
\mathbf{J}_q	\mathbf{j}_q	$\frac{\text{A}}{\text{m}^2}$	Eq. (3.95)	total ionic current density
$\mathbf{J}_q^E, \mathbf{J}_q^C$		$\frac{\text{A}}{\text{m}^2}$	Eq. (3.96)	electric and chemical part of \mathbf{J}_q
$(\mathbf{J}_q)^{\text{SS}}$		$\frac{\text{A}}{\text{m}^2}$	Eq. (3.120)	steady state current density
R_α	r_α	$\frac{\text{mol}}{\text{m}^3 \text{s}}$	Eq. (3.7)	concentration sink or source
$R_{q\alpha}$	$r_{q\alpha}$	$\frac{\text{A s}}{\text{m}^3 \text{s}}$	Eq. (3.10)	charge source
\mathbb{D}	\mathbf{d}	$\frac{\text{A s}}{\text{m}^2}$	Eq. (3.11)	electric displacement
\mathbb{E}	\mathbf{e}	$\frac{\text{V}}{\text{m}}$	Eq. (3.12)	electric field
\mathbb{P}	\mathbf{p}	$\frac{\text{A s}}{\text{m}^2}$	Eq. (3.13)	electric polarization
ω^{SC}		$\frac{\text{A s}}{\text{m}^2}$	Page 30	surface charge
R^H	r^H	$\frac{\text{J}}{\text{m}^3 \text{s}}$	Eq. (3.33)	heat source
\mathbf{J}^H	\mathbf{j}^H	$\frac{\text{J}}{\text{m}^2 \text{s}}$	Eq. (3.33)	heat flux
$E^{\text{int}}, E^{\text{kin}}$	J	J	Eq. (3.29)	internal and kinetic energy
L^M, L^H, L^E		$\frac{\text{J}}{\text{s}}$	Eq. (3.29)	power supply due to mechanics, heat and electrostatic
e_α		$\frac{\text{J}}{\text{kg}}$	Eq. (3.30)	specific internal energy of species α
$\tilde{\psi}$		$\frac{\text{J}}{\text{m}^3}$	Eq. (3.42)	total Helmholtz energy
ψ_α		$\frac{\text{J}}{\text{kg}}$	Eq. (3.42)	specific Helmholtz energy
$\tilde{\psi}^M, \tilde{\psi}^E, \tilde{\psi}_\alpha^C$		$\frac{\text{J}}{\text{m}^3}$	Eq. (3.63)	mech., elec. and chem. part of $\tilde{\psi}$
η_α		$\frac{\text{J K}}{\text{kg}}$	Eq. (3.40)	specific entropy of species α
δ_V		$\frac{\text{J}}{\text{m}^3 \text{s}}$	Eq. (3.40)	dissipation density
μ_α		$\frac{\text{J}}{\text{mol}}$	Eq. (3.44)	chemical potential of species α
$\mu_\alpha^C, \mu_\alpha^M$		$\frac{\text{J}}{\text{mol}}$	Eq. (3.77)	chemical and mechanical part of μ_α
Φ		V	Eq. (3.12)	electric potential
ω_α		$\frac{\text{J}}{\text{mol}}$	Eq. (3.50)	electrochemical potential of species α

Interface Kinetics

[symbol; unit; first appearance; description]

j^{BV}	$\frac{\text{A}}{\text{m}^2}$	Eq. (5.2)	current density by Butler-Volmer kinetics
$k^{\text{etr}}, k^{\text{ely}}$	$\frac{\text{A m}}{\text{mol}}$	Eq. (5.2)	rate constant
j_0	$\frac{\text{A}}{\text{m}^2}$	Eq. (5.25)	exchange current density
j_{00}	$\frac{\text{A}}{\text{m}^2}$	Eq. (5.24)	prefactor in exchange current density
j_{00}^{ref}	$\frac{\text{A}}{\text{m}^2}$	Eq. (5.41)	reference value of exchange current density
$\overrightarrow{j}, \overleftarrow{j}$	$\frac{\text{A}}{\text{m}^2}$	Eq. (5.20)	anodic and cathodic current
V_{Φ}^{eq}	V	Page 116	open circuit potential w.r.t. Φ
$V_{\omega_+}^{\text{eq}}$	V	Eq. (5.58)	open circuit potential w.r.t. ω_+
η	V	Eq. (5.29)	overpotential
G	$\frac{\text{J}}{\text{mol}}$	Eq. (5.2)	molar Gibbs energy
G^\ddagger	$\frac{\text{J}}{\text{mol}}$	Eq. (5.13)	energy barrier
β	1	Eq. (5.2)	symmetry coefficient
δ_k	1	Eq. (5.13)	prefactor to relate barrier and bulk energies
G_{Φ}	$\frac{\text{J}}{\text{mol}}$	Eq. (5.14)	molar Gibbs energy incl. electric potential
$\overrightarrow{r}, \overleftarrow{r}$	$\frac{1}{\text{s}}$	Eq. (5.18)	success frequency of forward/reverse reaction
c^S	mole/m^2	Eq. (5.20)	area density
Ψ^{dp}	$\frac{\text{J}}{\text{mol}}$	Eq. (5.40)	energy due to deposition and stripping
α^M	1	Eq. (5.63)	symmetry coefficient (mechanics)
R_{BV}	$\frac{\Omega}{\text{m}^2}$	Eq. (5.67)	interface resistance
K^{BV}	$\frac{\text{A}}{\sqrt{\text{m mol}}}$	Eq. (5.68)	prefactor for metal electrodes

Parameter

[material frame; spatial frame; unit; first appearance; description]

M_α		$\frac{\text{kg}}{\text{mol}}$	Eq. (3.1)	molar mass of species α
Ω_α		$\frac{\text{m}^3}{\text{mol}}$	Eq. (3.54)	molar volume of species α
$\hat{\Omega}_\alpha$		$\frac{\text{m}^3}{\text{mol}}$	Eq. (3.54)	molar volume of species α (deformed)
β^s		1	Eq. (3.61)	factor to account for non-ideality in swelling
z_α		1	Eq. (3.4)	charge number
ϵ_r^\diamond	ϵ_r	1	Eq. (3.13)	relative electric permittivity
c_α^{ref}		$\frac{\text{mol}}{\text{m}^3}$	Page 44	reference concentration
$\mathbf{M}_{\alpha\beta}^\diamond$	$\mathbf{M}_{\alpha\beta}$	$\frac{\text{mol}^2}{\text{m J s}}$	Eq. (3.80)	mobility matrix between species α and β
$\mathbf{M}_+^\diamond, \mathbf{M}_-^\diamond$	$\mathbf{M}_+, \mathbf{M}_-$	$\frac{\text{mol}^2}{\text{m J s}}$	Eq. (3.103)	mobility of cation and anion
\mathbf{M}_\pm^\diamond	\mathbf{M}_\pm	$\frac{\text{mol}^2}{\text{m J s}}$	Eq. (3.103)	cross mobility
$\mathbf{M}_{\text{amb}}^\diamond$		$\frac{\text{mol}^2}{\text{m J s}}$	Eq. (3.109)	ambipolar mobility matrix
$K_{\alpha\beta}, \tilde{K}_{\alpha\beta}$		J m	Eq. (3.88)	drag coefficient
	f_α	1	Eq. (3.69)	fugacity or activity coefficient
	$1 + \frac{\partial \ln f_\pm}{\partial \ln c}$	1	Eq. (3.118)	thermodynamic factor
κ^\diamond	κ	$\frac{1}{\Omega \text{m}}$	Eq. (3.96)	ionic conductivity
$(\kappa^\diamond)^{\text{SS}}$	$(\kappa)^{\text{SS}}$	$\frac{1}{\Omega \text{m}}$	Eq. (3.120)	steady state conductivity
κ_α^\diamond		$\frac{\text{mol}}{\text{V s m}}$	Eq. (3.93)	mass conductivity
t_α^\diamond	t_α	1	Eq. (3.97)	transference number
D^\diamond	D	$\frac{\text{m}^2}{\text{s}}$	Eq. (3.116)	diffusion coefficient
	Ne	1	Eq. (3.125)	Newman number
$\gamma_{\text{NH}}, \lambda_{\text{NH}}$		$\frac{\text{J}}{\text{m}^3}$	Eq. (3.66)	lamé constants
E, G		MPa	Eq. (3.68)	Young's and shear modulus
ν		1	Eq. (3.68)	Poisson ratio
A^P		meter	Page 94	amplitude of protrusion
R^P		meter	Page 94	radius of protrusion
λ		1	Eq. (6.5)	amplitude of heterogeneity

Macroscopic Properties

[symbol; unit; first appearance; description]

\mathbb{F}	N	Eq. (5.32)	force
W_1, W_2	J	Eq. (5.32)	potential energy (total)
ΔE	J	Eq. (5.35)	electrochemical energy (total)
A	m^2	Eq. (5.35)	electrode-electrolyte interface area
m_{Li}	kg	Eq. (7.9)	mass of the electrode

Network Model

[symbol; unit; first appearance; description]

Δj	$\frac{A}{m^2}$	Eq. (8.4)	in-plane current density
$A ^\text{deg}$	m^2	Eq. (8.4)	cylindrical surface of degraded zone
a	1	Eq. (8.5)	ratio of reference and degraded area
b	$\frac{1}{V}$	Eq. (8.6)	prefactor
χ	1	Eq. (8.9)	measure for interface resistance inhomogeneity
d	1	Eq. (8.13)	prefactor

Constants

[symbol; value; unit; first appearance; description]

F	964885	$\frac{As}{mol}$	Eq. (3.4)	Faraday constant
ϵ_0	$8.854 \cdot 10^{-12}$	$\frac{F}{m}$	Eq. (3.13)	electric permittivity of vacuum
k_B	$1.38 \cdot 10^{-23}$	$\frac{J}{K}$	Eq. (5.18)	Boltzmann constant
h	$6.626 \cdot 10^{-34}$	Js	Eq. (5.18)	Planck constant
R	8.314	$\frac{J}{K \cdot mol}$	Eq. (3.69)	universal gas constant

Indices

etr	electrode	.	iso	isotropic
ely	electrolyte		ref	reference
M	metal		eff	effective
+	Cation		PEO	poly(ethylene oxide)
-	Anion		PS-PEO	block copolymer
BIC	Binary conducting	BV		Butler-Volmer
ME	Metal electrode	app		applied
AP	Active particle	dep		deposition

Bibliography

- [1] M. S. Whittingham. Electrical Energy Storage and Intercalation Chemistry. *Science*, 192(4244):1126–1127, 1976.
- [2] Dingchang Lin, Yayuan Liu, and Yi Cui. Reviving the Lithium Metal Anode for High-Energy Batteries. *Nature Nanotechnology*, 12(3):194–206, 2017.
- [3] Statista. Number of Mobile Phone Users Worldwide from 2015 to 2020 (in Billions).
<https://www.statista.com/statistics/274774/forecast-of-mobile-phone-users-worldwide/> (visited 12/16/2018), 2018.
- [4] James Manyika, Michael Chui, Peter Bisson, Jonathan Woetzel, Richard Dobbs, Jacques Bughin, and Dan Aharon. The Internet of Things: Mapping the Value Beyond the Hype. Technical report, McKinsey Global Institute, 2015.
- [5] Axel Thielmann, Andreas Sauer, Ralf Isenmann, and Martin Wietschel. Technology Roadmap Energy Storage for Electric Mobility 2030. Technical report, Fraunhofer Institute for Systems and Innovation Research, Karlsruhe, 2012.
- [6] Philip Oltermann. Hamburg Becomes First German City to Ban Older Diesel Cars. *The Guardian*,
<https://www.theguardian.com/world/2018/may/23/hamburg-first-german-city-ban-older-diesel-cars-air-quality-pollution> (visited 12/02/2018), 2018.
- [7] Campagnol, Nicolo, Eddy, James, Hagenbruch, Toralf, Klip, Diederik, Mulligan, Chris, and van de Staaij, Jasper. Metal mining

- constraints on the electric mobility horizon. Technical report, MineSpans by McKinsey, 2018.
- [8] BBC. Samsung Confirms Battery Faults as Cause of Note 7 Fires. <https://www.bbc.com/news/business-38714461> (visited 12/03/2018), 2017.
 - [9] PHYS.ORG. US Investigating Battery Fire in Fatal Tesla Crash. <https://phys.org/news/2018-05-battery-fatal-tesla.html> (visited 12/02/2018), 2018.
 - [10] Xin-Bing Cheng, Rui Zhang, Chen-Zi Zhao, and Qiang Zhang. Toward Safe Lithium Metal Anode in Rechargeable Batteries: A Review. *Chemical Reviews*, 117(15):10403–10473, 2017.
 - [11] Ryan P Schultz. Lithium: Measurement of Young’s Modulus and Yield Strength. Technical Report FERMILAB-TM-2191, 804180, 2002. DOI: 10.2172/804180.
 - [12] S. Tariq, P. Hurh, R. Schultz, P. Liu, and J. Shang. Li Material Testing- Fermilab Antiproton Source Lithium Collection Lens. In *Proceedings of the 2003 IEEE Particle Accelerator Conference*, pages 1452–1454, Portland, OR, United States, 2003.
 - [13] Alvaro Masias, Nando Felten, Regina Garcia-Mendez, Jeff Wolfenstine, and Jeff Sakamoto. Elastic, plastic, and creep mechanical properties of lithium metal. *Journal of Materials Science*, 54(3):2585–2600, 2019.
 - [14] Chen Xu, Zeeshan Ahmad, Asghar Aryanfar, Venkatasubramanian Viswanathan, and Julia R. Greer. Enhanced Strength and Temperature Dependence of Mechanical Properties of Li at Small Scales and Its Implications for Li Metal Anodes. *Proceedings of the National Academy of Sciences*, 114(1):57–61, 2017.
 - [15] Yikai Wang and Yang-Tse Cheng. A Nanoindentation Study of the Viscoplastic Behavior of Pure Lithium. *Scripta Materialia*, 130: 191–195, 2017.

- [16] Kevin N. Wood, Eric Kazyak, Alexander F. Chadwick, Kuan-Hung Chen, Ji-Guang Zhang, Katsuyo Thornton, and Neil P. Dasgupta. Dendrites and Pits: Untangling the Complex Behavior of Lithium Metal Anodes through Operando Video Microscopy. *ACS Central Science*, 2(11):790–801, 2016.
- [17] Akihiro Kushima, Kang Pyo So, Cong Su, Peng Bai, Nariaki Kuriyama, Takanori Maebashi, Yoshiya Fujiwara, Martin Z. Bazant, and Ju Li. Liquid Cell Transmission Electron Microscopy Observation of Lithium Metal Growth and Dissolution: Root Growth, Dead Lithium and Lithium Flotsams. *Nano Energy*, 32: 271–279, 2017.
- [18] Peng Bai, Ju Li, Fikile R. Brushett, and Martin Z. Bazant. Transition of Lithium Growth Mechanisms in Liquid Electrolytes. *Energy Environ. Sci.*, 9:3221–3229, 2016.
- [19] Jens Steiger, Dominik Kramer, and Reiner Mönig. Mechanisms of Dendritic Growth Investigated by in Situ Light Microscopy During Electrodeposition and Dissolution of Lithium. *Journal of Power Sources*, 261:112–119, 2014.
- [20] Rui Zhang, Nian-Wu Li, Xin-Bing Cheng, Ya-Xia Yin, Qiang Zhang, and Yu-Guo Guo. Advanced Micro/Nanostructures for Lithium Metal Anodes. *Advanced Science*, 4(3):1600445, 2017.
- [21] Jialiang Lang, Longhao Qi, Yuzi Luo, and Hui Wu. High Performance Lithium Metal Anode: Progress and Prospects. *Energy Storage Materials*, 7:115–129, 2017.
- [22] T. Nishida, K. Nishikawa, M. Rosso, and Y. Fukunaka. Optical Observation of Li Dendrite Growth in Ionic Liquid. *Electrochimica Acta*, 100:333–341, 2013.
- [23] Kian Kerman, Alan Luntz, Venkatasubramanian Viswanathan, Yet-Ming Chiang, and Zhebo Chen. Review—Practical Challenges Hindering the Development of Solid State Li Ion Batteries. *Journal of The Electrochemical Society*, 164(7):A1731–A1744, 2017.

- [24] John B. Goodenough and Preetam Singh. Review—Solid Electrolytes in Rechargeable Electrochemical Cells. *Journal of The Electrochemical Society*, 162(14):A2387–A2392, 2015.
- [25] Jürgen Janek and Wolfgang G. Zeier. A Solid Future for Battery Development. *Nature Energy*, 1(9):16141, 2016.
- [26] Atsushi Sakuda, Akitoshi Hayashi, and Masahiro Tatsumisago. Sulfide Solid Electrolyte with Favorable Mechanical Property for All-Solid-State Lithium Battery. *Scientific Reports*, 3(1):2261, 2013.
- [27] Feng Zheng, Masashi Kotobuki, Shufeng Song, Man On Lai, and Li Lu. Review on Solid Electrolytes for All-Solid-State Lithium-Ion Batteries. *Journal of Power Sources*, 389:198–213, 2018.
- [28] Lukas Porz, Tushar Swamy, Brian W. Sheldon, Daniel Rettenwander, Till Frömling, Henry L. Thaman, Stefan Berendts, Reinhard Uecker, W. Craig Carter, and Yet-Ming Chiang. Mechanism of Lithium Metal Penetration through Inorganic Solid Electrolytes. *Advanced Energy Materials*, 7(20):1701003, 2017.
- [29] Yasuo Takeda, Osamu Yamamoto, and Nobuyuki Imanishi. Lithium Dendrite Formation on a Lithium Metal Anode from Liquid, Polymer and Solid Electrolytes. *Electrochemistry*, 84(4): 210–218, 2016.
- [30] C. Brissot, M. Rosso, J.-N. Chazalviel, and S. Lascaud. Dendritic Growth Mechanisms in Lithium/Polymer Cells. *Journal of Power Sources*, 81-82:925–929, 1999.
- [31] Katherine J. Harry, Kenneth Higa, Venkat Srinivasan, and Nitash P. Balsara. Influence of Electrolyte Modulus on the Local Current Density at a Dendrite Tip on a Lithium Metal Electrode. *Journal of The Electrochemical Society*, 163(10):A2216–A2224, 2016.
- [32] Wu Xu, Jiulin Wang, Fei Ding, Xilin Chen, Eduard Nasybulin, Yaohui Zhang, and Ji-Guang Zhang. Lithium metal anodes for

- rechargeable batteries. *Energy Environ. Sci.*, 7(2):513–537, 2014.
- [33] D. T. Hallinan, S. A. Mullin, G. M. Stone, and N. P. Balsara. Lithium Metal Stability in Batteries with Block Copolymer Electrolytes. *Journal of the Electrochemical Society*, 160(3):A464–A470, 2013.
- [34] C Brissot, M Rosso, J.-N Chazalviel, and S Lascaud. Concentration Measurements in Lithium/Polymer-Electrolyte/Lithium Cells During Cycling. *Journal of Power Sources*, 94(2):212–218, 2001.
- [35] Michel Rosso, Claire Brissot, Anna Teyssot, Mickaël Dollé, Lucas Sannier, Jean-Marie Tarascon, Renaud Bouchet, and Stéphane Lascaud. Dendrite Short-Circuit and Fuse Effect on Li/Polymer/Li Cells. *Electrochimica Acta*, 51(25):5334–5340, 2006.
- [36] MengXuan Tang, Hui Wang, Yong-Gun Lee, Yasuo Takeda, Osamu Yamamoto, Jiaqiang Xu, Anbao Yuan, and Nobuyuki Imanishi. Electrochemical and Mechanical Properties of Polyolefin Hard Segment with Polyethylene Oxide Conductive Phase Block Copolymers. *Solid State Ionics*, 289:188–193, 2016.
- [37] D. Golodnitsky, E. Strauss, E. Peled, and S. Greenbaum. Review—On Order and Disorder in Polymer Electrolytes. *Journal of The Electrochemical Society*, 162(14):A2551–A2566, 2015.
- [38] Weimin Wang, Eongyu Yi, Anthony J. Fici, Richard M. Laine, and John Kieffer. Lithium Ion Conducting Poly(ethylene oxide)-Based Solid Electrolytes Containing Active or Passive Ceramic Nanoparticles. *The Journal of Physical Chemistry C*, 121(5):2563–2573, 2017.
- [39] Rachna Khurana, Jennifer L. Schaefer, Lynden A. Archer, and Geoffrey W. Coates. Suppression of Lithium Dendrite Growth Using Cross-Linked Polyethylene/Poly(ethylene oxide) Electrolytes: A New Approach for Practical Lithium-Metal Polymer Batteries. *Journal of the American Chemical Society*, 136

- (20):7395–7402, 2014.
- [40] Kuirong Deng, Jiaxiang Qin, Shuanjin Wang, Shan Ren, Dongmei Han, Min Xiao, and Yuezhong Meng. Effective Suppression of Lithium Dendrite Growth Using a Flexible Single-Ion Conducting Polymer Electrolyte. *Small*, 14(31):1801420, 2018.
- [41] Qi Zheng, Lin Ma, Rachna Khurana, Lynden A. Archer, and Geoffrey W. Coates. Structure–Property Study of Cross-Linked Hydrocarbon/Poly(ethylene Oxide) Electrolytes with Superior Conductivity and Dendrite Resistance. *Chem. Sci.*, 7(11):6832–6838, 2016.
- [42] Haiping Wu, Yue Cao, Haiping Su, and Chao Wang. Tough Gel Electrolyte Using Double Polymer Network Design for the Safe, Stable Cycling of Lithium Metal Anode. *Angewandte Chemie*, 130(5):1375–1379, 2018.
- [43] Anthony J. D’Angelo and Matthew J. Panzer. Decoupling the Ionic Conductivity and Elastic Modulus of Gel Electrolytes: Fully Zwitterionic Copolymer Scaffolds in Lithium Salt/Ionic Liquid Solutions. *Advanced Energy Materials*, 8(26):1801646, 2018.
- [44] Tao Chen, Weihua Kong, Zewen Zhang, Lei Wang, Yi Hu, Guoyin Zhu, Renpeng Chen, Lianbo Ma, Wen Yan, Yanrong Wang, Jie Liu, and Zhong Jin. Ionic Liquid-Immobilized Polymer Gel Electrolyte with Self-Healing Capability, High Ionic Conductivity and Heat Resistance for Dendrite-Free Lithium Metal Batteries. *Nano Energy*, 54:17–25, 2018.
- [45] Mohit Singh, Omolola Odusanya, and Nitash P. Balsara. Effect of Molecular Weight on the Mechanical and Electrical Properties of Block Copolymer Electrolytes. *Macromolecules*, 40(13):4578–4585, 2007.
- [46] Takeshi Niitani, Mikiya Shimada, Kiyoshi Kawamura, Kaoru Dokko, Young-Ho Rho, and Kiyoshi Kanamura. Synthesis of Li Ion Conductive PEO-PSt Block Copolymer Electrolyte with

- Micropore Separation Structure. *Electrochemical and Solid-State Letters*, 8(8):A385, 2005.
- [47] Nicholas P. Young, Didier Devaux, Rachna Khurana, Geoffrey W. Coates, and Nitash P. Balsara. Investigating Polypropylene-Poly(ethylene Oxide)-Polypropylene Triblock Copolymers as Solid Polymer Electrolytes for Lithium Batteries. *Solid State Ionics*, 263:87–94, 2014.
- [48] G. M. Stone, S. A. Mullin, A. A. Teran, D. T. Hallinan, A. M. Minor, A. Hexemer, and N. P. Balsara. Resolution of the Modulus versus Adhesion Dilemma in Solid Polymer Electrolytes for Rechargeable Lithium Metal Batteries. *Journal of the Electrochemical Society*, 159(3):A222–A227, 2012.
- [49] R. Bouchet, T. N. T. Phan, E. Beaudoin, D. Devaux, P. Davidson, D. Bertin, and R. Denoyel. Charge Transport in Nanostructured PS-PEO-PS Triblock Copolymer Electrolytes. *Macromolecules*, 47(8):2659–2665, 2014.
- [50] Katherine J. Harry, Xunxun Liao, Dilworth Y. Parkinson, Andrew M. Minor, and Nitash P. Balsara. Electrochemical Deposition and Stripping Behavior of Lithium Metal across a Rigid Block Copolymer Electrolyte Membrane. *Journal of The Electrochemical Society*, 162(14):A2699–A2706, 2015.
- [51] Katherine J. Harry, Daniel T. Hallinan, Dilworth Y. Parkinson, Alastair A. MacDowell, and Nitash P. Balsara. Detection of Subsurface Structures Underneath Dendrites Formed on Cycled Lithium Metal Electrodes. *Nature Materials*, 13(1):69–73, 2013.
- [52] M. Mykhaylov, M. Ganser, M. Klinsmann, F.E. Hildebrand, I. Guz, and R.M. McMeeking. An elementary 1-dimensional model for a solid state lithium-ion battery with a single ion conductor electrolyte and a lithium metal negative electrode. *Journal of the Mechanics and Physics of Solids*, 123:207–221, 2019.

- [53] John S. Newman and Karen E. Thomas-Alyea. *Electrochemical Systems*. J. Wiley, Hoboken, N.J, 3rd ed edition, 2004.
- [54] Marc Doyle and John Newman. Comparison of Modeling Predictions with Experimental Data from Plastic Lithium Ion Cells. *Journal of The Electrochemical Society*, 143(6):1890, 1996.
- [55] Yanping Ma. The Measurement of a Complete Set of Transport Properties for a Concentrated Solid Polymer Electrolyte Solution. *Journal of The Electrochemical Society*, 142(6):1859, 1995.
- [56] Danielle M. Pesko, Ksenia Timachova, Rajashree Bhattacharya, Mackensie C. Smith, Irune Villaluenga, John Newman, and Nitash P. Balsara. Negative Transference Numbers in Poly(ethylene oxide)-Based Electrolytes. *Journal of The Electrochemical Society*, 164(11):E3569–E3575, 2017.
- [57] Ksenia Timachova, Irune Villaluenga, Lisa Cirrincione, Mallory Gobet, Rajashree Bhattacharya, Xi Jiang, John Newman, Louis A. Madsen, Steven G. Greenbaum, and Nitash P. Balsara. Anisotropic Ion Diffusion and Electrochemically Driven Transport in Nanostructured Block Copolymer Electrolytes. *The Journal of Physical Chemistry B*, 122(4):1537–1544, 2018.
- [58] A. Ferrese, P. Albertus, J. Christensen, and J. Newman. Lithium Redistribution in Lithium-Metal Batteries. *Journal of the Electrochemical Society*, 159(10):A1615–A1623, 2012.
- [59] A. Ferrese and J. Newman. Modeling Lithium Movement over Multiple Cycles in a Lithium-Metal Battery. *Journal of the Electrochemical Society*, 161(6):A948–A954, 2014.
- [60] A. Ferrese and J. Newman. Mechanical Deformation of a Lithium-Metal Anode Due to a Very Stiff Separator. *Journal of the Electrochemical Society*, 161(9):A1350–A1359, 2014.
- [61] John Christensen and John Newman. Stress Generation and Fracture in Lithium Insertion Materials. *Journal of Solid State Electrochemistry*, 10(5):293–319, 2006.

- [62] Markus Klinsmann, Daniele Rosato, Marc Kamlah, and Robert M. McMeeking. Modeling Crack Growth during Li Extraction in Storage Particles Using a Fracture Phase Field Approach. *Journal of The Electrochemical Society*, 163(2):A102–A118, 2016.
- [63] E. Bohn, T. Eckl, M. Kamlah, and R. McMeeking. A Model for Lithium Diffusion and Stress Generation in an Intercalation Storage Particle with Phase Change. *Journal of the Electrochemical Society*, 160(10):A1638–A1652, 2013.
- [64] Zhiwei Cui, Feng Gao, and Jianmin Qu. A Finite Deformation Stress-Dependent Chemical Potential and Its Applications to Lithium Ion Batteries. *Journal of the Mechanics and Physics of Solids*, 60(7):1280–1295, 2012.
- [65] A.F. Bower, P.R. Guduru, and V.A. Sethuraman. A Finite Strain Model of Stress, Diffusion, Plastic Flow, and Electrochemical Reactions in a Lithium-Ion Half-Cell. *Journal of the Mechanics and Physics of Solids*, 59(4):804–828, 2011.
- [66] Magalie Huttin and Marc Kamlah. Phase-Field Modeling of Stress Generation in Electrode Particles of Lithium Ion Batteries. *Applied Physics Letters*, 101(13):133902, 2012.
- [67] A. Salvadori, R. McMeeking, D. Grazioli, and M. Magri. A coupled model of transport-reaction-mechanics with trapping. Part I - Small strain analysis. *Journal of the Mechanics and Physics of Solids*, 114:1–30, 2018.
- [68] Giovanna Bucci, Yet-Ming Chiang, and W. Craig Carter. Formulation of the coupled electrochemical–mechanical boundary-value problem, with applications to transport of multiple charged species. *Acta Materialia*, 104:33–51, 2016.
- [69] Wei Hong, Xuanhe Zhao, Jinxiang Zhou, and Zhigang Suo. A theory of coupled diffusion and large deformation in polymeric gels. *Journal of the Mechanics and Physics of Solids*, 56(5):1779–1793, 2008.

- [70] J.A.V. Butler. Studies in Heterogeneous Equilibria. Part III. a Kinetic Theory of Reversible Oxidation Potentials at Inert Electrodes. *Transactions of the Faraday Society*, pages 734–739, 1924.
- [71] Charles Monroe and John Newman. The Effect of Interfacial Deformation on Electrodeposition Kinetics. *Journal of The Electrochemical Society*, 151(6):A880, 2004.
- [72] Charles Monroe and John Newman. The Impact of Elastic Deformation on Deposition Kinetics at Lithium/Polymer Interfaces. *Journal of The Electrochemical Society*, 152(2):A396, 2005.
- [73] Zeeshan Ahmad and Venkatasubramanian Viswanathan. Stability of Electrodeposition at Solid-Solid Interfaces and Implications for Metal Anodes. *Physical Review Letters*, 119(5), 2017.
- [74] Pallab Barai, Kenneth Higa, and Venkat Srinivasan. Lithium Dendrite Growth Mechanisms in Polymer Electrolytes and Prevention Strategies. *Phys. Chem. Chem. Phys.*, 2017.
- [75] Raimund Koerver, Wenbo Zhang, Lea de Biasi, Simon Schweieler, Aleksandr O. Kondrakov, Stefan Kolling, Torsten Brezesinski, Pascal Hartmann, Wolfgang G. Zeier, and Jürgen Janek. Chemo-Mechanical Expansion of Lithium Electrode Materials – on the Route to Mechanically Optimized All-Solid-State Batteries. *Energy & Environmental Science*, 11(8):2142–2158, 2018.
- [76] Sangtae Kim, Soon Ju Choi, Kejie Zhao, Hui Yang, Giorgia Gobbi, Sulin Zhang, and Ju Li. Electrochemically driven mechanical energy harvesting. *Nature Communications*, 7:10146, 2016.
- [77] J.-N. Chazalviel. Electrochemical aspects of the generation of ramified metallic electrodeposits. *Physical Review A*, 42(12):7355–7367, 1990.
- [78] M. Rosso, T. Gobron, C. Brissot, J.-N. Chazalviel, and S. Lascaud. Onset of dendritic growth in lithium/polymer cells. *Journal of*

- Power Sources*, 97-98:804–806, 2001.
- [79] J. L. Barton and J. Om. Bockris. The Electrolytic Growth of Dendrites from Ionic Solutions. *Proceedings of the Royal Society A: Mathematical, Physical and Engineering Sciences*, 268(1335): 485–505, 1962.
- [80] Guangyu Liu and Wei Lu. A Model of Concurrent Lithium Dendrite Growth, SEI Growth, SEI Penetration and Regrowth. *Journal of The Electrochemical Society*, 164(9):A1826–A1833, 2017.
- [81] Rohan Akolkar. Mathematical Model of the Dendritic Growth During Lithium Electrodeposition. *Journal of Power Sources*, 232: 23–28, 2013.
- [82] J. W. Diggle, A. R. Despic, and J. O'M. Bockris. The Mechanism of the Dendritic Electrocrysallization of Zinc. *Journal of The Electrochemical Society*, 116(11):1503, 1969.
- [83] Charles Monroe and John Newman. Dendrite Growth in Lithium/Polymer Systems. *Journal of The Electrochemical Society*, 150(10):A1377, 2003.
- [84] Zeeshan Ahmad and Venkatasubramanian Viswanathan. Role of Anisotropy in Determining Stability of Electrodeposition at Solid-Solid Interfaces. *Physical Review Materials*, 1(5), 2017.
- [85] Zeeshan Ahmad, Tian Xie, Chimmay Maheshwari, Jeffrey C. Grossman, and Venkatasubramanian Viswanathan. Machine Learning Enabled Computational Screening of Inorganic Solid Electrolytes for Suppression of Dendrite Formation in Lithium Metal Anodes. *ACS Central Science*, 4(8):996–1006, 2018.
- [86] Pallab Barai, Kenneth Higa, and Venkat Srinivasan. Effect of Initial State of Lithium on the Propensity for Dendrite Formation: A Theoretical Study. *Journal of The Electrochemical Society*, 164 (2):A180–A189, 2017.
- [87] R. Raj and J. Wolfenstine. Current Limit Diagrams for Dendrite Formation in Solid-State Electrolytes for Li-Ion Batteries. *Journal*

- of Power Sources, 343:119–126, 2017.
- [88] M. D. Tikekar, L. A. Archer, and D. L. Koch. Stability Analysis of Electrodeposition across a Structured Electrolyte with Immobilized Anions. *Journal of the Electrochemical Society*, 161(6):A847–A855, 2014.
- [89] M. D. Tikekar, L. A. Archer, and D. L. Koch. Stabilizing Electrodeposition in Elastic Solid Electrolytes Containing Immobilized Anions. *Science Advances*, 2(7):e1600320–e1600320, 2016.
- [90] Mukul D. Tikekar, Snehashis Choudhury, Zhengyuan Tu, and Lynden A. Archer. Design Principles for Electrolytes and Interfaces for Stable Lithium-Metal Batteries. *Nature Energy*, 1(9):16114, 2016.
- [91] Robert M. McMeeking, Markus Ganser, Markus Klinsmann, and Felix E. Hildebrand. Metal Electrode Surfaces Can Roughen Despite the Constraint of a Stiff Electrolyte. *Journal of The Electrochemical Society*, 166(6):A984–A995, 2019.
- [92] P.P. Natsiavas, K. Weinberg, D. Rosato, and M. Ortiz. Effect of prestress on the stability of electrode electrolyte interfaces during charging in lithium batteries. *Journal of the Mechanics and Physics of Solids*, 95:92–111, 2016.
- [93] Markus Klinsmann, Felix E. Hildebrand, Markus Ganser, and Robert M. McMeeking. Dendritic cracking in solid electrolytes driven by lithium insertion. *Journal of Power Sources*, 442:227226, 2019.
- [94] Tara Foroozan, Fernando A. Soto, Vitaliy Yurkiv, Soroosh Sharifi-Asl, Ramasubramonian Deivanayagam, Zhennan Huang, Ramin Rojaee, Farzad Mashayek, Perla B. Balbuena, and Reza Shahbazian-Yassar. Synergistic Effect of Graphene Oxide for Impeding the Dendritic Plating of Li. *Advanced Functional Materials*, 28:1705917, 2018.

- [95] Zijian Hong and Venkatasubramanian Viswanathan. Phase-Field Simulations of Lithium Dendrite Growth with Open-Source Software. *ACS Energy Letters*, 3(7):1737–1743, 2018.
- [96] Asghar Aryanfar, Daniel Brooks, Boris V. Merinov, William A. Goddard, Agustín J. Colussi, and Michael R. Hoffmann. Dynamics of Lithium Dendrite Growth and Inhibition: Pulse Charging Experiments and Monte Carlo Calculations. *The Journal of Physical Chemistry Letters*, 5(10):1721–1726, 2014.
- [97] Mahsa Ebadi, Luciano T. Costa, C. Moyses Araujo, and Daniel Brandell. Modelling the Polymer Electrolyte/Li-Metal Interface by Molecular Dynamics simulations. *Electrochimica Acta*, 234:43–51, 2017.
- [98] Gerhard A. Holzapfel. *Nonlinear solid mechanics: a continuum approach for engineering*. Wiley, Chichester ; New York, 2000.
- [99] Clifford Truesdell and Walter Noll. *The Non-Linear Field Theories of Mechanics*. Springer Berlin Heidelberg, Berlin, Heidelberg, 2004. DOI: 10.1007/978-3-662-10388-3.
- [100] Ingo Müller. *Thermodynamik - Grundlagen der Materialtheorie*. Bertelsmann, Düsseldorf, 1973.
- [101] Markus Ganser, Felix E. Hildebrand, Marc Kamlah, and Robert M. McMeeking. A Finite Strain Electro-Chemo-Mechanical Theory for Ion Transport with Application to Binary Solid Electrolytes. *Journal of the Mechanics and Physics of Solids*, 125:681–713, 2019.
- [102] Charles W. Monroe and Charles Delacourt. Continuum Transport Laws for Locally Non-Neutral Concentrated Electrolytes. *Electrochimica Acta*, 114:649–657, 2013.
- [103] R. Krishna and J.A. Wesselingh. The Maxwell-Stefan Approach to Mass Transfer. *Chemical Engineering Science*, 52(6):861–911, 1997.
- [104] Wolfgang Dreyer, Clemens Guhlke, and Ruediger Mueller. Modeling of Electrochemical Double Layers in Thermodynamic

- Non-Equilibrium. *Phys. Chem. Chem. Phys.*, 17(40):27176–27194, 2015.
- [105] Robert M. McMeeking and Chad M. Landis. Electrostatic Forces and Stored Energy for Deformable Dielectric Materials. *Journal of Applied Mechanics*, 72(4):581, 2005.
- [106] Bernard D. Coleman and Walter Noll. The Thermodynamics of Elastic Materials with Heat Conduction and Viscosity. *Archive for Rational Mechanics and Analysis*, 13(1):167–178, 1963.
- [107] M.A. Biot. Variational Lagrangian-Thermodynamics of Nonisothermal Finite Strain Mechanics of Porous Solids and Thermomolecular Diffusion. *International Journal of Solids and Structures*, 13(6):579–597, 1977.
- [108] Hüsnü Dal and Christian Miehe. Computational Electro-Chemo-Mechanics of Lithium-Ion Battery Electrodes at Finite Strains. *Computational Mechanics*, 55(2):303–325, 2015.
- [109] Xiaoxuan Zhang, Andreas Krischok, and Christian Linder. A Variational Framework to Model Diffusion Induced Large Plastic Deformation and Phase Field Fracture During Initial Two-Phase Lithiation of Silicon Electrodes. *Computer Methods in Applied Mechanics and Engineering*, 312:51–77, 2016.
- [110] Daniele Rosato and Christian Miehe. Dissipative Ferroelectricity at Finite Strains. Variational Principles, Constitutive Assumptions and Algorithms. *International Journal of Engineering Science*, 74: 162–189, 2014.
- [111] R. W Ogden. *Non-Linear Elastic Deformations*. Dover Publications, New York, 2013. OCLC: 868280590.
- [112] Martin Z. Bazant. Theory of Chemical Kinetics and Charge Transfer based on Nonequilibrium Thermodynamics. *Accounts of Chemical Research*, 46(5):1144–1160, 2013.
- [113] P. W Atkins, Julio De Paula, and Valerie Walters. *Physical Chemistry*. W H Freeman, New York, 8 edition, 2006. OCLC:

- 153577665.
- [114] F.C. Larche and J.W. Cahn. The Interactions of Composition and Stress in Crystalline Solids. *Journal of Research of the National Bureau of Standards*, 89(6):467, 1984.
 - [115] A. Latz and J. Zausch. Thermodynamic Consistent Transport Theory of Li-Ion Batteries. *Journal of Power Sources*, 196(6):3296–3302, 2011.
 - [116] Manuel Landstorfer and Timo Jacob. Mathematical Modeling of Intercalation Batteries at the Cell Level and Beyond. *Chemical Society Reviews*, 42(8):3234, 2013.
 - [117] Charles W. Monroe and John Newman. Onsager’s Shortcut to Proper Forces and Fluxes. *Chemical Engineering Science*, 64(22):4804–4809, 2009.
 - [118] Wei Hong and Xiao Wang. A Phase-Field Model for Systems with Coupled Large Deformation and Mass Transport. *Journal of the Mechanics and Physics of Solids*, 61(6):1281–1294, 2013.
 - [119] Todd R. Ferguson and Martin Z. Bazant. Non-Equilibrium Thermodynamics of Porous Electrodes. *Journal of The Electrochemical Society*, 159(12):A1967–A1985, 2012.
 - [120] Sun Ung Kim and Venkat Srinivasan. A Method for Estimating Transport Properties of Concentrated Electrolytes from Self-Diffusion Data. *Journal of The Electrochemical Society*, 163(14):A2977–A2980, 2016.
 - [121] Oleg Borodin, Grant D. Smith, and Wesley Henderson. Li^+ Cation Environment, Transport, and Mechanical Properties of the LiTFSI Doped *N*-Methyl-*N* -alkylpyrrolidinium $^+$ TFSI $^-$ Ionic Liquids. *The Journal of Physical Chemistry B*, 110(34):16879–16886, 2006.
 - [122] Wei Lai and Francesco Ciucci. Mathematical Modeling of Porous Battery Electrodes: Revisit of Newman’s Model. *Electrochimica Acta*, 56(11):4369–4377, 2011.

- [123] M. Gouverneur, F. Schmidt, and M. Schönhoff. Negative effective Li transference numbers in Li salt/ionic liquid mixtures: does Li drift in the “Wrong” direction? *Physical Chemistry Chemical Physics*, 20(11):7470–7478, 2018.
- [124] James Evans, Colin A. Vincent, and Peter G. Bruce. Electrochemical Measurement of Transference Numbers in Polymer Electrolytes. *Polymer*, 28(13):2324–2328, 1987.
- [125] Deivid Pugal, Kwangmok Jung, Alvo Aabloo, and Kwang J Kim. Ionic Polymer-Metal Composite Mechanoelectrical Transduction: Review and Perspectives. *Polymer International*, 59(3):279–289, 2010.
- [126] Zicai Zhu, Hualing Chen, Longfei Chang, and Bo Li. Dynamic Model of Ion and Water Transport in Ionic Polymer-Metal Composites. *AIP Advances*, 1(4):040702, 2011.
- [127] Zicai Zhu, Kinji Asaka, Longfei Chang, Kentaro Takagi, and Hualing Chen. Multiphysics of ionic polymer–metal composite actuator. *Journal of Applied Physics*, 114(8):084902, 2013.
- [128] Markus Ganser, Felix E. Hildebrand, Markus Klinsmann, Matthias Hanauer, Marc Kamlah, and Robert M. McMeeking. An Extended Formulation of Butler-Volmer Electrochemical Reaction Kinetics Including the Influence of Mechanics. *Journal of The Electrochemical Society*, 166(4):H167–H176, 2019.
- [129] Marc Doyle, Thomas F. Fuller, and John Newman. Modeling of Galvanostatic Charge and Discharge of the Lithium/Polymer/Insertion Cell. *Journal of The Electrochemical Society*, 140(6):1526, 1993.
- [130] Nitash P. Balsara and John Newman. Relationship between Steady-State Current in Symmetric Cells and Transference Number of Electrolytes Comprising Univalent and Multivalent Ions. *Journal of The Electrochemical Society*, 162(14):A2720–A2722, 2015.

- [131] Daniel J. Brooks, Boris V. Merinov, William A. Goddard, Boris Kozinsky, and Jonathan Mailoa. Atomistic Description of Ionic Diffusion in PEO–LiTFSI: Effect of Temperature, Molecular Weight, and Ionic Concentration. *Macromolecules*, 51(21):8987–8995, 2018.
- [132] COMSOL Multiphysics. Reference Manual 5.3a, 2017.
- [133] M Maitra, M Sinha, A Mukhopadhyay, T Midya, U De, and S Tarafdar. Ion-Conductivity and Young’s Modulus of the Polymer Electrolyte Peo Ammonium Perchlorate. *Solid State Ionics*, 178(3-4):167–171, 2007.
- [134] Taylor Kelly, Bahar Moradi Ghadi, Sean Berg, and Haleh Ardebili. In Situ Study of Strain-Dependent Ion Conductivity of Stretchable Polyethylene Oxide Electrolyte. *Scientific Reports*, 6:20128, 2016.
- [135] F Robert Warfield, RW and Barnet. Elastic Constants of Bulk Polymers. Technical Report NOLTR 71-226, NAVAL ORDNANCE LAB, WHITE OAK, Silver Spring, Maryland, 1972.
- [136] H. Lundgren, J. Scheers, M. Behm, and G. Lindbergh. Characterization of the Mass-Transport Phenomena in a Superconcentrated LiTFSI:Acetonitrile Electrolyte. *Journal of the Electrochemical Society*, 162(7):A1334–A1340, 2015.
- [137] Caibin Xiao and Peter R. Trentaine. Apparent Molar Volumes of Aqueous Sodium Trifluoromethanesulfonate and Trifluoromethanesulfonic Acid from 283 K to 600 K and Pressures up to 20 Mpa. *Journal of Solution Chemistry*, 26(3):277–294, 1997.
- [138] M. Landstorfer, C. Guhlke, and W. Dreyer. Theory and Structure of the Metal-Electrolyte Interface Incorporating Adsorption and Solvation Effects. *Electrochimica Acta*, 201:187–219, 2016.
- [139] Stefanie Braun, Chihiro Yada, and Arnulf Latz. Thermodynamically Consistent Model for Space-Charge-Layer Formation in a Solid Electrolyte. *The Journal of Physical Chemistry C*, 119(39):22281–22288, 2015.

- [140] M. Marzantowicz, J.R. Dygas, and F. Krok. Impedance of Interface Between Peo:litfsi Polymer Electrolyte and Blocking Electrodes. *Electrochimica Acta*, 53(25):7417–7425, 2008.
- [141] John J. Fontanella and Mary C. Wintersgill. Low Frequency Dielectric Properties of Polyether Electrolytes. In *Polymer Electrolyte Reviews 2*. Elsevier Applied Science, London, 1989.
- [142] Yizhak Marcus and Glenn Hefter. Standard Partial Molar Volumes of Electrolytes and Ions in Nonaqueous Solvents. *Chemical Reviews*, 104(7):3405–3452, 2004.
- [143] John O'M Bockris, Amulya K. N Reddy, and Maria Gamboa-Aldeco. *Modern Electrochemistry 2A: Fundamentals of Electrodics*. 2000.
- [144] Carl H. Hamann and Wolf Vielstich. *Elektrochemie*. Wiley-VCH-Verlag GmbH &Co. KGaA, Weinheim, 4 edition, 2005. OCLC: 76740384.
- [145] Hongxin Ma, Xilin Xiong, Panpan Gao, Xi Li, Yu Yan, Alex A. Volinsky, and Yanjing Su. Eigenstress Model for Electrochemistry of Solid Surfaces. *Scientific Reports*, 6(1), 2016.
- [146] Bo Lu, Yicheng Song, Qinglin Zhang, Jie Pan, Yang-Tse Cheng, and Junqian Zhang. Voltage Hysteresis of Lithium Ion Batteries Caused by Mechanical Stress. *Phys. Chem. Chem. Phys.*, 18(6): 4721–4727, 2016.
- [147] FuQian Yang. Generalized Butler-Volmer Relation on a Curved Electrode Surface Under the Action of Stress. *Science China Physics, Mechanics & Astronomy*, 59(11):114611, 2016.
- [148] Gogi K. Singh, Gerbrand Ceder, and Martin Z. Bazant. Intercalation dynamics in rechargeable battery materials: General theory and phase-transformation waves in LiFePO₄. *Electrochimica Acta*, 53(26):7599–7613, 2008.
- [149] Peng Bai, Daniel A. Cogswell, and Martin Z. Bazant. Suppression of Phase Separation in LiFePO₄ Nanoparticles During Battery

- Discharge. *Nano Letters*, 11(11):4890–4896, 2011.
- [150] E.M. Gutman. Empiricism or Self-Consistent Theory in Chemical Kinetics? *Journal of Alloys and Compounds*, 434-435:779–782, 2007.
- [151] Arnulf Latz and Jochen Zausch. Thermodynamic Derivation of a Butler Volmer Model for Intercalation in Li-Ion Batteries. *Electrochimica Acta*, 110:358–362, 2013.
- [152] Wolfgang Dreyer, Clemens Guhlke, and Ruediger Mueller. A New Perspective on the Electron Transfer: Recovering the Butler-Volmer Equation in Non-Equilibrium Thermodynamics. *Physical Chemistry Chemical Physics*, 18(36):24966–24983, 2016.
- [153] C. E. D. Chidsey. Free Energy and Temperature Dependence of Electron Transfer at the Metal-Electrolyte Interface. *Science*, 251 (4996):919–922, 1991.
- [154] John F. Smalley, Harry O. Finklea, Christopher E. D. Chidsey, Matthew R. Linford, Stephen E. Creager, John P. Ferraris, Keli Chalfant, Thomas Zawodzinsk, Stephen W. Feldberg, and Marshall D. Newton. Heterogeneous Electron-Transfer Kinetics for Ruthenium and Ferrocene Redox Moieties through Alkanethiol Monolayers on Gold. *Journal of the American Chemical Society*, 125(7):2004–2013, 2003.
- [155] Stephen W. Feldberg and Israel Rubinstein. Unusual Quasi-Reversibility (UQR) or Apparent Non-Kinetic Hysteresis in Cyclic Voltammetry. *Journal of Electroanalytical Chemistry and Interfacial Electrochemistry*, 240(1-2):1–15, 1988.
- [156] Jean-Michel Savéant. Concerted Proton-Electron Transfers: Fundamentals and Recent Developments. *Annual Review of Analytical Chemistry*, 7(1):537–560, 2014.
- [157] Peng Bai and Martin Z. Bazant. Charge Transfer Kinetics at the Solid–Solid Interface in Porous Electrodes. *Nature Communications*, 5(1):3585, 2014.

- [158] Yi Zeng, Raymond B. Smith, Peng Bai, and Martin Z. Bazant. Simple formula for Marcus–Hush–Chidsey kinetics. *Journal of Electroanalytical Chemistry*, 735:77–83, 2014.
- [159] Daniel A. Cogswell. Quantitative Phase-Field Modeling of Dendritic Electrodeposition. *Physical Review E*, 92(1):011301, 2015.
- [160] M. van Soestbergen. Frumkin-Butler-Volmer Theory and Mass Transfer in Electrochemical Cells. *Russian Journal of Electrochemistry*, 48(6):570–579, 2012.
- [161] Jun Huang, Jianbo Zhang, and Michael Eikerling. Unifying Theoretical Framework for Deciphering the Oxygen Reduction Reaction on Platinum. *Physical Chemistry Chemical Physics*, 20(17):11776–11786, 2018.
- [162] Eden E. L. Tanner, Edward O. Barnes, Caitlin B. Tickell, Peter Goodrich, Christopher Hardacre, and Richard G. Compton. Application of Asymmetric Marcus–Hush Theory to Voltammetry in Room-Temperature Ionic Liquids. *The Journal of Physical Chemistry C*, 119(13):7360–7370, 2015.
- [163] Martin C. Henstridge, Eduardo Laborda, Neil V. Rees, and Richard G. Compton. Marcus–Hush–Chidsey Theory of Electron Transfer Applied to Voltammetry: A Review. *Electrochimica Acta*, 84:12–20, 2012.
- [164] V. A. Sethuraman, V. Srinivasan, A. F. Bower, and P. R. Guduru. In Situ Measurements of Stress-Potential Coupling in Lithiated Silicon. *Journal of The Electrochemical Society*, 157(11):A1253, 2010.
- [165] A. K. Pannikat and R. Raj. Measurement of an Electrical Potential Induced by Normal Stress Applied to the Interface of an Ionic Material at Elevated Temperatures. *Acta materialia*, 47(12):3423–3431, 1999.

- [166] Niek J. J. de Klerk, Alexandros Vasileiadis, Raymond B. Smith, Martin Z. Bazant, and Marnix Wagemaker. Explaining Key Properties of Lithiation in TiO₂-Anatase Li-Ion Battery Electrodes Using Phase-Field Modeling. *Physical Review Materials*, 1(2):025404, 2017.
- [167] Jongwoo Lim, Yiyang Li, Daan Hein Alsem, Hongyun So, Sang Chul Lee, Peng Bai, Daniel A. Cogswell, Xuzhao Liu, Norman Jin, Young-sang Yu, Norman J. Salmon, David A. Shapiro, Martin Z. Bazant, Tolek Tylliszczak, and William C. Chueh. Origin and Hysteresis of Lithium Compositional Spatiodynamics Within Battery Primary Particles. *Science*, 353 (6299):566–571, 2016.
- [168] Peter Stein, Ying Zhao, and Bai-Xiang Xu. Effects of Surface Tension and Electrochemical Reactions in Li-Ion Battery Electrode Nanoparticles. *Journal of Power Sources*, 332:154–169, 2016.
- [169] Hector Mendoza, Scott A. Roberts, Victor E. Brunini, and Anne M. Grillet. Mechanical and Electrochemical Response of a LiCoO₂ Cathode using Reconstructed Microstructures. *Electrochimica Acta*, 190:1–15, 2016.
- [170] P. Joos. Kinetic Equations for Transfer-Controlled Adsorption Kinetics. *Journal of Colloid and Interface Science*, 171(2):399–405, 1995.
- [171] G. B. Appetecchi, S. Scaccia, and S. Passerini. Investigation on the Stability of the Lithium-Polymer Electrolyte Interface. *Journal of the Electrochemical Society*, 147(12):4448–4452, 2000.
- [172] Nicole S. Schausler, Katherine J. Harry, Dilworth Y. Parkinson, Hiroshi Watanabe, and Nitash P. Balsara. Lithium Dendrite Growth in Glassy and Rubbery Nanostructured Block Copolymer Electrolytes. *Journal of The Electrochemical Society*, 2014.
- [173] S. Liu, N. Imanishi, T. Zhang, A. Hirano, Y. Takeda, O. Yamamoto, and J. Yang. Lithium Dendrite Formation in

- Li/Poly(ethylene oxide)-Lithium Bis(trifluoromethanesulfonyl)imide and N-Methyl-N-propylpiperidinium Bis(trifluoromethanesulfonyl)imide/Li Cells. *Journal of The Electrochemical Society*, 157(10):A1092, 2010.
- [174] Kevin T. Chu and Martin Z. Bazant. Surface Conservation Laws at Microscopically Diffuse Interfaces. *Journal of Colloid and Interface Science*, 315(1):319–329, 2007.
- [175] Erik G. Herbert, Stephen A. Hackney, Nancy J. Dudney, and P. Sudharshan Phani. Nanoindentation of High-Purity Vapor Deposited Lithium Films: The Elastic Modulus. *Journal of Materials Research*, 33(10):1335–1346, 2018.
- [176] Erik G. Herbert, Stephen A. Hackney, Violet Thole, Nancy J. Dudney, and P. Sudharshan Phani. Nanoindentation of High-Purity Vapor Deposited Lithium Films: A Mechanistic Rationalization of Diffusion-Mediated Flow. *Journal of Materials Research*, 33(10):1347–1360, 2018.
- [177] Erik G. Herbert, Stephen A. Hackney, Violet Thole, Nancy J. Dudney, and P. Sudharshan Phani. Nanoindentation of High-Purity Vapor Deposited Lithium Films: A Mechanistic Rationalization of the Transition from Diffusion to Dislocation-Mediated Flow. *Journal of Materials Research*, 33(10):1361–1368, 2018.
- [178] Sooraj Narayan and Lallit Anand. A Large Deformation Elastic–Viscoplastic Model for Lithium. *Extreme Mechanics Letters*, 24:21–29, 2018.
- [179] Geoffrey K. Creffield, Michael G. Down, and Richard J. Pulham. Electrical Resistivity of Liquid and Solid Lithium. *Journal of the Chemical Society, Dalton Transactions*, (21):2325, 1974.
- [180] Chethan Parthasarathy, Suguna Thanagasundaram, and Tseng King Jet. Study of applied pressure on open circuit

- characteristics and capacity of lithium polymer pouch cells. In *2016 Asian Conference on Energy, Power and Transportation Electrification (ACEPT)*, pages 1–6, Singapore, 2016. IEEE.
- [181] Nadine Dannehl, Sven Ole Steinmüller, Dorothée Vinga Szabó, Mathias Pein, Florian Sigel, Lars Esmezjan, Ulrich Hasenkox, Björn Schwarz, Sylvio Indris, and Helmut Ehrenberg. High-Resolution Surface Analysis on Aluminum Oxide-Coated $\text{Li}_{1.2}\text{Mn}_{0.55}\text{Ni}_{0.15}\text{Co}_{0.1}\text{O}_2$ with Improved Capacity Retention. *ACS Applied Materials & Interfaces*, 10(49):43131–43143, 2018.
- [182] C. Brissot. In Situ Concentration Cartography in the Neighborhood of Dendrites Growing in Lithium/Polymer-Electrolyte/Lithium Cells. *Journal of The Electrochemical Society*, 146(12):4393, 1999.

Schriftenreihe des Instituts für Angewandte Materialien

ISSN 2192-9963

- Band 1 Prachai Norajitra
Divertor Development for a Future Fusion Power Plant. 2011
ISBN 978-3-86644-738-7
- Band 2 Jürgen Prokop
Entwicklung von Spritzgießsonderverfahren zur Herstellung von Mikrobauteilen durch galvanische Replikation. 2011
ISBN 978-3-86644-755-4
- Band 3 Theo Fett
New contributions to R-curves and bridging stresses – Applications of weight functions. 2012
ISBN 978-3-86644-836-0
- Band 4 Jérôme Acker
Einfluss des Alkali/Niob-Verhältnisses und der Kupfer-dotierung auf das Sinterverhalten, die Strukturbildung und die Mikrostruktur von bleifreier Piezokeramik ($K_{0,5}Na_{0,5}NbO_3$). 2012
ISBN 978-3-86644-867-4
- Band 5 Holger Schwaab
Nichtlineare Modellierung von Ferroelektrika unter Berücksichtigung der elektrischen Leitfähigkeit. 2012
ISBN 978-3-86644-869-8
- Band 6 Christian Dethloff
Modeling of Helium Bubble Nucleation and Growth in Neutron Irradiated RAFM Steels. 2012
ISBN 978-3-86644-901-5
- Band 7 Jens Reiser
Duktilisierung von Wolfram. Synthese, Analyse und Charakterisierung von Wolframlaminate aus Wolframfolie. 2012
ISBN 978-3-86644-902-2
- Band 8 Andreas Sedlmayr
Experimental Investigations of Deformation Pathways in Nanowires. 2012
ISBN 978-3-86644-905-3

- Band 9 Matthias Friedrich Funk
Microstructural stability of nanostructured fcc metals during cyclic deformation and fatigue. 2012
ISBN 978-3-86644-918-3
- Band 10 Maximilian Schwenk
Entwicklung und Validierung eines numerischen Simulationsmodells zur Beschreibung der induktiven Ein- und Zweifrequenzrandschichthärtung am Beispiel von vergütetem 42CrMo4. 2012
ISBN 978-3-86644-929-9
- Band 11 Matthias Merzkirch
Verformungs- und Schädigungsverhalten der verbundstrang-gepressten, federstahldrahtverstärkten Aluminiumlegierung EN AW-6082. 2012
ISBN 978-3-86644-933-6
- Band 12 Thilo Hammers
Wärmebehandlung und Recken von verbundstrang-gepressten Luftfahrtprofilen. 2013
ISBN 978-3-86644-947-3
- Band 13 Jochen Lohmiller
Investigation of deformation mechanisms in nanocrystalline metals and alloys by *in situ* synchrotron X-ray diffraction. 2013
ISBN 978-3-86644-962-6
- Band 14 Simone Schreijäg
Microstructure and Mechanical Behavior of Deep Drawing DC04 Steel at Different Length Scales. 2013
ISBN 978-3-86644-967-1
- Band 15 Zhiming Chen
Modelling the plastic deformation of iron. 2013
ISBN 978-3-86644-968-8
- Band 16 Abdullah Fatih Çetinel
Oberflächendefektausheilung und Festigkeitssteigerung von niederdruckspritzgegossenen Mikrobiegebalken aus Zirkoniumdioxid. 2013
ISBN 978-3-86644-976-3
- Band 17 Thomas Weber
Entwicklung und Optimierung von gradierten Wolfram/EUROFER97-Verbindungen für Divertorkomponenten. 2013
ISBN 978-3-86644-993-0

- Band 18 Melanie Senn
Optimale Prozessführung mit merkmalsbasierter Zustandsverfolgung. 2013
ISBN 978-3-7315-0004-9
- Band 19 Christian Mennerich
Phase-field modeling of multi-domain evolution in ferromagnetic shape memory alloys and of polycrystalline thin film growth. 2013
ISBN 978-3-7315-0009-4
- Band 20 Spyridon Korres
On-Line Topographic Measurements of Lubricated Metallic Sliding Surfaces. 2013
ISBN 978-3-7315-0017-9
- Band 21 Abhik Narayan Choudhury
Quantitative phase-field model for phase transformations in multi-component alloys. 2013
ISBN 978-3-7315-0020-9
- Band 22 Oliver Ulrich
Isothermes und thermisch-mechanisches Ermüdungsverhalten von Verbundwerkstoffen mit Durchdringungsgefüge (Preform-MMCs). 2013
ISBN 978-3-7315-0024-7
- Band 23 Sofie Burger
High Cycle Fatigue of Al and Cu Thin Films by a Novel High-Throughput Method. 2013
ISBN 978-3-7315-0025-4
- Band 24 Michael Teutsch
Entwicklung von elektrochemisch abgeschiedenem LIGA-Ni-Al für Hochtemperatur-MEMS-Anwendungen. 2013
ISBN 978-3-7315-0026-1
- Band 25 Wolfgang Rheinheimer
Zur Grenzflächenanisotropie von SrTiO₃. 2013
ISBN 978-3-7315-0027-8
- Band 26 Ying Chen
Deformation Behavior of Thin Metallic Wires under Tensile and Torsional Loadings. 2013
ISBN 978-3-7315-0049-0

- Band 27 Sascha Haller
Gestaltfindung: Untersuchungen zur Kraftkegelmethode. 2013
ISBN 978-3-7315-0050-6
- Band 28 Nicht erschienen
- Band 29 Gunnar Picht
Einfluss der Korngroße auf ferroelektrische Eigenschaften dotierter $Pb(Zr_{1-x}Ti_x)O_3$ Materialien. 2013
ISBN 978-3-7315-0106-0
- Band 30 Esther Held
Eigenspannungsanalyse an Schichtverbunden mittels inkrementeller Bohrlochmethode. 2013
ISBN 978-3-7315-0127-5
- Band 31 Pei He
On the structure-property correlation and the evolution of Nanofeatures in 12-13.5% Cr oxide dispersion strengthened ferritic steels. 2014
ISBN 978-3-7315-0141-1
- Band 32 Jan Hoffmann
Ferritische ODS-Stähle – Herstellung, Umformung und Strukturanalyse. 2014
ISBN 978-3-7315-0157-2
- Band 33 Wiebke Sittel
Entwicklung und Optimierung des Diffusionsschweißens von ODS Legierungen. 2014
ISBN 978-3-7315-0182-4
- Band 34 Osama Khalil
Isothermes Kurzzeitermüdungsverhalten der hoch-warmfesten Aluminium-Knetlegierung 2618A ($AlCu2Mg1,5Ni$). 2014
ISBN 978-3-7315-0208-1
- Band 35 Nicht erschienen
- Band 36 Christoph Hage
Grundlegende Aspekte des 2K-Metallpulverspritzgießens. 2014
ISBN 978-3-7315-0217-3
- Band 37 Barthomiej Albiński
Instrumentierte Eindringprüfung bei Hochtemperatur für die Charakterisierung bestrahlter Materialien. 2014
ISBN 978-3-7315-0221-0

- Band 38 Tim Feser
Untersuchungen zum Einlaufverhalten binärer alpha-Messinglegierungen unter Ölschmierung in Abhängigkeit des Zinkgehaltes. 2014
ISBN 978-3-7315-0224-1
- Band 39 Jörg Ettrich
Fluid Flow and Heat Transfer in Cellular Solids. 2014
ISBN 978-3-7315-0241-8
- Band 40 Melanie Syha
Microstructure evolution in strontium titanate Investigated by means of grain growth simulations and x-ray diffraction contrast tomography experiments. 2014
ISBN 978-3-7315-0242-5
- Band 41 Thomas Haas
Mechanische Zuverlässigkeit von gedruckten und gasförmig abgeschiedenen Schichten auf flexilem Substrat. 2014
ISBN 978-3-7315-0250-0
- Band 42 Aron Kneer
Numerische Untersuchung des Wärmeübertragungsverhaltens in unterschiedlichen porösen Medien. 2014
ISBN 978-3-7315-0252-4
- Band 43 Manuel Feuchter
Investigations on Joule heating applications by multiphysical continuum simulations in nanoscale systems. 2014
ISBN 978-3-7315-0261-6
- Band 44 Alexander Vondrouš
Grain growth behavior and efficient large scale simulations of recrystallization with the phase-field method. 2014
ISBN 978-3-7315-0280-7
- Band 45 Tobias Kennerknecht
Fatigue of Micro Molded Materials – Aluminum Bronze and Yttria Stabilized Zirconia. 2014
ISBN 978-3-7315-0293-7
- Band 46 Christopher Scherr
Elektrochemisches Verhalten von Lithium-Schwefel-Zellen mit unterschiedlicher Kathodenstruktur. 2015
ISBN 978-3-7315-0296-8

- Band 47 Konstantin Frölich
Der Decal-Prozess zur Herstellung katalysatorbeschichteter Membranen für PEM-Brennstoffzellen. 2015
ISBN 978-3-7315-0334-7
- Band 48 Benedikt Haspel
Werkstoffanalytische Betrachtung der Eigenschaften von mittels neuartiger RTM-Fertigungsprozesse hergestellten glasfaserverstärkten Polymerverbunden. 2015
ISBN 978-3-7315-0337-8
- Band 49 Marco Berghoff
Skalenübergreifende Modellierung und Optimierung vom atomistischen kristallinen Phasenfeldmodell bis zur mesoskopischen Phasenfeldmethode. 2015
ISBN 978-3-7315-0416-0
- Band 50 Michael Selzer
Mechanische und Strömungsmechanische Topologie-optimierung mit der Phasenfeldmethode. 2016
ISBN 978-3-7315-0431-3
- Band 51 Michael Mahler
Entwicklung einer Auswertemethode für bruchmechanische Versuche an kleinen Proben auf der Basis eines Kohäsivzonenmodells. 2016
ISBN 978-3-7315-0441-2
- Band 52 Christoph Bohnert
Numerische Untersuchung des Verformungs- und Bruchverhaltens von einkristallinem Wolfram auf mikroskopischer Ebene. 2016
ISBN 978-3-7315-0444-3
- Band 53 Stefan Guth
Schädigung und Lebensdauer von Nickelbasislegierungen unter thermisch-mechanischer Ermüdungsbeanspruchung bei verschiedenen Phasenlagen. 2016
ISBN 978-3-7315-0445-0
- Band 54 Markus Klinsmann
The Effects of Internal Stress and Lithium Transport on Fracture in Storage Materials in Lithium-Ion Batteries. 2016
ISBN 978-3-7315-0455-9

- Band 55 Thomas Straub
Experimental Investigation of Crack Initiation in Face-Centered Cubic Materials in the High and Very High Cycle Fatigue Regime. 2016
ISBN 978-3-7315-0471-9
- Band 56 Maren Lepple
Kupfer- und Eisenoxide als Konversions-Elektrodenmaterialien für Lithium-Ionen-Batterien: Thermodynamische und Elektrochemische Untersuchungen. 2016
ISBN 978-3-7315-0482-5
- Band 57 Stefan Andreas Slaby
Charakterisierung und Bewertung der Zug- und Ermüdungseigenschaften von Mikrobauteilen aus 17-4PH Edelstahl. Ein Vergleich von mikropulverspritzgegossenem und konventionell hergestelltem Material. 2017
ISBN 978-3-7315-0484-9
- Band 58 Kumar Ankit
Phase-field modeling of microstructural pattern formation in alloys and geological veins. 2016
ISBN 978-3-7315-0491-7
- Band 59 Kuo Zhang
Characterization and Modeling of the Ratcheting Behavior of the Ferritic-Martensitic Steel P91. 2017
ISBN 978-3-7315-0503-7
- Band 60 Nicht erschienen
- Band 61 Fabian Lemke
Untersuchung des Sinterverhaltens von SrTiO₃ unter Berücksichtigung der Defektchemie. 2016
ISBN 978-3-7315-0510-5
- Band 62 Johannes Kümmel
Detaillierte Analyse der Aufbauschneidenbildung bei der Trockenzerspanung von Stahl C45E mit Berücksichtigung des Werkzeugverschleißes. 2016
ISBN 978-3-7315-0518-1
- Band 63 László Hagymási
Modellierung der Stoffübertragung beim Niederdruck-carbonitrieren mit Ammoniak und Acetylen. 2016
ISBN 978-3-7315-0568-6

- Band 64 Reza Eslami
A novel micro-mechanical model for prediction of multiaxial high cycle fatigue at small scales. 2017
ISBN 978-3-7315-0583-9
- Band 65 Sebastian Schulz
Phase-field simulations of multi-component solidification and coarsening based on thermodynamic datasets. 2017
ISBN 978-3-7315-0618-8
- Band 66 Markus Stricker
Die Übertragung von mikrostrukturellen Eigenschaften aus der diskreten Versetzungs dynamik in Kontinuumsbeschreibungen. 2017
ISBN 978-3-7315-0658-4
- Band 67 Luis Straßberger
Untersuchung und Modellierung des viscoplastischen Verformungsverhaltens oxidpartikelverstärkter Stähle. 2018
ISBN 978-3-7315-0674-4
- Band 68 Mark Wobrock
Microplasticity of idealized single crystalline Ag cantilevers characterized with methods of high resolution. 2017
ISBN 978-3-7315-0682-9
- Band 69 Amritesh Kumar
Micromechanical study on the deformation behaviour of directionally solidified NiAl-Cr eutectic composites. 2017
ISBN 978-3-7315-0694-2
- Band 70 Johannes Hötzer
Massiv-parallele und großskalige Phasenfeldsimulationen zur Untersuchung der Mikrostrukturentwicklung. 2017
ISBN 978-3-7315-0693-5
- Band 71 Thomas Hupfer
Herstellung von LATP für den Einsatz als Festkörper-elektrolyt und dessen Eigenschaften. 2017
ISBN 978-3-7315-0702-4
- Band 72 Florentin Pottmeyer
Schädigungsverhalten von in CFK-Laminaten eingebetteten Inserts unter bauteilnahen Beanspruchungen. 2017
ISBN 978-3-7315-0719-2

- Band 73 Andres Höweling
Untersuchung der Hochvoltstabilität und Tiefentladung von dotierten LiNi_{0,5}Mn_{1,5}O₄-Hochvoltspinellen. 2018
ISBN 978-3-7315-0728-4
- Band 74 Tabea Gisela Schwark
Deformation and Fracture Properties of the Soft Magnetic Composite Somaloy 700 3P on Different Length Scales. 2018
ISBN 978-3-7315-0759-8
- Band 75 Klaudia Lichtenberg
Metallmatrixverbunde mit Verstärkungselementen aus metallischem Glas Ni₆₀Nb₂₀Ta₂₀ – Herstellung und Charakterisierung. 2018
ISBN 978-3-7315-0782-6
- Band 76 Claudio Findeisen
Charakterisierung und Modellierung von instabilen Metamaterialien. 2019
ISBN 978-3-7315-0869-4
- Band 77 Nilessha Mishra
Influence of strain on the functionality of ink-jet printed thin films and devices on flexible substrates. 2019
ISBN 978-3-7315-0853-3
- Band 78 Simon Werner Bonk
Plastische Verformungsmechanismen in hochgradig kaltgewalzten, ultrafeinkörnigen Wolframblechen. 2019
ISBN 978-3-7315-0878-6
- Band 79 Tim Gräning
Herstellung, Charakterisierung und Optimierung von austenitischen ODS Stählen. 2019
ISBN 978-3-7315-0732-1
- Band 80 Peter Rupp
Herstellung, Prüfung und Modellierung neuartiger hybrider Aluminiumschaum-CFK-Sandwichverbunde. 2019
ISBN 978-3-7315-0880-9
- Band 81 Benjamin Sebastian Ehreiser
Einfluss mechanischer Lasten auf die Herstellung von Stahl-Glaskeramik-Verbunden. 2019
ISBN 978-3-7315-0954-7

- Band 82 Hans Giel
Weiterentwicklung experimenteller Methoden zur Ermittlung thermodynamischer Werkstoffdaten von Lithium-Ionen-Batterien. 2020
ISBN 978-3-7315-0981-3
- Band 83 Anna Trauth
Characterisation and Modelling of Continuous-Discontinuous Sheet Moulding Compound Composites for Structural Applications. 2020
ISBN 978-3-7315-0950-9
- Band 84 Jonas Johannes Hüther
The Impact of Recycling on the Fibre and the Composite Properties of Carbon Fibre Reinforced Plastics. 2020
ISBN 978-3-7315-0983-7
- Band 85 Nicolas A. Mayer
Thermodynamik von Kobaltoxid Anodenmaterialien für Lithium-Ionen-Batterien und ihr elektrochemisches Verhalten. 2020
ISBN 978-3-7315-0996-7
- Band 86 Ulrich Führer
Untersuchung und Modellierung des Haltezeiteinflusses auf die zyklische Entfestigung ferritisch-martensitischer Stähle. 2020
ISBN 978-3-7315-0837-3
- Band 87 Ebru Cihan
Structure evolution in tribological interfaces studied by multilayer model alloys. 2020
ISBN 978-3-7315-0999-8
- Band 88 Markus Sudmanns
Entwicklung einer Kontinuumsbeschreibung für die Versetzungsmobilität in Versetzungsnetzwerken. 2020
ISBN 978-3-7315-1001-7
- Band 89 Tao Zhang
Phase-field Modeling of Phase Changes and Mechanical Stresses in Electrode Particles of Secondary Batteries. 2020
ISBN 978-3-7315-1002-4

Band 90 Markus Ganser
**On the Electro-Chemo-Mechanical Coupling
in Solid State Batteries and its Impact
on Morphological Interface Stability.** 2021
ISBN 978-3-7315-1047-5

KARLSRUHER INSTITUT FÜR TECHNOLOGIE (KIT)
SCHRIFTENREIHE DES INSTITUTS FÜR ANGEWANDTE MATERIALIEN

Solid state batteries with a lithium metal electrode are considered the next generation of high energy battery technology. Unfortunately, lithium metal is prone to harmful protrusion or dendrite growth which causes dangerous cell failure. Although solid state electrolytes have shown a promising potential to stabilize the interface morphology, a clear understanding of the related mechanisms and material requirements is still missing. Within this work the problem of protrusion growth is tackled by deriving a novel electro-chemo-mechanical theory tailored for binary solid state batteries which is then used to discuss the impact of mechanics on interface stability by extensive numerical studies.

ISSN 2192-9963
ISBN 978-3-7315-1047-5



GEDRUCKT AUF FSC-ZERTIFIZIERTEM PAPIER